EXPLORING MULTI-ANNUAL CHANGES IN THE BIOPHYSICAL ENVIRONMENT OF THE BLACK SEA

Thesis submitted in accordance with the requirements of the University of Liverpool for the degree of Doctor of Philosophy

By

Valérie Nahir Renée Le Guennec

Department of Earth and Ocean Sciences

University of Liverpool

National Oceanography Center

January 2020

Declaration

I certify that the work described in this thesis is my own except where otherwise stated and has not previously been submitted for any degree at this or any other University.

Valérie N. R. Le Guennec

Acknowledgements

Looking back at the years I dedicated to work on my PhD, I realize that it would not have been possible without the help and support of numerous people. As the proverb goes: “If you want to go fast, go alone. If you want to go far, go together.”

I would like to express my gratitude to my supervisors Dr. Heather Cannaby, Dr. Alessandro Tagliabue, Dr. Jason Holt and Dr. Sarah Wakelin for their support, guidance, and patience over the last couple of years. Your advices and overlapping expertise were very helpful and allowed me to approach a science problem with different perspectives. A special thank you to Sarah Wakelin for teaching me how to use the modelling tools and helping me debug the code when necessary.

I would like to extend my deepest gratitude to the people from the modelling group in the National Oceanography Center (Gaby, Nico, Ash, Sarah, Yujuan, Jason, Maria), who supported me during my PhD and shared their expertise in numerical modelling, an important skill I developed along the journey. I am also grateful to Dr. Jan Freund for his help on the mathematical aspects for time series analysis.

A big thank you as well to the researchers from the University of Liverpool for their support (especially Pascal and Ric). I also would like to thank Dr. Alessandro Tagliabue for giving me the opportunity to take part in a research cruise onboard the James Cook. This was a unique and amazing experience that I will never forget. Thank you to the amazing people I got to meet during this expedition: Malcolm, Azyzy. Special thanks to Jason for giving me the opportunity to conduct a short research internship with the NOC. The knowledge acquired was very useful for the next steps in my PhD.

I am extremely grateful to my insightful mentor Gaby, who was very supportive while she was at NOC and even after she left Liverpool for Ecuador. Thank you for believing in my abilities and your unwavering support. You were a good listener and above all, a great friend. A big thank you to Nico, I was very amazed by how quickly you could solve problems, I really enjoyed our discussions, and I appreciated all the insights you provided regarding my work. I also wish to thank Ash for his invaluable help in my research. All the coffee sessions added a great working atmosphere and led to fruitful discussions that guided me in the right direction. Besides that, I really enjoyed learning very cool things in Matlab (vectorization, parallel computing, and particle tracking). I also would like to recognize the assistance I received from

Prof. Ric Williams. Thank you for being available any time I needed, and for your constructive suggestions regarding an entire Chapter of my PhD.

I am grateful for my supervisors and Gino, for proof – reading the manuscript. A great thank you should also go to the examiners Dr Tim Smyth and Prof. Chris Hughes for taking the time to read and correct this manuscript.

Thank you to all the wonderful people I met along the way (Tony Lee, Theo, Rafael, Christina, Dakui, …) and especially the ones from the Archery and Coding and Robotics Club. A very big thank you is addressed to the best security guards Dave and Steve, whose personality, curiosity, and presence were a major source of motivation to keep going.

The journey would not have been the same without you, Jonathan. As a French, I learned to appreciate some of the quirks that English people do. Thank you for being here and for being very supportive. It has been a beautiful adventure when you were by my side. You always believed in me, encouraged me, and I will never forget.

I am deeply thankful to my beloved grandparents (Papi Dédé and Mamie Nono), who always reached out to me and showed an immense amount of support, no matter what. You both are a great source of inspiration for me. I cannot end without mentioning the people closest to my heart, who always took care of me, my parents: Malena and Bernard. Your love and everlasting support gave me the strength and resources to continue. I am proud to be your daughter and no words can fully express my profound gratitude. I also feel blessed to have two wonderful brothers. Many thanks to my sweet brothers David and Alexis, I knew I could always count on your kindness and support.

To my family, that I love above all else.

For my dear parents,

Contents **Page**

Table of contents **Page**

Table of contents **Page**

Table of contents **Page**

Table of contents **Page**

List of figures **Page**

List of figures **Page**

List of figures **Page**

List of figures **Page**

List of figures **Page**

List of figures **Page**

List of figures **Page**

List of figures **Page**

List of figures **Page**

List of figures **Page**

List of figures **Page**

List of figures **Page**

List of figures **Page**

List of figures **Page**

List of tables **Page**

List of tables **Page**

List of tables **Page**

List of tables **Page**

Chapter 1: Introduction and background

The science explored in this thesis focuses especially on the marine basin that is the Black Sea. This thesis aims at describing and understanding patterns in chlorophyll *a* concentration over long time scales and explores possible relations with the formation of a local water mass. Satellite observations, along with some *in situ* observations are used to study this natural laboratory (Stanev, 2005), but this is also complemented with a strong "*in silico*" approach through numerical modelling. On the one hand, the Black Sea is an ideal choice as its relatively small scale allows the study biophysical responses to environmental variability. But, on the other hand, studying this regional basin is quite challenging because in many aspects, it is distinct from the typical conditions described in the global ocean. Those specificities are first introduced to the reader before stating clearly the objectives of the thesis.

1.1 Black Sea setting and physics

1.1.1 Main characteristics of the basin

The Black Sea is the largest semi-enclosed basin in the South-Eastern part of Europe (Fig. 1.1) with a surface area of 423 500 km^2 (Kideys, 1994) which is about a fifth of the surface area of the Mediterranean Sea in comparison. The total volume is about 537 000 km^3 (Kideys, 1994). It is bordered by several countries (Bulgaria, Romania, Ukraine, Russia, Georgia and Turkey) and has only two restricted connections.

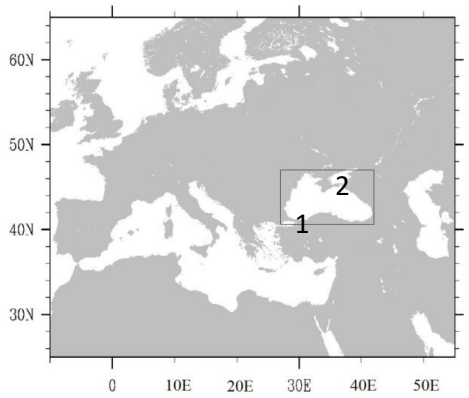

Figure 1.1: Map of Europe with indication of the Black Sea under the black rectangle. The numbers 1 and 2 indicate the location of respectively the Bosphorus Strait and the Kerch Strait.

The first connection is with the Sea of Marmara and consequently with the Mediterranean basin through the narrow (0.76 - 3.60km) and shallow (32-34m at its still) Bosphorus Strait (Number 1 in Fig.1.1). The second connection is the shallow Kerch Strait (Number 2 in Fig.1.1), allowing the exchanges with the Azov Sea (a smaller, otherwise enclosed, sea) located in the North-Eastern part of the Black Sea. The Black Sea has two main deep basins (Western and Eastern) reaching a maximal depth of 2212 m (Zaitsev, 1992; Mee, 1992). These basins contrast with a shallow shelf with a maximum depth of 200 m. The shelf is narrow all around the Black Sea basin but expands on the North Western part. The North Western Shelf (later referred as NWS) represents about 13% of the total area (Capet et al., 2012).

1.1.2 Circulation

The Black Sea basin scale circulation is characterized by a strong cyclonic (anti-clockwise) Rim Current which circulates along the continental slope of the Black Sea and is intensified during winter (Oguz et al., 1993). Indeed, according to Stanev et al. (2014), the horizontal transport almost doubles in winter. The off-shelf region is dominated by two cyclonic gyres located on the Western and Eastern sides of the basin (Kubryakov et al., 2016). The instability of the Rim Current contributes to the emergence of various anti-cyclonic eddies between this current and the coast (Korotaev et al., 2003; Zatsepin et al., 2003, see Fig.1.2) but also, more rarely, in the center of the basin (Zatsepin et al., 2003; Kubryakov and Stanichny, 2015; see Fig.1.2). Although the Rim current acts as a barrier and restricts the transfer between the coast and the open Black Sea, the formation of mesoscale eddies can drive horizontal exchanges between the shelf and deep areas (Oguz et al., 2002). The positive curl of the wind stress (cyclonic wind pattern) is known to be the main forcing explaining the cyclonic circulation of the Rim Current and the gyres (Özsoy and Ünlüata, 1997; Kubryakov and Stanichny, 2015). Technological improvements, notably with the use of satellite and the development of sophisticated models (Stanev, 1990; Oguz et al., 1995; Staneva et al., 2001; Zatsepin et al., 2003) helped develop the description and understanding of this general circulation.

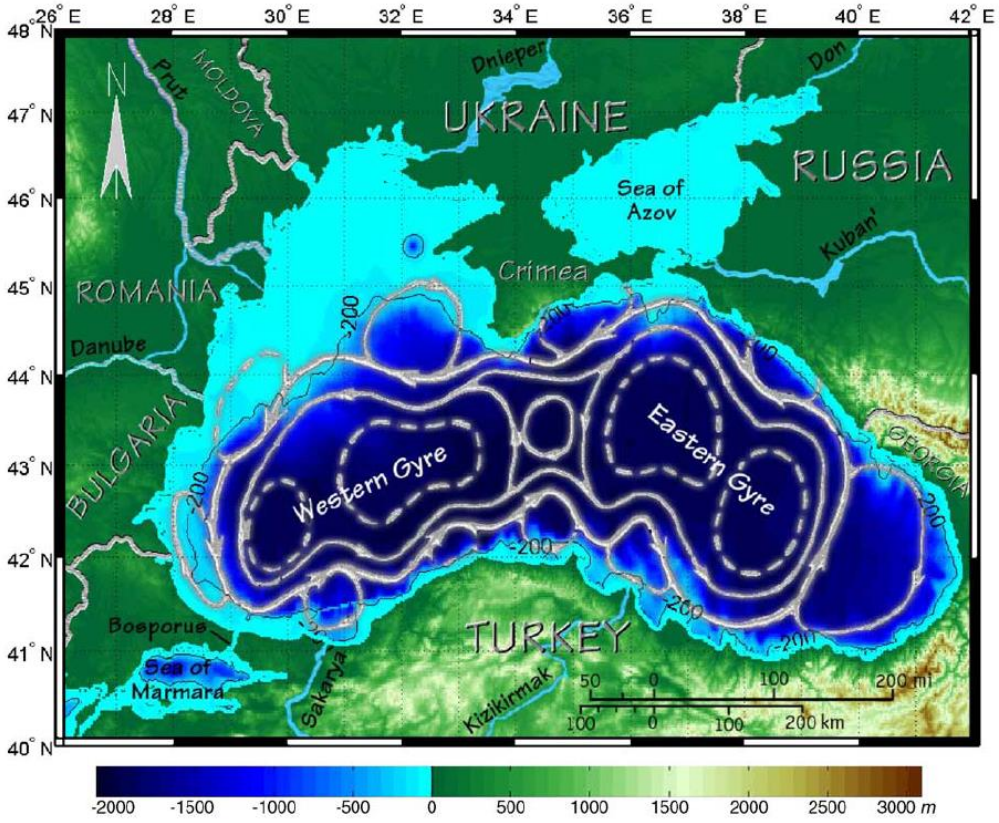

Figure 1.2: Black Sea geography, bottom topography and circulation (figure from Chu et al., 2005).

1.1.3 Stratification and anoxicity

The Black Sea has a strong vertical density gradient caused by the halocline (described in detail in Section 1.3.2 below), resulting in a significant reduction of the vertical mixing (Tolmazin, 1985). Below 500 m depth, the waters are stagnant, with a residence time of few years at the layer of the main pycnocline (Buesseler et al., 1994), to 330-1500 years for the deepest waters (Stewart et al., 2007). Besides that, data from Stanev (1990) state that the vertical circulation is weaker by a factor of 10 compared to the integrated horizontal circulation. The restricted mixing between the surface and deep waters leads to a lack of ventilation of the waters below the permanent pycnocline. These conditions favour the formation and stabilization of a large reservoir of anoxic waters that represented about 85% of the total water volume (Yakushev et al., 2007). The deep waters are also marked by high concentration of hydrogen sulfide H_2S (see Fig.1.3).

As a consequence of the strong vertical stratification, the surface layer (from 0 to 50-200m) is nearly saturated in oxygen and is the place of biological production (Fig.1.3a). At the surface, the oxygen is at saturation (around 250µM) and it decreases progressively until the detection limit around 5 µM (~150m depth). Below this oxygenated zone there is a high concentration of hydrogen sulfide which increases with depth and can reach concentrations of 425 µM (Murray et al., 1989). The level of the strong pycnocline is accompanied by a chemocline which marks the transition from the oxygenated to the anoxic part. This is the so-called sub-oxic layer. It is defined by a decrease of oxygen concentration below the limit of detection (5µM) and by the onset of hydrogen sulfide concentration (Murray et al., 1995).

On the one hand, this stratification constrains the complex vertical biogeochemical structure (Fig.1.3b), and on the other hand, it influences deeply the biodiversity which is only approximately one third of that in the Mediterranean (Zaitsev et al., 2002).

There is a decoupling between the surface and the deep waters of the Black Sea and the surface layer is then very sensitive to environmental changes (Konovalov and Murray, 2001; Oguz and Velikova, 2010) and to anthropogenic pressures (Mee, 1992; Kideys, 2002; Oguz et al., 2008). This feature combined with a restriction of the exchange with other basins across the Straits, make the Black Sea the largest anoxic basin in the world (Murray et al., 1989; He et al., 2012). The role of global warming in enhancing the vertical stratification and therefore decreasing the ventilation in the deep layers also has an impact on the oxygen content (He et al., 2012; Capet et al., 2016).

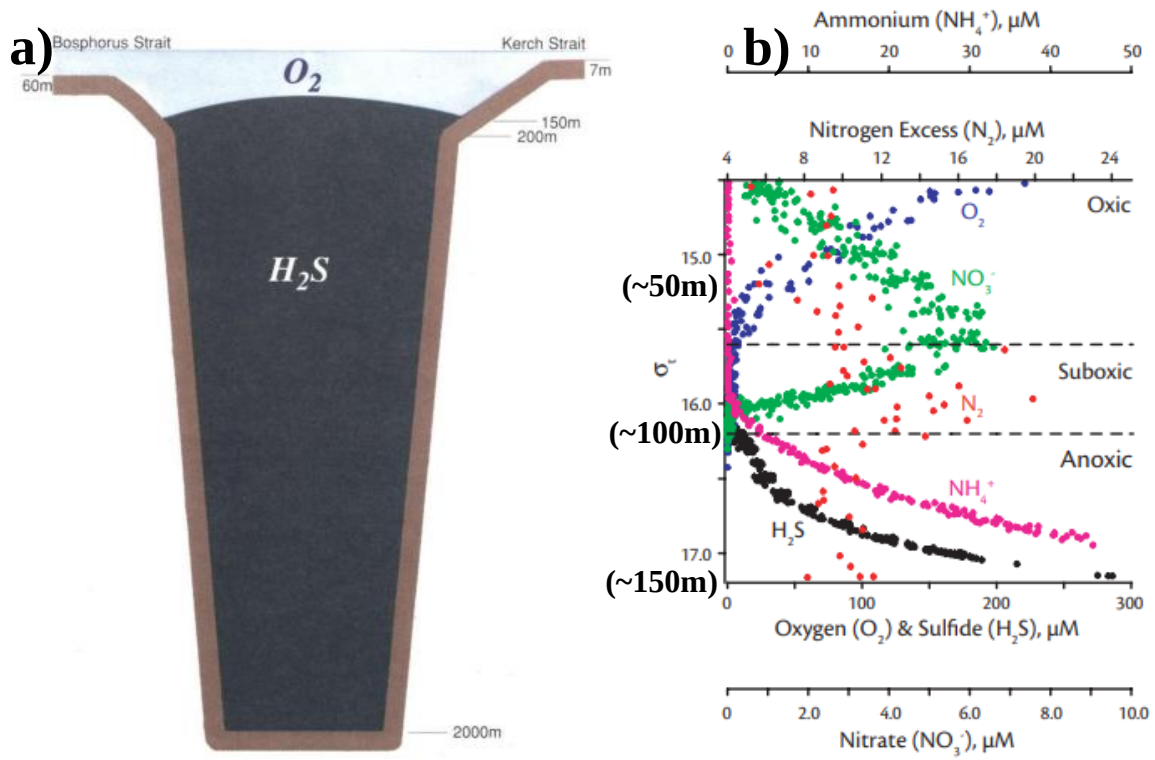

Figure 1.3: (a) Profile of hydrogen sulphide in the Black Sea (from Zaitsev and Mamaev, 1997), constraining the life in the upper 200 m. (b) Typical vertical distribution of chemical components (oxygen O_2, sulfide H_2S, nitrate NO_3^-, ammonium NH_4, and di-nitrogen N_2) on the Black Sea (from Konovalov et al., 2005)

This distinct vertical biogeochemical structure justifies the name of "Axeinos Pontus", given by the ancient Greeks, which can be translated into the "inhospitable sea" (West et al., 2003).

1.2 Productivity of the Black Sea – bloom types

Despite these harsh conditions, productivity occurs in the upper part of the water column. Phytoplankton, located at the base of the food web is a fundamental component of any marine ecosystem. Understanding the factors that govern their dynamics is necessary as they support fisheries, a crucial sector for the Black Sea economy. Indeed, according to a report from the Food and Agriculture Organization of the United Nations (FAO) (2019, www.fao.org), fisheries in the Black Sea generate an annual revenue of USD 350 million, with more than 350 tonnes fished every year. Policy measures are implemented towards sustainable fish resources

and food security and encouraging results for commercial fish species in the Mediterranean and Black Sea were pointed out in FAO (2018) report. The data showed that the overexploitation of commercial fish decreased from 88% in 2014 to 78% in 2016. Social benefits through employment are also a major benefit of this sector. In the Black Sea, over 23 500 persons are employed in fishing vessels, but it also affects 39 000 persons in derived related sectors (Malta MedFish4Ever Declaration, https://ec.europa.eu/commission/presscorner/detail/en/IP_17_770). Around the Black Sea, small scale coastal fisheries are also an important component and significantly impact the tourism industries.

Within different regions of the global ocean, the annual cycle of phytoplankton biomass differs, mainly due to changes in the environmental conditions, such as solar irradiance, water column stratification, nutrient supply or grazing pressures. However, common patterns for different "clusters" of latitudes can be described. The most renowned dynamic observed in temperate latitudes (Fig.1.4, green curve), presents a bi-modal structure (Longhurst, 1995; Sathyendranath et al., 1995). During spring, thermal stratification occurs, and more light is available compared to the winter conditions. This strong stratification will prevent vertical mixing and allow both phytoplanktonic cells and nutrients to remain in the euphotic zone. The euphotic zone is defined as a surface layer with enough light for photosynthesis to occur (usually 1% of the photosynthetic active radiation or PAR). These high nutrients and high light conditions favour and stimulate phytoplankton growth, resulting in a well pronounced bloom (Sverdrup, 1953). During summer, stratification intensifies, and nutrient concentration decreases through phytoplankton uptake. Minimum values of surface chlorophyll *a* are then observed, notably due to resource limitation (Platt et al., 2005), but also due to the action of grazing (Pommier et al., 2008; Takahashi et al., 2008). Below the surface, the thin layer with optimal conditions for phytoplankton growth is referred as the deep chlorophyll maximum. This is a common feature of the world ocean (Cullen, 1982) and it is also observed in the Black Sea during summer (Chu et al., 2005). Its formation arises from several processes (see the review from Cullen 2015 for details) and is favoured in a system with strong stratification (Yunev et al., 2005) due to episodic mixing up of nutrients.

A second and reduced bloom can occur in early autumn due to the action of wind induced mixing that can inject nutrients back into the mixed layer (Longhurst, 1995). Also, the release in grazing pressure can contribute to the occurrence of the second bloom. In the tropics, which

are not light limited compared to the temperate seas, such clear variations in the chlorophyll *a* concentration are less defined. Nonetheless, it usually reaches maximum values in winter due to convective mixing that enhances the replenishment of nutrients into the surface waters (Follows and Dutkiewicz, 2001).

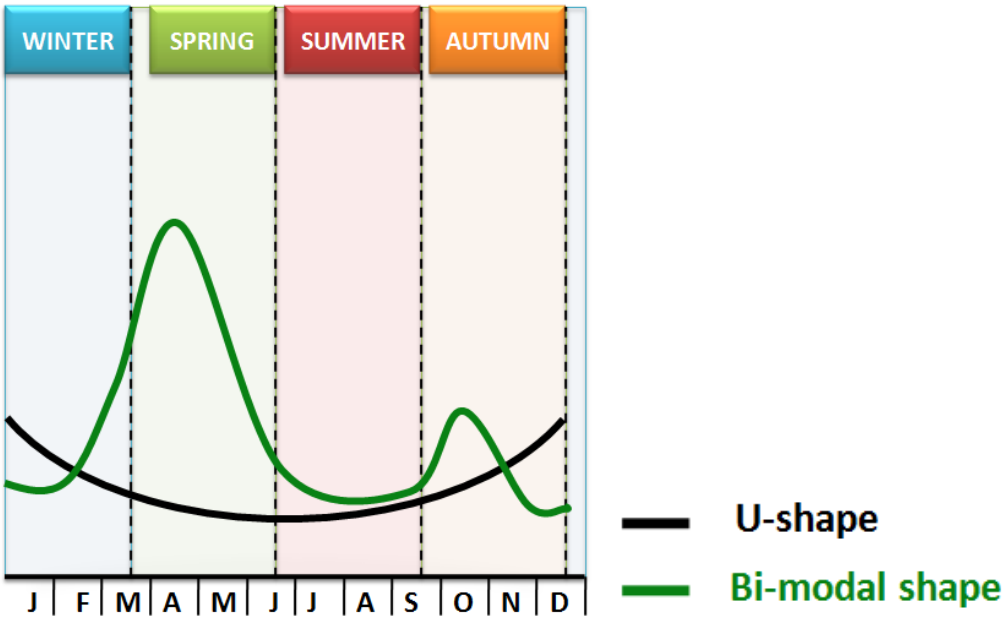

Figure 1.4: Schematic of the two main bloom types occurring in the Black Sea. (Adapted from Yoder et al., 1993). The green curve depicts the bi-modal structure (temperate seas) whereas the black curve indicates the U-shaped behaviour (tropical seas).

Within the Black Sea basin, the seasonal cycle of chlorophyll *a* is not spatially uniform and the two bloom types described above can be observed. The patterns are further explored in Chapter 2. The open Black Sea can experience the U-shape structure (Fig.1.4, black line) with maximum during winter and minimum in summer (*e.g.* Vinogradov et al., 1999). In contrast, the two blooms type (bi-modal structure) can be described in the coastal areas (Sorokin et al., 2002). These patterns are not fixed and are evidently subjected to environmental changes (Cleland et al., 2007).

1.3 Nutrient supply to the Black Sea

The Black Sea has a large drainage area and takes inorganic nutrients not only directly from the land, but also from the atmosphere. The distribution of nutrients can then be affected by internal processes such as its own intermediate layer waters. The mixture of these diverse sources being regulators of nutrients concentration is introduced below.

1.3.1 Riverine and atmospheric nutrient inputs

The Black Sea has a positive freshwater balance (Tolmazin, 1985; Özsoy and Ünlüata, 1997), with freshwater inputs from rivers and precipitation exceeding losses by evaporation, hence the designation as a dilution basin. Sorokin (2002) reports riverine freshwater fluxes of 369 km^3 yr^{-1}, 224 km^3 yr^{-1} for precipitation and 395 km^3 yr^{-1} for evaporation. The remainder of the water budget is balanced by the net flux through the Bosphorus. The NWS is strongly influenced by rivers and one of Europe's largest rivers (Danube) dominates the freshwater discharge. The Danube river, which has a large drainage area and collects effluents from 8 European countries, is the main contributor and supplies about 70% of the total river runoff into the Black Sea (Humborg et al., 1997). The total discharge of both the Dniestr and Dniepr is about three times smaller than the Danube (Table 1.1). The total riverine freshwater into the Black Sea is about 350-400 km^3 yr^{-1} (Ludwig et al., 2009).

Table 1.1: Main rivers over the NWS (Data from Zaitsev and Mamaev, 1997)

Name	**Catchment Area (km^2)**	**Length (km)**	**Total runoff (km^3 yr^{-1})**
Danube	817 000	2860	208
Dniester (Dnestr,Dniestr)	71 990	1328	10.2
Dnieper (Dnepr, Dniepr)	505 810	2285	51.2

Rivers are not only a source of freshwater, but they also bring nutrients into the system. The intensification of agriculture and the use of agrochemicals and phosphate detergents (Llop et al., 2011), alongside the use of pesticides, PCB's, metals and radionuclides (Mee, 1992), contributed significantly to riverine pollution. The overall indicator "Merged Nutrient Indicator" which is based on two other indicators ("Nitrogen load" and "Nutrient Ratio", see http://onesharedocean.org/LME_62_Black_Sea for details), suggests a high score of 4 out of 5 for the year 2000. Since 1970s, those anthropogenic nutrient and pollution loads affected severely the chemical and biological regimes in the coastal areas of the Black Sea (Borysova et al., 2005; Zaitsev and Mamaev, 1997; Yunev et al., 2007).

One direct and visible example of this man induced change is the increase in the average phytoplankton biomass (*e.g.* Borysova et al., 2005). Phytoplankton is a beneficial actor in a marine system as it enhances biological productivity and also regulates atmospheric carbon through its scavenging into deeper waters (Falkowski and Oliver, 2007). However, negative outcomes arise when phytoplankton growth is overstimulated. Indeed, high levels of nutrients concentration contribute to rapid increase of phytoplankton growth and it is the main cause of eutrophication (Yunev et al., 2007). When planktonic algae are able to synthetize toxins, it leads to the development of harmful algal blooms (HABs). Those were observed in the coastal waters of the Northeast Black Sea from June 2000 to April 2002 (Vershinin et al., 2005) and were also studied in the Bulgarian Black Sea coast between 1987-1997 (Velikova et al., 1999). The toxins produced can spread through the food chain and even end up poisoning human beings, with lethal consequences in rare cases. Eutrophic conditions arising from such intense productivity started by the early 1970s and was reported in several studies, with a strong focus in the North part of the Black Sea near the Danube area (see for instance Cociasu et al., 1996; Humborg et al., 1997; Lancelot et al., 2002; Ragueneau et al., 2002 or Ludwig et al., 2009). Those blooms can cause a significant decrease of oxygen levels (hypoxia and even anoxia) which can become unsuitable for benthos organisms (Kideys, 1994) and demersal/pelagic fish population (Leppäkoski, 1996). According to the article of Strokal et al. (2013), eutrophication issues affected 14 000 km^2 of the total area of the Black Sea (mainly in the Northwest shelf) for the year 2000. This led to a general decrease in biodiversity (Zaitsev, 1992) and change of the structure and functioning of the entire pelagic food web (Bodeanu, 2002; Kideys, 2002). Near 60 million tons of living marine resources were lost between 1973 and 1990 due to nutrient enrichment (Strokal et al., 2013). Overall, eutrophication issues can have a dramatic

effect on fisheries, aquaculture, tourism and public health that often generates severe economic losses.

Nitrogen and phosphorus are key nutrients for the ecological status of marine systems. Especially in the Black Sea, nutrients inputs are high in comparison to other European Seas. For example, the total nitrogen inputs were 6 times more in the North part of the Black Sea in the 1990s compared to the Baltic Sea. But, the export of total phosphate is comparable between the Baltic Sea and the North part of the Black Sea (Strokal et al., 2013). A state of environment report for the Black Sea (Shiganova et al., 2006/2007) indicates that between 1970 and 1980, 80% of the total load of nutrients transported to the sea came from the Danube river (Alkan et al., 2013). The report contains long term changes in the total nitrogen and phosphorus emission from the Danube river catchment and is shown in Figure 1.5. The highest values in nitrogen were observed in 1985-1990 (900 kt y^{-1}) but then decrease to the values of 760 kt y^{-1} in 2000-2005 (Fig.1.5b). Phosphorus emissions were an order of magnitude smaller and reached maximal values in 1990-1995 (115 kt y^{-1}) and then also decrease until 70 kt y^{-1} in 2000-2005 (Fig.1.5a). The significant decreasing trends observed in the early 1990s can be explained by dams constructions and political changes (Ludwig et al., 2010). Data between 2000 and 2005 estimated that nitrogen and phosphorus emissions were around 1.5 times higher than the ones in 1950s (Oguz et al., 2008).

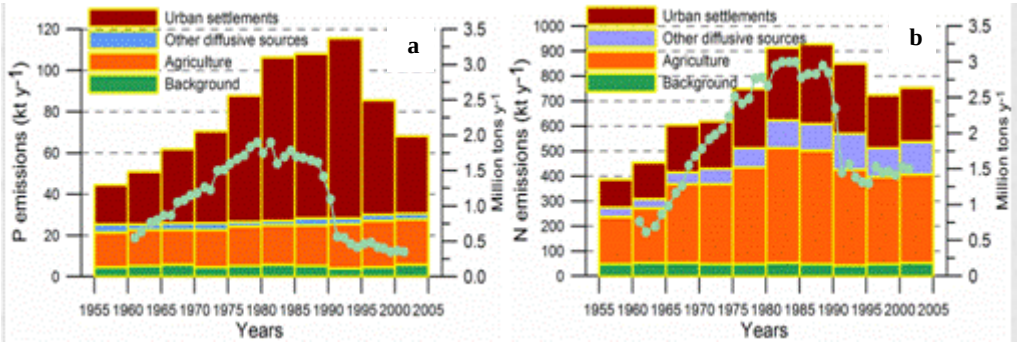

Figure 1.5: Relative contributions of different point and diffuse sources to the emissions of (a) total phosphorus and (b) total nitrogen (N) averaged over 5-year bins. The solid circles represent the amounts of total nitrogen and phosphorus fertilizer consumption in the Danube catchments basin. Figure from the Black Sea commission report (http://www.blacksea-commission.org/_publ-SOE2009-CH2.asp).

A lot of publication focuses on the role of rivers as a source of nutrients (for instance Ludwig et al., 2010). However, another important pathway for the transport of both natural and anthropogenic compounds from land sources to the marine system is the atmosphere (Jickells, 1995). Considering sources from the atmosphere is especially important as the Black Sea is bordered by industrialized countries that act as a continuous source of anthropogenic aerosols (Kubilay et al., 1995; Karakaş et al., 2004). With the decrease in river loads of 20% for nitrogen and 30% for phosphorus from 1988 to 1998 (Ludwig et al., 2009) after the implementation of nutrients reduction measures by the riparian countries, the role of atmospheric inputs might not be negligible. Rivers, alongside atmospheric deposition act as the main external sources of nutrients enrichment to the Black Sea, but their relative contribution is poorly quantified (Kubilay et al., 1995; Theodosi et al., 2013). Assessing the different sources of nutrients loads become a priority that needs to be addressed (Black Sea Commission, 2010). The role of atmospheric deposition is therefore considered with greater attention as they may be of extreme importance for the open and off coasts areas of the Black Sea. Some studies assessed the atmospheric deposition of nitrogen and phosphorus over the Western Black Sea (Medinets and Medinets, 2012; Varenik et al., 2015) and for the South and West coastline of the Black Sea (Koçak et al., 2016).

1.3.2 Thermohaline structure (Cold Intermediate Layer)

Rivers bring cold and fresh waters which overlies warm and saltier waters originating from the Mediterranean (about 38psu) (Spencer and Brewer, 1971). The upper part of the water column has an average salinity of 17-18psu (Özsoy and Ünlüata, 1997) whereas in the deeper part, there is a stable salinity of 22-24psu (Özsoy and Ünlüata, 1997). This gradient of salinity mainly explains the pronounced permanent two-layers stratification observed in the Black Sea (Murray et al., 1991; Özsoy and Ünlüata, 1997) and is reflected by a strong and permanent pycnocline (Fig.1.6). This feature classifies the Black Sea as a meromictic basin.

In summer, the initiation of the seasonal thermal stratification leads to the formation of a second pycnocline, below which is the Cold Intermediate Layer (referred later as CIL) (Tolmazin, 1985; Stanev, 1990; Altiok et al., 2012). The CIL persists during summer (see Fig. 1.7) and is

sandwiched between warm surface waters (over 25°C in some areas) and deep waters (around 9°C, which is relatively warm compared to the typical global ocean values). This inversion in temperature is maintained by the strong vertical salinity gradient in the permanent pycnocline, which prevent mixing of the CIL with adjacent layers. In spring, following stratification, the winter thermocline is trapped in the CIL. An interesting idea was first proposed by Tugrul and Salihoglu (2003) who suggested a link between the formation of the Cold Intermediate Layer in the NWS and the subduction of nutrients. Those nutrients would then be removed from the euphotic zone and become unavailable to the phytoplankton. This hypothesis is tested in Chapter 2.

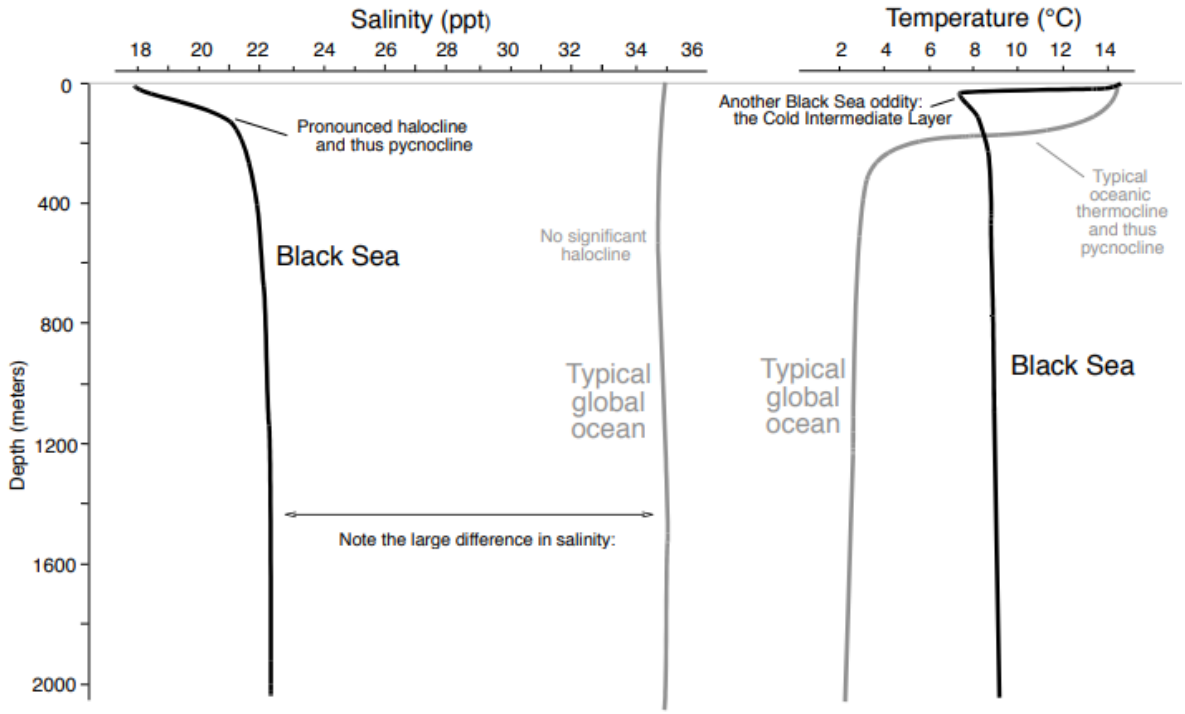

Figure 1.6: Illustration of the thermohaline structure as observed in the Black Sea and comparison with the typical global ocean. The figure comes from http://railsback.org/Oceanography.html, and uses the source from Yakushev et al. (2007): The Black Sea Environment: Springer Handbook of Environmental Chemistry v. 5Q, p. 277 - 307.

By convention, the CIL is delimited by isothermes of 8°C for its upper and lower boundaries (Ivanov et al., 1997; Özsoy and Unlüata, 1997). However, this conventional definition was revisited by few authors (Stanev et al., 2013; Capet et al., 2014) who applied instead the

threshold of 8.35°C. This new definition was suggested for the identification of the CIL in recent times, when the temperature does not go below 8°C.

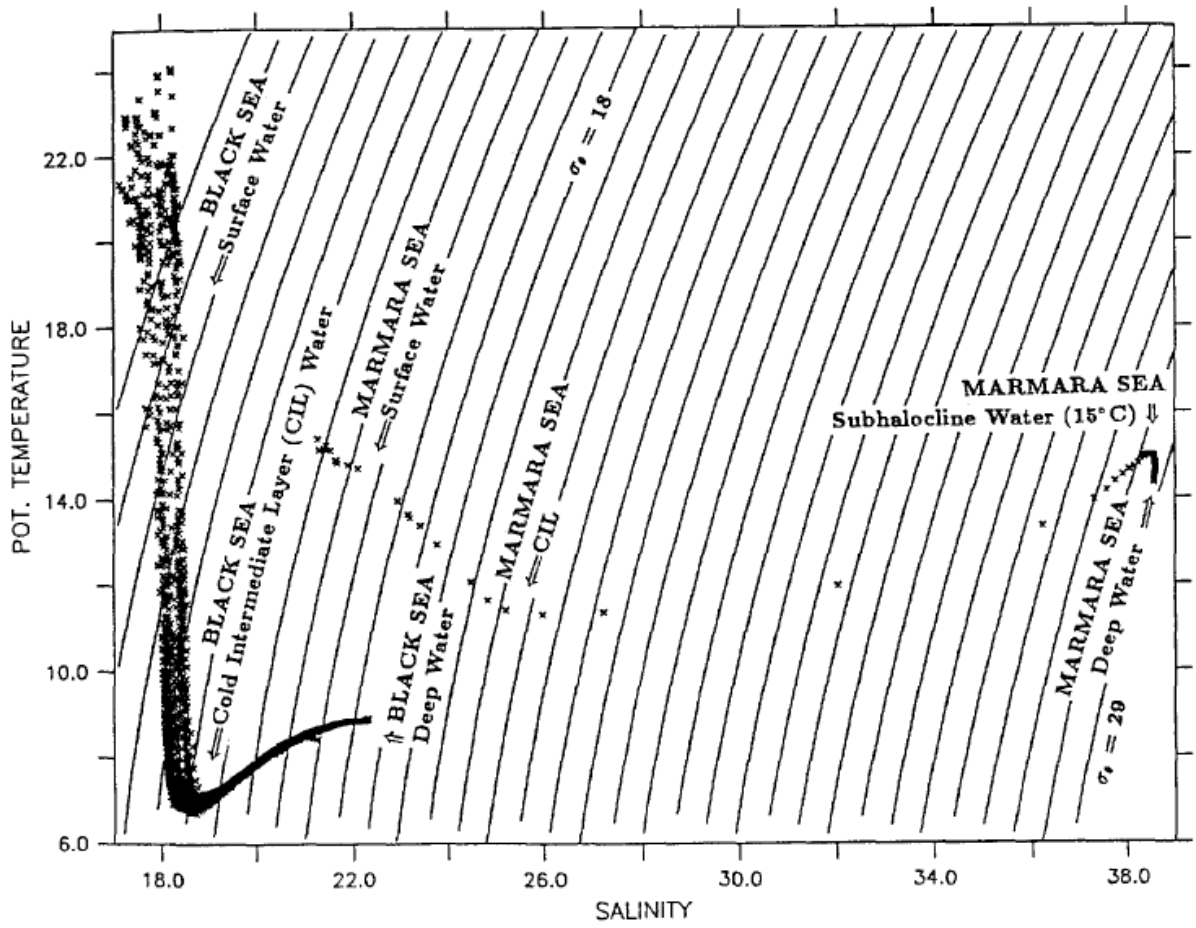

Figure 1.7: Potential temperature versus salinity of data inside the Black Sea from the R/V Knorr Leg 4 Cruise in summertime 1988 (from Özsoy et al., 1991) in the southern part of the basin, with indication of the Cold Intermediate Layer (CIL).

The CIL is usually located at a depth of 50-150 m. Due to the dome shape of the pycnocline that results from the geostrophic current of the cyclonic mean circulation (Capet at al., 2012), the core of the CIL (minimum of temperature), is shallower in the central basin (30 - 60m) but deeper towards the continental slope (80m) (Murray et al., 1991). The thickness of the layer tends as well to be higher in the margins compared to the internal gyres.

In the literature, different theories are given to explain the origin of the CIL. The first hypothesis that dominated until the 1980s, was the formation of the CIL by advection from the

NWS during winter (Tolmazin, 1985; Oguz and Beşiktepe, 1999), which is the coldest part of the Black Sea. Indeed, the occurrence of dry, cold, northerly winds along with the decrease of riverine discharge would enhance the cooling and salinification of water and lead to an increase of its density. The cold and dense water would then be subducted and spread horizontally on isopycnal surfaces over the Black Sea (Murray et al., 1989; Oguz and Beşiktepe, 1999). Several authors found that this mechanism could also occur near the Kerch Strait (Filippov 1965; Tolmazin, 1985). Besides that, the development of new instruments highlighted an alternative view for the CIL formation which might originate in the central gyres via a convective process during a severe winter (Gregg and Yakushev, 2005). Furthermore, findings made by Ivanov et al. (1997) and supported by modelling studies from Stanev et al. (1999), indicated that CIL formation could occur within coastal anticyclonic eddies under certain conditions. Those results indicate how complex the mechanism of formation of the CIL can be.

The CIL is a fundamental and unique feature observed inside the Black Sea, and a particular attention will be given to it in this manuscript.

1.4 Role and utility of satellites and models

To study marginal sea processes, it is important to choose the appropriate tool. Satellites and numerical models are the two main ones that are considered in this thesis. Although they both allow a basin wide scale approach, they each have their own strengths and limitations which has to be carefully addressed in the analysis of the results.

Phytoplankton contains various type of photosynthetic pigments (Roy et al., 2011), the most important of them being chlorophyll *a* as it is ubiquitous among phytoplankton species. Although they are microscopic organisms, a large number of them can have a major impact on the surface water colour of the ocean which is visible from space (Fig. 1.8). Chlorophyll *a* is a proxy for phytoplankton biomass and such quantity can be obtained from satellite derived estimates (*e.g.* O'Reilly et al., 1998).

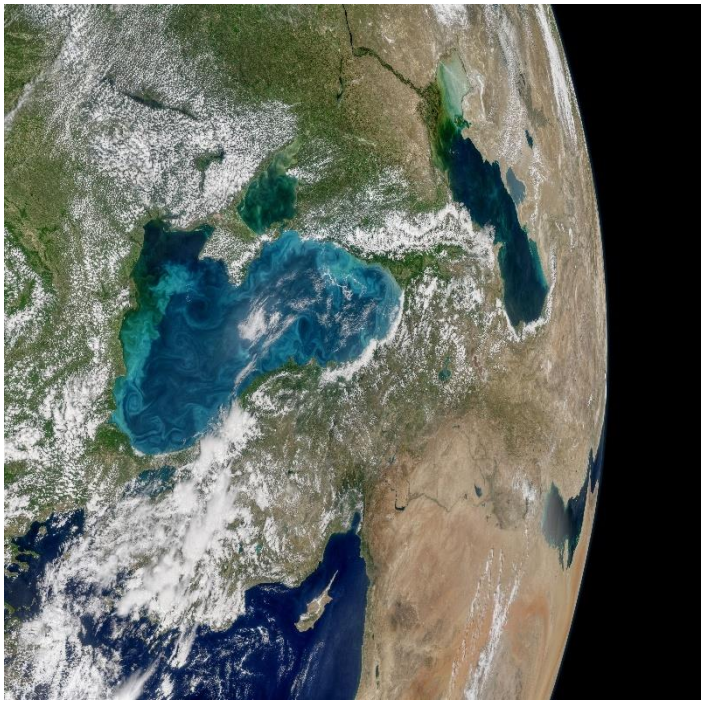

Figure 1.8: Example of image obtained from a satellite (MODIS) that clearly shows the discoloration of the surface water due to an algal bloom. Removing the atmospheric signal (clouds) from the water signal is a challenging aspect of ocean colour remote sensing.

Satellite ocean colour measurements became an essential tool in oceanography and helped the scientific community to detect changes in phytoplankton dynamics on a global scale, with high resolution in space and time. Satellite sensors do not measure directly chlorophyll *a*, but rather the remote sensing reflectance (Rrs). Rrs is a standard product delivered by space agencies that describes the light exiting a water mass. By definition, this is the ratio of upwelling radiance to the downwelling irradiance at the ocean surface (Dutkiewicz et al., 2019). Within the water, there are optically active constituents (OAC) that impact the fate of the incident light through absorption and scattering. Among such OACs, there is phytoplankton, but also dissolved organic matter (CDOM) and non-algal particles, such as suspended particulate matter (SPM). CDOM includes humic and fulvic acids released through the degradation of plant tissues in soils or in water (Blough and Del Vecchio, 2002). Both absorption and scattering determine the intensity and spectral shape of the light exiting the water (*i.e.* the water leaving radiance) and can consequently change the colour of the ocean which can then be captured from a satellite sensor (green arrow in Fig.1.9). The study of the spectral reflectance spectrum can provide information on the content of the upper ocean (Werdell et al., 2018; Mascarenhas and Keck, 2018) and this area of research has been rightly referred under the discipline of "ocean colour".

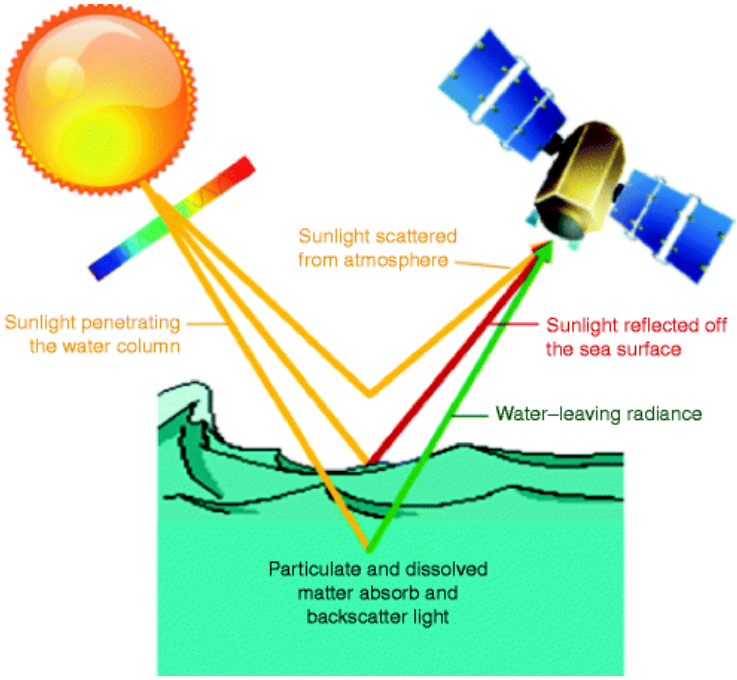

Figure 1.9: Illustration of the radiances measured by a satellite. Besides the water leaving radiance (green arrow), there is also the light scattered by the atmosphere and the one reflected off the sea surface which are both removed after applying some atmospheric correction. Most of the incident light propagate downward into the water column (not shown in the figure) and this is only a small fraction (few percent) that is scattered out of the water column and measured remotely.

Each OACs modify the properties of the incoming radiations and affect consequently the water colour in different ways. Chlorophyll *a* is a green pigment which absorbs strongly in the blue and red wavelengths of the visible light and is low in the green portion of the spectrum (Fig.1.10). Therefore in high concentration, phytoplankton influence the colour of the near-surface ocean (Gordon, 1983).

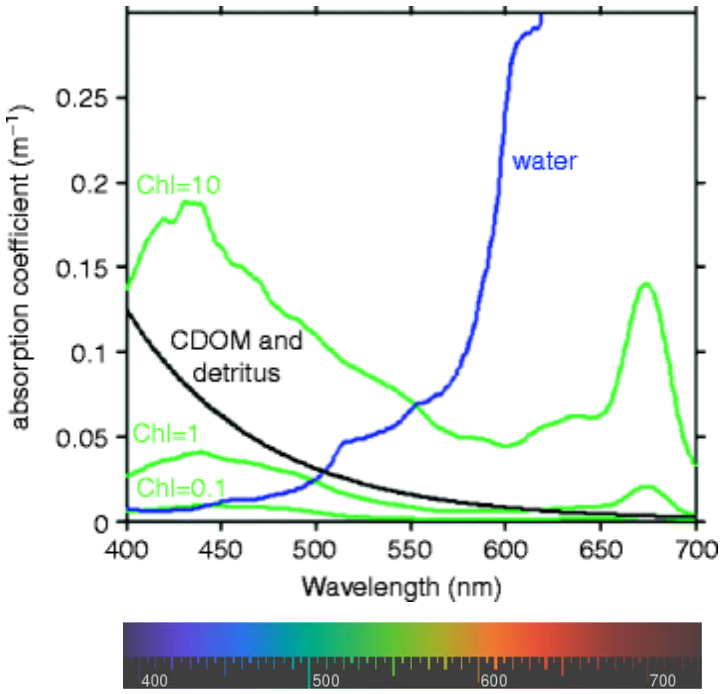

Figure 1.10: Example of oceanic constituents that are responsible for absorption of photons. Pure water absorbs light at wavelengths greater than 550 nm and is minimum in the blue and green portion of the visible light. CDOM absorbs maximally in the UV and blue portion of the spectrum. Chlorophyll *a* concentration has units in mg m^{-3}. Figure from Dierssen et al. (2012).

A lot of effort has been put in the development of algorithms (*e.g.* reflectance band-ratio algorithms) for accurate retrievals of chlorophyll *a* concentration based on the Rrs measurements (O'Reilly et al., 2001; Maritorena et al., 2002; Werdell et al., 2018). There is a classification of the aquatic systems based on their colour properties (Jerlov, 1974). Case 1 waters define areas where the optical properties are mainly determined by phytoplankton (Morel and Prieur, 1977). In practice, an increase in absorption, or reduction in reflectance, in the blue relative to the green portion of the spectrum can be empirically related to chlorophyll *a* concentration. Where there is more phytoplankton, more blue light is absorbed and the reflected colour changes from blue to green (Dierssen et al., 2012). For the more optically complex waters, classified as Case 2 waters (generally near the coasts), there is a need to use other spectral bands because the blue-green reflectance alone is less sensitive to changes in chlorophyll *a* due to the presence of other OACs (CDOM and SPM) (Mobley et al., 2004).

There is a “nearly” continuous global data record of space-based ocean colour which started in 1978 with NASA’s Coastal Zone Color Scanner (CZCS). It was then followed by Sea-viewing Wide Field of View Sensor (SeaWiFS; 1997–2010), NASA Moderate Resolution Imaging Spectroradiometers onboard Aqua (MODISA; 2002-present) and the ESA Medium Resolution Imaging Spectrometer (MERIS; 2002–2012). These ocean colour sensors usually have 6 to 7 spectral bands that cover the visible wavelengths (400-700 nm, Fig.1.11b). Most of the channels are selected to match reflectance related to phytoplankton pigment absorption features and other constituents. The succession of the different sensors (see Fig.1.11a) provides a better understanding of phytoplankton distribution and concentration in the ocean from seasonal to interannual timescales (McClain, 2009). Such variability is explored in Chapter 2 using MODIS satellite, and a merged product.

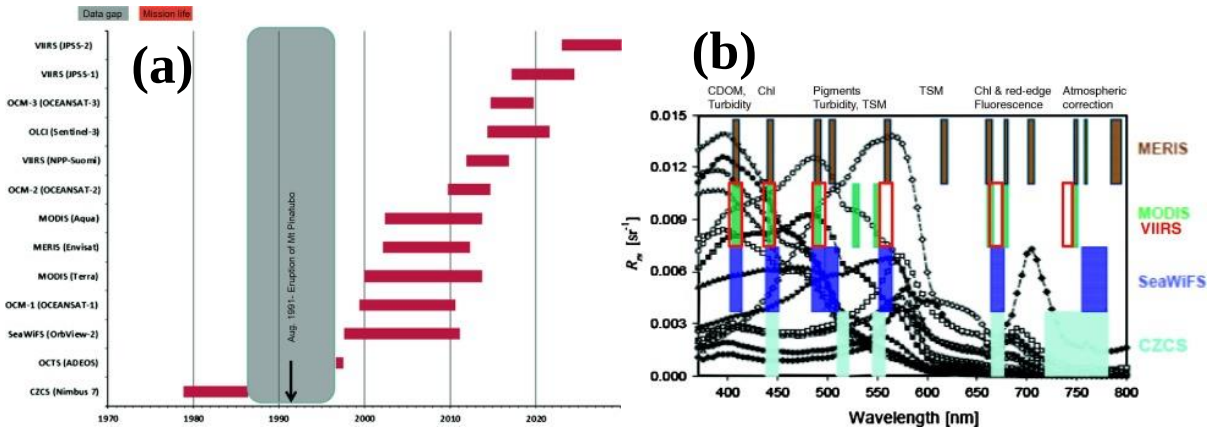

Figure 1.11: (a) History of the different satellite sensors for ocean colour studies. (b) Wavelengths of the ocean colour sensors. Both figures are extracted from Blondeau-Patissier et al. (2014).

Ocean colour observations are limited to the near-surface chlorophyll concentration and thus do not capture the deep chlorophyll maximum (DCM, Cullen, 1982). Chapter 2 look at an application of ocean colour remote sensing for the Black Sea.

The results provided from the observations can be integrated into regional numerical models. Model and observations work “hand in hand” as they both add value to one another. Indeed, having access to observational sources is a necessity for the development of numerical models (initialization, validation and data assimilation procedures). Then, models can be used as a complementary tool and connect sparse spatiotemporal observations (*e.g.* compensate for the lack of values in winter from satellite observations). Depending on the objectives, the model

can be quite simple (1D, *e.g.* Yakushev et al., 2007) or substantially more complex and realistic (3D, *e.g.* Grayek et al., 2010 or Kara et al., 2005). In this thesis, a 3D numerical model was used in Chapter 3 to study in particular the CIL. By gaining confidence in the model simulations through comparison with observations, a great range of application is then possible and the individual response of the system from a specific driver can be investigated.

1.5 Outstanding questions

The thesis aims to further advance the understanding of some of the biological component inside the Black Sea and investigate its link with the physical properties which are usually both interconnected. This thesis is articulated into three main science chapters with research questions that are listed below.

In Chapter 2, the factors that may account for changes in the bloom structure (*i.e.* the phenology) in the Black Sea are extensively explored. The main questions investigated are:

- What is the regionalization of the Black Sea based on the study of the phenology of chlorophyll *a* using only satellite observations?
- What is the impact of rivers and sea surface temperature on the seasonal dynamic of chlorophyll *a* inside the different sub-regions?
- What is the effect of water flow (precipitation, river discharge, CIL) and sea surface temperature on the interannual variability of chlorophyll *a*?

Then, Chapter 3 looked at some of the physical properties inside the Black Sea, with a strong focus on the Cold Intermediate Layer dynamic. For this purpose, a 3D numerical model is then used to address the following questions:

- What is the effect of the light and mixing scheme in representing the main thermohaline features inside the Black Sea?
- What is the long-term variability of the simulated CIL using the best configuration obtained from the sensitivity analysis?
- What is the impact of the riverine inputs on the volume of the simulated CIL?

Lastly, Chapter 4 focuses only on understanding the Cold Intermediate Layer formation using a specific method based on densities surfaces. The research question addressed is the following:

- What processes impact the interannual variations of the CIL formation and what is the regional contribution to its formation?

Chapter 2: Seasonal and interannual variability of chlorophyll *a* in the Black Sea

2.1 Introduction

The primary drivers of biogeochemical processes in the ocean are phytoplankton as they constitute the "backbone" of the aquatic food web. Phytoplankton is very sensitive to changes in its environment (Käse et al., 2018), and respond to both short term (seasonal) and long-term changes. The biophysical status of the water, especially the degree of eutrophication, can be related to phytoplankton biomass. There is a need to assess the environmental state of the Black Sea by way of monitoring chlorophyll *a* concentration, which is typically used as a proxy to assess phytoplankton biomass. The first measurements of chlorophyll *a* started in 1960 (Finenko et al. (2014) cited Vinberg et al. (1964)) and in recent years, several articles have addressed the seasonal cycle of chlorophyll *a* in the Black Sea (Yunev et al., 2002; Chu et al., 2005; Nezlin, 2006; McQuatters-Gollop et al., 2008; Demidov et al., 2008; Finenko et al., 2014). However, there is not a clear consensus between authors and the different seasonal patterns described in the literature are reported in Table 2.1. This inconsistency is particularly noticeable between *in situ* and remote sensing studies.

On the one hand, there is a signal similar to the one that is typically observed for the mid latitudes (temperate areas) and shaped with a bi-modal structure (Longhurst et al., 1995; Sathyendranath et al., 1995, see also Fig.1.4 in the Introduction Chapter). It corresponds to a first bloom occurring in spring (usually in February/March) and a second in autumn (September/October). On the other hand, a signal more typical of the subtropical regions (Longhurst et al., 1995; Longhurst, 2010) has been described and it is referred as a U-shape structure (see Fig.1.4 in the Introduction Chapter). In this case, the chlorophyll *a* maximum occurs in winter and the minimum in summer. Furthermore, some authors also observed several maxima of chlorophyll *a* (>2) over one year (Finenko et al., 2014). The timing and magnitude (*i.e*. the phenology) of chlorophyll *a* is important as it affects higher trophic levels. The differences in the seasonal cycle of chlorophyll *a* may be due to different factors, such as local

specificities in the mixing, water depth, turbidity, circulation, riverine inputs, the type of dataset (whether it is *in situ* or satellite data) and also the period of time examined (Table 2.1).

Table 2.1: State of the art of the type of seasonal signal reported in the Black Sea.

Articles	**Type of dataset**	**Period of time**	**Sub-Regions delimited**	**Seasonal dynamic**
Finenko et al. (2014)	Satellite (SeaWiFS)	1998-2008	11	U shape (deep regions)
Demidov et al. (2008)	*In situ*	1973-1997	10	2 or 3 maximums in winter (Feb-March) summer (June-August) and autumn (Oct-Nov) nearly in all areas of the sea (Shelf region (<200m), Continental slope (200-1500m) and Deep region (>1500m)
McQuatters-Gollop et al. (2008)	Satellite (SeaWiFS)	1997-2005	3	U shape (deep regions)

Table 2.1 (Continue): State of the art of the type of seasonal signal reported in the Black Sea.

Nezlin (2006)	Satellite (SeaWiFS and MODIS)	1997-2006	4	U shape (deep regions)
Chu et al. (2005)	*In situ*	1980-1995	Stations spread all around the Black Sea (NWS + deep basin)	Bi-modal (winter/spring and fall bloom) : February-March and September-October
Yunev et al. (2002)	*In situ*	1988-1992	Open Black Sea (>1000m)	Bi-modal (winter/spring and fall bloom) : February-March and November
Nezlin et al. (2002)	Satellite (SeaWiFS)	1997-2000	Open Black Sea	U shape (deep regions)
Oguz et al. (2003)	Satellite (SeaWiFS)	1997-2002	Basin average (exclude the coastal regions shallower than 200m)	U shape (deep regions)

Table 2.1 (Continue): State of the art of the type of seasonal signal reported in the Black Sea.

Kopelevich et al. (2002)	Satellite (CZCS)	1978-1986	8	U-shape (deep regions)
Nezlin et al. (1999)	Satellite (CZCS)	1978-1986	8	U-shape (deep regions)

To sustain their growth, phytoplankton rely on light, temperature and nutrients (Falkowski and Raven, 2013). On the North Western Shelf (NWS), river discharge is the main source of nutrients (Cociasu et al., 1996) and they can be transported further South via the Rim Current (Oguz and Beşiktepe, 1999). Nutrients supplied by rivers can also propagate into the deep regions of the Black Sea via the eddies of the Rim Current. But generally, in the deep-water regions inside the central gyres, phytoplankton production is mainly dependent on nutrient resupply by wind mixing and vertical convection, primarily during winter (Mikaelyan et al., 1995). Lastly, recent work has highlighted wet and dry deposition of aerosols as a source of nutrients over the Western part of the Black Sea (Medinets and Medinets, 2012). Between the 1960s and the late 1980s, anthropogenic activities led to an increase by a factor 5 and 3 for respectively the riverine nitrogen and phosphorus inputs to the North Western Black Sea (Cociasu et al., 1996). This substantial change was due to the development of both economic activities (industrial and agricultural) and urbanisation (Tolmazin, 1985; Mee, 1992). In contrast, silica (Si) fluxes decreased significantly by a factor 3 (Cociasu et al., 1996) during this period due to hydraulic management programs (Tolmazin, 1985; Humborg et al., 1997). Inhibition of diatom growth due to Si limitation can result in suitable environment for non-siliceous species and potentially develop into harmful algal blooms (Garnier et al., 2010).

The interannual variability of chlorophyll *a* and the intensity of a bloom have been linked to the severity of winter. For instance, a cold, severe winter is thought to be associated with a larger bloom due to greater winter upwelling of nutrients (Finenko et al., 2014; Oguz et al., 2003). In contrast, McQuatters-Gollop et al. (2008) found the intensity of a bloom to be greatest during the warmest years. Understanding the mechanisms regulating the interannual variability of chlorophyll *a* is important as it can affect the upper trophic levels and impact fish resources through bottom-up control. An interesting idea was first proposed by Tugrul and Salihoglu (2003) who suggested a link between the formation of the Cold Intermediate Layer (CIL, layer

defined in Section 1.3.2 in Chapter 1) in the NWS and the subduction of nutrients. Those nutrients would then be removed from the euphotic zone and become unavailable to the phytoplankton. McQuatters-Gollop et al. (2008) then proposed that the volume of the CIL formed would modulate the interannual variability of chlorophyll *a*. Therefore, in a warm year, the CIL formation rates should decline and lead to high nutrient concentrations, further available for phytoplankton growth.

The aim of this chapter is to first describe the spatial variability in the seasonal cycle of chlorophyll *a* across the Black Sea using satellite observations for the period 1998-2017. Then, understanding what mechanisms drives the seasonal cycle of chlorophyll *a* is investigated, with an emphasis on the role of river discharge and sea surface temperature. Finally, the interannual variability is analysed and the hypothesis suggesting that it is controlled either by riverine inputs and/or the variability in the CIL volume is tested. While *in situ* measurements are crucial in assessing local patterns over a short period of time (Demidov et al., 2008), the data coverage from *in situ* observations remains sparse in the Black Sea. An alternative is the use of surface chlorophyll *a* derived from ocean colour which is then used in this Chapter. This chapter is outlined as follows. Section 2.2 describes the properties of the datasets and the types of analysis that have been performed. Section 2.3 indicates the results of the chlorophyll *a* observations from satellite on the seasonal and interannual scales. Finally, section 2.4 discusses the patterns of chlorophyll *a* in the Black Sea.

2.2 Data and Methods

2.2.1. Satellite remote sensing data

Datasets of chlorophyll *a* used in this chapter came from two different sources. The first one is acquired from the Moderate Resolution Imaging Spectroradiometer (MODIS), available on the NASA website (https://oceandata.sci.gsfc.nasa.gov/). The second dataset is reprocessed and uses merged satellites data (including MEdium Resolution Imaging Spectrometer (MERIS), Sea-viewing Wide Field-of-View Sensor (SeaWiFS) and MODIS), available via the Copernicus Marine Environment Project (http://marine.copernicus.eu/). For simplicity, they

are later referred as NASA chlorophyll *a* (or NASA - Chla) and CMEMS chlorophyll *a* (or CMEMS - Chla).

NASA - Chla concentration was quantified using the standard bio-algorithm OC3 (O'Reilly, 1998) and combined with the color index (CI) of Hu et al. (2012) (see Eq.A.1 to Eq.A.3 in Appendix A for the details of the algorithms). NASA's standard algorithms sometimes lack the ability to reproduce reasonable values of *in situ* observation of chlorophyll *a* and regional algorithms can then be applied to reduce these bias (Zibordi et al., 2015). These issues arise because standard algorithms have been mainly developed to fit with Case 1 waters. However, the Black Sea contains both Case 1 and Case 2 waters, especially over the North Western area. In Case 1 waters, it is assumed that optical properties of the water are correlated with phytoplankton concentration whereas the other substances are either optically insignificant or covary with phytoplankton concentration (Morel and Prieur, 1977). On the other hand, Case 2 waters are more complex and contains independent parameters (*e.g.* suspended inorganic particles and/or colored dissolved organic matter (CDOM, also often referred to as yellow substances)) which also influence the optical properties of the water. This leads to difficulty in extracting only the optical properties produced by the phytoplankton concentration. For Case 2 waters, regional algorithms can then be used to re-assess the estimated chlorophyll *a* concentration from satellites.

In response to the issues associated with NASA algorithm, the merged product from multi-sensors satellites CMEMS - Chla was also used. The name of the dataset downloaded in the Copernicus website is " DATASET-OC-BS-CHL-MULTI_CCI-L4-CHL_1KM_MONTHLY-REP-V02". The resolution of this dataset is 0.0101° for both latitude and longitude. A regional algorithm (BSAlg, Kopelevich et al., 2013) has been applied to the ESA-CCI Remote Sensing Reflectance (RRS) (see Eq.A.5 and Eq.A.6 in Appendix A). For both datasets of chlorophyll *a*, the monthly average have been used. Both datasets (NASA and CMEMS) are based on radiance measurements but their difference lies in the algorithm used thereafter.

Sea surface temperature (SST) used in the analysis was extracted from the MODIS sensor, available on the NASA website (https://oceandata.sci.gsfc.nasa.gov/). NASA satellite provides for both chlorophyll *a* and SST monthly averaged temporal resolution and are mapped onto a grid regularly spaced with 4 km resolution in latitude/longitude.

2.2.2 Harmonic analysis

The goal of this section is to introduce the method used to reconstruct a periodic signal using both sine and cosine waves with the frequency f. This is done using a harmonic analysis, in which time series of chlorophyll *a* are fitted to a model composed of an annual and semi-annual harmonic oscillation:

$$(Eq.\,2.1)\ H(t) = b_1 \sin(2\pi tf) + a_1 \cos(2\pi tf) + b_2 \sin(4\pi tf) + a_2 cos(4\pi tf) + c$$

t is in months with the time series starting in January, $\{b_1;\ a_1;\ b_2;\ a_2;\ c\}$ are coefficients and f is the frequency $\left(f = \frac{1}{12}\right)$ in month^{-1}. By trigonometric theorem (see Appendix A for details), the above can be re-written as:

$$(Eq.\,2.2)\ H(t) = A_1 cos(2\pi tf - \varphi_1) + A_2 cos(4\pi tf - \varphi_2)$$

The peak amplitude of the annual cycle (A_1 in mg m^{-3}) and the phase ($\varphi_1$in radians) were both calculated:

$$(Eq.\,2.3)\ A_1 = \sqrt{{b_1}^2 + {a_1}^2} \text{and } \varphi_{1,radians} = \tan^{-1}(\frac{b_1}{a_1})$$

The phase can be interpreted as the months (t_m) in which the maximum of the cycle is observed (considering the semi-annual component of minor importance, *i.e.* A_2 and φ_2):

$$(Eq.\,2.4)\ t_m = \frac{\varphi_{1,radians}}{2\pi} * 12 = \frac{\varphi_{1,degree}}{360} * 12$$

A nonlinear regression function (nlinfit) from Matlab (Seber (2015) and Holland et al. (1977)) has then been used to assess the values of the coefficients that best fitted the satellite chlorophyll *a* data (not log-transformed). The associated root mean squared deviation (RMSD) was calculated as followed:

$$(Eq.\,2.5)\quad RMSD = \sqrt{\frac{1}{n}\sum_{i=1}^{n}(Y_i - Sat_i)^2}$$

where n is the total number of months, Y_i is the prediction obtained with the harmonic model and Sat_i is the observation from satellite. The fraction of variance (f_{var}) explained by the fit was assessed as followed:

$$(Eq.\,2.6)\quad f_{var} = 1 - (\frac{RMSD}{STD_{sat}})^2$$

with STD_{sat}, the standard deviation of chlorophyll *a* for all the months, using satellite data.

The phase provides here an objective method of regional delimitation. The choice of the sub-regions aims to group spatial areas with the same characteristics. The Azov Sea is considered as a separate entity, located between [45.19°N- 47.3°N] and [34.75°E -39.35°E]. The NWS was determined based on a bathymetry criterion, and has a depth shallower than 200 m depth (latitude > 43.52°N and longitude < 33.73°E). The grid used for the bathymetry was downloaded from EMODNET-Hydrography (http://portal.emodnet-bathymetry.eu/mean-depth-full-coverage), and the latitude and longitude resolution were 0.0021°. As this grid had a higher resolution compared to both chlorophyll *a* dataset (0.0417° for NASA and 0.0101° for CMEMS), the bathymetry grid was interpolated into the NASA grid, which was the coarsest.

2.2.3. Comparison of satellite chlorophyll *a* with *in situ* chlorophyll *a*

The article of Agirbas et al. (2015) contained a time series of *in situ* surface chlorophyll *a* from 2002 to 2011 which was measured via spectrophotometer. A standard of chlorophyll *a* was used for the calibration (JGOFS 1994). The station was located 1.5 km away from the coast on the South Eastern part of the Black Sea. The data from CMEMS have been interpolated on the NASA grid to allow the inter-comparison of the extracted time series. The exact coordinates of the station are 40°58′66.2″ (40.98506°) N and 39°51′27.5″ (39.85764°) E (Alkan et al., 2013). We calculated the mean of chlorophyll *a* (for NASA and CMEMS) for the four closest pixels that surrounds the location of the station ([40.9792°N; 39.8125°E], [40.9792°N; 39.8542°E], [41.0208°N; 39.8125°E], [41.0208°N; 39.8542°E]). To remove pixels with high

variability, the mean values (of the 4 closest pixels that surrounds the location of the station) that had a standard deviation strictly higher than 3 mg m^{-3} have not been considered for both datasets.

2.2.4. Local analysis

The local analysis consists of a pixel by pixel correlation between time series of chlorophyll *a* and SST. The typical p_{value} of 0.05 is used as a threshold for a significant correlation. The correlation analysis has been made using monthly time series, monthly anomalies and finally the annual mean time series from 2003 until 2017. The monthly anomalies have been calculated by subtracting from each monthly value the seasonal climatology (from 2003 to 2017), and so removing the monthly mean value allows the seasonality to be removed.

2.2.5. Catchment area and flow datasets

The whole catchment area of the Black Sea (including all the main rivers) is six times larger than its surface. The Danube river is the main in-flow. The enviroGRIDS project contributes to the Global Earth Observation System of Systems (GEOSS) and it aims at gathering key environmental data (*e.g.* precipitation, temperature) for the Black Sea catchment area. The datasets are available from the BSC-OS Portal inside the enviroGRIDS website (http://www.envirogrids.net/) and cover only the catchment area of the Black Sea. By downloading any of the layer of information available, we can then obtain the grid coordinates specific to the catchment area, originally on the EPSG projection (ETRS89/LAEA Europe). An online tool called MyGeodata Cloud (https://mygeodata.cloud/cs2cs/), was then used to transform the original coordinates system into the WGS84 projection which gave coordinates in degree decimals. The resolution of the catchment area is 0.25°.

The parameter "total precipitation" has been extracted from ECMWF (European Centre for Medium-Range Weather Forecasts) ERA-Interim reanalysis (Berrisford et al. (2011); http://apps.ecmwf.int/datasets/data/interim-full-daily/levtype=sfc/). As this is an accumulated parameter, the times 00:00 and 12:00 were selected and added together in order to get the daily total precipitation with the units in m. In order to extract the precipitation values only for the

catchment area, the precipitation dataset which has a resolution of 0.125° was interpolated into the grid of the catchment area (0.25° resolution).

The Global Runoff Data Centre (GRDC; Fekete et al., 1999) is an international archive of data that gather global long-term hydrological studies. The Danube discharge was then downloaded from the GRDC website (http://www.bafg.de/GRDC) at the station Ceatal Izmail located at 45.22°N and 28.72°E, which is at the mouth of the Danube.

2.2.6. Assessing the potential volume of CIL

The CIL is a water mass delimitated by isotherms of 8°C for its upper and lower depths (Konovalov et al., 2005). In order to assess the potential volume of CIL formed in the Black Sea, it is assumed that the CIL is characterized by temperature below 8°C and by a specific range of salinity obtained with the method described below on section 2.2.7.

2.2.7. *In situ* profiles of temperature and salinity

Vertical profiles of temperature and salinity have been downloaded from the Met Office Hadley Centre (https://www.metoffice.gov.uk/hadobs/en4/download-en4-2-0.html) for three different sub-regions of the Black Sea (Western Gyre, Eastern Gyre and South Coast). The version number of the datasets is EN4.2.0 (Good et al., 2013) and it provide a collection of global datasets of ocean temperature and salinity profiles that cover the period 1900 to present. The main data source comes from the World Ocean Database 13 (WOD13; Boyer et al. (2013); http://www.nodc.noaa.gov/OC5/WOD13/). The second source used for the EN4 datasets come from the Artic Synoptic Basin wide Observations (ASBO) project, which is a collection of profiles from various other sources (see Good et al. (2013) for the details). The third source is from the Global Temperature and Salinity Profile Program (GTSPP; U.S. National Oceanographic Data Center, 2006). Lastly, data from the Argo global data assembly centres (GDACs; https://www.seanoe.org/data/00311/42182/). A quality control flag is associated to the temperature and salinity profiles and the information is freely available when downloading

the data. The Met Office Hadley Centre had implemented multiple automatic/external quality control checks to flag bad quality data in the EN4 datasets. Those are extensively detailed in the article of Good et al. (2013).

The coordinates and time period of the selected *in situ* stations are indicated in Table A.1 of Appendix A. For each sub-region, the upper and lower values of salinity associated with a temperature below 8°C was extracted using T-S diagrams (Fig.2.1). The red square on each plot highlights *in situ* measurements that have a temperature below 8°C. When we investigate the volume of the CIL in section 2.3.6.3, the CIL detection is not based on the temperature criteria, but also in a salinity range. Indeed, the CIL needs to be cold and dense enough to constitute the CIL and this is why the range of salinity was also extracted from the T-S profiles. The range of salinity obtained for each of the sub-regions of the Black Sea has been averaged. The range of [17.98-19.84] psu was obtained and this is the salinity criteria used to detect the CIL.

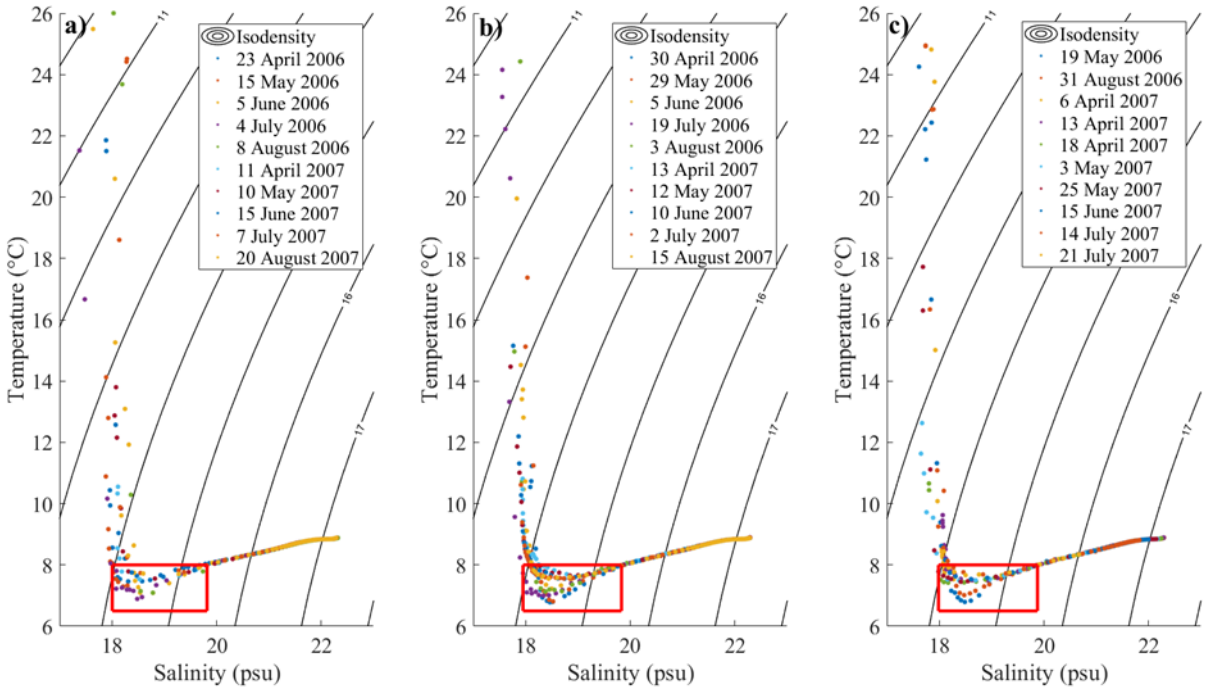

Figure 2.1: TS diagrams at different period of times for a) Western Gyre; b) Eastern Gyre c) South Coast of the Black Sea. The red square highlights potential CIL water masses with temperature below 8°C.

2.2.8. Salinity and temperature from a model Reanalysis

Three-dimensional gridded salinity and temperature data were obtained from a numerical model of the Black Sea and distributed by the Copernicus Marine Environment Monitoring Service (CMEMS; https://marine.copernicus.eu). The service provide access to a catalogue of products using information from both satellite and in situ observations. It aims at delivering information on the state of the physical oceans and regional seas (which includes the Black Sea). The product used on CMEMS is named Black Sea Physics Reanalysis (https://doi.org/10.25423/CMCC/BLKSEA_REANALYSIS_PHYS_007_004; Palazov et al., 2019) and the period 1998 to 2017 was downloaded (ftp://my.cmems-du.eu/Core/BLKSEA_REANALYSIS_PHYS_007_004/sv04-bs-cmcc-tem-rean-d and ftp://my.cmems-du.eu/Core/BLKSEA_REANALYSIS_PHYS_007_004/sv04-bs-cmcc-sal-rean-d). It relies on three main components. Firstly, the ocean model is a hydrodynamic model based on NEMO v3.4 (Nucleus for European Modelling of the Ocean). Secondly, the data assimilation scheme is a 3D variational data assimilation scheme (OceanVar) and thirdly, the assimilated data are *in situ* hydrographic profiles (temperature and salinity) from the UK MetOffice Hadley Center EN4.1.1, along-track sea level anomalies from all available missions distributed by the CMEMS Sea level TAC (Thematic Assembly Centre), and gridded sea surface temperature data also provided by the CMEMS Ocean and sea ice TAC (for more details, refers to the quality information document : https://resources.marine.copernicus.eu/documents/QUID/CMEMS-BS-QUID-007-004.pdf).
The model was validated by comparing model estimates with *in-situ* data from EN4.1.1 of the UK Met Office (an earlier version compared to the one we used in section 2.2.7), and the results suggests a satisfactory performance of the model reanalysis. The deviation between the datasets was assessed with the use of the RMS error and bias, where RMS is an estimation of the model precision, while bias indicates the mean error in the reanalysis. The summary of the model performance over depth ranges and the time period 1995 - 2015 and 2005 - 2015 is presented in the Appendix A (Table A.2). The procedure of the model validation is detailed on the quality information document associated with the product (https://resources.marine.copernicus.eu/documents/QUID/CMEMS-BS-QUID-007-004.pdf).

The space resolution of the model is around 0.0276° in latitude and around 0.0370° in longitude. The vertical grid is unevenly spaced over the 31 layers with the maximal depth of

2140 m. For each pixel of the Black Sea and for all the depth, we examine the criteria for the CIL (temperature below 8°C and salinity in the appropriate range of values). Both the salinity and temperature products are daily datasets.

2.2.9. Climatic indexes

The Black Sea oceanic parameters (*e.g.* sea surface temperature, hydrology) have been shown to be sensitive to global climate variability (Oguz et al., 2006; Ginzburg et al., 2007; Kazmin et al., 2010; Rimbu et al., 2012). The large-scale variability can be studied through climate indexes (defined thereafter), such as the North Atlantic Oscillation (NAO), the East Atlantic/West Russia (EA/WR) and the Multivariate ENSO index (MEI). The NAO is defined as the normalized difference of atmospheric pressure between Iceland and the Azores or Portugal (Barnston and Livezey, 1987) and its effect is mostly sensible during the winter (Greatbatch 2000). Studies shows that a positive phase of the NAO is highly correlated with rain and temperature regimes, with enhanced precipitation over Northern Europe and less precipitation over Central/Southern Europe and Mediterranean regions (Hurrell 1995). The EA/WR index is another important European teleconnection pattern (Barnston and Livezey, 1987), but in comparison to the NAO index, less studies assessed the role of the EA/WR pattern in the European weather (Krichak and Alpert, 2005). The EA/WR teleconnection pattern (is also active during winter and) has two main large-scale anomalies centers, one over the Caspian Sea and one over the Western Europe. Its impact extends across the European mainland and reaches the Middle East (Krichak et al., 2002). The positive phase is associated with low pressure over the South-Western Russia and Western Europe but high pressure over the North-Western Europe. During the positive (negative) phase of the EA/WR, drier (wetter) conditions prevail across Europe and the Mediterranean Region, but wetter (drier) conditions are observed over the Middle East (Barnston and Livezey, 1987; Krichak et al., 2000; Ionita 2014). Monthly average values of these indexes are produced by the National Oceanic and Atmospheric Administration (NOAA) Climate Prediction Center. The exact link of the data for the NAO and EA/WR is the following: https://www.cpc.ncep.noaa.gov/data/teledoc/telecontents.shtml. For both the NAO and EA/WR indices, each monthly data was normalized by subtracting the long-term mean of the corresponding month and by dividing by its long-term standard deviation. Both long-term means and standard deviations are based on the climatology from 1981 – 2010. The normalized monthly time series for the NAO and EA/WR indices from 1980

to 2018 are shown in the Appendix A (Figs. A.2 and A.3). The MEI index is a multivariate measure of El Niño Southern Oscillation (ENSO) signal. Indeed, it combines both oceanic and atmospheric variables, which facilitates the assessment of the ENSO signal in a single and comprehensive index (Mazzarella et al., 2010). The MEI index time series was downloaded in the following link: https://www.esrl.noaa.gov/psd/data/correlation/meiv2.data.

2.3 Results

2.3.1 Comparison of *in situ* chlorophyll *a* with satellites

The monthly mean chlorophyll *a* from NASA are higher compared to the *in-situ* data for almost the whole period (2003 to 2011) as shown in Figure 2.2. The RMSE between chlorophyll *a* from CMEMS and the *in-situ* datasets is 0.507 mg m^{-3} and it is 1.386 mg m^{-3} between NASA chlorophyll *a* and the *in-situ* datasets. Therefore, for the very localized region described in Section 2.2.3, the dataset from CMEMS under represents the range of variation compared to NASA but its RMSE is smaller compared to NASA.

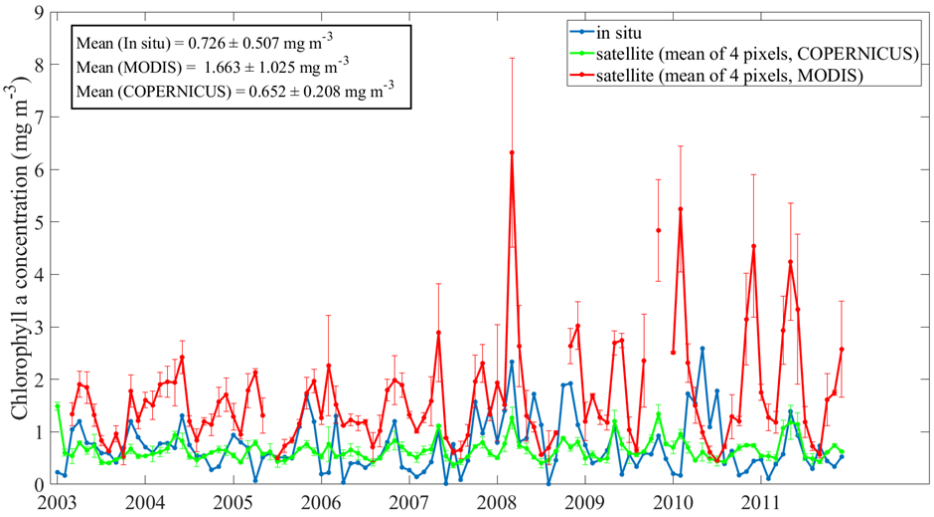

Figure 2.2: *In-situ* time series of chlorophyll *a* (blue curve) along the continental shelf area of the Southern Eastern Black Sea (from Agirbas et al., 2015). The mean of four pixels closest to the station using either NASA (red curve) or CMEMS (green curve) is plotted. From the mean of 4 pixels, the ones with a standard deviation strictly higher than 3 mg m^{-3} have not been considered. The errors bars show the standard deviation. The black square represents the mean over the whole analysed period and the associated standard deviation.

2.3.2 Harmonic analysis

Figures 2.3a) &d) reveal how well the model based on harmonics oscillations fits to the time series of NASA and CMEMS Chlorophyll *a* respectively.

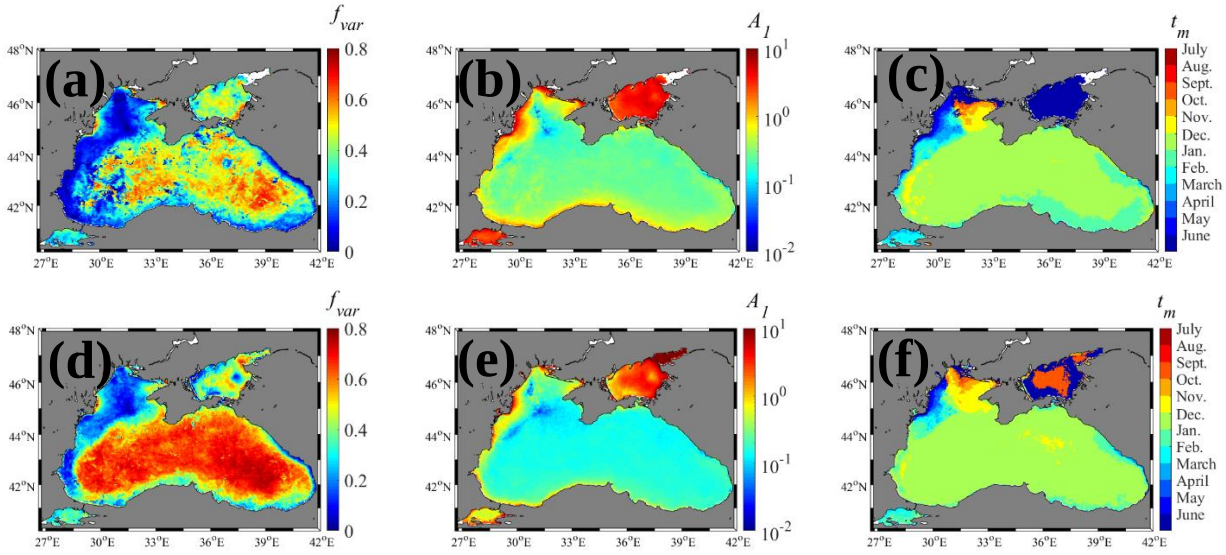

Figure 2.3: Top panel figures a) b) c) uses NASA product and bottom panel figures d) e) f) uses CMEMS product. a) d) f_{var} is the fraction of variance explained by the fit, see equation 2.6 for details, b) e) Amplitude of the annual cycle (A_1 in mg m^{-3}), c) f) Phase (t_m, expressed in months), *i.e.* timing of the peak. The results consider the period 2003 to 2017. CMEMS data has been interpolated to NASA grid for the comparison.

The fraction of variance explained by the fit (f_{var}) reached the highest values in the deep regions of the Black Sea for both datasets. For NASA data (Fig.2.3a), the best values are spread between [0.4 – 0.7], whereas for CMEMS (Fig. 2.3d), values around 0.7 are uniformly observed. This suggests a good fit of the harmonic model with the chlorophyll *a* signal. However, for the shallow regions, especially along the western shelf, the values of f_{var} are the lowest for both datasets. They are around or below 0.1 for both NASA and CMEMS. This suggests a poor fit of the harmonic with the chlorophyll *a* signal over the coastal areas.

Figure 2.3b) &e) show the calculated amplitude over the whole Black Sea for NASA and CMEMS product. The same patterns are observed for both. The amplitude of the signal is homogeneous almost over the entire Black Sea with values around 0.3 mg m^{-3} and 0.15 mg m^{-3} for respectively NASA and CMEMS. The signal is highest near the Danube mouth, going up to 8 mg m^{-3} for NASA and 5 mg m^{-3} for CMEMS. There is a west to east gradient of the peak

amplitude over the AS with values going from around 3 to 5 mg m^{-3} for NASA and from 1.4 mg m^{-3} to more than 5 mg m^{-3} for CMEMS. The last metric analysed is the phase of the harmonic signal (t_m), presented in Figure 2.3c) &f) for NASA and CMEMS respectively. The results of the phase are an indication for the timing of the chlorophyll *a* peak. The main basin is characterized by a homogeneous phase (t_m) occurring mainly between December – January for NASA and CMEMS. With the NASA product, the Azov Sea has a homogeneous phase around June. Concerning CMEMS, the AS has also a phase around June, except for its inner part, which presents phase values around September. The values of the phase show greater variability inside the NWS for both datasets. Indeed, the coastal areas of the NWS have phase around June whereas the offshore part of the shelf has phase values being more heterogeneous around December to March. For both NASA and CMEMS products, the central Black Sea is characterized by homogeneous values of the fraction of variance explained by the fit (f_{var}), amplitude (A_1) and phase (t_m).

Overall, both satellite products give similar qualitative patterns but CMEMS has lower errors. By using NASA datasets, there is a limitation in the length of the time series available as it only starts in the year 2003. However, CMEMS data permit the analysis to start in 1998. Therefore, to facilitate the presentation of the results and avoid any repetition, only the CMEMS data is now used for further analysis.

2.3.3 Seasonal cycle of chlorophyll *a*: regional analysis

The geographical distribution of the chlorophyll *a* peak timing observed from the harmonic phase (t_m) is used as a criterion for the delimitation of sub-regions inside the Black Sea. Simple histograms (Fig. 2.4 a&b) have been used to determine an optimal number of sub-regions. The AS is considered as a separate entity. The phase inside the NWS is grouped into 5 sub-regions, presented in Figure 2.4a. The main basin (excluding the Azov Sea and the NWS) was separated into 3 phases classes (Fig.2.4b). The main basin (excluding the Azov Sea and the NWS) was separated into 2 phases classes (Fig.2.4b, the inner part in orange versus the coastal part in red). The results in the Black Sea sub-regions are then presented in Figure 2.5.

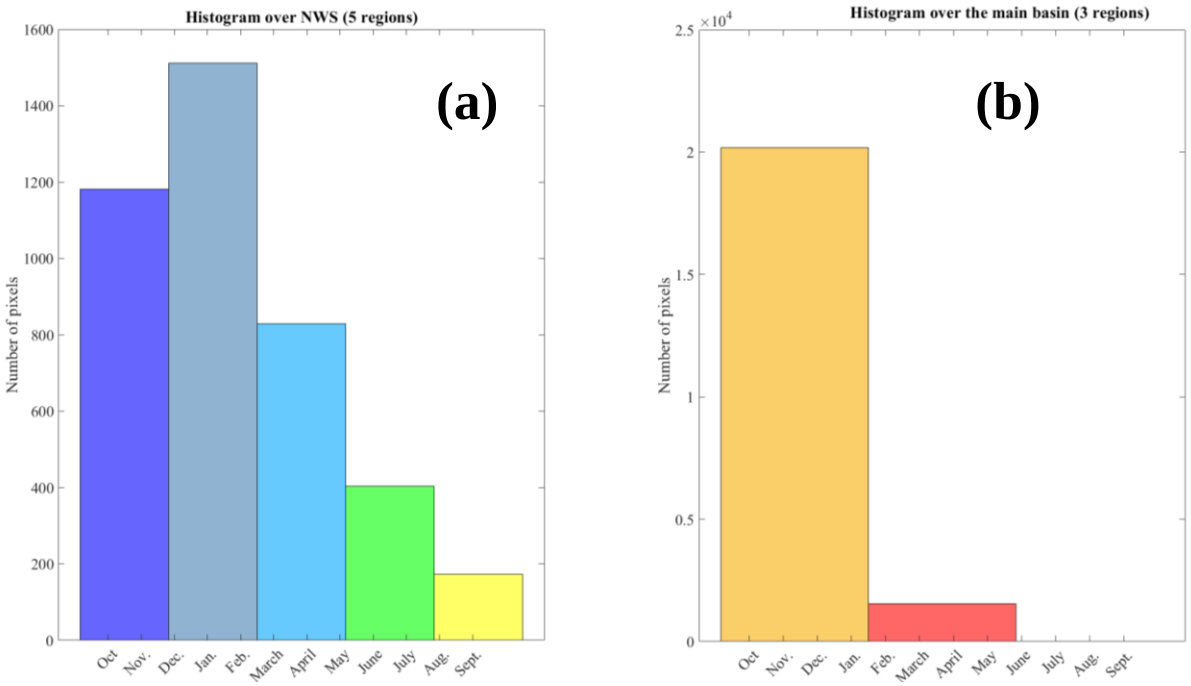

Figure 2.4: Histogram accounting for the number of pixels inside different phase classes (t_m) over a) the NWS and b) the main basin. For the main basin, two classes were merged as one of them does not have many pixels. The color code represents the sub-regions presented in Fig. 2.5.

For each sub-region, the mean seasonal cycle is computed over the period 1998 to 2017 (Fig. 2.5). The main basin of the Black Sea (Regions 6 and 7) is characterized by relatively low values of chlorophyll *a* across the whole seasonal cycle. The central basin (Region 6) can be related to the U-shape pattern. Indeed, the mean maximum value of chlorophyll *a* is observed during winter months (November-December-January) with values around 0.5-0.6 mg m^{-3}, whereas the mean minimum of chlorophyll *a* occurs during summer (July-August) with a concentration around 0.25 mg m^{-3}. This type of seasonal dynamic is different from what is usually observed for temperate zones. Over the whole period, the maximal values were reached in December 2014, reaching 0.95 mg m^{-3}. In May 2001, the maximal value reached was 2.4 times higher compared to the climatological mean of the seasonal cycle, going up to 0.79 mg m^{-3}.

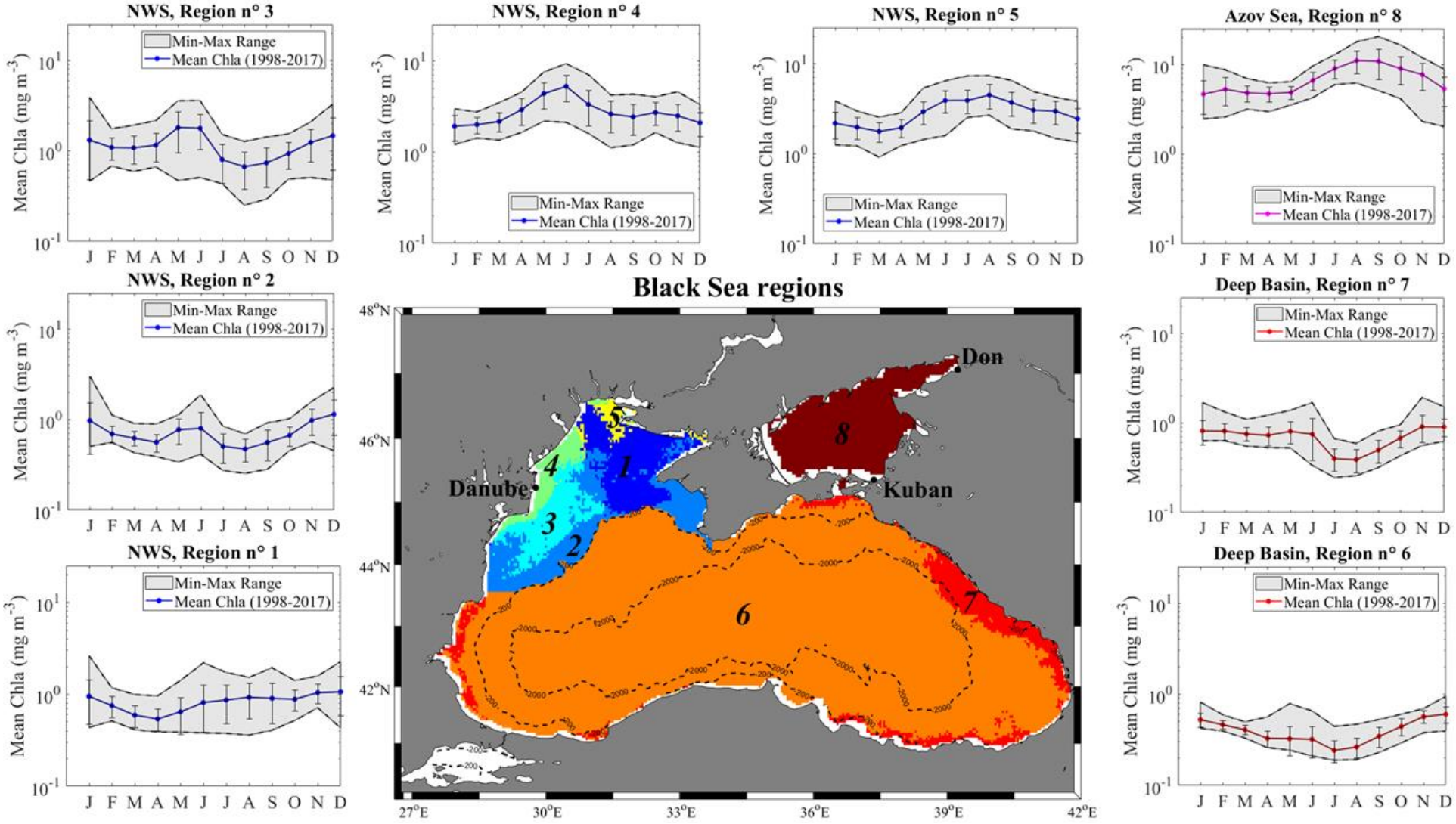

Figure 2.5: Sub-regions obtained from the phase values in the harmonic analysis from 1998 - 2017. Each color represents a different region, cumulating a total of 8 regions. The 200 and 2000 isobaths are represented. The surrounding plot indicates the associated seasonal chlorophyll *a* for the 8 sub-regions inside the Black Sea, using CMEMS data from 1998 to 2017. The vertical bars are the standard deviation, indicated for each month. The range of the minimum-maximum is shown with the "shaded envelop".

The seasonal dynamic inside the NWS shows a lot of variability among its different sub-regions (Region 1 to 5). Regions 4 and 5 which are along the coast, presents significantly higher mean values compared to the other sub-regions of the NWS (Regions 1 to 3). Region 4 surrounds the Danube river mouth and its mean chlorophyll *a* concentration is maximum in June, with values around 5.3 mg m^{-3}. For this month, the maximum value was reached during the year 2000, being around 9.3 mg m^{-3}. In the vicinity of the break shelf (Region 2), the mean chlorophyll *a* increases from around 0.56 mg m^{-3} in April to 0.78 mg m^{-3} in May/June. It is then minimum in August with values around 0.47 mg m^{-3}, before increasing again until a maximum in December with values around 1.14 mg m^{-3}. Concerning the Azov Sea, the mean chlorophyll *a* reach a maximum around 11 mg m^{-3} in August/September, whereas the mean minimum chlorophyll is observed in April/May and is about 4.7 mg m^{-3}. The timing of the maximum values in the seasonal dynamic of chlorophyll *a* for the sub-regions, agrees with the values of the phase previously described.

2.3.4 Seasonal cycle of chlorophyll *a*: assessing controlling factors with a local analysis

The coefficients of correlation between monthly time series of chlorophyll *a* and surface temperature are displayed in Figure 2.6a. As temperature is generally linked to the degree of stratification and mixing, this provide insight regarding the mechanisms controlling the seasonal dynamics of chlorophyll *a*.

The inner basin of the Black Sea has negative and significant coefficients of correlation with values around -0.5. The Azov Sea on the other hand, displays significant and positive coefficients of correlation in the range + [0.2-0.6]. The NWS is more variable, with the coastal side having positive and significant correlation coefficients around +0.3, whereas the area around the break shelf is negative with values around -0.2. The inner part of the NWS does not show any significant correlation (p_{value}>0.05). Figure 2.6b compares the mean SST between the Azov Sea (Region 8), the inner basin (Region 6) and a sub-region inside the NWS (Region 2) from 2003 to 2017. The maximum of surface temperature is observed in summer (July/August) and reach similar values around 26°C for the three regions.

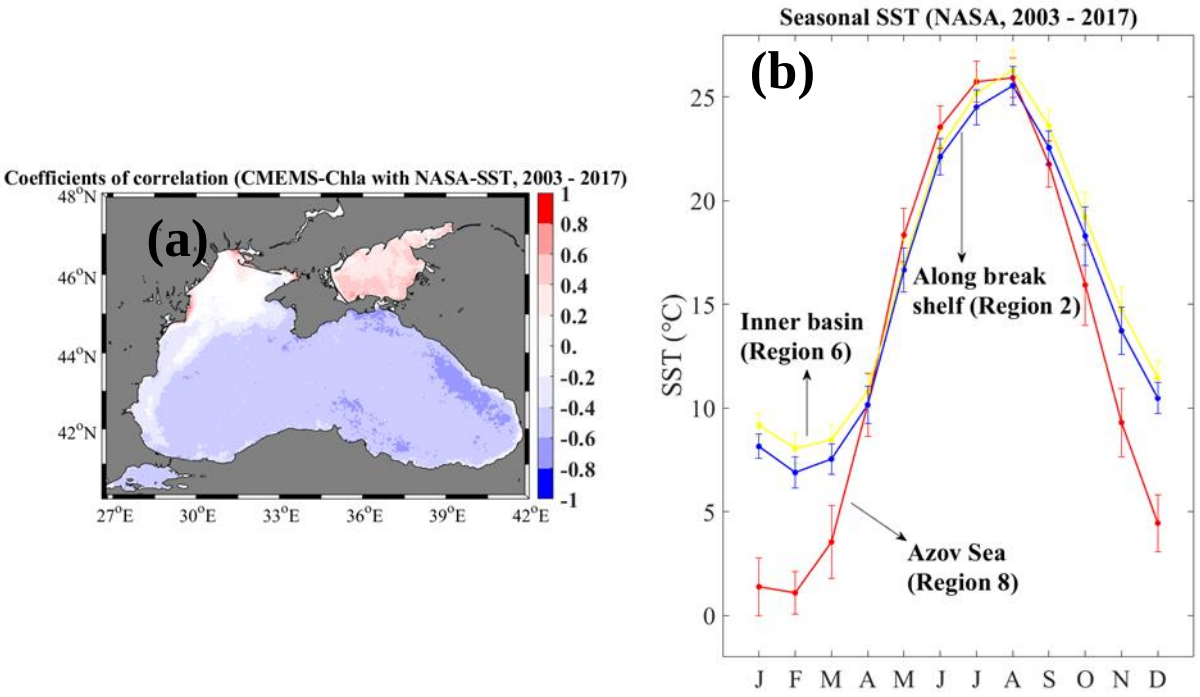

Figure 2.6: a) Map of the coefficient of correlation that are only significant ($p<0.05$) between CMEMS-Chla and NASA-SST, using monthly time series over the period 2003 - 2017. b) Seasonal SST for the regions 2, 6 and 8, over the period 2003 to 2017.

The minimum is significantly lower in the Azov Sea, going down to 1.1°C in February. The conditions typical of the AS (low salinity and shallowness), makes it susceptible to freeze during winter. Region 2 and 6 also reach minimum temperature in February, with the respective values of 6.9°C and 8.1°C.

The impact of the river discharge on the seasonal chlorophyll *a* was investigated. As nutrients are supplied to the Black Sea by the rivers, they can influence the growth of the phytoplankton and therefore affect the chlorophyll *a* dynamic on a seasonal scale. As both chlorophyll *a* and river discharge are subject to intense interannual variability, only overlapping period (1998 - 2008) for both datasets were used to compute the seasonal climatology.

The seasonal Danube discharge reach maximum values in April (9865 $m^3 s^{-1}$) and is minimum in September (5095 $m^3 s^{-1}$). Region 4 which is located around the Danube mouth, does not show a significant correlation with the Danube discharge ($R^2 = 0.082$, see Table 2.2). However, when considering a time lag of a month, Regions 3 and 4 have a significant correlation with the Danube discharge, with the values of $R^2 = 0.527$ and $R^2 = 0.567$ respectively (Table 2.2 and Fig.2.8).

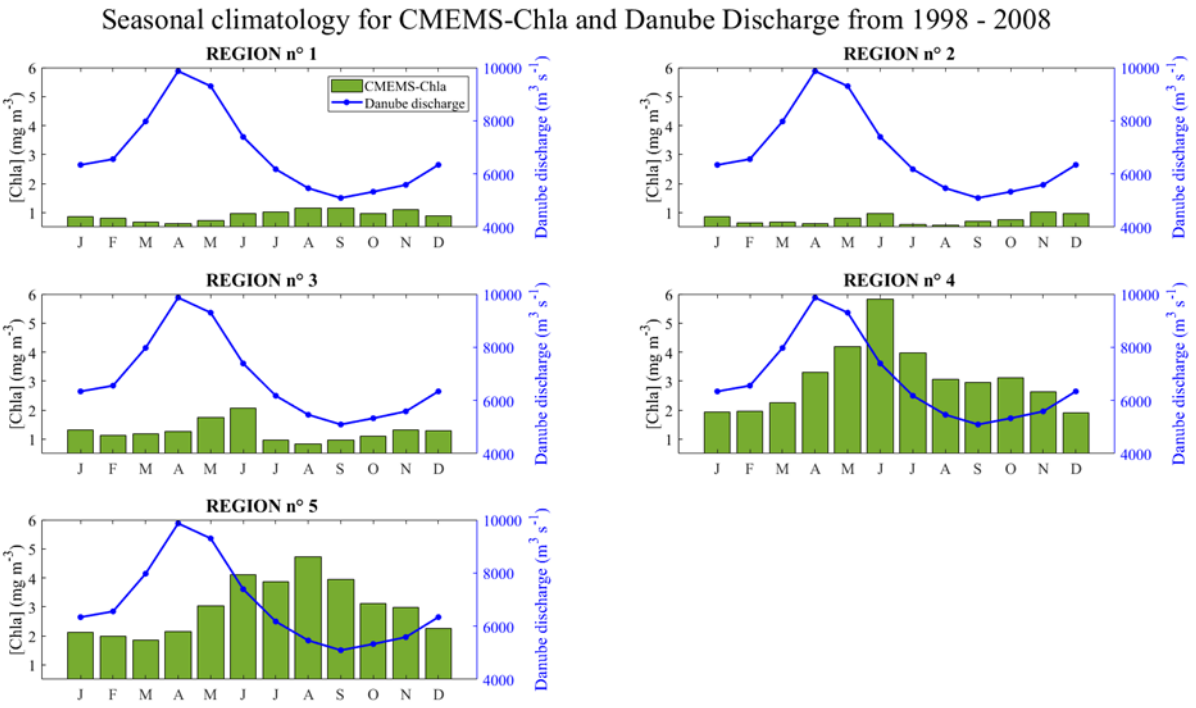

Figure 2.7: Seasonal climatology of the Danube discharge at Ceatal Izmail Station (blue line) compared with the seasonal climatology of chlorophyll *a* from CMEMS (green bars) from 1998 to 2008. The 5 sub-regions inside the NWS are considered.

Table 2.2: Coefficient of correlation between the seasonal Danube discharge (m^3 s^{-1}) and the seasonal chlorophyll *a* from CMEMS (from 1998 - 2008). Significant correlation to the p_{value} of 0.05 are shown with an asterisk.

Sub-regions (inside the NWS area)		1	2	3	4	5
Coefficients of (R^2 ; r) and sign of the correlation	No lags	(0.735;0.857) (-)*	(0.008;0.08) (-)	(0.276;0.526) (+)	(0.082;0.287) (+)	(0.171;0.414) (-)
	1 month lag	(0.211; 0.459) (-)	(0.001;0.039) (+)	(0.527;0.726) **(+)***	(0.567;0.753) **(+)***	(0.009; 0.095) (+)

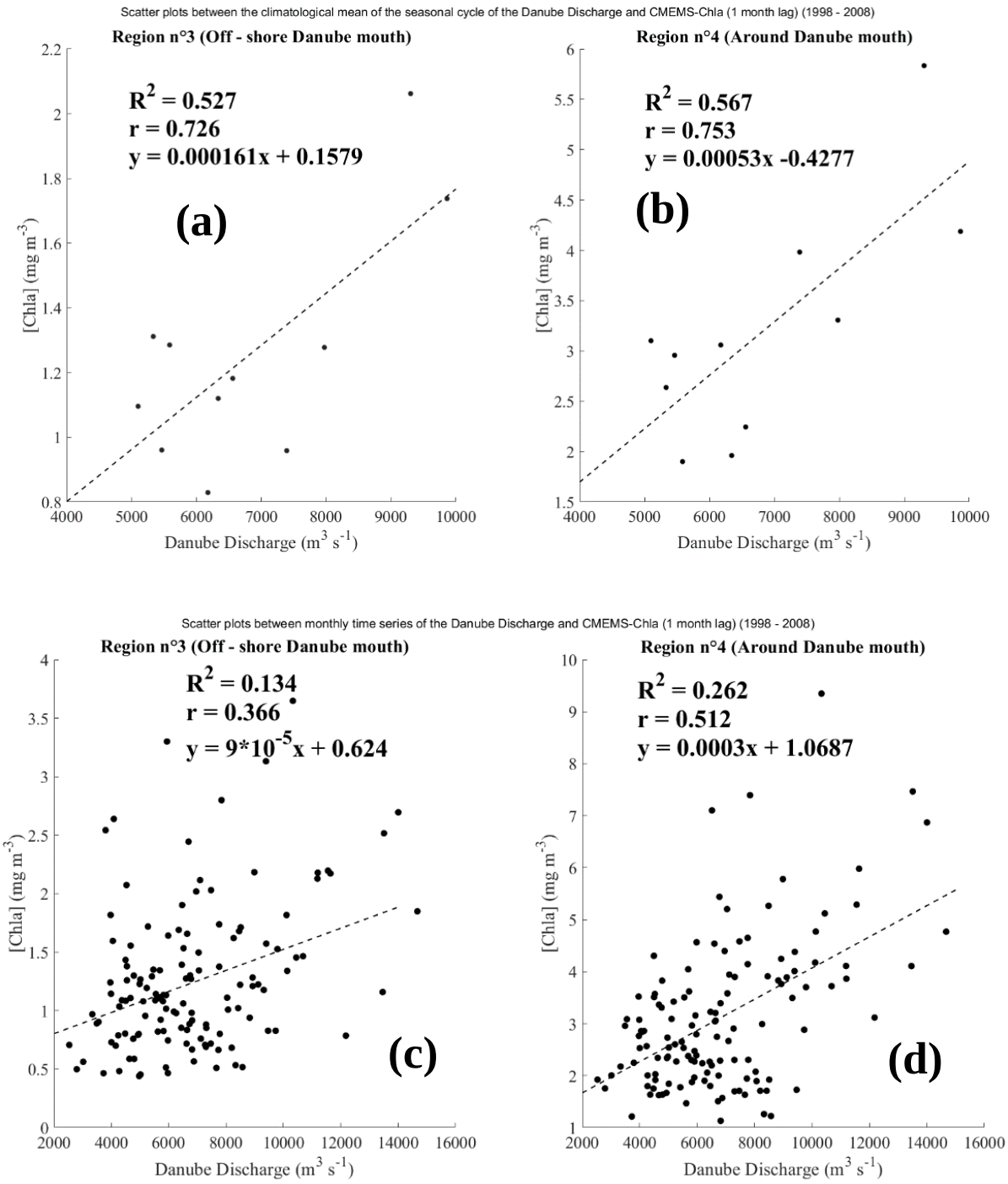

Figure 2.8: Scatter plot between the Danube discharge (m^3 s^{-1}) and CMEMS - Chla for (a) region 3 and (b) region 4, considering one-month lag (this is why only 11 points are displayed). The correlation between the Danube discharge and CMEMS – Chl*a* using instead all the monthly data in the time series is also shown for information in c) for region 3 and d) for region 4.

Don and Kuban rivers are the two main rivers that discharge in the Azov Sea. Their variability was also investigated and linked with the chlorophyll *a* cycle in this region. No clear correlation was observed between the seasonal chlorophyll *a* and Kuban discharge (Fig. 2.9d). However, a negative correlation (R^2 = 0.55) is observed with Don discharge. Such result suggests that the variability in chlorophyll *a* in the Azov Sea is not mainly driven by the riverine inputs.

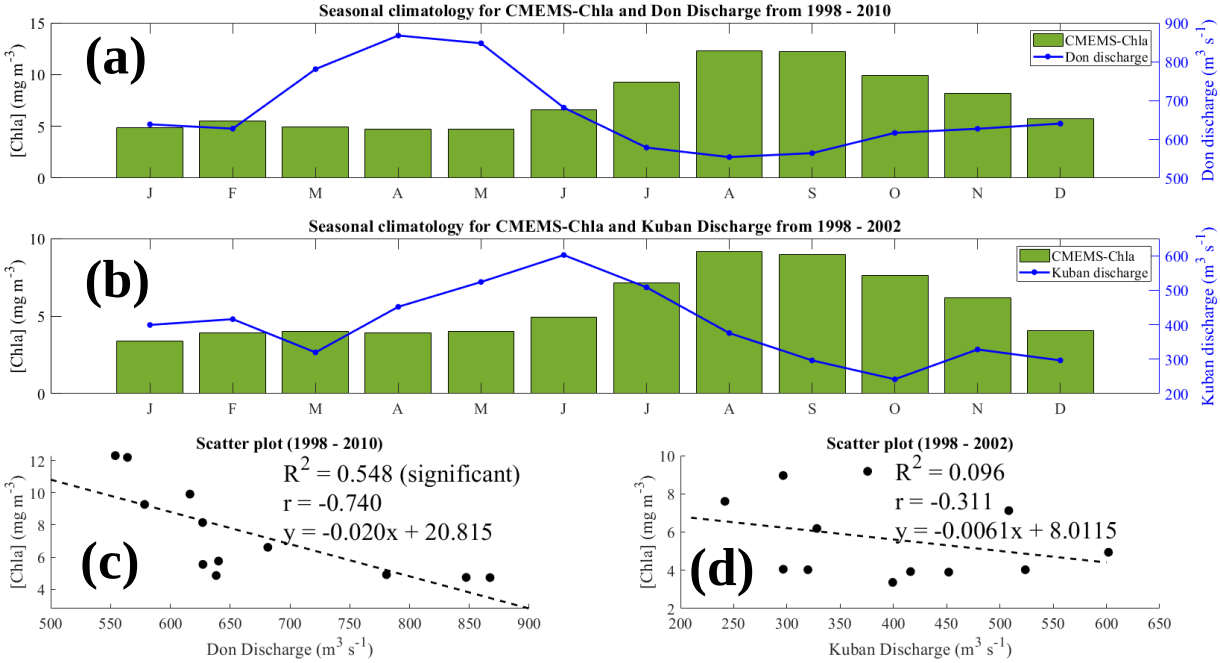

Figure 2.9: Seasonal climatology of (a) Don discharge (blue line) and (b) Kuban discharge, compared with the seasonal climatology of chlorophyll *a* from CMEMS (Region 8, green bars). (c) and (d) are the associated scatter plots between the seasonal river discharge and the chlorophyll *a*.

2.3.5 Correlation of monthly anomalies

The climatological mean of the seasonal cycle from 2003 to 2017 is first computed and the anomaly results in the difference between the observed monthly mean and the climatological mean of the seasonal cycle, leading to a time series that includes a total of 180 data points. The areas that show a significant correlation coefficient between the monthly anomalies of chlorophyll *a* (CMEMS-Chla) and the SST (NASA-SST) are sparse and the values are low (Fig.2.10). The Black Sea has only small values of the coefficient of correlation and they are

positive in both the North coast of the NWS and the AS (around [+0.2; +0.3]), but negative in the South Western coast (around [-0.2; -0.3]).

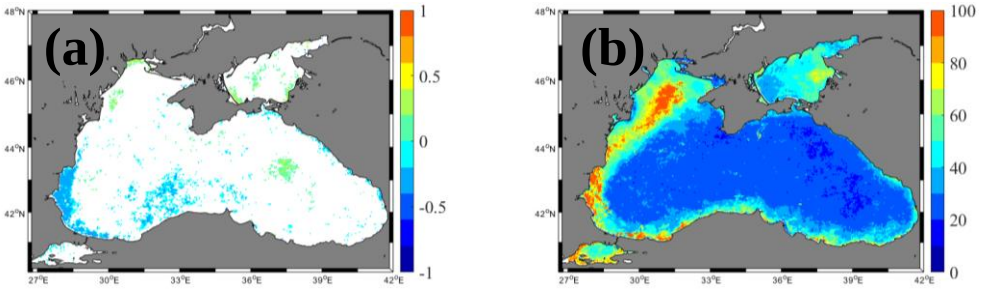

Figure 2.10: a) Significant areas (p_{value} < 0.05) for the coefficient of correlation between the monthly anomalies of CMEMS-Chla and NASA-SST. b) Normalised standard deviation (it has been divided by the total mean of chlorophyll *a* and is expressed in percentage).

The associated maps of the relative standard deviation of the chlorophyll *a* (Fig.2.10b)) shows that the NWS and the south west coast of the Black Sea have high values compared to the rest of the basin (between 60%-100%) . The inner gyres have a small value of the relative standard deviation of chlorophyll *a* that is around 25%. This result suggests that there is low variability on the seasonal cycle of chlorophyll *a* on the inner gyres for CMEMS-Chla. The AS shows intermediate values of standard deviation that are around 30-70%.

2.3.6 Interannual analysis of chlorophyll *a*

In this section, the role of the precipitation, rivers, the sea surface temperature and the volume of the CIL is investigated on interannual time scales and related to the annual chlorophyll *a*.

2.3.6.1 Investigation of the role of precipitation and rivers

The catchment area from Envirogrid used for the analysis is presented on Fig.2.11.

Figure 2.11: Illustration of the catchment area of the Black Sea with country names, along with the location of the main rivers around the Black Sea (Danube, Dniester and Dnieper). Figure extracted from http://www.envirogrids.net.

The spatial distribution of the annual precipitation over the catchment area of the Black Sea is presented in Fig 2.12. Two extreme years, 2003 and 2010, are used as examples.

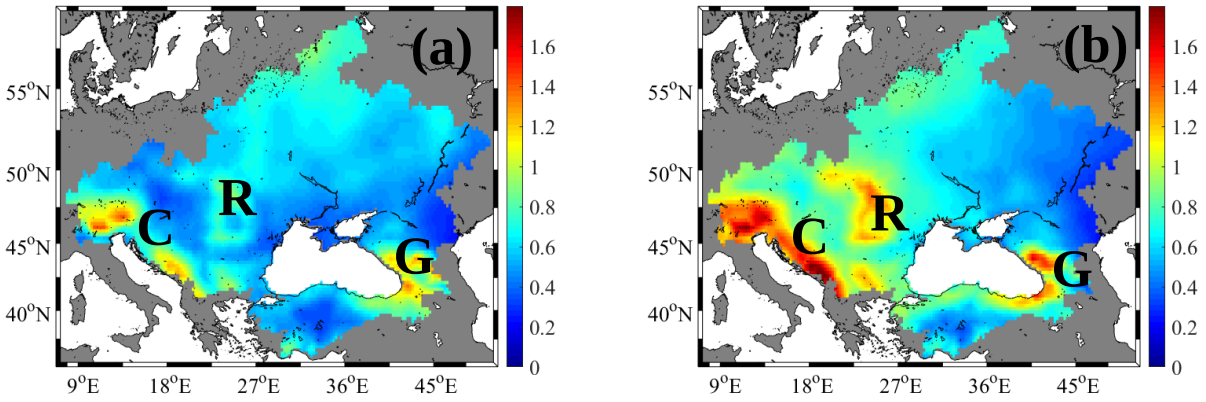

Figure 2.12: Spatial maps of the total precipitation (m) over the entire catchment area of the Black Sea for a) 2003 and b) 2010. The letters G, C and R refers to Georgia, Croatia and Romania. They are indicated to facilitate the description of the patterns in precipitation.

For the year 2003 (Fig. 2.12a), the total precipitation (*i.e.* the precipitation values were multiplied by the grid point area and then averaged over the whole catchment area) is around 3.16×10^8 m^3, whereas for the year 2010, an additional 7.63×10^7 m^3 of precipitation is observed. For both years, the maximum precipitation is observed along the eastern and south eastern part of the Black Sea, on the side of Georgia (indicated with the letter G in Fig.2.12). The values are

around 1.1 m in 2003, and around 1.5 m in 2010. Other maxima are observed, for example along Croatia (letter C in Fig.2.12), where it goes up to 1.2 m in 2003, and 1.7 m in 2010. For the year 2010, there is a localised increase of precipitation over Romania (letter R in Fig.2.12), with values around 1.3 m. For the two years analysed, most of the north eastern area of the catchment that includes Russia, has low values of precipitation, around 0.5 m. The annual time series of the catchment precipitation is then computed from 1998 to 2017 and compared with the available annual discharge from the Danube, monitored at Ceatal Izmail station from 1998 to 2010 (Fig. 2.13a&b). The year 2009 has no record of the Danube discharge.

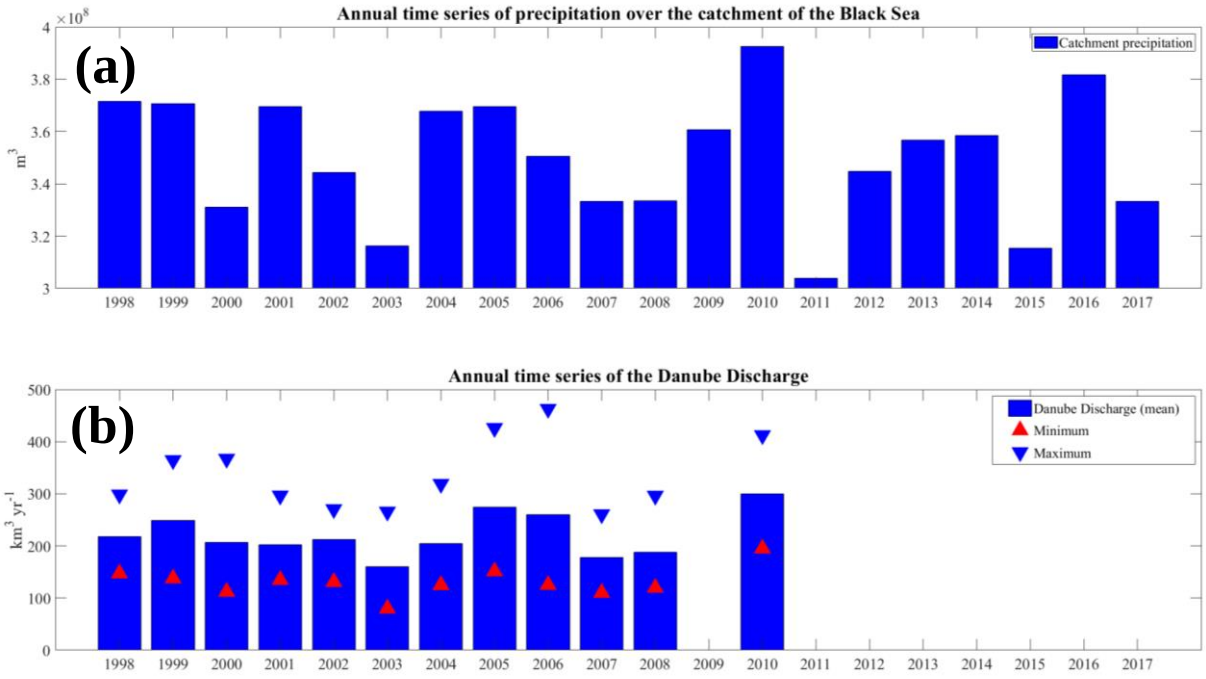

Figure 2.13: (a) Annual time series of the total precipitation (m^3) over the entire catchment area of the Black Sea from 1998 to 2017. (b) Annual time series of the Danube discharge ($km^3\ yr^{-1}$) at Ceatal Izmail station with the maximum (blue inversed triangle) and minimum (red triangle) range from 1998 to 2010.

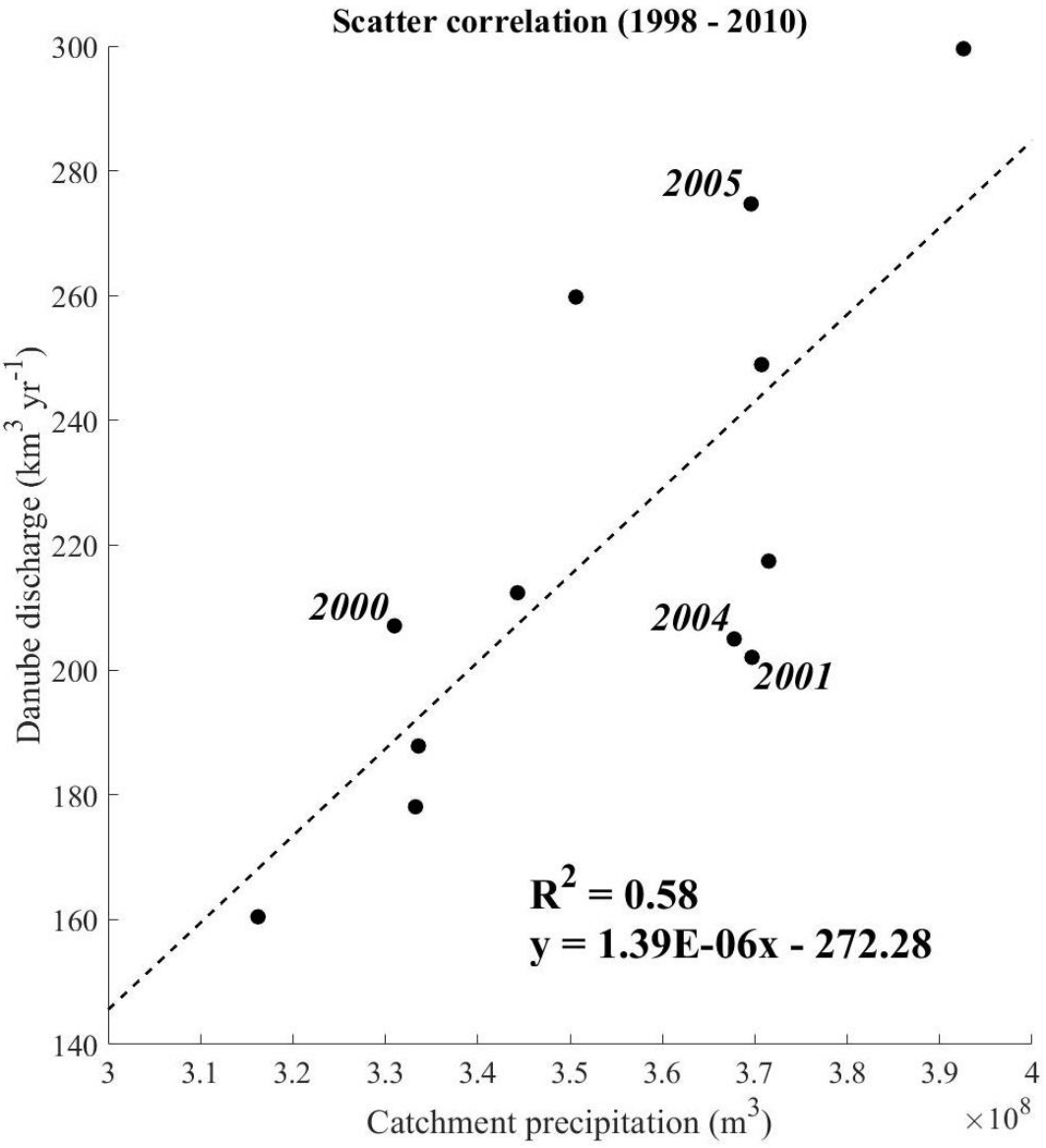

Figure 2.14: Scatter correlation between the Danube discharge (km^3 yr^{-1}) and the catchment precipitation (m^3) from 1998 to 2010.

As river flow depends directly to precipitation, the correlation between the two variables was then investigated. The annual time series of precipitation over the catchment of the Black Sea shows strong variability from 1998 to 2017 (Fig. 2.13a). In the period that overlaps with the Danube data, *i.e.* 1998 to 2010, the lowest amount of precipitation over the catchment is observed in 2003 with values around $3.16x10^8$ m^3, which is also associated with the lowest mean discharge of the Danube, around 160 km^3 yr^{-1}. In contrast, the highest amount of precipitation over the catchment is observed in 2010, going up to $3.93x10^8$ m^3, and the discharge from the Danube shows the highest mean values, around 300 km^3 yr^{-1}. Although the extreme values of precipitation seem to be linked with the discharge of the Danube, such correlation is

not always noticeable for other years in the time series. For example, the precipitation in 2001 is higher than in 2000, with an additional amount of 3.87×10^7 m^3 in precipitation, but the Danube discharge stays almost constant for those years, around 200 km^3 yr^{-1}. The spatial maps of annual precipitation over the catchment for the years 2000 and 2001 is shown in the Appendix A (Figs.A.5 & A.6). Similar changes are observed between the year 2000 and 2004 where the discharge is around 200 km^3 yr^{-1}, but the precipitation goes from 3.31×10^8 m^3 in 2000 to 3.67×10^8 m^3 in 2004. Besides that, it is noticeable that the Danube discharge is higher in 2005 (275 km^3 yr^{-1}) compared to 2001 (202 km^3 yr^{-1}), but the precipitation over the whole catchment has similar values, around 3.69×10^8 m^3.

Using the data over the whole period available, a significant positive correlation ($R^2 = 0.58$, Fig.2.14) is observed between the precipitation over the catchment and the Danube discharge. The record of the Danube discharge also presents strong variability, especially in the maximum values reached in a particular year (blue reversed triangle in Fig. 2.13b). In 2006, the mean annual discharge is around 260 km^3 yr^{-1}, but for the same year, the month of March recorded maximum values of 462 km^3 yr^{-1}. The lowest minimum discharge of the whole record, was observed in September 2003, going down to 80 km^3 yr^{-1}.

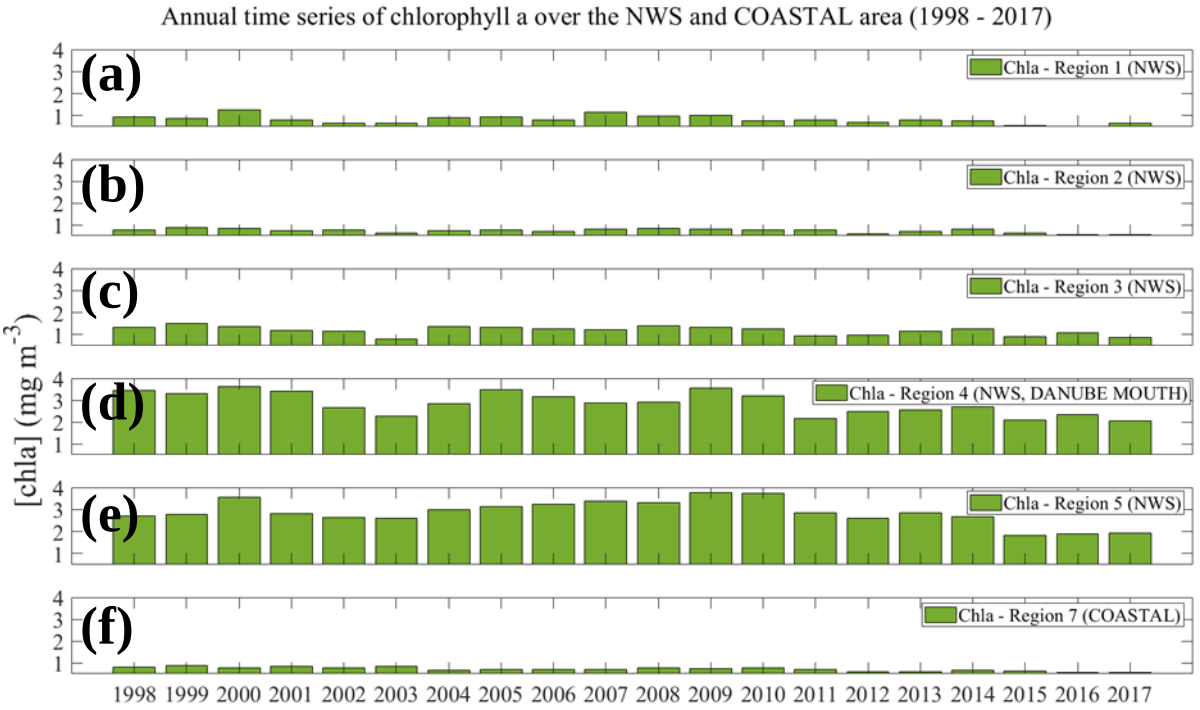

Figure 2.15: (a) to (e) Annual time series of chlorophyll *a* (mg m^{-3}) over the 5 sub-regions in the NWS from 1998 to 2017. (f) Annual time series of chlorophyll *a* (mg m^{-3}) over the Coastal area (Region 7).

The interannual variability of chlorophyll *a* over Regions 3 and 4 (Fig. 2.15c&d) which are the closest to the Danube mouth, are then compared to the river flow of the Danube and the total catchment precipitation (Table 2.3). There is no significant correlation between the Danube discharge and the mean chlorophyll *a* over Region 4 (adjacent to the Danube delta) on interannual time scales. A significant positive correlation was observed between the total catchment precipitation and chlorophyll *a* for Region 3 and 4 with the respective values of R^2 = 0.323 and R^2 = 0.299 (Fig. 2.16).

Table 2.3: Correlation (R^2) between the total precipitation over the catchment of the Black Sea (m), the Danube discharge ($km^3\ yr^{-1}$) and the chlorophyll *a* ($mg\ m^{-3}$) over the 5 sub-regions in the NWS (Regions 1 to 5) and in the COASTAL area (Region 7). The sign of the correlation is indicated in parenthesis and significant correlation are shown by an asterisk (*).

R^2 values	**Chlorophyll *a***					
	Region 1	Region 2	Region 3	Region 4	Region 5	Region 7
Total precipitation over the catchment (1998 - 2017)	0.0005 (+)	0.017 (+)	**0.323* (+)**	**0.299* (+)**	0.040 (+)	0.002 (+)
Danube discharge (1998 - 2010)	0.023 (-)	0.029 (+)	0.192 (+)	0.284 (+)	0.144 (+)	/

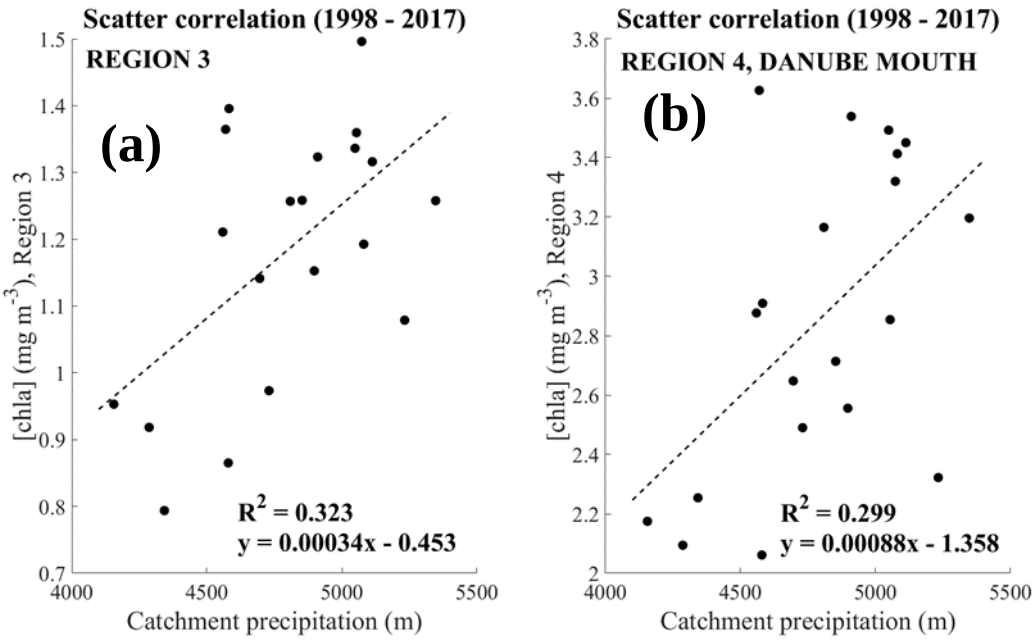

Figure 2.16: Scatter correlation between the annual catchment precipitation (m) and the chlorophyll *a* concentration in (a) Region 3 and (b) Region 4, from 1998 to 2017.

For completeness, the correlation (not shown to be significant) between the annual variation in chlorophyll *a* in the AS with discharge from Don and Kuban, is put in the Appendix A (Figs.A.7 and A.8).

2.3.6.2 Investigation of the role of sea surface temperature

The annual time series of chlorophyll *a* and SST was computed for each pixels of the basin and their correlation was analysed (Fig.2.17).

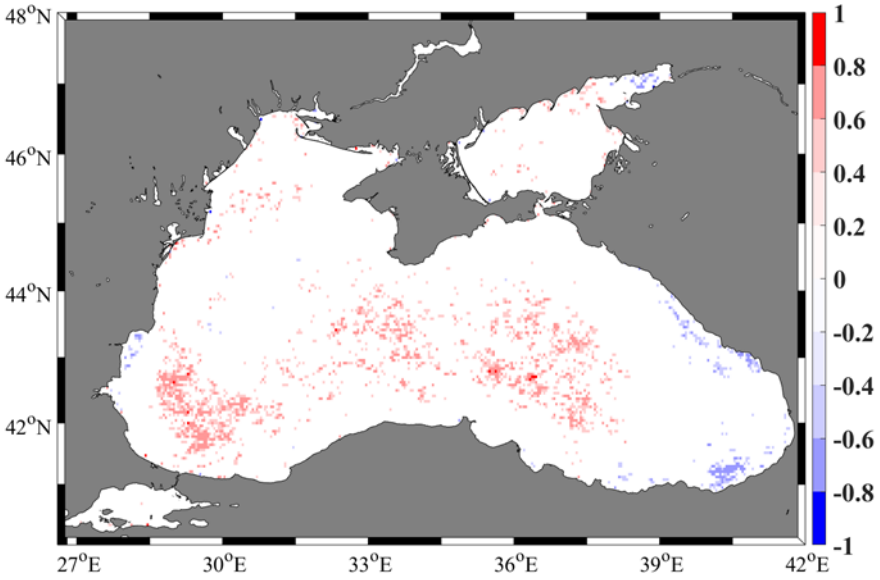

Figure 2.17: Coefficient of correlation (r) between annual time series of Chlorophyll *a* - CMEMS and SST-NASA from 2003 to 2017. Only the significant values are shown.

Figure 2.17 presents the results of the annual correlation of chlorophyll *a* and SST-NASA. The inner part of the Black Sea and the South Western area, shows mainly positive coefficient of correlations around [+0.5; +0.8], where they are significant. Few pixels display negative correlation coefficients and are located on the South Eastern coast of the Black Sea with values around [-0.5; -0.8]. The results are sparse and a comparison of the correlation for two close pixels (one that is significant and one that is not) is presented in the Appendix A (Fig.A.9). This result was compared with the area-averaged chlorophyll *a* and sea surface temperature of Region 6, which is the inner part of the basin (Fig.2.18a&b). The positive correlation was not significant for the p_{value} of 0.05 (Fig.2.18c).

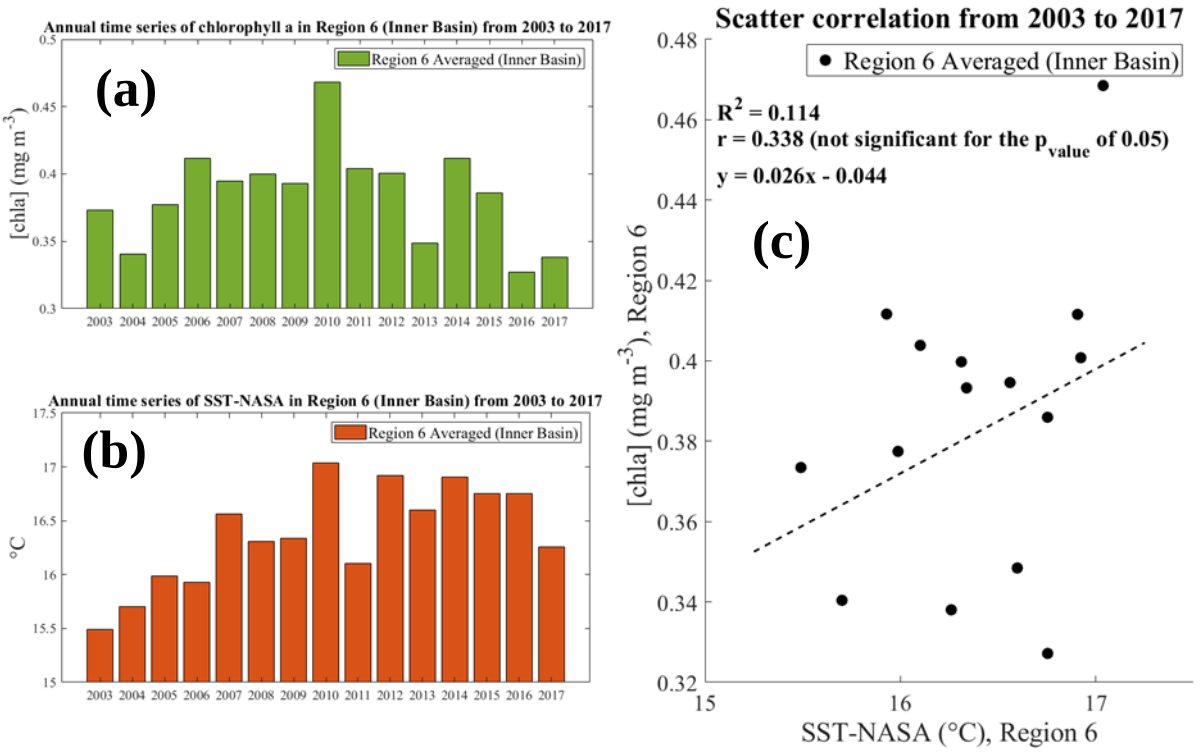

Figure 2.18: Annual time series of (a) CMEMS-Chla (mg m^{-3}) and (b) SST-NASA (°C), both in Region 6 (Inner basin) from 2003 to 2017. (c) Scatter correlation from 2003 to 2017 between CMEMS-Chla and SST-NASA.

2.3.6.3 Investigation of the role of the Cold Intermediate Layer

From the Black Sea Reanalysis model extracted from the Copernicus service (see Section 2.2.8 for details), the potential volume of CIL was assessed. For each volume grid cells, if the temperature is below 8°C and the salinity in the range of [17.98-19.84] psu, then it is considered as CIL. The total volume of the CIL is then assessed over the whole Black Sea and indicated on Figure 2.19. The figure is obtained by integrating annually and over the whole basin, all the volume that has the characteristics of the CIL on an annual basis.

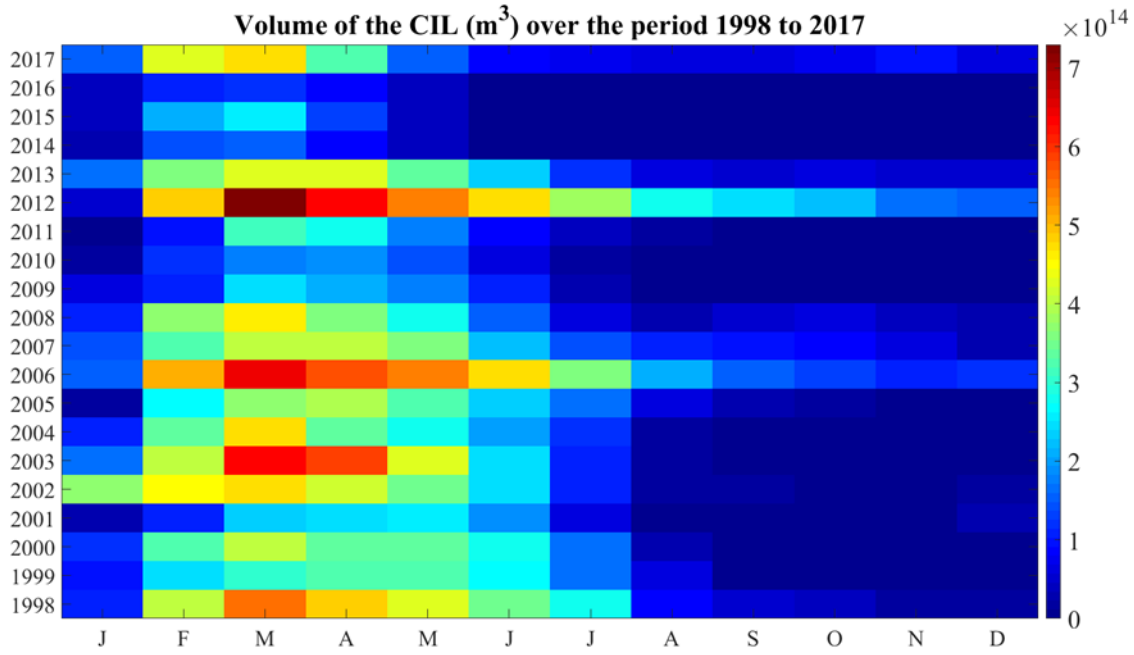

Figure 2.19: Monthly volume (m^3) that has temperature below 8°C and salinity in the range [17.98-19.84] psu, criteria used to detect the CIL for the period 1998 to 2017.

The results of figure 2.19 indicates that according to the criteria used to detect the CIL, the CIL is preferentially formed between February and May. There is a strong variability of the signal in terms of its dynamics and intensity from 1998 to 2017. The years 2003, 2006 and 2012 are associated with the highest CIL volume during March with respectively the values of $6.4x10^{14}$, $6.4x10^{14}$ and $7.3x10^{14}$ m^3. However, the volume of the CIL in March was lower than $2x10^{14}$ m^3 in 2010, 2014 and 2016. The correlation between the CIL volume and the chlorophyll *a* concentration was investigated in Figure 2.20 and 2.21.

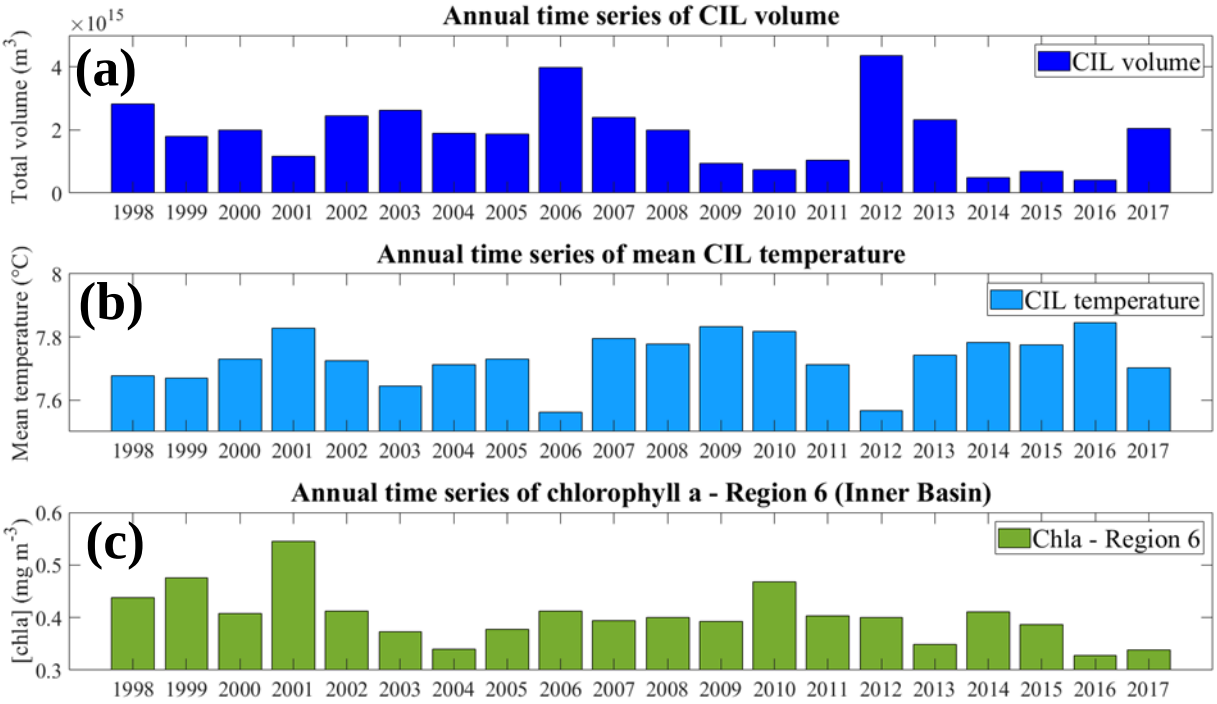

Figure 2.20: (a) Total volume of CIL (m^3). (b) Mean temperature of the CIL. (c) Annual mean chlorophyll *a* concentration from CMEMS-Chla over Region 6 (Inner Basin). All time series are from 1998 to 2017.

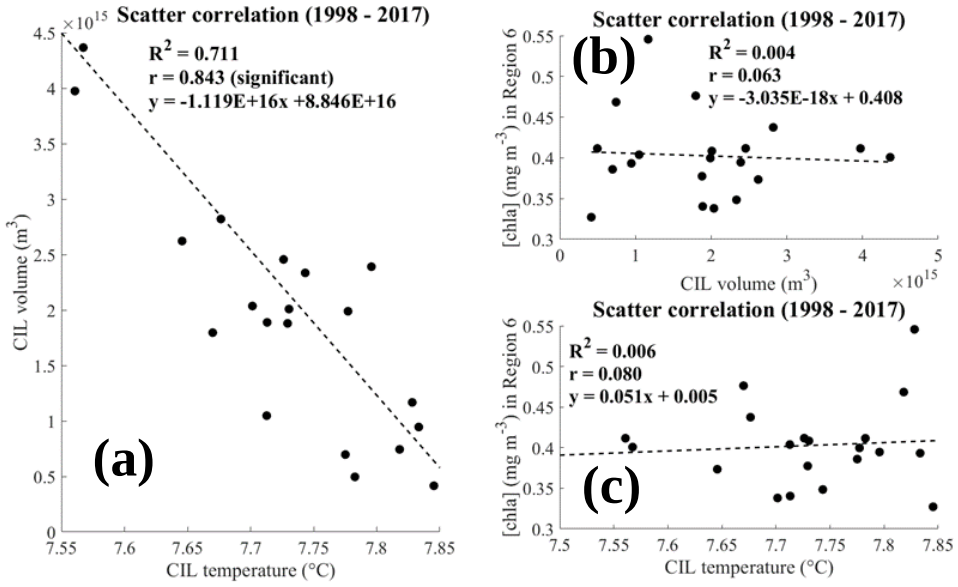

Figure 2.21: Scatter correlation between (a) the CIL temperature and the CIL volume, (b) the CIL volume and the chlorophyll *a* concentration in Region 6 and (c) the CIL temperature and the chlorophyll *a* concentration in Region 6.

There is a negative correlation between the CIL temperature and the CIL volume, with R^2 = 0.7111 (Fig.2.21a). No significant correlation is observed either between the CIL volume or the CIL temperature with the chlorophyll *a* concentration in Region 6 (Inner Basin).

The same analysis was done but instead of considering the annual values, the warm season which is defined from May until November (Belokopytov, 2011; Shapiro et al., 2011; Miladinova et al., 2018) was used. No significant correlation was observed, the results are put inside the Appendix A (Figs.A.11).

2.4 Discussion

2.4.1 Seasonal cycle of chlorophyll *a*: shape of the signal

The shape of the seasonal chlorophyll *a* dynamic was described using metrics (amplitude, phase) obtained from the harmonic analysis between 2003 to 2017. Similar patterns were described for the two chlorophyll *a* products, namely NASA and CMEMS (Fig.2.3). The amplitude (A_1) of the signal inside the main basin and the offshore part of the NWS (Region 6 and 1 to 3 respectively) is homogeneous and has low values (less than 0.4 mg m^{-3}) compared to the Azov Sea (Region 8) which can go up to 6 mg m^{-3} (Fig.2.3b&e). A phase between December-January was commonly observed for the main basin of the Black Sea (Region 6), whereas the NWS showed a more complex pattern in the timing of the phase (Fig.2.3c&f). Based on the phase values, a total of 8 sub-regions were defined and the associated seasonal climatology of chlorophyll *a* using only CMEMS was computed from 1998 to 2017 (Fig.2.5). The seasonal cycle of chlorophyll *a* for the inner basin (Region 6) of the Black Sea was described as U-shaped with minimum values in summer and maximal ones in winter. The dynamic of chlorophyll *a* obtained over the NWS was variable across its different sub-regions (Regions 1 to 5). The seasonal chlorophyll *a* mean in the region close to the Danube area (Region 4) is maximum in June and correlates with the Danube discharge only when one-month lag is considered (R^2 = 0.57, Fig.2.8b).

The table 2.1 in the introduction summarizes the seasonal patterns of chlorophyll *a* described in the literature, which we compare with our findings. The articles of Finenko et al. (2014), McQuatters-Gollop et al. (2008), Nezlin (2006; 2002; 1999), Oguz et al. (2003) and Kopelevich et al. (2002) also described a U-shape for the chlorophyll *a* dynamic over the deep regions of the Black Sea, all using satellite datasets (mainly SeaWiFS or CZCS). The articles that analysed *in situ* data (*e.g.* Chu et al. (2005) and Yunev et al. (2002)) tend to characterize the seasonal dynamic of chlorophyll *a* with a bi-modal shape. In Chu et al. (2005), the Optimal Spectral Decomposition (OSD) method is used to reconstruct the seasonal signal of chlorophyll *a* using *in situ* measurements from both the shelf and deep-sea waters between 1980 to 1995. A bi-modal shaped was observed with a winter/spring (February to March) and an autumn (September/October) bloom. In the article of Yunev et al. (2002), the bi-modal shape was observed with datasets from the deep basin (larger than 200m) over 1988 to 1992. The first bloom was in the winter/spring period (February-March) and the second one in November.

The description of the chlorophyll *a* signal does not always fit into one of the two categories previously introduced. Indeed, as mentioned in the article of Chu et al. (2005), the second bloom characteristic of the bi-modal structure is sometimes not observed using *in situ* data. This can be due to *e.g.* irregular sampling in space and time, measurement accuracy, method of collection and treatment of the sample or even due to interannual variability. Moreover, as *in situ* data are sparse and noisy, a further processing of the dataset can be applied using different statistical analysis (*e.g.* simple averaging method, optimal spectral decomposition method or empirical orthogonal functions). Concerning the satellite data, algorithms and/or the calibrations used to estimate the surface chlorophyll *a* concentration can differ among different articles. Besides that, the period of time analyzed can also explain the variability in the seasonal cycle of chlorophyll *a*. The increase in sea surface temperature on the basin scale over this period is thought to be a contributing factor for changes on the classical pattern (U-shape) of chlorophyll *a*. Indeed, a direct effect of the surface warming is a decrease of the turbulent mixing during winter and hence a reduction of the supply of nutrients across the nutricline. Another point is the region considered for the analysis, which can also be a factor of variability (See section 2.3.3). The patterns of chlorophyll *a* obtained with *in situ* observations are localized whereas with satellite data, it is possible to get a signal for the whole Black Sea through the delimitation of sub-regions (*e.g.* deep sea and shelf areas). Usually, the choice of the boundaries for the sub-regions is based on the bathymetry and hydrological features. In this Chapter, a regionalization

of the seasonal pattern of chlorophyll *a* based on the results of the phase from the harmonic analysis was done.

2.4.2 Seasonal cycle of chlorophyll *a*: why such patterns?

A principal factor that plays a role on the shape of the seasonal cycle of chlorophyll *a* is the depth of the pycnocline and its seasonal variation. At similar latitudes in temperate regions, where the seasonal phytoplankton cycle with two typical maxima (spring and autumn) is described (Figure 2.22), deep winter convection and wind mixing occurs and can reach a depth of several hundred meters (Longhurst, 1995). This process brings the phytoplanktonic cells below the euphotic zone preventing a winter bloom due to light limitation (Sverdrup, 1953; Figure 2.22b), leaving this deep mixing layer replete with nutrients. Over the spring period, the decrease of wind mixing and the heating of the upper layer favours the shoaling of the seasonal thermocline. Both the absence of light, and nutrient limitation will then lead to the intense spring bloom (Sverdrup, 1953). Then over the summer, when the water stratification is at its maximum, the bloom decreases because of nutrient limitation. In autumn, the increase of wind mixing and the decrease of SST will result in the erosion of the seasonal thermocline, entraining nutrients into the upper mixed layer, causing an autumn bloom (Longhurst, 1995).

Regarding the situation of the deep basin of the Black Sea, the depth of the pycnocline is relatively shallow. The enhanced winter chlorophyll *a* concentration in the deep Black Sea is regulated by wind mixing and convection, replenishing the upper mixed layer with nutrients (Oguz et al., 2008). Because of the shallowness of the winter pycnocline compared with the euphotic depth, phytoplanktonic cells are not carried below the euphotic zone and the lack of nutrient limitation would favor the bloom (Vedernikov and Demidov, 2002; Figure 2.22b). There is little seasonal light limitation at these latitudes, which allows year-round production, unlike in more northern latitudes.

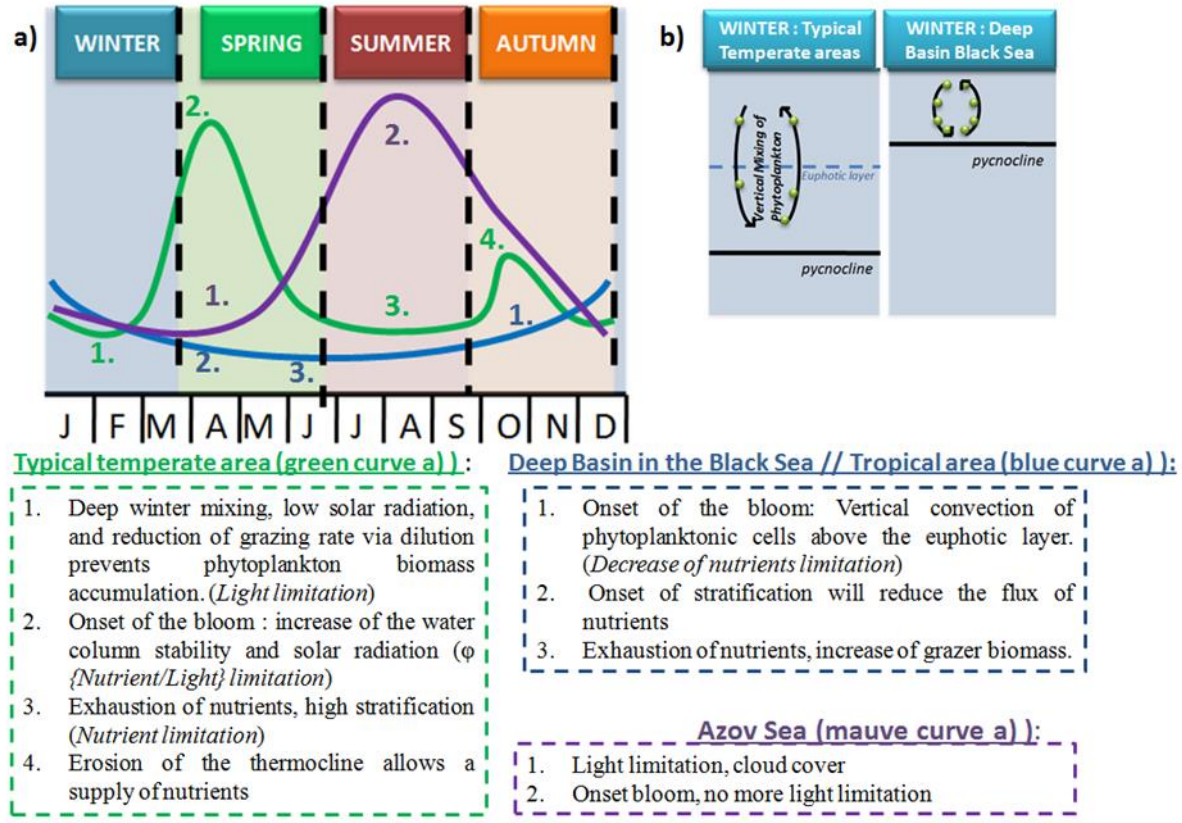

Figure 2.22: a) Comparison of the chlorophyll *a* seasonal dynamic in a typical temperate area (green curve) with the Central Basins in the Black Sea (blue curve) and the Azov Sea (mauve curve). b) Configuration of the pycnocline in regards of the euphotic layer during winter for a typical temperate (left) are and the Central Basins in the Black Sea (right).

The even shallower pycnocline and reduced mixing that occurs during spring would reduce the fuel of nutrients into the mixed layer. Besides the depletion of nutrients, the increase in grazer biomass (Vinogradov et al., 1999) would contribute to the end of the bloom. The temperate-like dynamic observed in the NWS might be controlled by riverine discharge or enhanced turbidity reducing the euphotic depth relative to the pycnocline. As we observed with our results, the occurrence of the spring bloom is associated with a maximum of Danube's discharge considering a one-month lag (Figs.2.7 and 2.8). Then the same factors as described previously for the mid-latitude might also take part in the regulation of the seasonal dynamics over the NWS. In the Azov Sea, minimum of chlorophyll *a* is observed from December to April, probably due to the cloudiness and the decrease of water temperature close to the freezing point (Borysova et al., 2005).

The motivation for comparing the monthly chlorophyll *a* with SST was to get information on the mechanism that can exert a control on the seasonal dynamic of chlorophyll *a*. Indeed, besides the fact that temperature has an important role in the physiological rates of phytoplankton (Geider et al., 1987), it can also indirectly influence physical mechanisms as for example stratification and nutrient availability. The negative correlation we obtained between the monthly time series of chlorophyll *a* and SST over the Central basin, suggested that this region is nutrient limited.

A positive correlation (as observed for the AS) would suggest a light limited area. However, the AS is a region that is very shallow and well-mixed, and so unlikely to be light limited by depth of mixing. The AS is a very turbid basin and the reconstruction of chlorophyll *a* dynamic is not straightforward (Moses et al., 2009).

2.4.3 Interannual variability of chlorophyll *a*

The influence of four main factors (Danube river discharge, precipitation over the catchment, sea surface temperature and CIL) on the interannual variability of chlorophyll *a* has been investigated from 1998 to 2017. In this section, the results are compared with the literature and the link with global atmospheric indices is discussed.

2.4.3.1 River flow and precipitation

The precipitation over the entire catchment area of the Black Sea (and not only the Danube river catchment) indicates that it influences 55% of the variability of the Danube discharge from 1998 to 2010. The influence of precipitation on the flow of the Danube was also observed in Starosolszky and Gauzer (1998) (cited in Rîmbu et al., 2002). Furthermore, the decadal variation of the Danube river flow (also considered at the station Ceatal Izmail) was shown to be influenced (positive relation) by the decadal variations of precipitation in the Danube river catchment basin (Rîmbu et al., 2002).

The variation of the annual chlorophyll *a* over the NWS (Regions 3 and 4) between the years 1998 to 2017 showed a positive correlation (R^2 around 0.3) with the total catchment

precipitation, but no correlation was directly observed with the Danube discharge. It is possible that those variables are part of a larger scale climate process influencing their dynamics independently on a regional scale.

For example, the decadal variability of the North Atlantic Oscillation (NAO) has been shown to influence the decadal precipitation variability (*e.g.* Hurrell, 1995; Rîmbu et al., 2001). The article of Valty et al. (2015) observed a strong negative correlation between the interannual precipitation over the catchment of the Black Sea obtained from a data-assimilative model and the NAO between 2002 and 2010 (Fig.2.23).

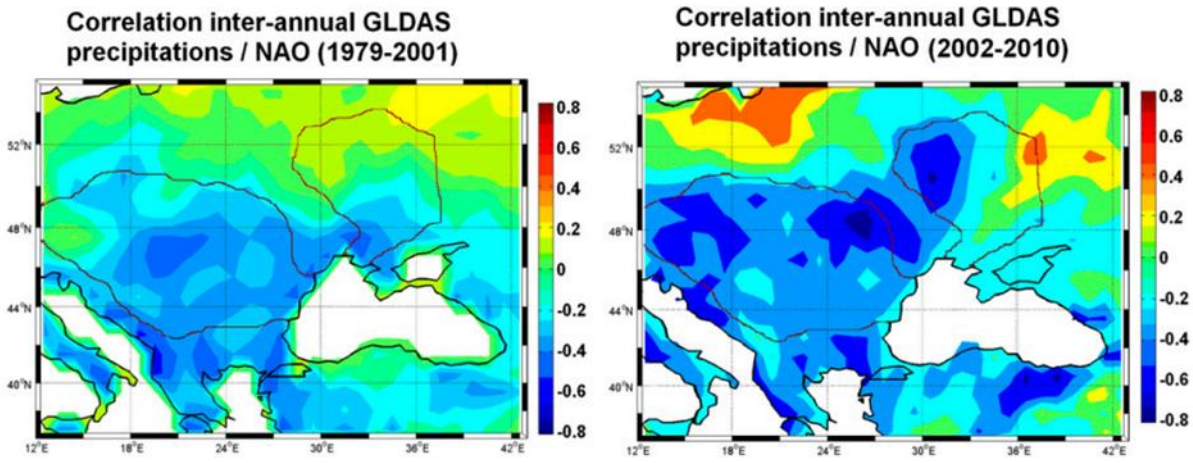

Figure 2.23: Correlations between the NAO and the interannual precipitation from the GLDAS-Noah model (left) between 1979 and 2001 and (right) between 2002 and 2010. Figure extracted from Valty et al. (2015).

The same negative relation was also observed in Ivanov et al. (2014), who analysed the variability of the precipitation in the Southern Coast of Crimea in regard to the NAO. They observed that during the maximum values of NAO, minimal values of precipitation were recorded. On the contrary, when the NAO index was small, the anomalies of total annual precipitation were positive.

The link between the annual NAO and the catchment precipitation datasets used in this chapter was also analysed and a similar correlation was also observed from 1998 to 2018, with R^2 = 0.206 (Fig. 2.24). The correlation with other climatic indices (MEI and EA/WR) is put in the Appendix A for completeness (Figs.A.12 and A.13).

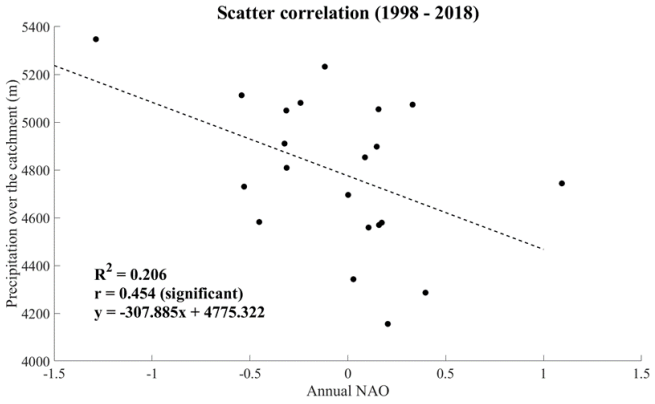

Figure 2.24: Correlation plot between the annual NAO and the precipitation over the catchment from 1998 to 2018.

In Rîmbu et al. (2002), they were interested to see if the NAO signal is present in the Danube river time series on the decadal variability and they found a negative correlation (r = -0.75), based on a 5-year running means. During a positive phase of the NAO, the river flow tends to be lower than normal in central and southern Europe (Fig.2.25). The time series of Danube discharge used in this Chapter contains only 13 years (including one year with no data) and the correlation analysis indicates no clear link with the NAO.

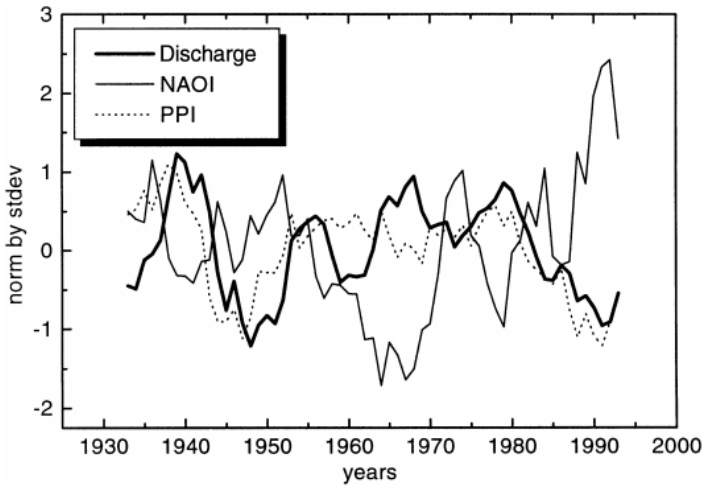

Figure 2.25: Time series of normalized anomalies of the Danube discharge at Ceatal Izmail (solid line) and NAO Index (thin line). All time series were normalized and smoothed with a 5-year running filter. For information, PPI is an index of the average of normalized precipitation anomalies over a large area that includes the Danube basin. Figure from Rîmbu et al. (2002).

For the interannual variability of the chlorophyll *a*, a possible effect of NAO on the ecological properties in the Black Sea is mentioned in the article of Oguz and Ediger (2006). The physical

mechanisms to supply inorganic nutrients into the euphotic zone from the subsurface pool, could be enhanced by strong wind stress and cooling which is associated with a strong positive NAO cycle. However, the stimulation of the biological production through this process of vertical advection and convection could occur only if there is a consequent pool of subsurface nutrients available.

2.4.3.2 Sea surface temperature

The other variable that was investigated in relation to the chlorophyll *a* was the sea surface temperature. The pixel by pixel analysis performed between the annual mean chlorophyll *a* and the annual mean SST indicated a significant and positive correlation for some localised areas inside both gyres (Fig.2.17). This result is consistent with the work McQuatters-Gollop et al. (2008), who also found a positive correlation and then hypothesized the role of the CIL in driving chlorophyll dynamics. Indeed, they suggested that the anomalously warm winter of 2000-2001 induced the reduction of nutrient subduction into the CIL, which almost certainly explained the anomalously high phytoplankton biomass in the Black Sea. Other studies from Nezlin et al. (2006) and Kubryakov et al. (2016) observe the same relation between the variability of the surface chlorophyll *a* and the surface temperature.

However, not all the studies made for the Black Sea described the same correlation between the chlorophyll *a* and the sea surface temperature. In general, in the tropical to mid-latitude regions (Behrenfeld et al., 2005), this is usually an opposite (negative) correlation that is observed, where the warming of the SST can reduce nutrient entrainment because of the stratification, leading to a decrease of the productivity. One study from Finenko et al. (2014) made inside the Black Sea found a negative correlation between the water temperature and the average chlorophyll a concentration. (Fig.2.26).

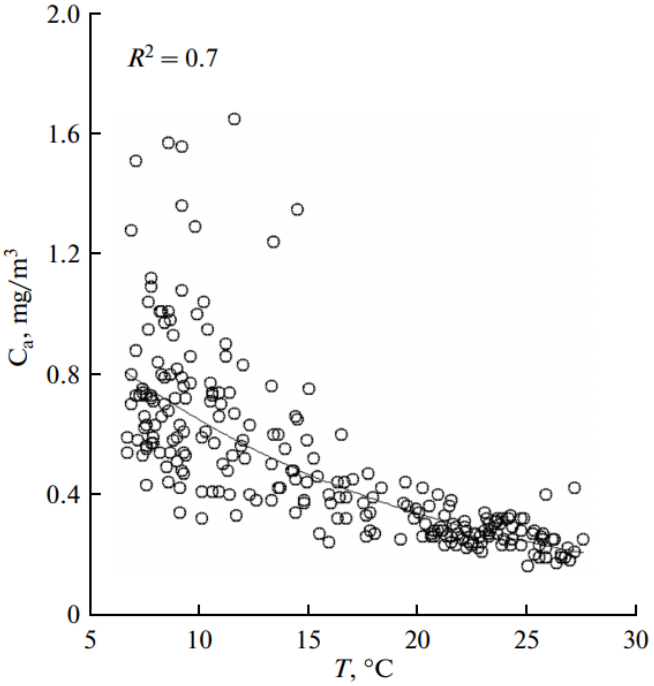

Figure 2.26: Correlation between the chlorophyll *a* concentration and the water temperature in the surface layer of the Black Sea in 1998-2008, averaged for 2-week periods within the calendar year. Figure from Finenko et al. (2014).

2.4.3.3 Cold Intermediate Layer

Lastly, the volume of the CIL formed annually was investigated, using both temperature and salinity criteria. The hypothesis tested here, stated that an increase of the CIL volume (thickness) might lead to a decrease of the nutrient available for the phytoplankton and therefore affect negatively its concentration. The role of the CIL as a key biogeochemical feature has been reported in some articles (*e.g.* McQuatters-Gollop et al. (2008) and Belokopytov (2011)). A significant negative correlation between the annual CIL temperature and the CIL volume was observed, with R^2 = 0.711 (Fig.2.21a). The volume of the CIL showed a clear interannual variability. However, the results did not indicate a clear negative correlation between the annual chlorophyll *a* from CMEMS Reanalysis and the volume of the CIL (Fig.2.21b). The lack of correlation in our results might be due to the method used to estimate the CIL volume. Indeed, other factors that were not studied here, might interplay and affect the formation of the CIL (*e.g.* the role of the circulation).

Besides that, it is important to keep in mind that the CIL is a sub-surface feature which might impact the deeper chlorophyll *a* signal, that cannot be caught by satellite sensors as they are restricted to only measure the top layer of the water column.

2.5 Conclusion

The seasonal and interannual variability of chlorophyll *a* was studied in the Black Sea through the analysis of two satellite products (NASA and CMEMS). The main results of Chapter 2 are:

i) A reconciliation of the bimodal/U-shaped curve dilemma by separating the sea into different regions with different behaviours.

Using an harmonic analysis to separate the Black Sea in different sub-regions is a new approach that has not been done in previous articles. The amplitude and the phase of the harmonic signal are the two main metrics used to characterize chlorophyll a pattern over the whole basin (Figs. 2.3 and 2.5). NASA and CMEMS products display similar patterns in the amplitude and phase of the signal in chlorophyll *a* from 2003 to 2017. The amplitude is minimum inside the main basin (Regions 6 and 7) whereas highest values are located near the Danube mouth (Region 4) and in the Azov Sea (Region 8). The phase is an indication of the timing of the peak of the signal and is homogeneous over the central basin and occurs mainly between December to January. In contrast, the NWS has a heterogeneity in the phase hence a high variability in the seasonal cycle across its different sub-regions (Regions 1 to 5, Fig. 2.5). The seasonal cycle of chlorophyll *a* for the inner basin (Region 6) of the Black Sea was described as U-shaped with minimum values in summer and maximal ones in winter. We obtained a map of the Black Sea delimited into a total of 8 sub-regions that regroups area of homogenous behaviour in terms of chlorophyll a variability. The regionalisation includes (Fig. 2.5): 5 regions for the NWS, 2 regions in the main basin (Deep and Coastal areas) and the Azov Sea.

ii) On seasonal time scales, a positive correlation between the Danube river flow and the chlorophyll a concentration considering one-month lag was obtained.

The impact of three main rivers was investigated on the seasonal time scale. The most important inside the Black Sea is the Danube river which discharge into Region 4, and for the Azov Sea, seasonal time series of Don and Kuban were analysed. The seasonal climatology of the Danube

discharge from 1998 to 2008 was positively correlated with Region 3 (off-shore the Danube mouth) and Region 4 (close to the Danube mouth) when considering one-month lag (respectively R^2 = 0.53 and R^2 = 0.57, Fig. 2.8). In the Azov Sea region, only a negative correlation (R^2 = 0.55) between the seasonal chlorophyll *a* and the Don discharge was observed (Fig. 2.9). A localized analysis (pixel by pixel) between monthly chlorophyll *a* and SST indicated a significant negative correlation in the main basin of the Black Sea, suggesting this area to be nutrient limited (Fig. 2.6).

iii) The analysis of the effect of both water flow (precipitation, river discharge and CIL) and sea surface temperature on the interannual variability of chlorophyll *a*, produced only weak evidence of their influence.

The interannual variability of chlorophyll *a* over Region 3 (off-shore of the Danube mouth) and Region 4 (close to the Danube mouth) were positively correlated with the total precipitation over the catchment from 1998 to 2017 (R^2 was around 0.3 for both Regions, Fig. 2.16), but no correlation was directly observed with the Danube discharge (Table 2.3). The localized analysis between annual temperature and chlorophyll *a* suggested a positive correlation for some areas inside the main Black Sea (Fig. 2.17). However, the average values of annual chlorophyll *a* and NASA-SST over Region 6 (inner basin) did not show a significant correlation (Fig. 2.18). In this study, the CIL volume was the last factor analysed and it did not clearly show a link with chlorophyll *a* on interannual scale (Fig. 2.21b).

Satellites are a powerful tool and provide time series of consistent observations, but they are not able to catch all the process that can interplay in the regulation of chlorophyll *a* dynamic (*e.g.* the impact of predators through grazing), neither are they able to capture sub-surface phytoplankton (*e.g.* at the intersection of the pycnocline and the nutricline). Also, our analysis mainly focused on the effect of temperature, but the seasonal cycle of chlorophyll *a* result from the combination of physical ocean factors (*e.g.* wind, currents). Such results can then be integrated into modelling studies to broaden the range of processes that can potentially affect chlorophyll *a* dynamic (top down control).

"Just as a drop of water in the ocean cannot avail much; but if a great river runneth into it, that maketh a great commotion."

Jakob Böhme

Chapter 3: Influence of river run-off on the Cold Intermediate Water mass in the Black Sea

3.1 Introduction

The catchment area of the Black Sea covers areas in Europe and Asia and the land sea ratio of the Black Sea drainage basin is around 5.21 (Fig.3.1), which is about 10 times greater than the Mediterranean basin in comparison (Ludwig et al., 2009). One of the second largest river in Europe outflow into the Black Sea, and this is the Danube river, with a catchment area of 817 000 km^2 (Sommerwerk et al., 2009). From its source in Germany to the river mouth in the North Western Area of the Black Sea basin, the Danube flows across 2826 km, spanning 19 different countries which makes it the most international river in the world. The other main rivers are the Dnieper, Don, Rioni, Kuban, Dniester, Coruh, Kizil Irmak, Sakarya and Yesil Irmak, which altogether (including the Danube) carry about 85% of the riverine freshwater inputs to this sea (Ludwig et al., 2009; Jaoshvili, 2002). However, the Danube is by far the major contributor to the runoff as it accounts for about half of the total water influx (Sur et al., 1994). The total discharge of both Dniestr and Dnieper rivers is about a third of the Danube, whereas the rest of the rivers supply only a small fraction of the total river runoff, being less than a fifth (Sur et al., 1994).

As mentioned in the Introduction Chapter (Section 1.3.1), the total freshwater supply is around 350-400 $km^3\ year^{-1}$ (Ludwig et al., 2009) and this is quite large in comparison with the discharge of the river Volga that is the main supplier in the Caspian Sea, with an average of 237 $km^3\ year^{-1}$ (Arpe et al., 2000). The Caspian Sea is used for comparison as its area (436 000 km^2, Ieva and Otto (2011)) is close to the Black Sea. This makes the Black Sea a typical example of an estuarine basin. The large freshwater flux (river runoff, plus precipitation minus evaporation), added to the restricted exchange with the Mediterranean Sea, leads to a strong vertical stratification. Besides that, there is also a strong haline front close to the coast in the western Black Sea that is due to the river discharge (Stanev and Beckers, 1999).

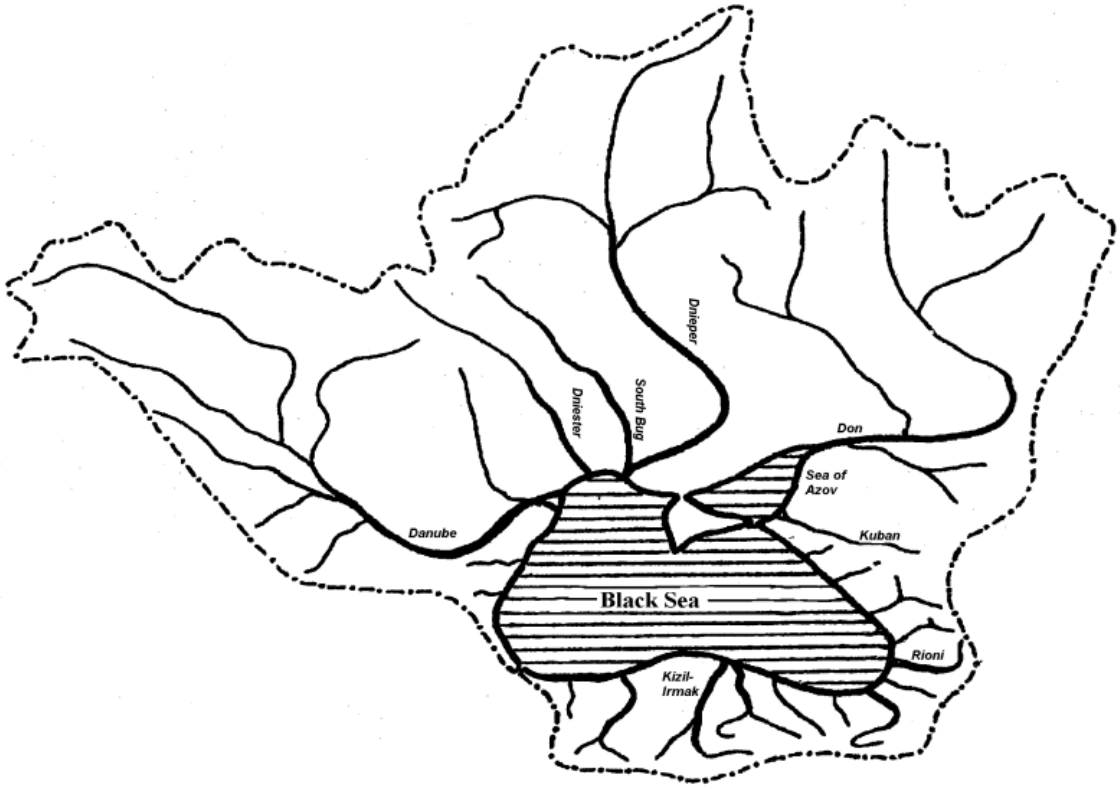

Figure 3.1: Sketch of the Black Sea catchment area with indication of some of the main rivers (Figure extracted from Jaoshvili (2002)).

This oceanographic basin is therefore expected to be sensitive to the freshwater balance, mainly observed in changes of the sea surface height during the year (Grayek et al., 2010; Stanev and Beckers, 1999).

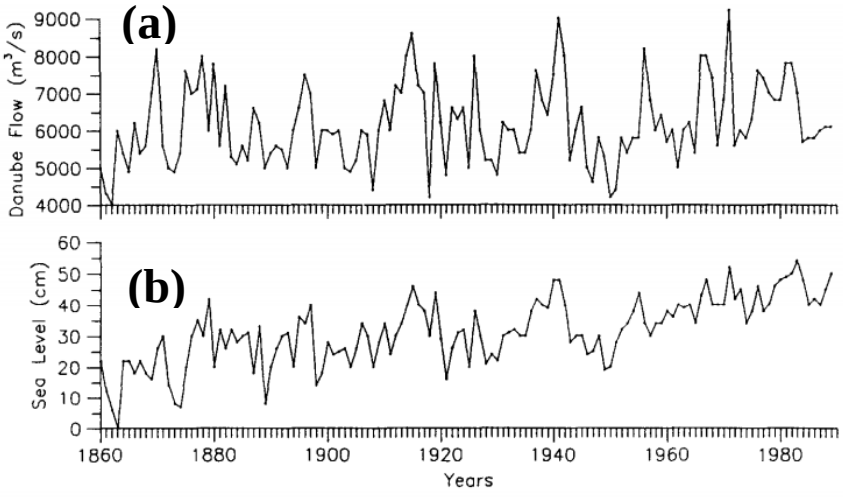

Figure 3.2: Example of long-term time series of (a) annual Danube discharge and (b) sea level at Sulina on the Romanian coast (Figure from Sur et al. (1994)).

On Figure 3.2, the long-term monitoring of the Danube discharge from 1860 to 1980 indicates a strong interannual variability, with values that fluctuate in the range of 126 to 283 km^3 yr^{-1}. A direct effect of the river inflow is the impact on the mean sea level (Fig. 3.2b, see also Bondar (2007) and Özsoy et al. (1995)). The Danube has a very important economic role, and the natural variability in its river flow can be modulated by anthropogenic factors. A typical example is the construction of dams to generate hydropower. This happened for the Danube river with the construction of a high density of dams. For example, in the Upper Danube (defined by the first 1000 km), it reached about 1 dam every 17 km (Zinke, 1999). An important dam was constructed in the Lower Danube in 1970 to 1972 and was called the Iron Gates I (see Fig.B.1 in the Appendix B). This was not without consequences and was shown to have significant impact on the biogeochemistry and ecosystem structure not only in the river and the adjacent coastal waters, but also in the entire basin (Humborg et al., 1997). A noticeable change was the annual decreasing trend (by approximately two thirds, Cociasu et al. (1996)) in dissolved silica inputs to the Black Sea (Fig. 3.3), as they were postulated to be trapped inside the reservoir (Humborg et al., 1997). However, a more recent study by Friedl et al. (2004) revealed that the retention of silicate was about an order of magnitude lower than the values initially suggested by Humborg et al. (1997). Concerning the water discharge, the effect of the dam is less clear, as it was shown to either have a significant change in the Danube discharge (Popa et al. (1993) cited in Humborg et al. (1997)) or have no significant impact (Panin, 1996; cited in Teodoru et al. (2005)).

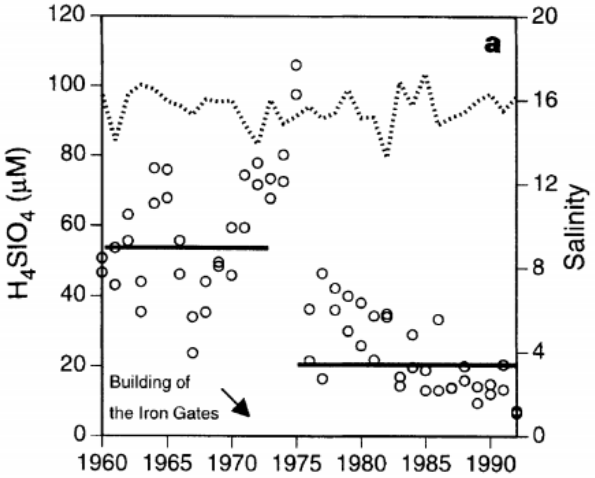

Figure 3.3: Mean winter (January and February) silicate concentrations at Constanta station with indication of the median values from 1960-72 and 1973-92. The figure and the details on the measurements are found in Humborg et al. (1997).

The alteration of the Danube inputs can have serious impacts which can be assessed and studied through numerical modelling approaches. The choice and setup of the model depends on the questions that need to be addressed (*e.g.* Grayek et al. (2010) or Lancelot et al. (2002)).

The first objective of this Chapter is to develop a regional 3D numerical model that has the ability to capture and maintain the main hydrological characteristics (with a focus on the Cold Intermediate Layer) of the Black Sea over a long period of time from 1980 to 2018. The second objective is to understand the long-term changes in the CIL structure over interannual time scales, using the model results. Finally, the importance of the river discharges in driving such variability is also investigated.

The method section contains technical aspects that were required to produce a satisfactory representation of the Black Sea physics using the Nucleus for European Modelling of the Ocean (NEMO). The metrics used to analyse specifically the Cold Intermediate Layer over interannual time scales (from 1980 to 2018) are also introduced. Two scenarios run that either increase or decrease the river discharge are presented. Then the results section focuses on thermohaline fields for the sensitivity analysis and the model validation. The variability in the CIL structure from 1980 to 2018 and the influence of the river discharge is described afterwards.

3.2 Methods

The main setup used for the application of the model NEMO in the Black Sea is first described in the following sections.

3.2.1 Model Description

The hydrodynamics is supplied by the Nucleus for European Modeling of the Ocean (NEMO v3.6), initially designed for the open ocean. NEMO is a 3D hydrostatic, baroclinic primitive equation model (Madec et al., 2015), that uses a curvilinear orthogonal grid formulated on the Arakawa C-type grid (Mesinger and Arakawa, 1976; Appendix B, Fig. B.2), with masking of the land area. The domain of the model used in this study extends from 27.43°E x 40.93°N to 42°E x 47.30°N, and includes simulations in the Azov Sea, but excludes the Sea of Marmara. The bathymetry for the model (Fig.3.4) is based on the General Bathymetric Chart of the Oceans (GEBCO08) grid version 20100927 released in 2010 (https://www.gebco.net/), which was the most up-to-date and accurate data set for the Black Sea, with 30 arc-seconds resolution. The horizontal grid of the model has a resolution of about 1/33°= 0.03° (approximately 3.3 km) in both directions, leading to a mesh of 466 longitudinal by 280 latitudinal grid points. This initial configuration of the model was supplied by the Turkish partners (Dokuz Eulul University and Istanbul Technical University) in the NEWTON project that partly funded this work. The model was then further developed as described in the following sections.

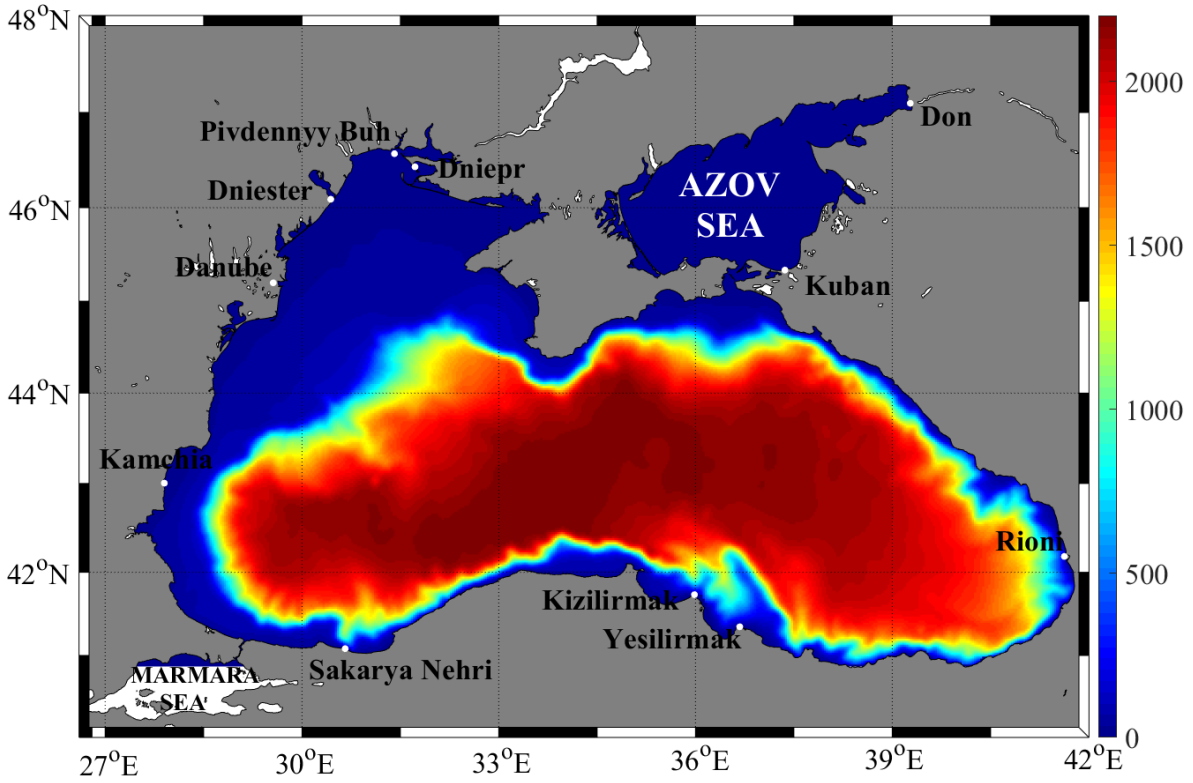

Figure 3.4: Model domain and bathymetry (m) used for the numerical model (NEMO - BLACK SEA). River mouths are indicated with white dots, leading to a total of 11 rivers (Dniepr, Pivdennyy Buh, Dniester, Danube, Kamchia, Sakarya Nehri, Kizikirmak, Yesilirmak, Rioni, Kuban and Don).

For the representation of the bottom topography, the model implementation uses z-coordinates with partial steps over 60 depths levels, whose separation varies from 2 m to 33.5 m in the upper 309 m, and reaches 200 m near the ocean bottom (cf Appendix B, Fig. B.3). See Appendix B, Fig. B.4 for the comparison with full step z-coordinate. The choice of z-coordinate is chosen to suit the application. A range of different options can be used for ocean circulation models, but three basic types are commonly used (z-, σ- and isopycnal coordinates, see Appendix B, Fig. B.5), and each of them has its own advantages and disadvantages (*e.g.* Chassignet et al. (2006) or Griffies (2018)). The Black Sea owns a complex topography and the model domain considered in this study combines both the shelf and the deep areas, transitioned by a steep and narrow slope.

In Shapiro et al. (2013), a sensitivity analysis on different vertical schemes was applied to the Black Sea case, and assessed their respective accuracy to reproduce processes at the shelf break and in the open sea, with a focus on the CIL representation. In comparison to σ-coordinates, z-

coordinates had limitations near the bottom layer of the shelf due to its lack of resolution, and the resulting dense water was described as a "broken" plume (Fig.3.5). This step-like structure of the bottom relief could affect the efficiency of the CIL replenishment, but might be alleviated through the use of a partial step configuration as done in this study. However, despite those drawbacks, Shapiro et al. (2013) demonstrated that the z-level grid conserved well the CIL in the deeper part of the Black Sea, when the σ-coordinate failed to conserve it (Fig. 3.5b), as σ-coordinates can be more diffusive and create spurious currents.

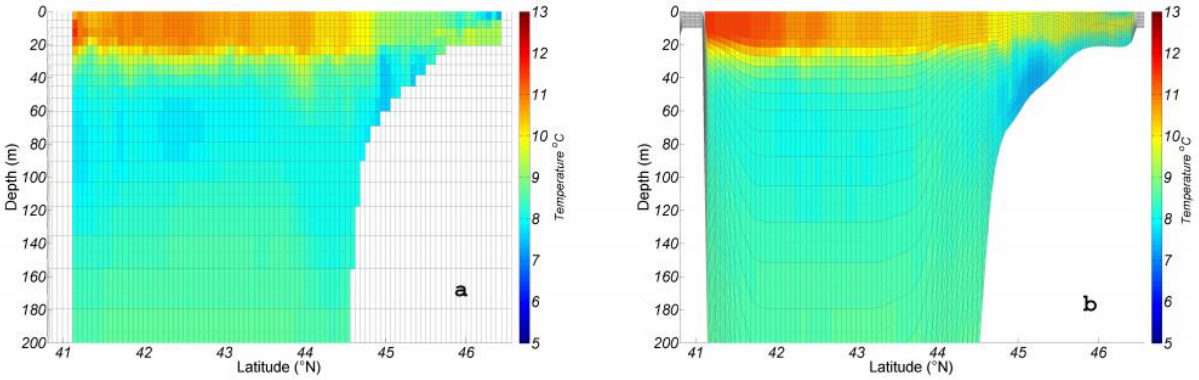

Figure 3.5: 2D transect of modeled temperature along 31°E for 16 April 2007, extracted from Shapiro et al. (2013). The model uses either (a) z-coordinate or (b) σ-coordinate level.

Those findings suggest that using z-coordinates should be acceptable for the study of the CIL in the Black Sea. Particularly as, the model used here, NEMO - BLACK SEA uses a high number of vertical levels (60) compared to the 33 levels used in Shapiro et al. (2013).

As the CIL is the main object of study in this chapter, it is therefore important to indicate the ability of the model to generate such a feature and simulate the cascading of dense water from the shelf. The same transect location in time as in Shapiro et al. (2013) (16 April 2007; Fig.3.6) was plotted. 3D field of temperature and salinity are the main variables that are analysed in the model outputs. The detailed justification of the full model parametrization is shown in Section 3.3.1 and the meaning of the tuned parameters is introduced before in Section 3.2.2. The mix layer outputted from the model uses the variable $mldr10\_1$, and is defined at the base of the isopycnal layer, where the density changed by the amount $d\sigma_\theta$= 0.01 kg m^{-3} from the density at a reference depth of 10m. Given the results in the Figure 3.6, the choice of the vertical coordinate scheme is acceptable.

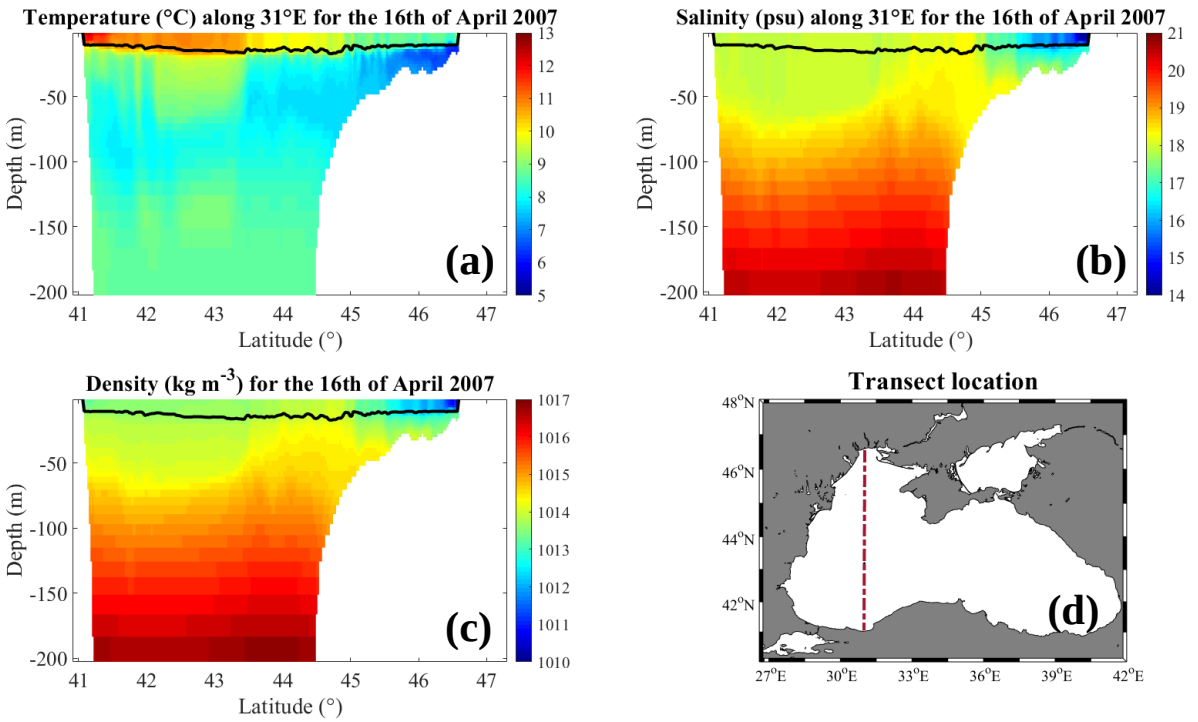

Figure 3.6: Transect along 31°E on the 16th April 2007 from NEMO - BLACK SEA (same location as in Shapiro et al. (2013)). (a) Profile of temperature (°C) where the penetration of the CIL into the interior of the sea is observed. (b) Profile of salinity (psu). (c) Profile of density (kg m^{-3}), computed using Roquet et al. (2015) expression. The black line on (a), (b) and (c), indicates the mix layer depth ($mldr10\_1$). (d) Location of the transect (dashed line).

The initial conditions of the model (see Appendix B, Figs. B.6 and B.7) come from the CoMSBlack cruise, made during 2-26 July 1992. The datasets were created by the Turkish partners and it is described in detail in the article of Gunduz et al. (2020).

There is one open boundary in the model configuration that simulates the exchanges at the Bosporus Strait with the Sea of Marmara. The strait is narrow (0.76-3.60 km), shallow (maximal depth of 65.25 m) and long (~31 km). The boundary forcings for the current (see Appendix B, Fig. B.8) were derived from literature (*e.g.* Gregg and Özsoy, 2002; Jarosz et al., 2011) and provided by a researcher from the National Oceanography Center. It was assumed that the flow is out of the Black Sea above the halocline and into the Black Sea below the halocline.

The profiles of temperature and salinity are daily constant values over the year (see Appendix B, Figs. B.9 and B.10). The lateral momentum boundary condition uses a no slip condition (the

same condition was used in Cannaby et al. (2015)). See the Appendix B, Fig. B.11 for the explanation of no-slip.

The model configuration uses the total variation diminishing (TVD) advection scheme for tracers (Madec et al., 1998). The surface pressure gradient option uses the split-explicit free surface method (also called the time-splitting formulation, Shchepetkin and McWilliams (2005)), activated via the key_dynspg_ts during the compilation of the code. The lateral diffusion scheme for tracers and the lateral diffusion for momentum both use the laplacian operator (ln_traldf_lap = true and ln_dynldf_lap = true respectively), with an iso-neutral direction of action (ln_traldf_iso= true and ln_dynldf_iso = true respectively). The turbulent closure scheme used is the generic length scale (GLS, Umlauf and Burchard (2003)) turbulence scheme and activate via key_zdfgls during the compilation. Some parameters allow the model to be more or less diffusive in the vertical. In the GLS scheme, the mix layer depth and the strength of the pycnocline can be controlled by changing the parameters referred in Table 3.1.

Table 3.1: Example of parameters in the model that affect the mix layer depth and the strength of the pycnocline (Luneva et al., 2019).

Parameters	**Definition**	**Impact**
nn_stab_func	Stability function	= 0 (GALP, Galperin et al. (1988)): strongest pycnocline, shallow MLD = 3 (CanutoB, Canuto et al. (2001)): weaker pycnocline, thicker MLD but can result in warming of below-pycnocline temperature. Canuto configuration is more diffusive
rn_clim_galp	Galperin limit	Smaller values give stronger pycnocline. Typically, observations range from 0.25 to 0.6

The current setting of the model does not include data assimilation, or relaxation towards a climatology.

Surface forcing is computed by means of CORE bulk formula using the atmospheric data provided by ERA5 (https://cds.climate.copernicus.eu/), the most recent climate reanalysis dataset which is the fifth generation produced by the European Centre for Medium-Range Weather Forecasts (ECMWF). The data used in the experiments were extracted for the period 1980 to 2018, with 0.25° horizontal resolution and hourly frequency. The variables used are the two components of surface wind speed (u10 and v10), the 2m air temperature (t2m), mean sea level pressure (msl), mean snowfall rate (msr), mean surface downward long wave radiation flux (msdwlwrf), mean surface downward short-wave radiation flux (msdwswrf) and mean total precipitation rate (mtpr). The specific humidity is computed from surface pressure (sp) and 2m dew point temperature (d2m). In Capet et al. (2012), the wind component was downscaled to 0.2° by spline interpolation to allow a better conservation of the wind curl, but they were using ERA40 with a resolution of 1.125°, so this was not a necessary step in our implementation. For a detailed description of the variables, refer to the Appendix B, Table B.1 and Figs.B.12 to B.18.

River runoff is based on monthly long-term climatology of gauge data, computed from monthly datasets from The Global Runoff Data Centre (GRDC), 56068 Koblenz, Germany (https://www.bafg.de/GRDC/EN/02_srvcs/21_tmsrs/riverdischarge_node.html). All the available stations close to the Black Sea's river mouths have been extracted, giving a total of 11 rivers, namely: Kamchia, the Danube, Dniester, Sakarya Nehri, Dniepr, Pivdennyy Buh, Kizilirmak, Yesilirmak, Kuban, Don and Rioni. Due to missing values in the monthly time series in the archive, and the differences in the period available, the period averaged is not the same for each river analysed. River outflow from the Danube was spread over a total of 3 model wet cells located in the vicinity of the Danube Delta in order to reduce the numerical increase of temperature associated with a high localized flow.

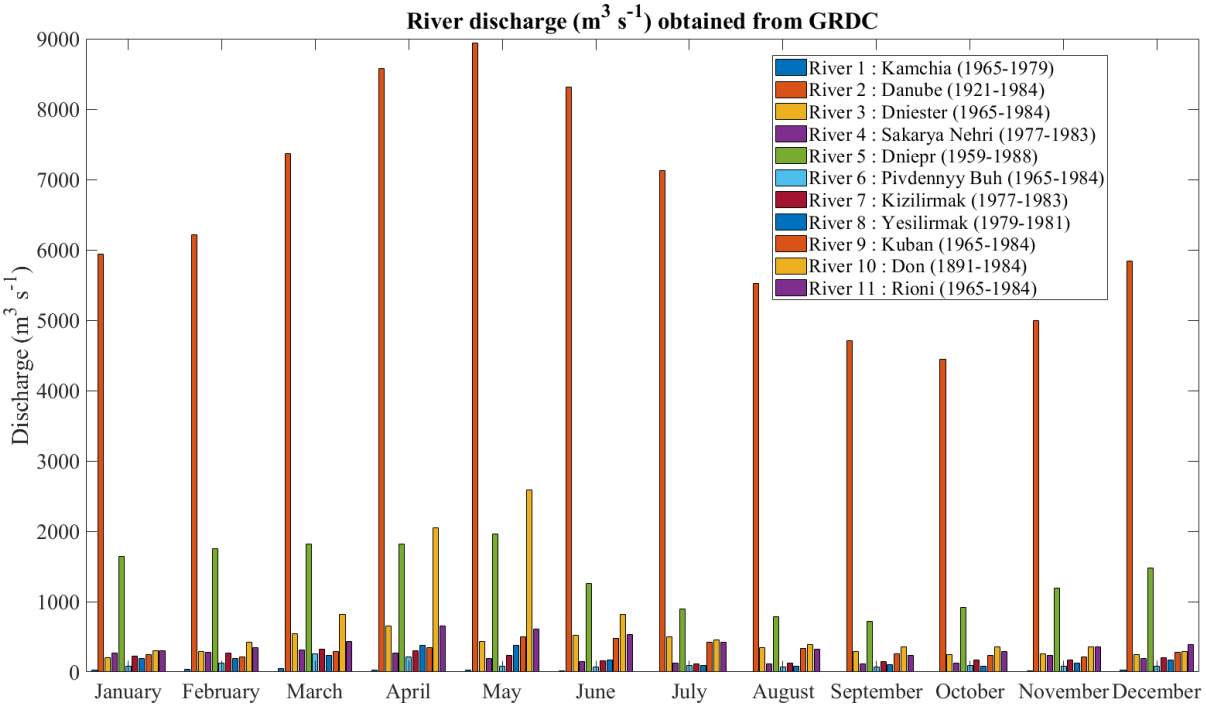

Figure 3.7: Monthly climatology of river discharge (m^3 s^{-1}) for 11 rivers used as forcing for the model. The associated averaged period is indicated in parenthesis (see Appendix B for the setting up of the river file).

As the initial conditions did not correspond to the initial day of the desired period of run (*i.e.* 1st of January 1980), an initial spin-up period was considered, going from 1st of July 2010 to 31st of December 2010, forced with the atmospheric forcing of the year 2010. The model output of the last day of integration was then used as the initial value (restart file) for the long period run (Fig 3.8).

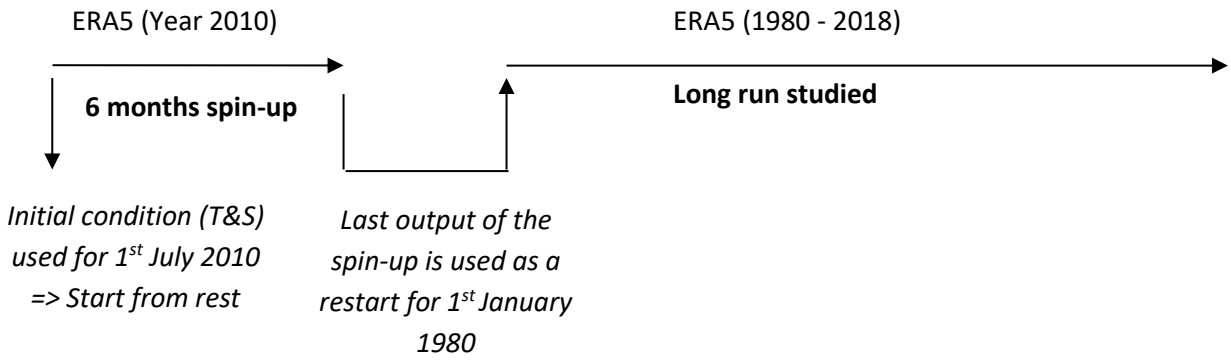

Figure 3.8: Procedure to spin-up the model and associated datasets used to drive the model

Results, saved as daily, 5 days and monthly averages were considered over the 39 years period from 1980 to 2018, set by the length of the forcing time-series. The runs were performed on the UK National Supercomputing Service called ARCHER (https://www.archer.ac.uk), on 192

processors, using 24 processors for outputs. Using a time step of 240s, the model took around 5h to simulate a year.

By definition, numerical models are a simplification of reality and cannot provide a prefect representation of all processes. They can only provide an approximated solution of the real problem and are usually dependent on various parameters (Kantha and Clayson, 2000). The main scope of this chapter is linked to the CIL, therefore extra effort is directed at providing the best representation of this feature.
Initial runs that used the main setup provided by the Turkish side, simulated the CIL but used an unrealistic light scheme (no light penetration was considered). Moreover, the sea surface temperature would increase too drastically during the summer period (reaching sometimes 35°C). Therefore, to ensure an adequate model performance, a series of sensitivity tests were conducted, with an investigation on the light scheme and the mixing scheme. The most adequate parameters were then selected from the sensitivity response. The detail of the numerical values and the model response to those sensitivity tests are detailed in the Appendix B.

3.2.2 Model tuning: sensitivity experiments

The model version that was initially provided did not include the light penetration, *i.e.* all light was absorbed in the top grid cells (see Appendix B Figs. B20 to B22 for model results associated to the initial configuration). Light penetration is an essential component that needs to be activated, especially if coupling to an ecosystem model.

Initial runs showed that by switching on the light penetration using the Red-Green-Blue (later referred as RGB) band option, the cold intermediate layer (initially well observed without light penetration) would not persist through time. Therefore, to improve the model performance, an investigation on both the light and mixing scheme was conducted through a sensitivity analysis. For each experiment, the model was run for 10 years (from 2000 to 2010), using ERA5 forcing, all the runs started with the same initial condition, in January 2010.

LIGHT EXPERIMENTS

A total of 3 configurations was tested (Table 3.2), investigating the impact of chlorophyll *a* concentration, the coefficient of attenuation and the number of wavelengths (either the typical Red-Green-Blue -> RGB or 2 bands options) for the penetrative solar radiation. The control run is the initial configuration but with the light penetration activated (with RGB option), and without chlorophyll *a* data.

Table 3.2: Sensitivity analysis on the light scheme, with details on the configurations used.

Experiments name	Detail of the configurations	Namelist NEMO v3.6 (namtra_qsr) (*)
Control Run	Light penetration (RGB); ∅ Chla	ln_traqsr = .true. ; ln_qsr_rgb = .true. ; nn_chldta = 0
Light1	Light penetration (Kd); ∅ Chla	sn_kd490 = 'kd490_2003_2018'; ln_traqsr = .true. ; ln_qsr_rgb = .false. ; nn_chldta = 0 ; nn_kd490dta = 1
Light2	Light penetration (RGB); + Chla	sn_chl ='chla_2003_2018'; ln_traqsr = .true. ; ln_qsr_rgb = .true. ; nn_chldta = 1 ;
Light3	Light penetration (2 bands); + Chla	sn_chl ='chla_2003_2018'; ln_traqsr = .true. ; ln_qsr_2bd = .true. ; nn_chldta = 1

(*) Details of the parameters: ln_traqsr: allows the activation or deactivation of the light penetration. ln_qsr_rgb : activation or deactivation of the Red-Blue-Green band light. nn_chldta (0): uses constant values of chlorophyll *a*. nn_chldta (1): uses a user defined file for chlorophyll *a* concentration. sn_kd490: contains the name of the file with the coefficient of attenuation values. nn_kd490dta (1): allow to consider a self-generated file for the coefficient of attenuation. sn_chla: contains the name of the file with the chlorophyll *a* concentration. ln_qsr_2bd: uses 2 bands for the light penetration.

Both chlorophyll *a* and diffuse attenuation coefficient datasets come from the satellite MODIS (NASA, http://oceandata.sci.gsfc.nasa.gov/MODISA/), with monthly resolution. A monthly climatology was then computed over the period 2003 to 2018 (see maps of climatology in Fig. B.23 and Fig. B.24 of the Appendix B) and used for the light experiments.

MIXING EXPERIMENTS

A variety of ocean models is investigated to find reasonable values to use in the different mixing parameterizations. Those models include AMM7 (Atlantic Margin Model, 7km; O'Dea et al., 2017), NEMO (Madec et al., 2015**)** and GOTM (Umlauf et al., 2006) configurations (see Appendix B, Table B.5). The selected parameters are mostly part of the Generic Length Scale (GLS) scheme (Table 3.3). GLS is a turbulent closure scheme based on the turbulent kinetic energy and the generic length scale (see Umlauf et al. (2003) for details).

Table 3.3: Sensitivity analysis on the mixing scheme, with details on the configuration used.

Experiments name	**Detail of the configurations**	**GLS scheme: Namelist NEMO v3.6 (namlbc and namzdf_gls)**	**References**
Control Run (= Light2)	Light penetration (RGB); + Chla	Default (*)	
GLS1	Light penetration (RGB); + Chla	rn_shlat = 0	AMM7
GLS2	Light penetration (RGB); + Chla	nn_stab = 0	Shapiro et al. (2013)
GLS3	Light penetration (RGB); + Chla	Rn_clim_galp = 0.267	AMM7

GLS4	Light penetration (RGB); + Chla	Rn_hsro = 0.003	AMM7
GLS5	Light penetration (RGB); + Chla	GLS parameters rn_emin = 1.0e-6 rn_clim_galp = 0.267 rn_charn = 100000. rn_hsro = 0.003 nn_z0_met = 1 nn_bc_surf = 0 nn_stab_func = 0	Similar to Shapiro et al. (2013)
GLS6	Light penetration (RGB); + Chla	eps_min = 10^{-12}	AMM7 / GOTM
GLS7	Light penetration (RGB); + Chla	rn_clim_galp = 0.6	Close to GOTM value (0.53)
GLS8	Light penetration (RGB); + Chla	rn_emin = 10^{-7}	GOTM
GLS9	Light penetration (RGB); + Chla	Rn_avevd = 100	AMM7
GLS10	Light penetration (RGB); + Chla	nn_z0_met = 1	AMM7
GLS11	Light penetration (RGB); + Chla	nn_bc_surf = 0	Shapiro et al. (2013)

(*): Refer to the Appendix on section "Default parameters values for the mixing scheme" to obtain the values of all the parameters.

For both the light and mixing experiments, vertical profiles of temperature and salinity from 1d outputs were compared with EN4 observations using all the profiles available for the year 2010.

Only the observations with a good quality flag were retained. The observations were extracted from the Met Office Hadley Centre using the Gouretski and Reseghetti (2010) corrections (https://www.metoffice.gov.uk/hadobs/en4/download-en4-2-0.html). The closest point in space and time from the model was extracted for the comparison with EN4 profiles.

Table 3.4: Number of profiles (inside the main basin) used for the comparison with *in situ* data from EN4 for temperature and salinity

Seasons	**Temperature**	**Salinity**
Winter (December - March)	34	34
Spring (April - May)	41	25
Summer (June - August)	49	49
Autumn (September - November)	50	50

3.2.3 Model validation

Annual and monthly model results are compared with the 4 km resolution MODIS satellite SST (https://oceandata.sci.gsfc.nasa.gov), the temperature/salinity and MLD of the Black Sea Physics Reanalysis model provided by Copernicus (latter referred as Black Sea Reanalysis) service and the data available from Dorofeev et al. (2017) that uses a data assimilated model of the Black Sea.

When compared to satellite, NEMO - BLACK SEA and BLACK SEA REANALYSIS data have been interpolated onto the MODIS grid (coarser resolution) to allow comparison. Also, for consistency in the comparison, the values inside the Azov Sea for NEMO - BLACK SEA and MODIS have been removed when computing average values, because the Black Sea Reanalysis model does not include this region in its dataset.

The model is able to reproduce the main anti-clockwise flow of the Rim current (Fig 3.9).

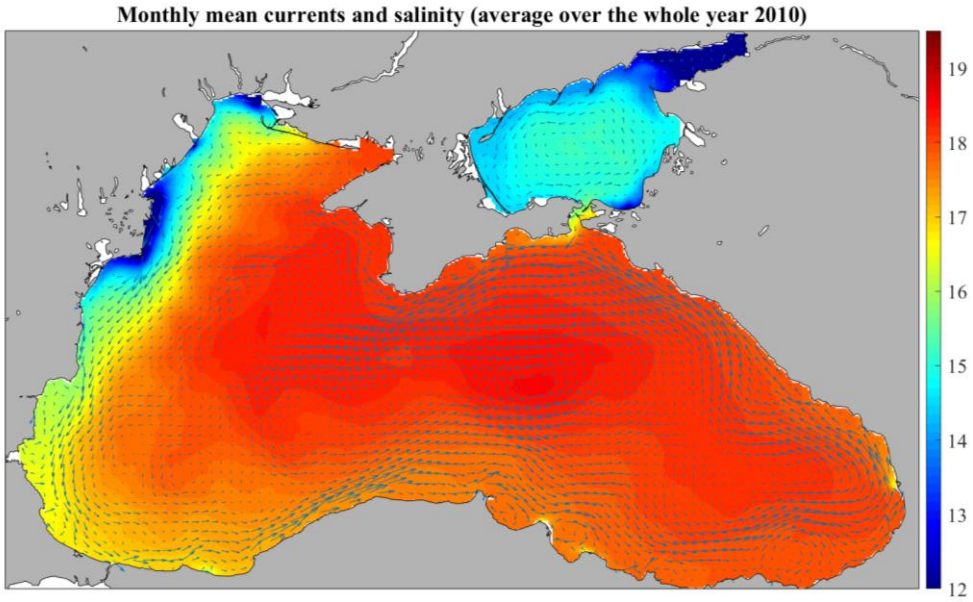

Figure 3.9: Mean velocities obtained from NEMO - BLACK SEA for the year 2010. The velocities overlay salinity (psu).

The improved model set up that is named NEMO – BLACK SEA is the configuration that will be used for the analysis in Chapter 4.

3.2.4 CIL metrics

In this section, the quantitative parameters used for the CIL description are listed in Table 3.5. A total of 6 metrics is then used to understand the long-term changes in the CIL variability from 1980 to 2018. For each of the metrics, the averages account only for areas where a CIL exists, and the regions with values of 0 *i.e.* nonexistence of the CIL, are not considered. From these averages, annual means were also calculated.

Table 3.5: Metrics definition for the CIL

Metric number	Nomenclature and units	Metric definition	References
1)	Depth of the minimum (D_{min}) in m	Associated depth of the minimum temperature of the CIL. Only the values in	Dorofeev et al. (2017)

		the abyssal part of the sea are considered (>200m)	
2)	Thickness (D_z) in m	Distance between the upper (h_1) and lower (h_2) 8°C isotherms	Altiok et al. (2012) ; Demyshev et al. (2002) ; Mikaelyan et al. (2013) ; Miladinova et al. (2018)
3)	Temperature of the minimum depth (T_{min}) in °C	Average values of temperature of water at depth corresponding to the minimum of CIL. Only the values in the abyssal part of the sea are considered (>200m)	Belokopytov (2011)
4)	Average temperature ($T_{CIL,av}$) in °C	Mean CIL temperature in the abyssal part of the sea (>200m)	Akpinar et al. (2017) (from Belokopytov (2011))
5)	CIL cold content (CC_{CIL}) in °C x m	$\int_{h1}^{h2}(8-T)dz$	Dorofeev et al. (2017)
6)	Volume of CIL (V_{CIL}) in m^3		Cf. Chapter 2

For the metric 5 defining the cold content in Table 3.5, h1 and h2 delimits respectively the upper and lower part of the CIL. The metrics are illustrated in the diagram from Figure 3.10.

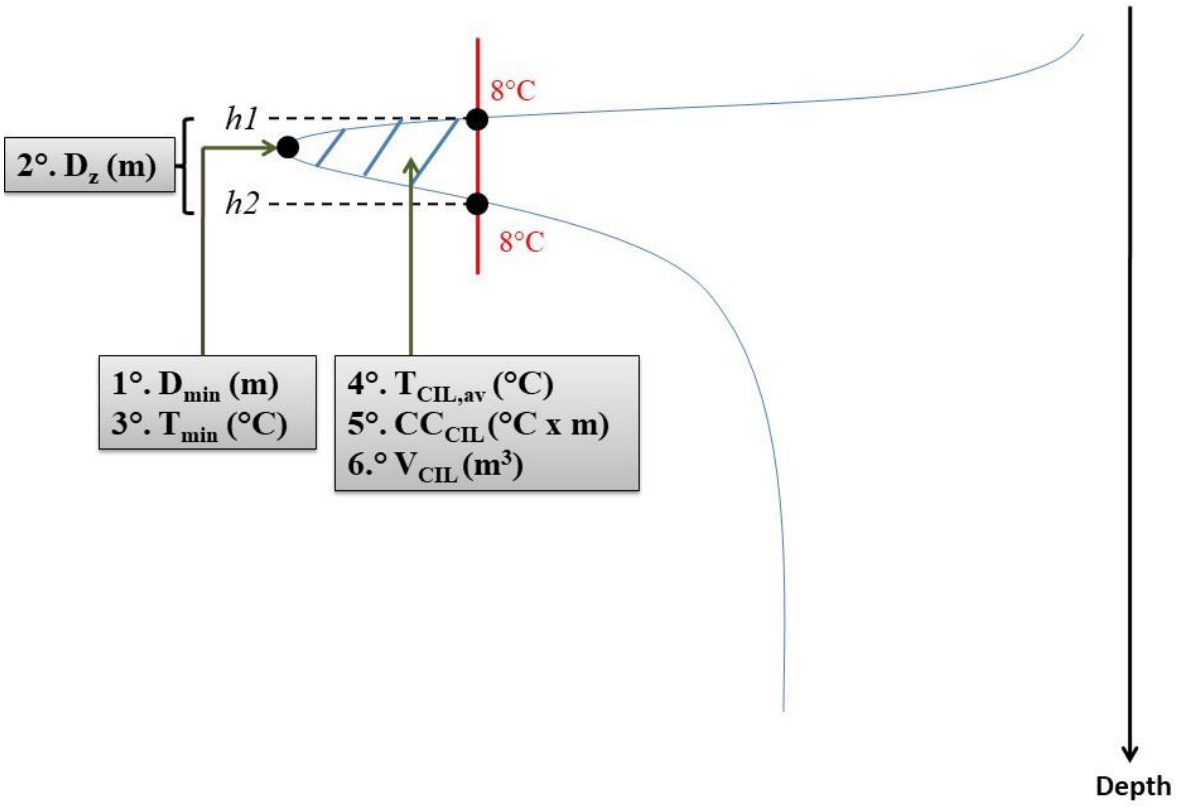

Figure 3.10: Conceptual diagram of the metrics used to characterize the CIL.

3.2.5 Scenarios run (rivers)

This section explains the modifications that were made in the river datasets from the model (NEMO - BLACK SEA) to simulate two different riverine discharge scenarios (named EXP1 and EXP2). In the first scenario (EXP1), an increase of the freshwater discharge for all the rivers is simulated, whereas in the second scenario (EXP2), this is a decrease of the freshwater discharge that is considered. To apply a reasonable constant factor to the datasets, the annual time series of the Danube river from 1998 - 2010 was used. The factor of variability chosen is 2 times the standard deviation (2σ) of the Danube annual time series in river flows ($km^3\ yr^{-1}$) and equals 37.4% of the mean. Then, each month in the climatology of the rivers is adjusted by either multiplying by (1 + 0.374) in EXP1 (see Eq. 3.1) or by (1 - 0.374) in EXP2 (see Eq. 3.2).

For all the 11 rivers considered in the model, we have:

(Eq. 3.1) EXP1 (increase scenario): $F_{(i,j)} = F_{(i,j)} + \left(0.374 * F_{(i,j)}\right) = F_{(i,j)} * 1.374$

(Eq. 3.2) EXP2 (decrease scenario): $F_{(i,j)} = F_{(i,j)} - \left(0.374 * F_{(i,j)}\right) = F_{(i,j)} * 0.626$

with F being the freshwater discharge, i the months and j the river number.

The total freshwater in each of the three scenarios is around 329 $km^3\ yr^{-1}$ (Reference run), 452 $km^3\ yr^{-1}$ (EXP1) and 206 $km^3\ yr^{-1}$ (EXP2). The results of the scenario experiments are then compared with the Reference Run over the period 1980 to 2018.

3.3 Results

3.3.1 Model tuning: sensitivity experiments

To allow the comparison with the Black Sea Reanalysis model, the region of the Azov Sea in the model was excluded in the analysis and the data were interpolated onto the Black Sea Reanalysis grid.

LIGHT EXPERIMENTS

The results of the runs (Light1 to Light3) that investigate the impact of the light scheme are shown in Fig. 3.11 and Fig. 3.12 and compared with the Black Sea Reanalysis model. A first observation is that all the four new runs have warmer summers (closer to observations) compared to the no-light-penetration run (Appendix B, Fig. B.20).

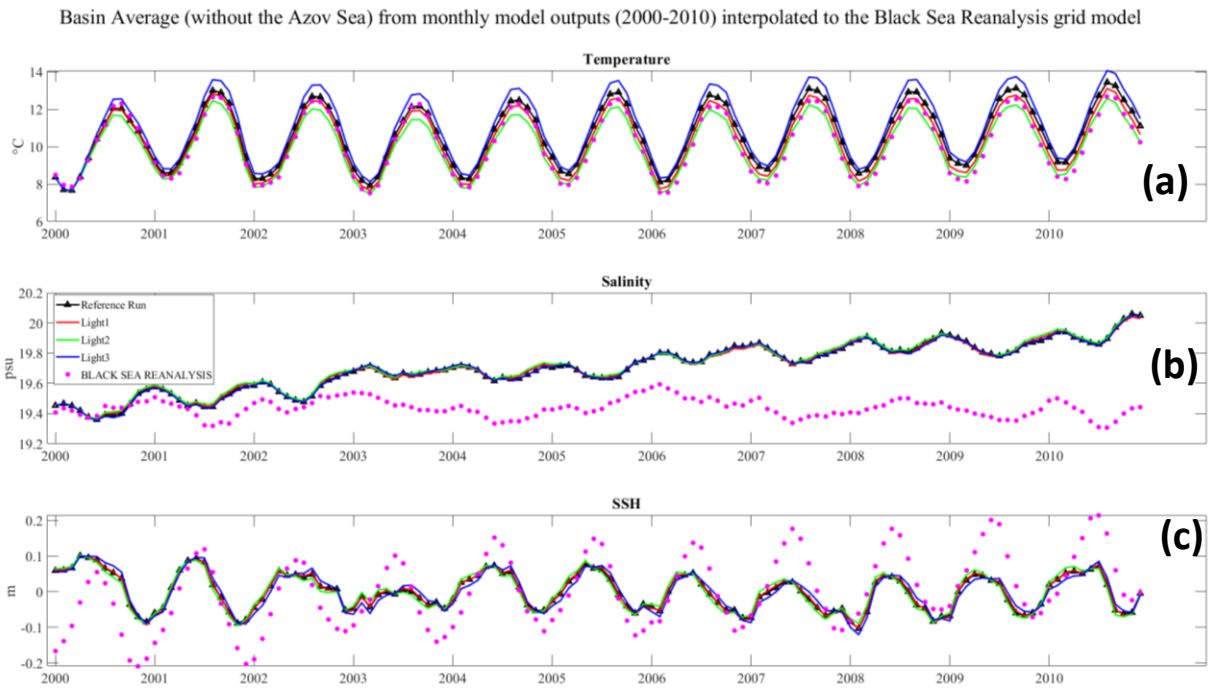

Figure 3.11: Results of the light sensitivity experiments in regards of (a) temperature (°C), (b) salinity (psu) and (c) SSH (m). For the SSH, the mean of each time series has been subtracted over the time period.

The main differences in the average temperature is observed during the winter period (minimum values) and summer period (maximum values). Light3 experiment shows consistently the highest values in temperature during summer, reaching 14.1°C in August 2010, against 13.4°C, 13.1°C and 12.6°C in respectively the reference run, Light1 and Light2. In comparison, the Black Sea Reanalysis model reach the value of 12.7°C in August 2010. In winter, the lowest values are observed in Light2 experiment and overlap well with the Black Sea Reanalysis data. For example, in February 2010 Light2 has the value of 8.5°C (against 9.2°C, 8.7°C and 9.4°C in the control run, Light1 and Light3) and the Black Sea Reanalysis model reaches 8.4°C. Over the 10 years analyzed, the lowest RMSE between the experiments and the Black Sea Reanalysis model in regard of the temperature is observed with Light2 with the value of 0.28°C (Table 3.6).

For all the experiment runs, an increase of the basin average salinity is observed over the period 2000 to 2010. The four runs (Control run and Light1 to 3) start with an average salinity value of 19.4 psu in January 2000, and reach the value of 20.0 psu at the end of 2010. The values of salinity from the Black Sea Reanalysis model fluctuate around the value of 19.4 psu over the

whole period analyzed. A similar RMSE is observed between the experiments and the Black Sea Reanalysis model in regards of the salinity, with values around 0.3 psu.

Table 3.6: RMSE associated to the comparison of the basin average (No Azov) from experiment runs with the Black Sea Reanalysis model. Results for the temperature (°C) and salinity (psu) are indicated.

Experiments	**RMSE (Temperature, °C); nb_points = 132**	**RMSE (Salinity, psu); nb_points = 132**
Control Run - Black Sea Reanalysis model	0.609	0.316
Light1 - Black Sea Reanalysis model	0.314	0.314
Light2 - Black Sea Reanalysis model	0.282	0.323
Light3 - Black Sea Reanalysis model	0.972	0.315

In Fig. 3.12, the average temperature profile in Light3 and the Control Run shows the highest differences with the Black Sea Reanalysis profile, with an RMSE of 1.16 °C and 0.79 °C respectively. Light1 and Light2 allows the model to reach lower values of temperature around the depth of the CIL (~60m depth). Their comparison with the Black Sea Reanalysis model indicates an RMSE of 0.38 °C and 0.21 °C for Light1 and Light2.

The average profile of salinity is not significantly different between Light1 to Light 3 experiments, and they all have slightly higher values of salinity at the surface, around 18.2 psu against 17.7 psu for the Black Sea Reanalysis model.

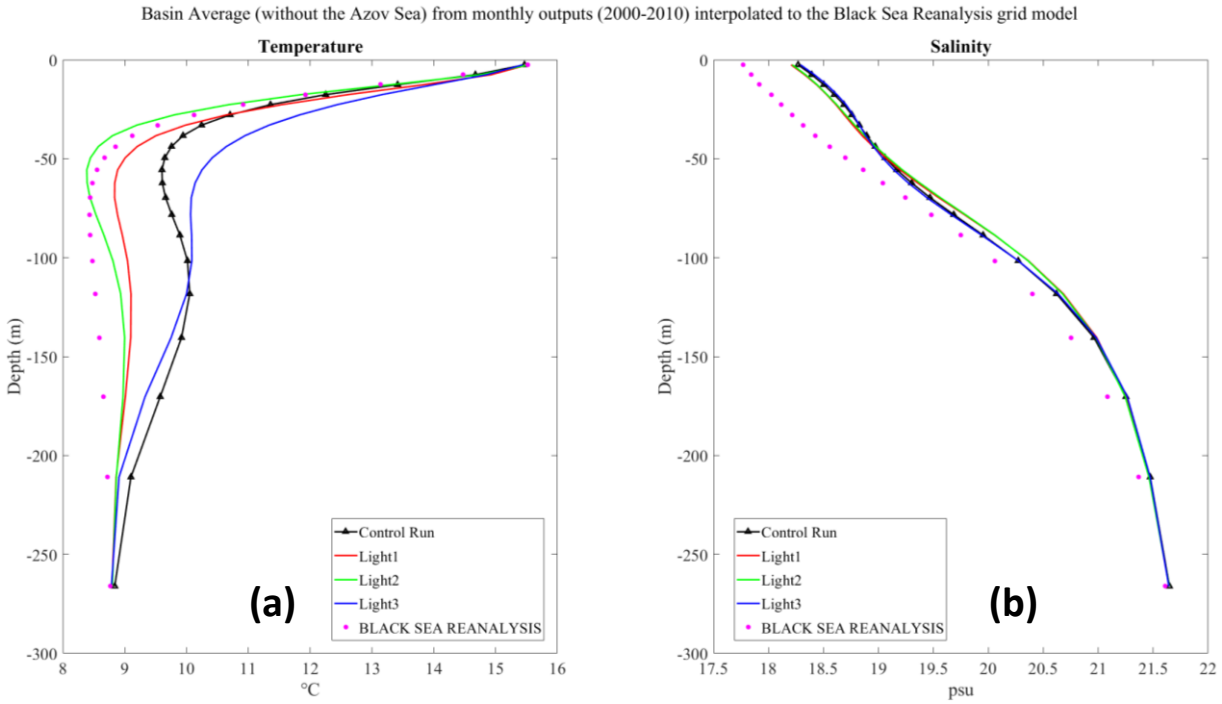

Figure 3.12: Vertical profiles of (a) temperature (°C) and (b) salinity (psu) averaged over the basin without the Azov Sea for the different light experiments.

Table 3.7: RMSE associated to the comparison of the vertical profiles averaged over the basin from the light experiment runs with the Black Sea Reanalysis model. Results for the temperature and salinity are indicated.

Experiments	**RMSE (Temperature, °C); n = 30**	**RMSE (Salinity, psu); n = 30**
Control Run - Black Sea Reanalysis model	0.793	0.321
Light1 - Black Sea Reanalysis model	0.381	0.308
Light2 - Black Sea Reanalysis model	0.207	0.316
Light3 - Black Sea Reanalysis model	1.165	0.325

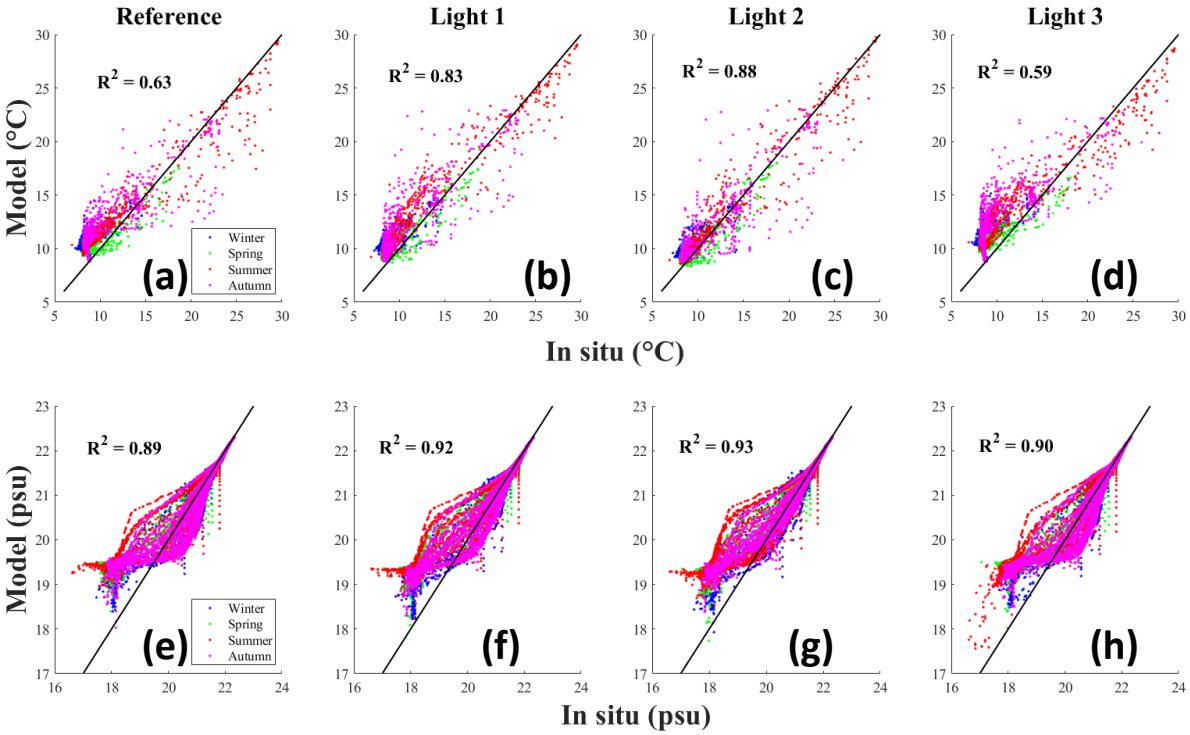

Figure 3.13: Top panel (a) to (d) represents the scatter plot comparison for temperature (°C) between *in situ* (EN4) versus interpolated modeled values for all the light sensitivity experiments. Bottom panel (e) to (h) is the same but for salinity (psu). The color indicates different seasons: winter (December - March), Spring (April - May), summer (June - August) and autumn (September - November). The black line is a 1:1 line, not the linear regression. The R^2 from the linear regression is indicated for each graph.

When compared to *in situ* profiles of temperature (Fig. 3.13), the experiments Light1 and Light2 are the closest to the observations. In the control run and Light3, most of the modeled values for all the seasons overestimate the temperature. The surface salinity from the model (values below 19 psu) overestimate the observations.

In conclusion, the results from the light sensitivity experiments indicate that the choice of the light penetration scheme (RGB, 2 bands, coefficient of attenuation coefficient or the use of chlorophyll *a* data) has no significant effect on the vertical and basin average salinity. However, all the runs indicate an increasing trend of 0.003 psu per year from 2000 to 2010, and reach at the end of the run a value that is 0.64psu greater than the Black Sea Reanalysis model.

When using the RGB option, adding chlorophyll *a* (Light2) significantly improve the vertical average of temperature, by reducing the temperature values around the depth of the CIL. Also, if no chlorophyll *a* data is used, using coefficient of attenuation data (Light1) provide better

vertical representation of the average temperature, compared to the use of RGB option (Control Run).

Based on the overall results of the sensitivity analysis, the scheme that use RGB light penetration and chlorophyll *a* data (Light2) was then selected and used as a new reference run for the mixing sensitivity experiments.

MIXING EXPERIMENTS

The same analysis as in the light sensitivity section are presented here in Fig. 3.14 and Fig. 3.15.

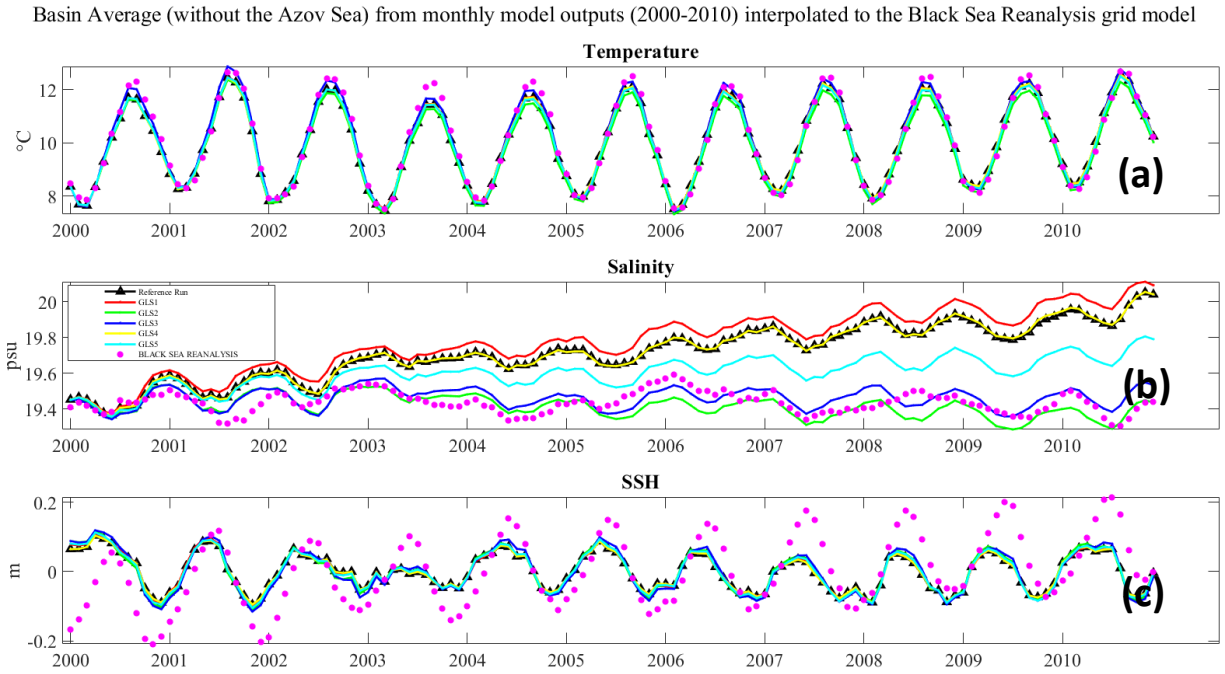

Figure 3.14: Results on the mixing sensitivity experiments (GLS1 to GLS5) in regards of (a) temperature (°C), (b) salinity (psu) and (c) SSH (m). For the SSH, the mean of each time series has been subtracted over the time period.

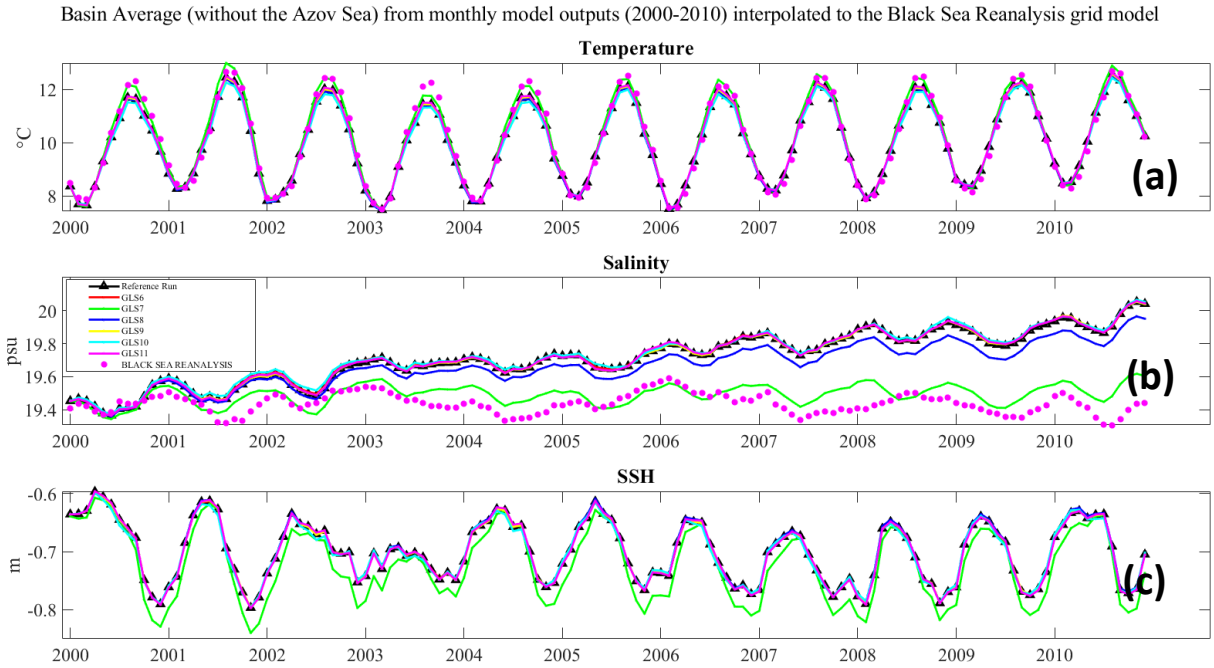

Figure 3.15: Results on the mixing sensitivity experiments (GLS6 to GLS11) in regards of (a) temperature (°C), (b) salinity (psu) and (c) SSH (m). For the SSH, the mean of each time series has been subtracted over the time period.

Changing the mixing parameterization did not have a significant impact on the basin average temperature (Fig.3.14a and Fig.3.15a). The increasing trend in the basin averaged salinity previously observed in the light sensitivity is still observed for most of the runs, except GLS2, GLS3 and GLS7 (Fig.3.14b and Fig.3.15b), with respectively an RMSE of 0.06, 0.06 and 0.08 when compared to the Black Sea Reanalysis model.

Table 3.8: RMSE associated to the comparison of the basin average (No Azov) from the mixing experiment runs with the Black Sea Reanalysis model. Results for the temperature and salinity are indicated.

Experiments	**RMSE (Temperature, °C); n = 132**	**RMSE (Salinity, psu); n = 132**
Control Run (= Light2)	0.282	0.323
GLS1	0.276	0.386
GLS2	0.369	0.062
GLS3	0.194	0.059

GLS4	0.282	0.324
GLS5	0.281	0.189
GLS6	0.283	0.327
GLS7	0.205	0.08
GLS8	0.318	0.267
GLS9	0.281	0.325
GLS10	0.345	0.333
GLS11	0.266	0.326

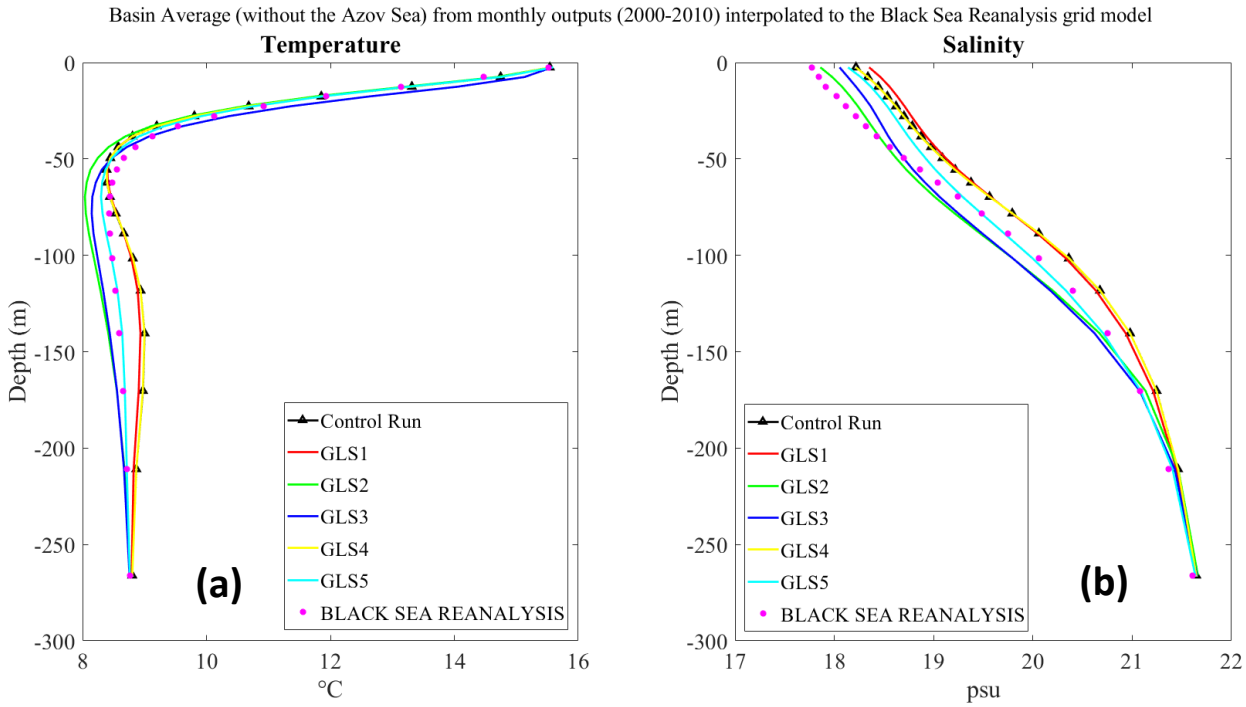

Figure 3.16: Vertical profiles of (a) temperature (°C) and (b) salinity (psu) averaged over the basin without the Azov Sea for the different mixing experiments (GLS1 to GLS5).

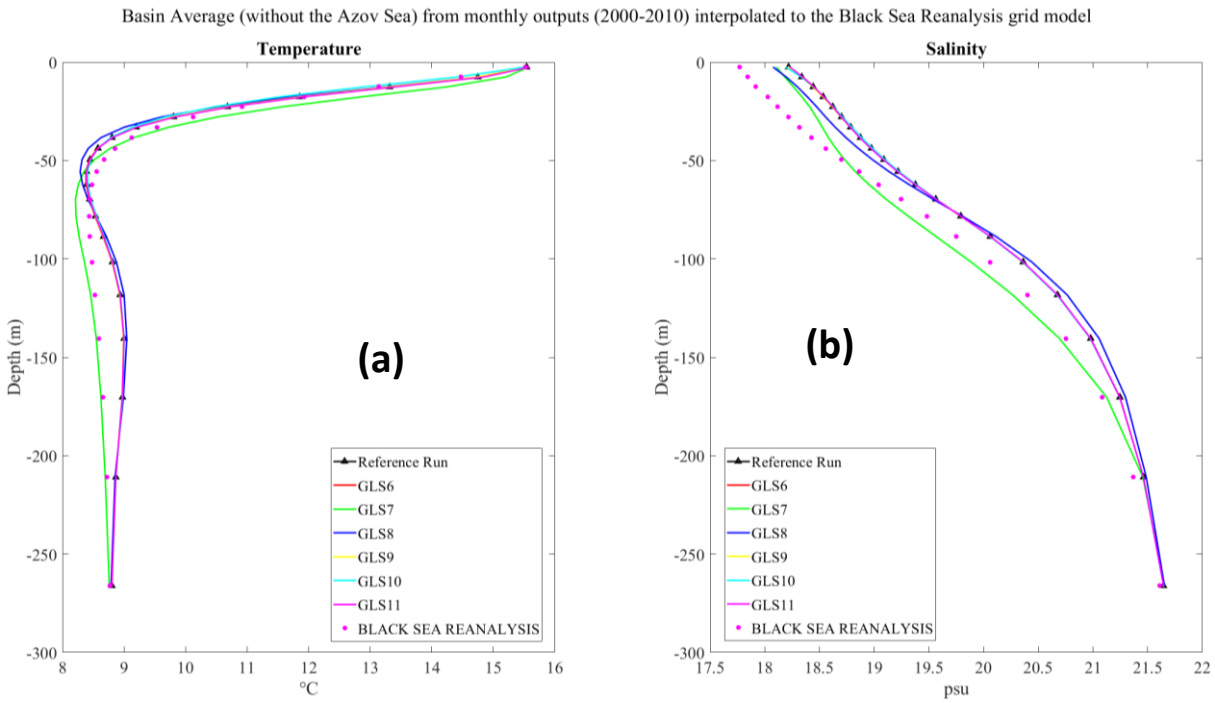

Figure 3.17: Vertical profiles of (a) temperature (°C) and (b) salinity (psu) averaged over the basin without the Azov Sea for the different mixing experiments (GLS6 to GLS11).

GLS1, GLS4, GLS8 and GLS11 are very close to the control run for the vertical basin average of temperature and salinity (Fig. 3.16ab and Fig. 3.17ab). For the temperature, the lowest RMSE between the model and the Black Sea Reanalysis model is observed for GLS5 with 0.12. For the salinity, it is observed for GLS2 with the value of 0.13.

Table 3.9: RMSE associated to the comparison of the vertical basin average from the mixing experiment runs with the Black Sea Reanalysis model. Results for the temperature and salinity are indicated.

Experiments	**RMSE (Temperature, °C); n = 30**	**RMSE (Salinity, psu); n = 30**
Control Run (= Light2)	0.207	0.316
GLS1	0.197	0.357
GLS2	0.262	0.129
GLS3	0.294	0.164
GLS4	0.208	0.315

GLS5	0.124	0.218
GLS6	0.208	0.316
GLS7	0.346	0.166
GLS8	0.277	0.259
GLS9	0.205	0.314
GLS10	0.238	0.318
GLS11	0.212	0.316

For the comparison with *in situ* profiles of temperature and salinity, only the runs that didn't have the increasing trend of salinity over the basin averaged were analysed.

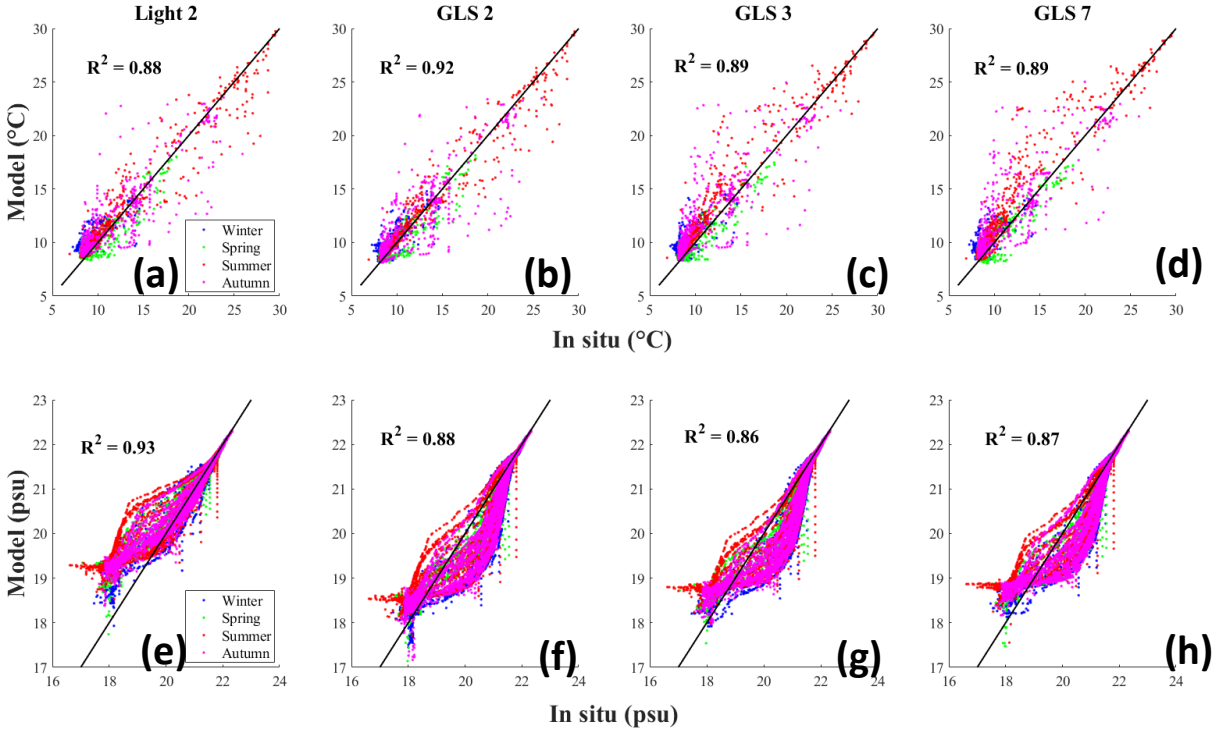

Figure 3.18: Top panel (a) to (d) represents the scatter plot comparison for temperature (°C) between *in situ* (EN4) versus interpolated modeled values for all the mixing experiments sensitivity. Bottom panel (e) to (h) is the same but for salinity (psu). The color indicates different seasons: winter (December - March), Spring (April - May), summer (June - August) and autumn (September - November). The black line is a 1:1 line, not the linear regression. The R^2 from the linear regression is indicated for each graph.

GLS2 showed the best agreement with *in situ* vertical profiles for the temperature. For GLS3 and GLS7, the modeled temperature in autumn and winter overestimate the observations. The model reproduces well the salinity in any configuration for deep values (higher than 21 psu).

In conclusion, the different choice of the mixing scheme did not significantly impact the basin average (full depth means) temperature. However, the drift of salinity previously observed was stabilized by changing the stability function from CanutoA to Galp (GLS2), or by increasing the Galperin limit from the value of 0.1 (initial value set up by the Turkish partners when they built the model) to higher and more standard values. Indeed, the value of 0.267 used in GLS3 was also used in Holt and Umlauf (2008) and the value of 0.6 used in GLS7 is close to the default Galperin value of 0.53 (Galperin et al., 1988). In the GLS scheme, the Galperin number (unitless constant) refers to limit of the dissipation rate under stable stratification.

From all the sensitivity analysis regarding the mixing scheme, GLS2 and GLS7 seemed to provide the best results when compared to the Black Sea Reanalysis model and *in situ* data for temperature and also eliminate the salinity drift. As each of the two separate configuration tested (GLS2 and GLS7) provided a good improvement of the physics inside the Black Sea, there was a need to assess whether using the combination of both settings would reduce the mixing even more. This is why long run were performed over 1980 to 2018 using GLS2 configuration, GLS7 configuration but also GLS2 + GLS7 (this is a valid setting and it was simply done by choosing the stability function from Galp *i.e.* nn_stab = 0 and using a high Galperin value *i.e.* rn_clim_galp = 0.6).

MIXING EXPERIMENTS: LONG RUNS

The results of the long runs are shown in Fig. 3.19 and Fig. 3.20.

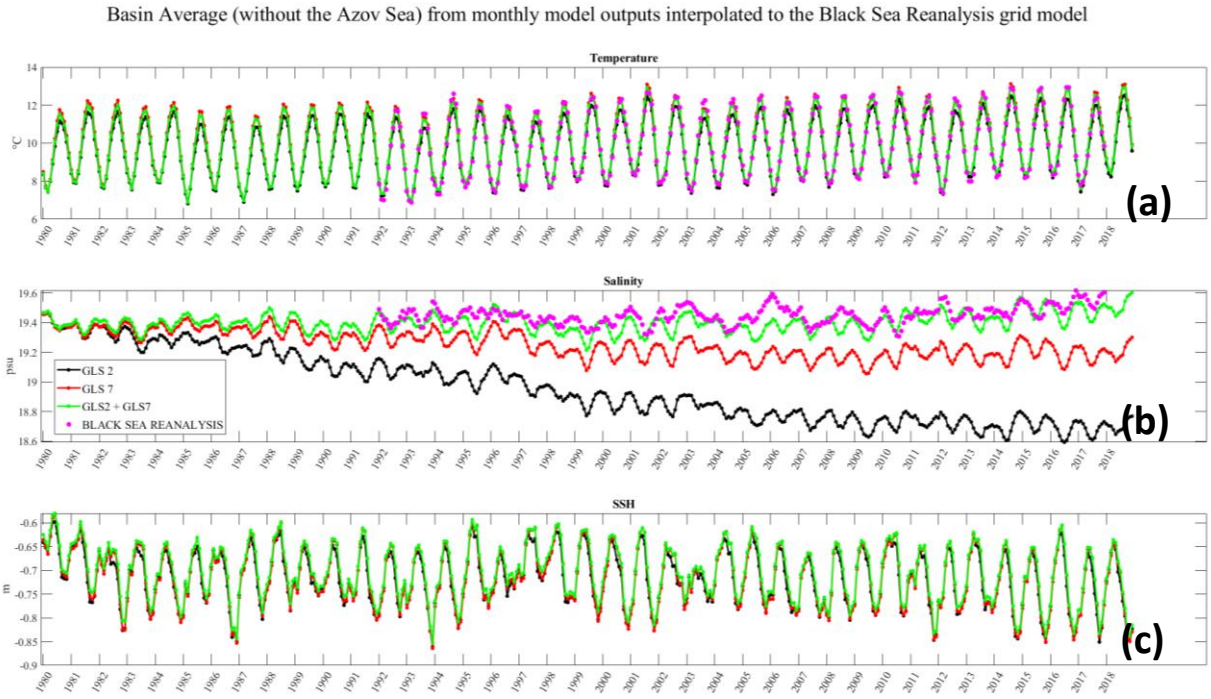

Figure 3.19: Results on the sensitivity experiments (GLS2, GLS7 and GLS2 + GLS7) over long period of time (1980 to 2018) in regards of (a) temperature (°C), (b) salinity (psu) and (c) SSH (m). For the SSH, the Black Sea Reanalysis model data are not indicated as they use a different reference level.

For GLS2, GLS7 and GLS2+GLS7, they all show very similar variations in the basin average temperature from 1980 to 2018. With GLS2, a decreasing trend in salinity is well observed, going from around 19.46 psu to 18.77 psu. In the configuration GLS2 + GLS7, the salinity follows well the variations from the Black Sea Reanalysis model (Fig. 3.19b).

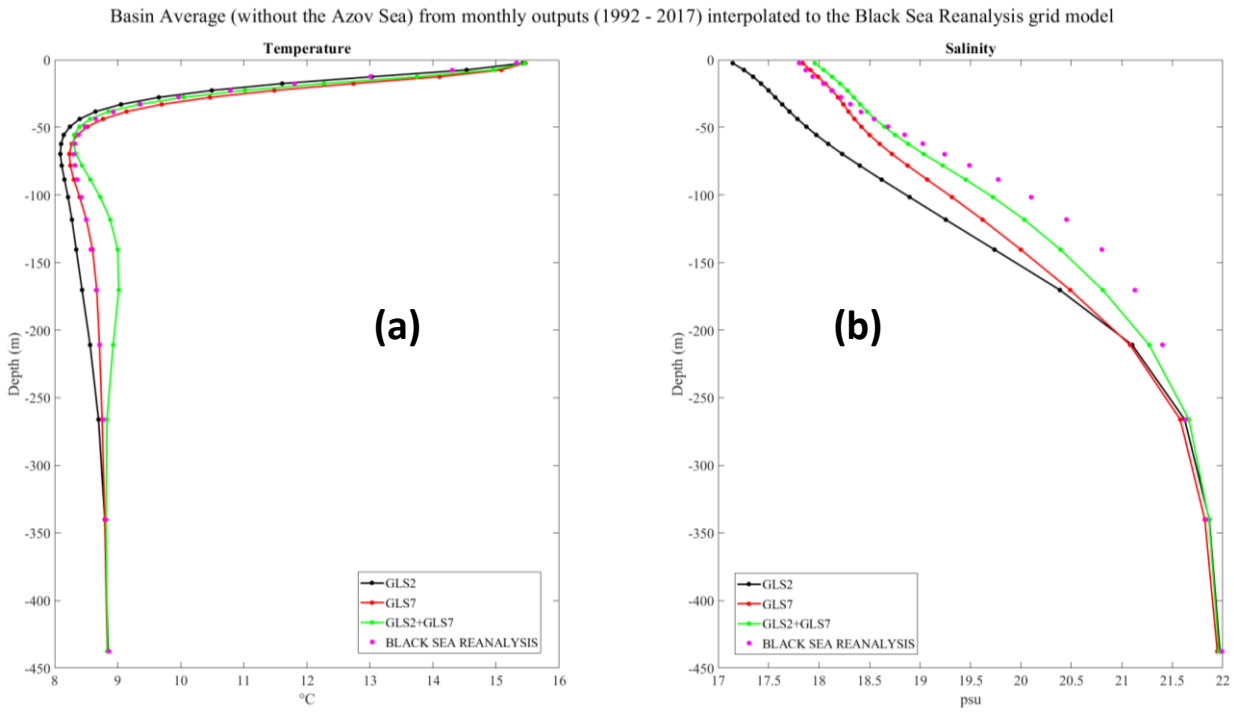

Figure 3.20: Vertical profiles of (a) temperature (°C) and (b) salinity (psu) averaged over the basin without the Azov Sea for the different mixing experiments (GLS2, GLS7 and GLS2+GLS7).

The vertical basin average of temperature from 1992 to 2017 (Fig. 3.20a) shows that GLS7 is the closest to the Black Sea Reanalysis model values. For GLS2 + GLS7, the average temperature deviate from the Black Sea Reanalysis model around 65m depth and shows a slight peak of increased temperature around 150m. The vertical basin average of salinity from GLS2 is lower than the Black Sea Reanalysis model over the 260 upper m depth. The surface values are around 17.14psu for GLS2 against 17.8psu for the Black Sea Reanalysis model. The surface values for GLS7 and GLS2+GLS7 are close to the Black Sea Reanalysis model but in GLS7, the values remain lower than the Black Sea Reanalysis model for increasing depth (until around 260m).

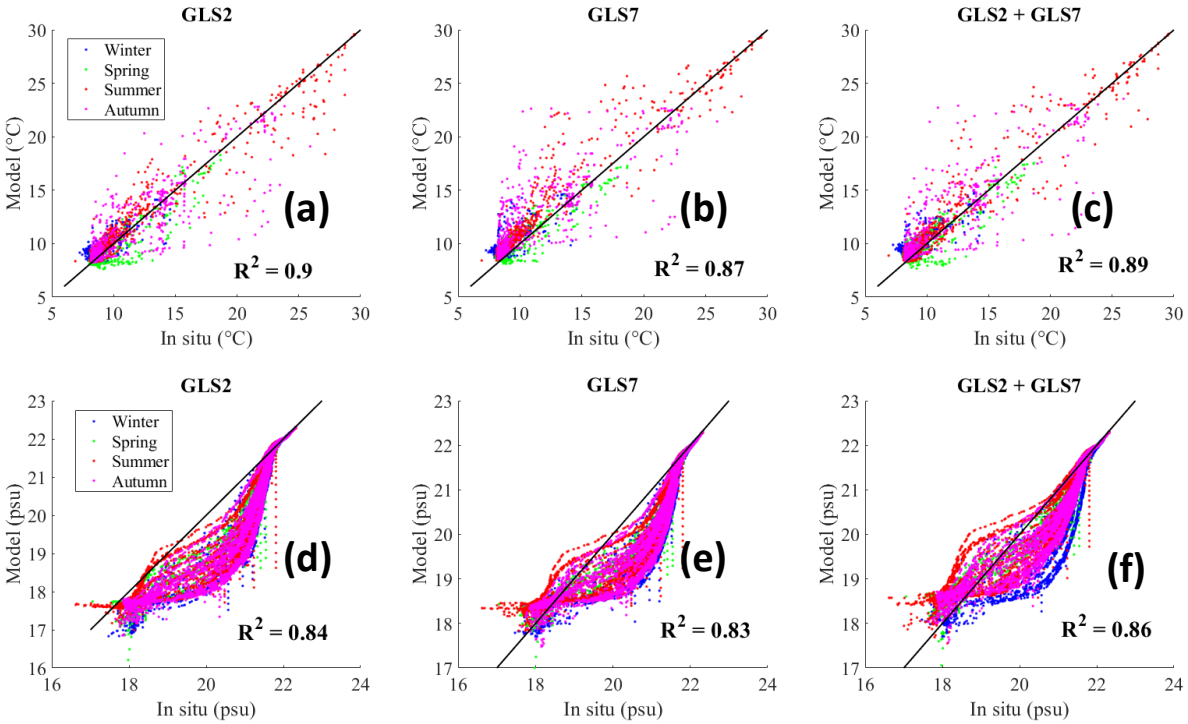

Figure 3.21: Top panel (a) to (d) represents the scatter plot comparison for temperature (°C) between *in situ* (EN4) versus interpolated modeled values for all the long runs experiments (GLS2, GLS7 and GLS2 + GLS7). Bottom panel (e) to (h) is the same but for salinity (psu). The color indicates different seasons: winter (December - March), Spring (April - May), summer (June - August) and autumn (September - November). The black line is a 1:1 line, not the linear regression. The R^2 from the linear regression is indicated for each graph.

Despite the very good agreement of GLS2+GLS7 in regards of salinity with the Black Sea Reanalysis model and the in-situ profiles, it was disregarded due to the recurring peak of temperature observed in the model results for depths below the CIL. This is why the configuration selected for further analysis was GLS7, accepting this has a modest drift in basin average salinity.

Once the most accurate configuration is selected from the sensitivity analysis, an evaluation of the model was studied over the long period.

3.3.2 Model validation

The interannual variability of SST between different datasets shows similar variation for the overlapping periods (Fig. 3.22a) and the results from NEMO - BLACK SEA are closer to the Black Sea Reanalysis model than to satellites data or datasets from Dorofeev et al. (2017). Annual values from satellite are higher compared to all the other datasets, with a positive offset close to 0.5°C from 2003 to 2018. This might be explained by the reduced coverage of satellite data during winter, which then leads to "overweighting" the summer values.

All the datasets have a positive trend in the analyzed period, underlying a surface temperature increase. The model NEMO - BLACK SEA shows a positive trend of 0.04°C per year from 1980 to 2018.

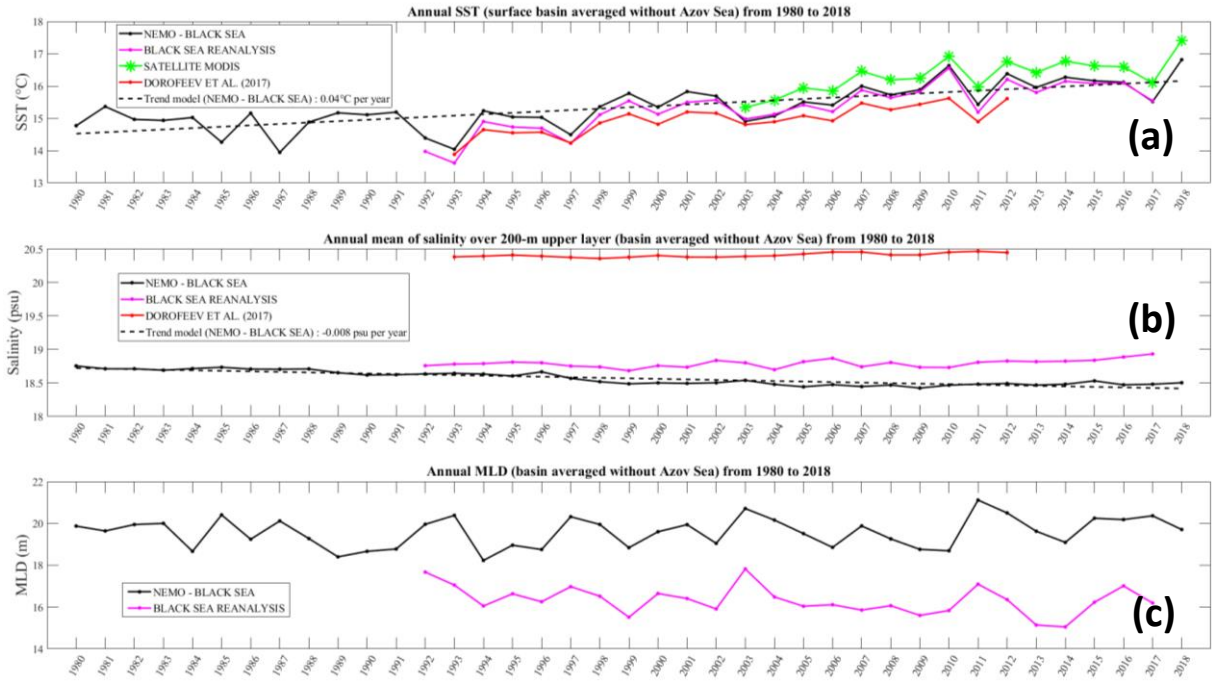

Figure 3.22: Comparison of interannual variability between NEMO - BLACK SEA, the Black Sea Reanalysis model, satellite MODIS and Dorofeev et al. (2017) for (a) SST (b) upper 200m salinity and (c) MLD.

Annual Salinity from Dorofeev et al. (2017) shows higher values from 1993 to 2012, being around 20.5 psu compared to the Black Sea Reanalysis model which are around 19 psu. The comparison in the trends values over the upper 200m layer are referred in Table 3.10.

The MLD from the model NEMO shows similar annual variations with the Black Sea Reanalysis model but has a positive off-set by around 2-3 m.

Table 3.10: Trends comparison in sea surface temperature (°C) and averaged salinity (psu) in the upper 200m layer.

		TREND per year	
		SST in °C	SALINITY (upper 200-m layer) in psu
MODEL (1993 - 2012)	Model (NEMO - BLACK SEA)	0.073	-0.009
	Black Sea Reanalysis model	0.087	No significant trend
	Dorofeev et al. (2017)	0.059	0.004
OBSERVATION (2003 - 2018)	Satellite (MODIS)	0.082	-

After looking at the surface properties, the sub-surface ones are also analysed.

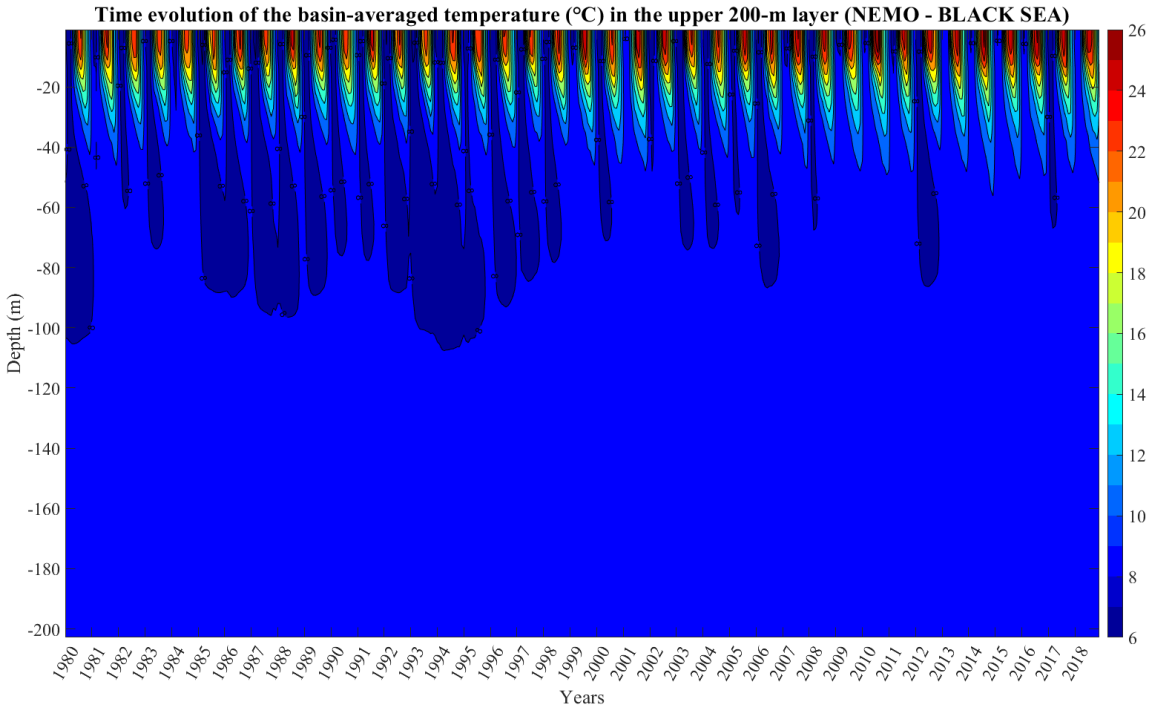

Figure 3.23: Time evolution of the basin-averaged temperature (°C) in the upper 200-m layer from NEMO - BLACK SEA (1980 to 2018).

The interannual variability in the basin average of the CIL volume is well observed in Fig.3.23. The 8°C isotherm is observed at the surface of the water column in winter and can penetrate up until 100m depth. The CIL can remain below the seasonal thermocline as observed for most of the years. We can notice that the occurrence and the volume of the CIL (8°C isotherms in Fig.3.23) is reducing (except in 2012). This indicates an heating of the subsurface temperature, in addition to the surface positive trend previously described. This result is also observed from model results in Dorofeev et al. (2017) and outputs from the Black Sea Reanalysis model (Fig.3.24).

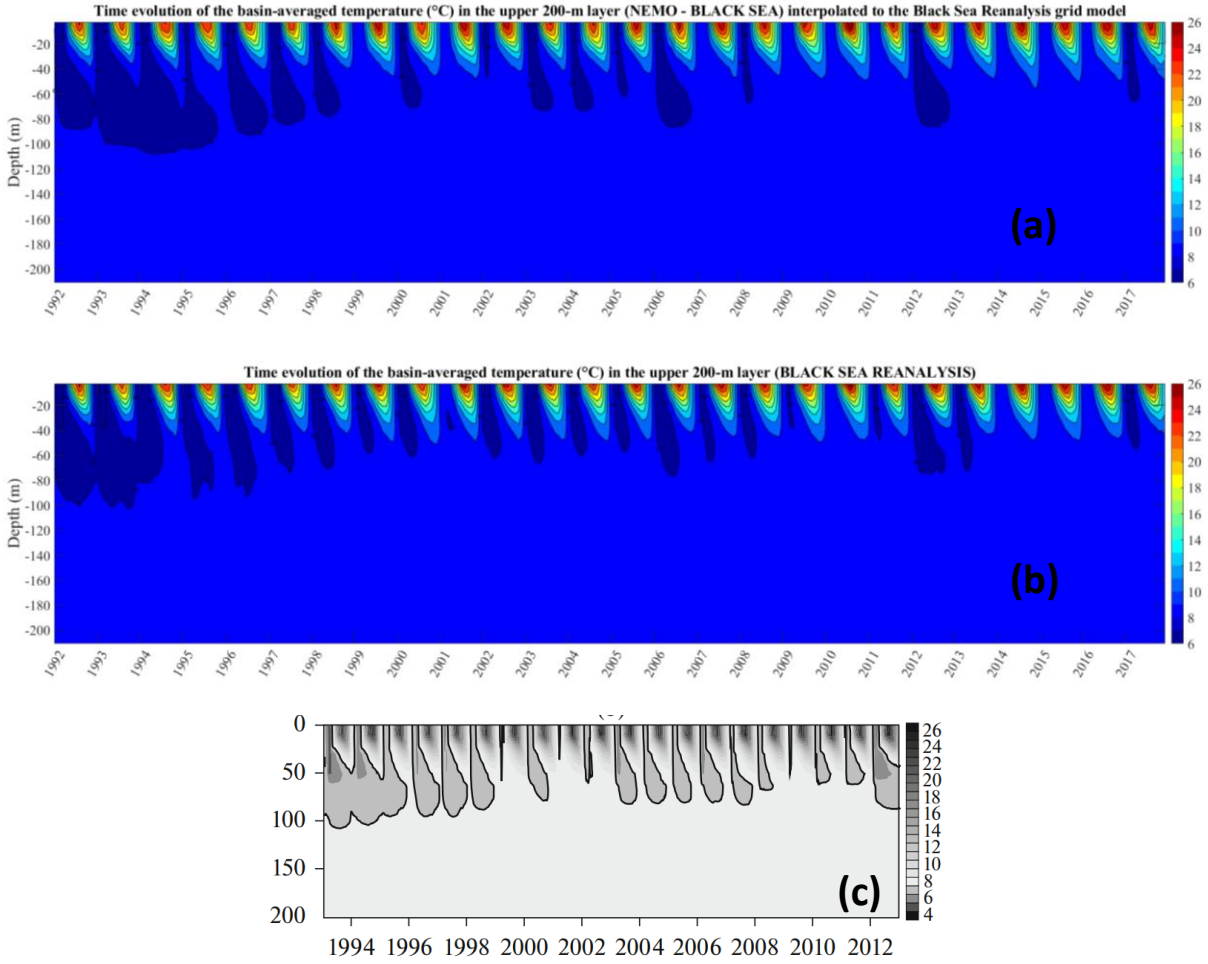

Figure 3.24: Time evolution of the basin-averaged SST(°C) in the upper 200-m layer from (a) NEMO – BLACK SEA (1992 to 2017) or b) the Black Sea Reanalysis model (1992 to 2017) or c) Dorofeev et al. (2017) (1993 - 2012) In a) &b) &c), the isotherm of 8°C is indicated.

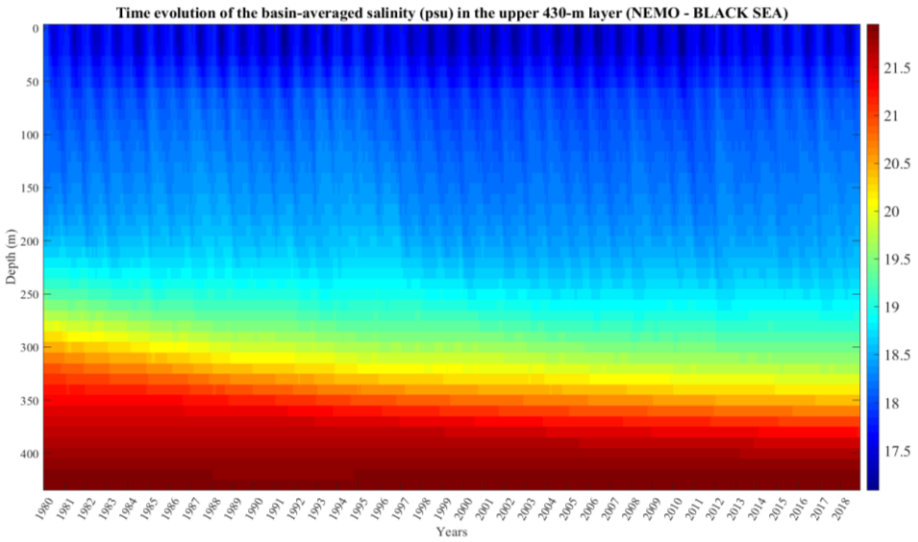

Figure 3.25: Time evolution of the basin-averaged salinity (psu) in the upper 430-m layer from NEMO - BLACK SEA (1980 to 2018).

The salinity above 200m is stable over the whole period of simulation. But around 300m, the halocline depth increases (from around 300m at the beginning of the run, to around 350 at the end of the run). This is consistent with the drift in Figure 3.19. The density is also shown in Fig.3.26.

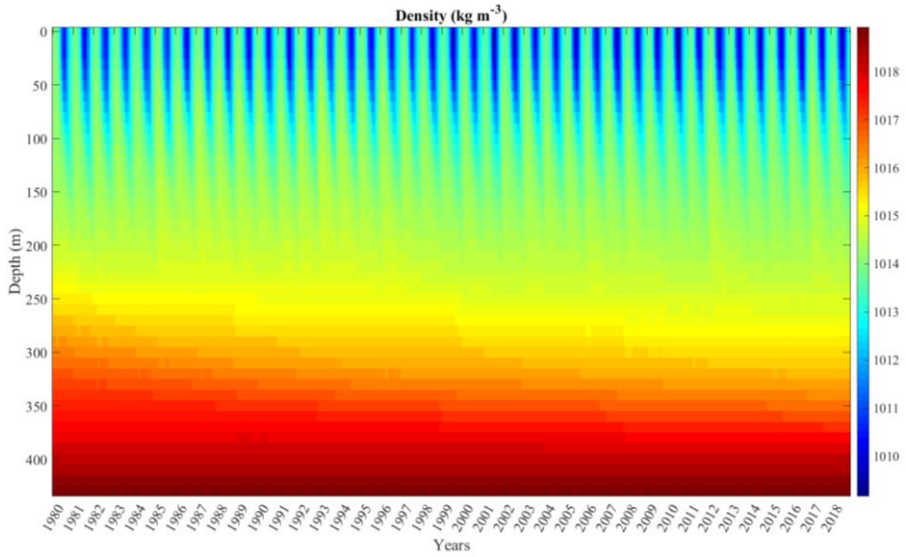

Figure 3.26: Time evolution of the basin-averaged density (kg m^{-3}) in the upper 430-m layer from NEMO - BLACK SEA (1980 to 2018).

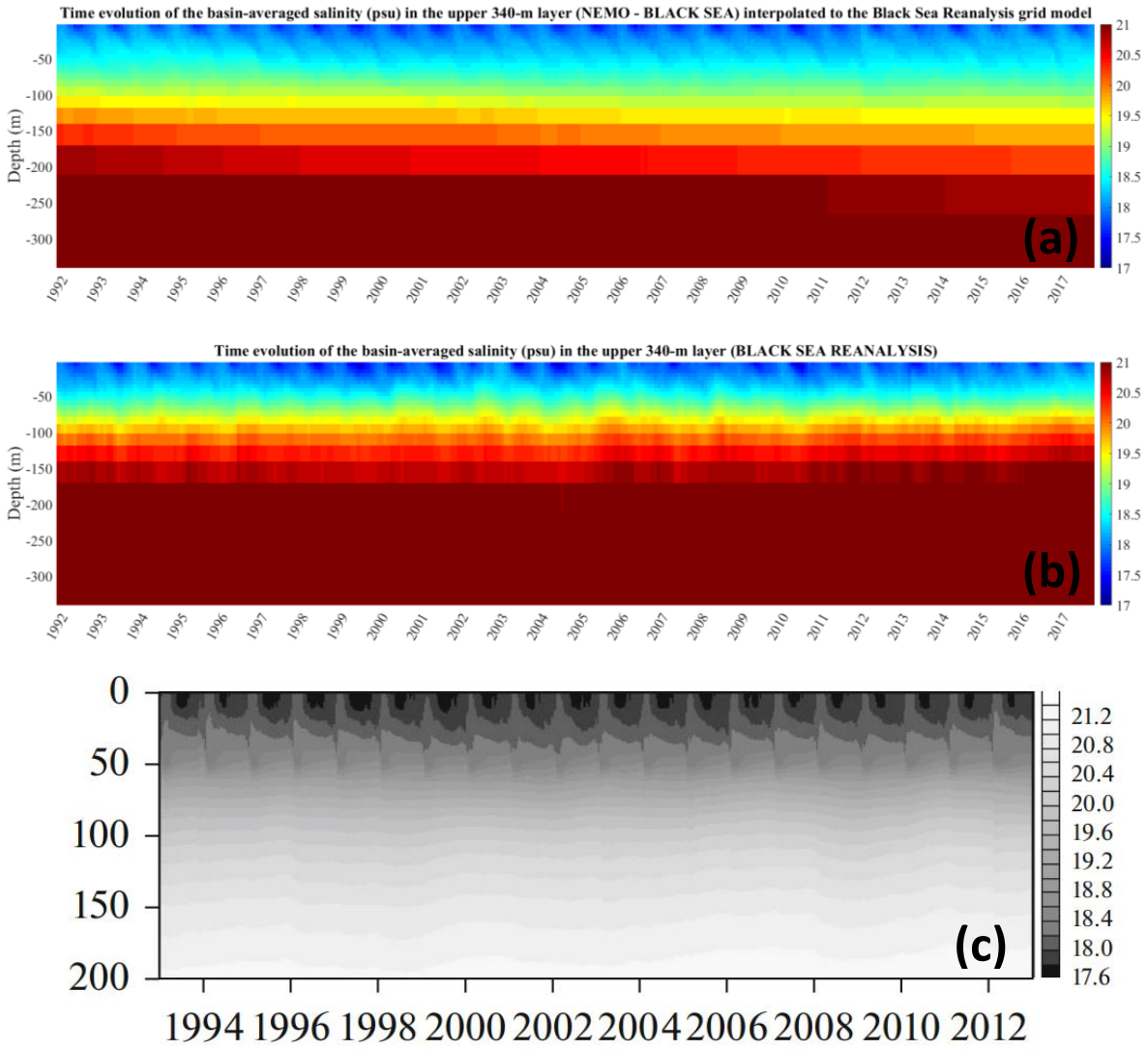

Figure 3.27: Time evolution of the basin-averaged salinity in the upper 340-m layer for (a) NEMO - BLACK SEA and (b) Black Sea Reanalysis model. (c) Time evolution of the basin averaged salinity in the upper 200 m layer, data from Dorofeev et al. (2017).

3.3.3 Long-term changes in the CIL structure (1980 - 2018)

In this section, a focus on the interannual variability in the CIL is made. To study this particular layer, a set of metrics are introduced.

3.3.3.1 Sea surface temperature during winter from the model

The severity of winter conditions is known to affect the amount of CIL formed (Oguz et al., 2006; Oguz and Ediger, 2006; Kazmin et al., 2010). In Ivanov et al. (2001), a winter severity index is calculated as the sum of negative air temperature (*i.e.* the number of days on which temperature becomes negative at a given time) for a meteorological station of interest. The annual anomalies of air temperature from ERA5 are strongly correlated with the annual anomalies of the modeled sea surface temperature (Fig. 3.27), with $R^2 = 0.96$. Therefore, the comparison of the CIL metrics that are introduced thereafter is directly done with the winter SST (presented in Fig. 3.28) from the model and not the air temperature. In the following sections, the winter SST for a specific year goes from January to March and it also includes December from the previous year (DJFM). (for example, the winter SST of the year 2003 consider December-2002 and January to March of 2003).

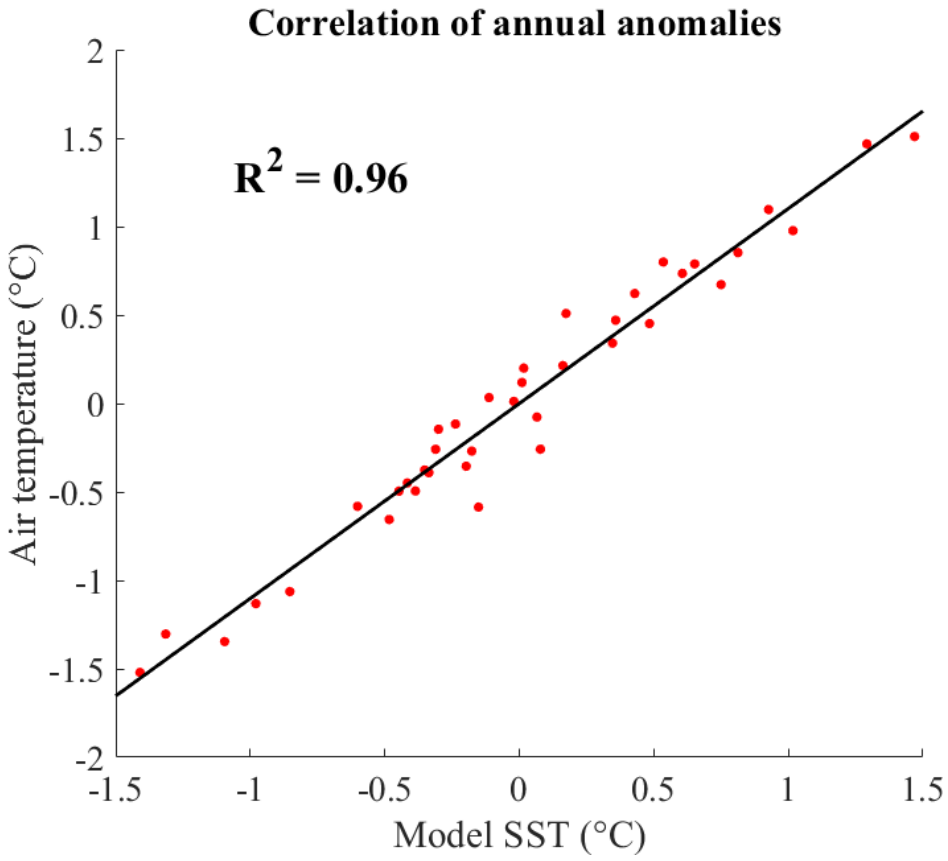

Figure 3.28: Scatter plot between the annual anomalies of air temperature (°C) and the modeled SST (°C). The annual anomalies are basin averaged and exclude the Azov Sea for both datasets.

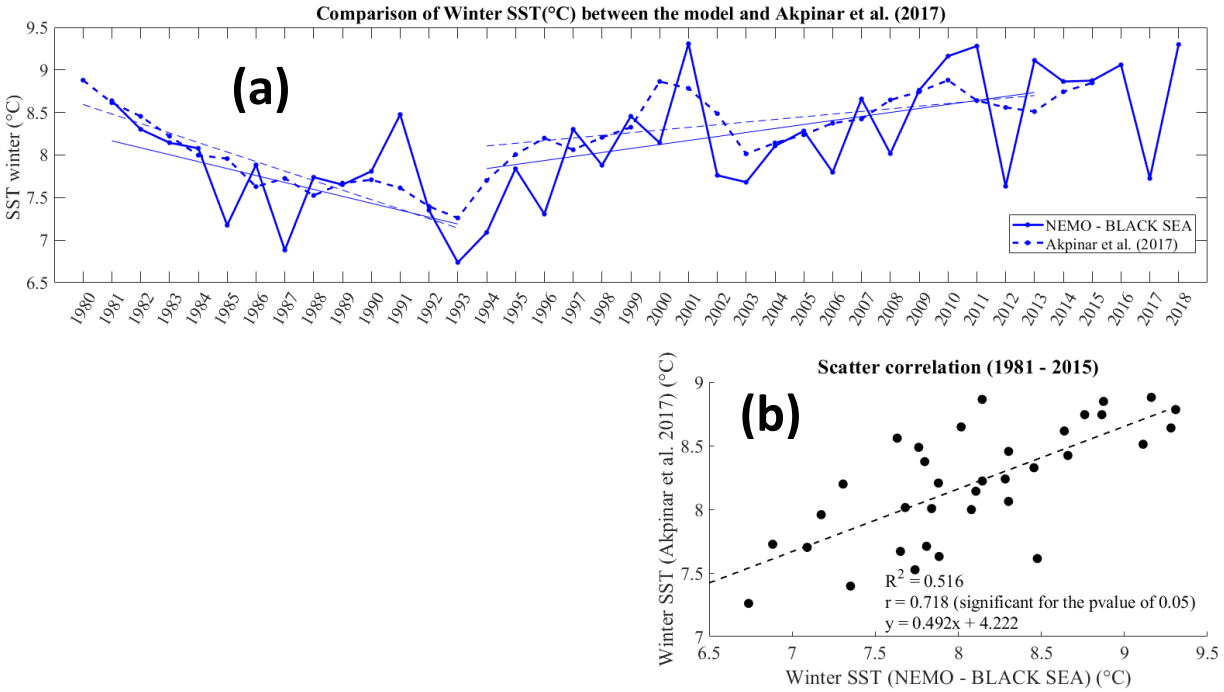

Figure 3.29: a) Time series of winter SST (DJFM) from the model (solid line) and compared with results from Akpinar et al. (2017) (dashed line). Trends for the cooling and warming period are also indicated for both time series. (b) Associated scatter correlation plot.

In Akpinar et al. (2017), they observe a cooling phase from 1980 to 1993 and a subsequent warming phase in 1993 to 2013 using data from the Hadley Centre, UK MetOffice (http://www.metoffice.gov.uk/hadobs/hadisst/) (see the linear regression from Fig.3.29).

3.3.3.2 Long term changes in the CIL structure

The interannual variations of the depth, the thickness, the minimum temperature, the average temperature, the cold content and the volume in the CIL are introduced here as the CIL metrics. Their annual means are investigated.

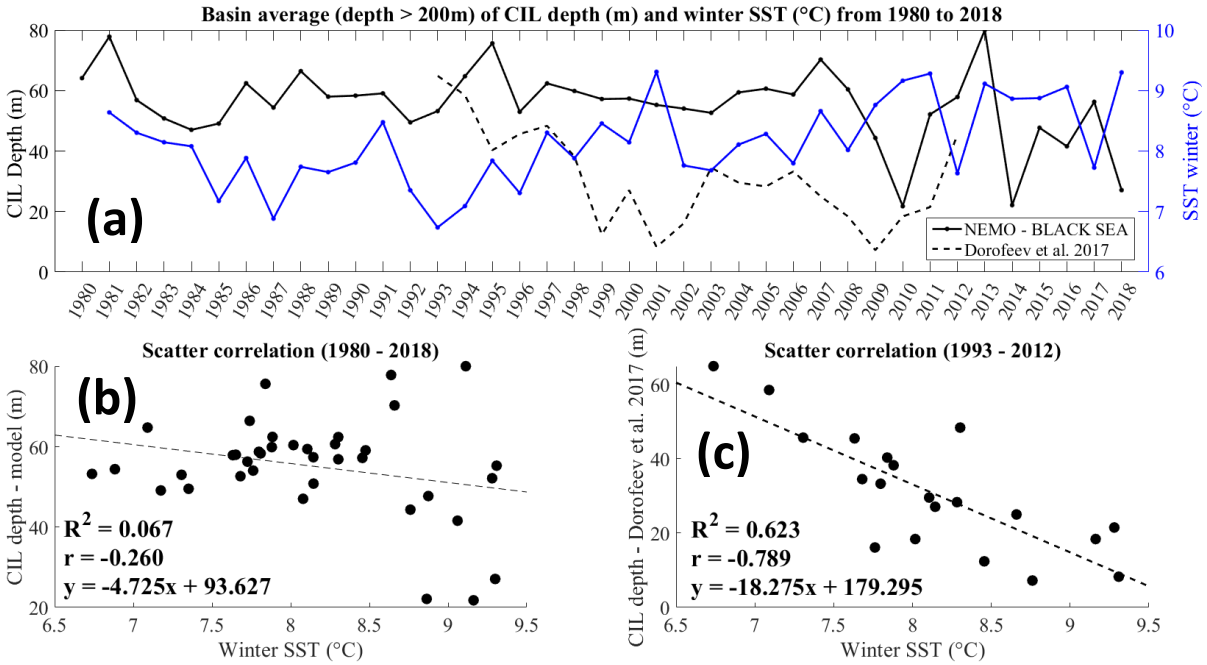

Figure 3.30: (a) Comparison of the basin average CIL depth (m, left axis) and the winter SST (°C, right axis) from 1980 to 2018. The CIL depth from the model (solid line) is compared with results from Dorofeev et al. (2017) (dashed line). (b) Scatter correlation between the Winter SST and (b) the CIL depth from the model or (c) the CIL depth from Dorofeev et al. (2017).

There is no significant correlation between the winter SST and the depth of the minimum temperature from the CIL using the model NEMO - BLACK SEA (Fig. 3.30). In contrast to the article of Dorofeev et al. (2017), they observed that a colder temperature during winter is associated with a deeper annual mean of the CIL depth, with $R^2 = 0.62$ (Fig. 3.30c).

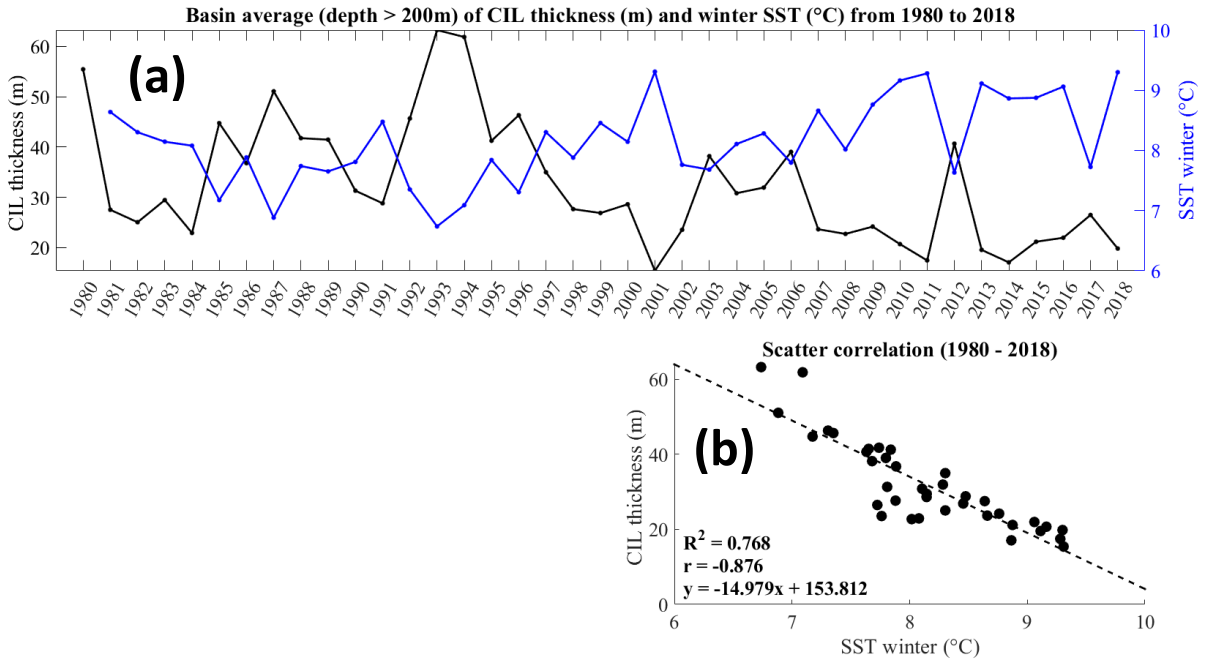

Figure 3.31: (a) Comparison of the CIL thickness (m, left axis) with the winter SST (°C, right axis) with (b) the corresponding scatter plot from 1980 to 2018.

In Fig. 3.31, a negative correlation is observed between the winter SST and the CIL thickness (R^2 = 0.77). Colder winters are then associated with thicker CIL.

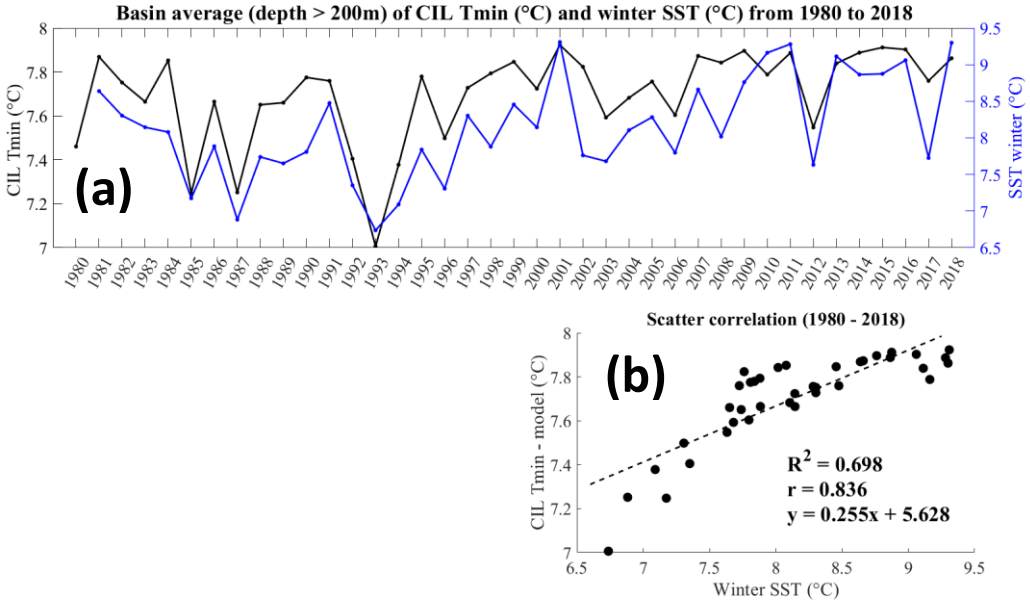

Figure 3.32: (a) Comparison of the minimum temperature of the CIL (°C, left axis) with the winter SST (°C, right axis) with (b) the corresponding scatter plot from 1980 to 2018.

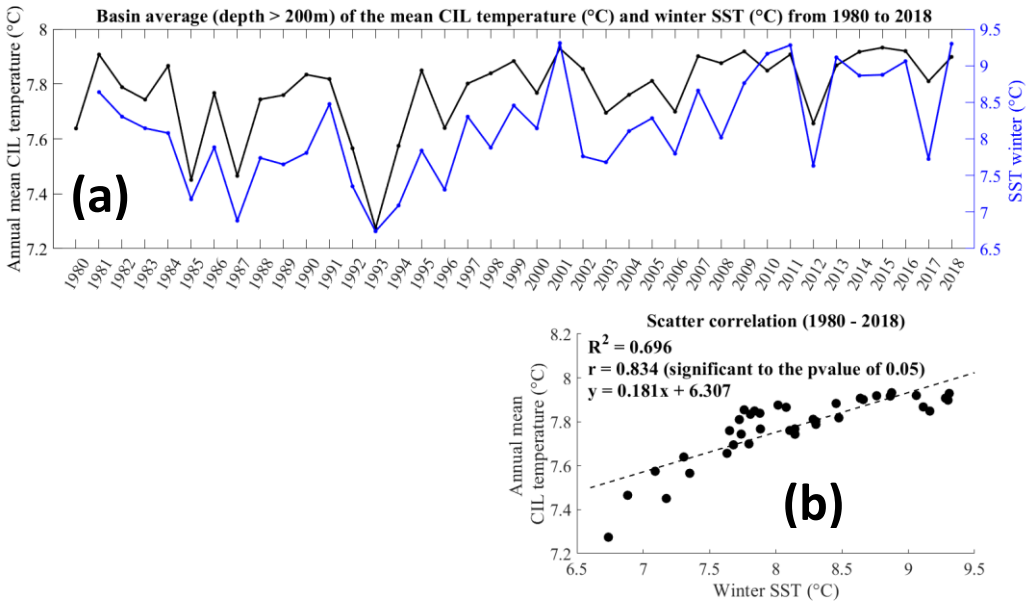

Figure 3.33: (a) Comparison of the mean temperature of the CIL (°C, left axis) with the winter SST (°C, right axis) with (b) the corresponding scatter plot from 1980 to 2018.

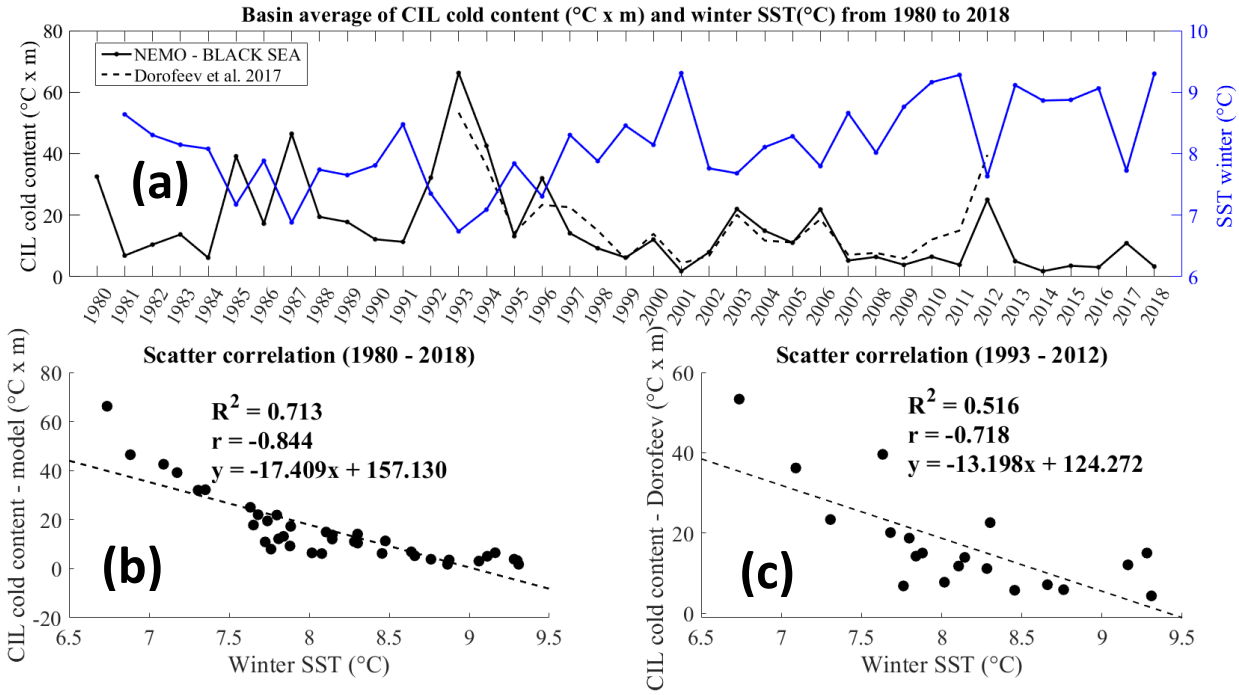

Figure 3.34: Comparison of both the CIL cold content (°C x m) from NEMO - BLACK SEA (full line) and the data from Dorofeev et al. (2017) (dashed line) with winter SST (°C, blue line).

Results from Fig.3.34 shows that the CIL cold content from the model follows similar variations to the one from Dorofeev et al. (2017). The cold content is negatively correlated to winter SST

(R^2 = 0.71 for Nemo and R^2 = 0.52 for Dorofeev et al. (2017)). The colder the winter is, the higher is the cold content.

3.3.3.3 Scenario runs (rivers)

Here are presented the results of the two scenario runs (EXP1 and EXP2) that investigate the impact of either increasing or decreasing the river discharge in the model simulation from 1980 to 2018. Also, the results from the less realistic scenario that removed the discharge from all the rivers is also presented for comparison.

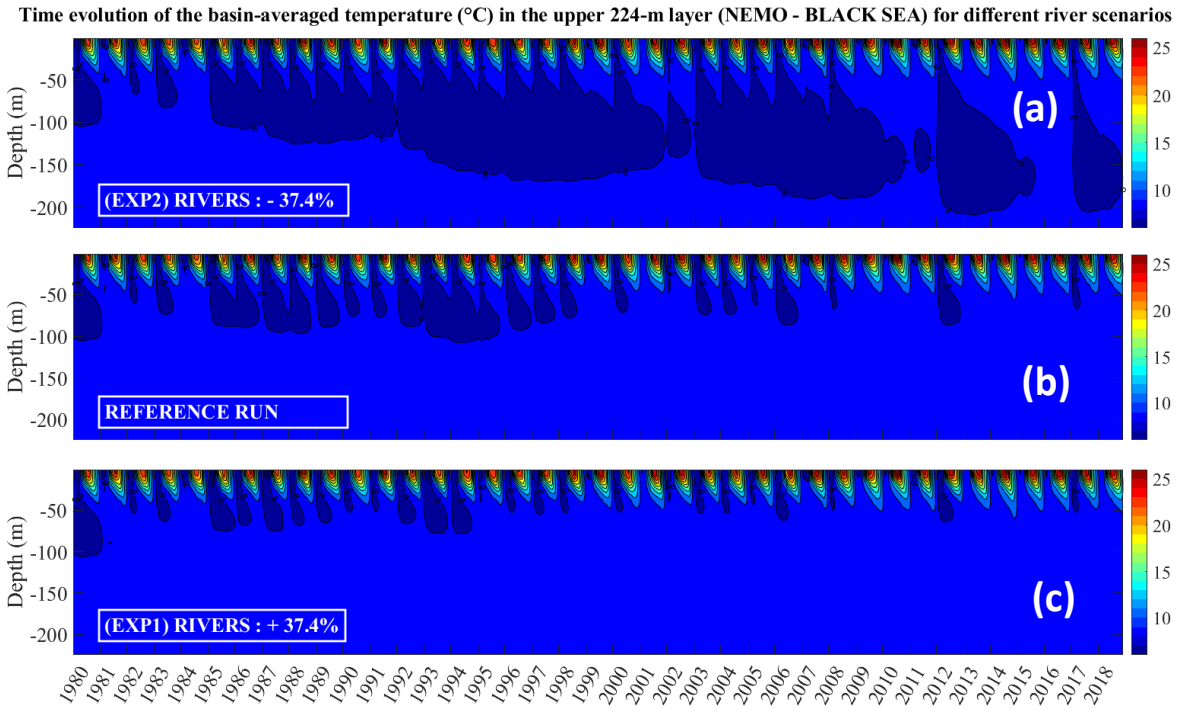

Figure 3.35: Basin averaged temperature from 1980 to 2018 in the upper 224-m layer. (a) Results using the scenario run of -2σ in the river discharge (EXP2). (b) Results for the Reference Run and (c) Results using the scenario run of +2σ in the river discharge (EXP1). The 8°C isotherm is shown.

From Figure 3.35 that indicates the basin average values in temperature, it is clearly seen that a change in the river discharge has a significant impact on the volume of the CIL delimited by isotherms of 8C. When the river discharge is decreased by 37.4% (EXP2, Fig.3.35a), the total volume of water (from 1980 to 2018) below 8C reached around 1.3324e+16 m3, which is around 3 times more than the reference run (4.3154e+15 m^3). However, an increase in the river discharge of 37.4% is associated with a significant decrease in the CIL volume, by a factor of 1.6. There is an asymmetric effect on the change of the CIL volume resulting from the variation in the river discharge, where the fractional change in the CIL volume is greater in the scenario of a decrease in the river discharge. From Fig.3.35, it can also be seen that the depth of the minimum temperature and the thickness of the CIL are consequently affected. Such metrics have higher values in the river discharge decrease scenario in comparison to the reference run. The impact on the average value of the metrics from 1980 to 2018 is shown in Table 3.11. The position metrics are the one that are most affected. In comparison with the reference run, the depth of the minimum D_{min} is increased by a factor 2.4 in EXP2 whereas it decreases by a factor of 0.75 in EXP1. The minimum of temperature is not significantly affected by the change in river discharge.

Table 3.11: Influence of the river discharge on the CIL structure

CIL STRUCTURE (1980 – 2018)	**EXP2 (-37.4% in river discharge)**	**REFERENCE RUN**	**EXP1 (+37.4% in river discharge)**
D_{min} (depth of the minimum, m)	98.773	55.404	41.378
D_z (thickness, m)	81.262	32.504	24.073
T_{min} (temperature of the minimum depth, °C)	7.6101	7.696	7.699
Total volume (m^3)	$1.332x10^{16}$	$4.315x10^{15}$	$2.626x10^{15}$

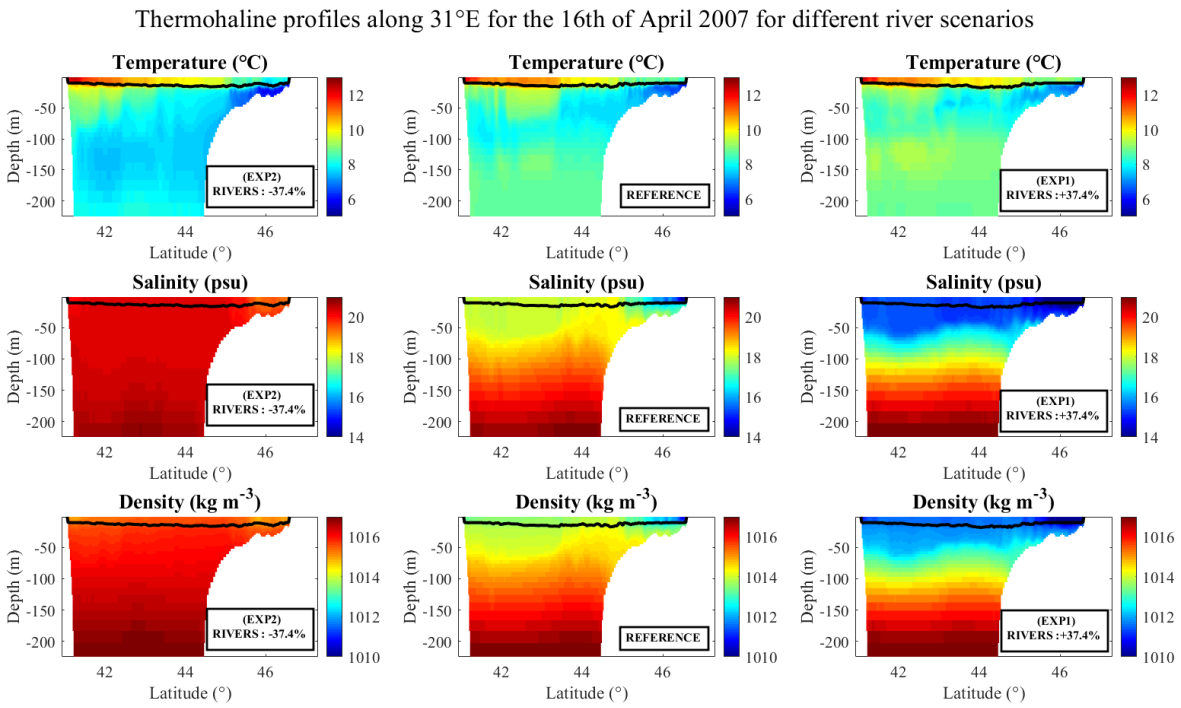

Figure 3.36: Impact of the river discharge (+/- 37.4%) on the temperature, salinity and density profiles along the transect 31°E for the 16th of April 2007. Left column represents results for the scenario -37.4% in the river discharge (EXP2), Middle column is for the reference run and Right column represents the increase of 37.4% in river discharge (EXP1).

The same transect as presented in the method Section 3.2.1 is used and plotted in terms of temperature, salinity and density for the river experiments (Fig.3.36). First are presented the results of the reference scenario. In the reference case, the overall salinity distribution shows low values near the coast (close to river mouth) which increase towards the interior basin. A strong vertical gradient in salinity is observed, which reached maximum values towards greater depths (from around 18 at the surface in the interior basin to 22 psu around -220m). The temperature value is minimum in the shelf area (reaching around 7C) and is also observed in the inner part of the basin around -100m depth. The density gradient is similar to the salinity.

A decrease in the discharge (Fig. 3.36, left column) led to a strong reduction in the freshwater plume signal near the coast. The values of salinity are much more homogeneous over the whole transect, around 20 psu. However, the signal of temperature is stronger near the coast and a clear cascading of cold water is observed on the shelf break. Such cold water penetrates to depths of around 150m and is observed across the whole transect. Density values are more homogeneous with values around 1017 kg m^{-3}. In the case of an increase of river discharge, a strong vertical stratification in the salinity and density is observed. The volume in the CIL is less and reaches shallower depths.

3.4 Conclusion

The Black Sea dynamics, with a special focus on the Cold Intermediate Layer structure, was studied in model simulations of almost four decades (1980 to 2018), which is 12 years longer than the Black Sea Reanalysis model from the Copernicus service. Such analysis were carried out with a self-developed 3D numerical model that was tested and verified (spatial resolution of 3.3 km and 60 vertical levels that are thinner towards the surface). The atmospheric forcing were simulated using ERA5 datasets. The analysed results were 3D arrays of the hydrophysical fields and were compared with both an observation constrained numerical model (Black Sea Reanalysis) and *in situ* data quality controlled of temperature and salinity profiles from EN4. The main results from this chapter are the following:

i) The activation of the light penetration and its good configuration was a crucial condition in representing correctly the CIL. The light attenuation model needs to be spectrally resolved and account for the presence of phytoplankton.

This Chapter demonstrated the key role of the light attenuation model for a good representation of the CIL. By only activating the penetration of light, the basin average temperature during summer was closer to the observations in comparison with the no-light-penetration run (Appendix B, Fig. B20). The best representation of the CIL was obtained by having both the light penetration spectrally resolved and considering the presence of phytoplankton (Light 2 experiment, Fig. 3.12). For the runs that did not account for the presence of chlorophyll *a*, using the coefficient of attenuation (Light 1 experiment) is a better option than having only the light spectrally resolved (Control Run in the light sensitivity experiments) for the simulation of CIL (Fig. 3.12). However, the choice of the light penetration model had no significant impact on the vertical and basin average salinity, but in all the light sensitivity experiments, a salinity trend of 0.003 psu was observed from 2000 to 2010 (Fig. 3.11).

ii) An increase of the mixing in the 3D numerical model helped stabilize the salinity budget.

In addition to the light sensitivity experiments **(i)**, another set of experiments assessed the effect of the mixing scheme (Figs. 3.13 to 3.17) on the thermohaline features of the Black Sea. One major result is the control of the salinity budget through an increase in mixing. Indeed, the

initial drift of the basin average salinity was stabilized by either changing the stability function from CanutoA to Galp (GLS2 experiment) or by increasing the Galperin limit from 0.1 to higher values like 0.267 (GLS3 experiment) or 0.6 (GLS7 experiment). The Galperin value controls how the density stratification limits mixing. By increasing the mixing, it could reduce the SST and consequently reduce the evaporation leading to a better stability of the salinity. Among the three configurations that stabilized the salinity (GLS2, GLS3 and GLS7), the simulated temperature from the configurations GLS2 and GLS7 showed the best agreement with the model Reanalysis from the Copernicus service and *in situ* data. All the simulations for the sensitivity experiments were done from 2000 to 2010 but the model validation was done over the long time period of 1980 to 2018. Although the configuration for GLS2 + GLS7 showed very good agreement with the Black Sea model Reanalysis in terms of the basin average salinity (Fig. 3.19), it was still disregarded due to a recurring and unrealistic peak in temperature over depth below the CIL. The model was then validated using GLS7 configuration (Galperin limit of 0.6), accepting a modest drift (negative trend) in the basin average salinity. In the study of Dorofeev et al. (2017), they observe an increase in the annual mean of salinity in the upper 200m layer from 1993 - 2012, whereas in our study, a negative trend was observed for the same period (Table 3.10). The absence of data assimilation in our model, and the unconstrained and inconsistent forcing functions (*i.e.* precipitation, evaporation, river inflow and Bosphorus inflow could all be put off balance) might explain such drift in salinity.

iii) The air temperature is shown to affect not only the sea surface temperature, but also the sub-surface temperature inside the CIL. The CIL structure was strongly correlated with the winter sea surface temperature and a disappearance of the CIL was observed in the most recent years, associated with a warming trend.

The results of the sensitivity tests on the effect of the turbulence scheme **(ii)** allowed to choose the best configuration of the model (GLS7) which was then used to analyse long-term variability of the CIL structure (Figs. 3.29 to 3.34). For this purpose, few metrics were used to characterize the CIL and those include: the depth of the minimum temperature, the thickness, the minimum temperature, the average temperature, the cold content and the volume. Because a strong and positive correlation was observed between the annual anomalies of the modeled sea surface temperature and the air temperature (R^2 = 0.96, Fig. 3.28), all the analysis on the CIL structure were done directly using the modeled SST (during winter). The results indicate that colder winter are correlated with a thicker CIL (R^2 = 0.77, Fig. 3.31) and also with a greater

cold content (R^2= 0.71, Fig. 3.34). The long-term changes of the cold content followed similar variations with Dorofeev et al. (2017). A positive correlation (R^2 = 0.70) was observed between the winter SST and the minimum temperature of the CIL but also with the average temperature of the CIL (R^2 = 0.70, Figs. 3.32 and 3.33). Besides that, the long-term analysis revealed a clear positive annual trend of surface temperature of 0.04°C during the period under study (1980 – 2018, Fig. 3.22). The changes in atmospheric forcing affect not only the surface temperature but its effect is also transferred into deeper depth around the CIL. Recent years of the simulation showed a disappearance of the CIL, and this result was also observed in the article of Stanev et al. (2019), who showed that climate change contributed to its disappearance due to warmer winter over the last 14 years, especially after 2010.

iv) The riverine discharge had a strong influence on the volume of the CIL, where a decrease in the river discharge is associated with an increase in the basin average volume of the CIL.

Another major result from this Chapter is the large-scale impact of the rivers on the volume of the CIL. An anti-correlation is observed, where a decrease in the river discharge is associated with an increase in the basin average volume of the CIL (Fig. 3.36). Rivers are normally known for their local effect by being a source of freshwater (favoring stratification) but also by providing high concentration of nutrients. Such signal is noticeable on the surface of the water and can be transported further away from the river mouth. For example, the river signal coming out of the Danube can be measured in the South area of the Black Sea basin (Sur et al., 1994) because of the cyclonic flow of the Rim Current. However, on top of those surfaces changes, the results presented here show that the river runoff has a strong influence on the inner properties of the water column (volume of the CIL) and such influence has been observed basin wide. Despite having no significant trends in the river discharge, the Black Sea basin is sensitive to climate change and a study from Levang and Schmitt (2015) predict in the coming century an intensification of the global water cycle using climate model runs. Therefore, the repercussion on the river discharge might not be negligible. It is possible to speculate that in the scenario of an increase in the river discharge, more nutrients would be directly provided and the volume of the CIL would decrease according to the result of the simulations. We can further hypothesize that by decreasing the volume of the CIL, less nutrients would then be subducted, leading to an increase in the pool available for the biology (directly resulting from the increased riverine inputs and from a reduction in the amount subducted).

Such changes in the thermohaline structure can have significant impact in the exchange of nutrients and biological matter which consequently can affect the dynamics of the ecosystem (Daskalov, 2003). It is therefore important to maintain an effort in understanding and monitoring such changes as they can have drastic and unexpected impact on both the physical and biological component of the Black Sea basin.

“Essentially, all models are wrong, but some are useful. “

--- Box, George E. P.; Norman R. Draper (1987). Empirical Model-Building and Response Surfaces, p. 424, Wiley. ISBN 0471810339.

Chapter 4: Cold Intermediate Layer transformation and formation rates in the Black Sea, diagnosed from a 3D numerical model

4.1 Introduction

As presented in the introduction of the thesis, the Cold Intermediate Layer (later referred as CIL in this Chapter) is an historically well observed layer that is widely detectable over the entire basin (Fig. 4.1). To compare with the hydrographic data from Figure 4.1, a similar map that shows the CIL core depth from the model run (NEMO- BLACK SEA) is presented in Figure C.1 of the Appendix C. The source of its renewal was questionable and this raised disagreements among authors. The motivation to study this layer led to an accumulation of data which agree upon the fact that the CIL has two main origins of formation taking place during winter.

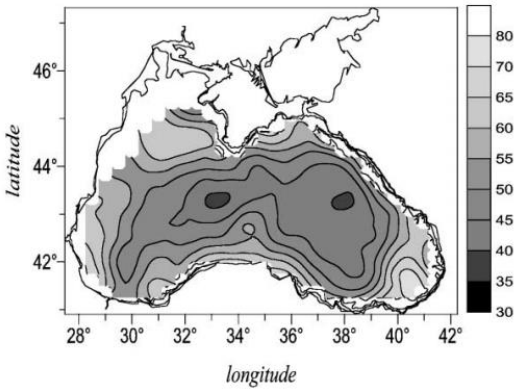

Figure 4.1: Position of the CIL core (in m depth) for May - February, obtained from hydrographic data of the 1980s and 1990s (extracted from Ivanov et al. (2001)).

On the one hand, it can be formed in the center of cyclonic gyres via cooling of the surface waters (Ovchinnikov and Popov, 1984). On the other hand, it can occur in the continental slope of the North Western Shelf, (later referred as NWS in this Chapter) (Sorokin, 2002; Stanev et al., 2003; Shapiro et al., 2011) where the cold water can directly penetrate into the CIL depth and then be spread around the basin by the Rim Current. Quantifying the relative contribution of specific regions in the Black Sea to the CIL volume is not a trivial task, and only a few estimates are available in the literature (*e.g.* Belokopytov, 2004; Stanev et al., 2003). In Stanev

et al. (2003) their estimates underline a strong regional variation. Indeed, the CIL volume formed in the North Western area was estimated to contribute to 62% to the total CIL volume (it splits into 42% continental slope of the NWS and 20% NWS). Those are model based results and the other regional contributions to the total CIL water mass were 28% for both gyres and 10% for the easternmost part of the basin. However, in Polonsky and Popov (2011) (mentioned in Mikaelyan et al. (2013)), the shelf water contribution to the total CIL water mass was less important, with only 16-25%. Miladinova et al. (2018) not only pointed out this inconsistency in the reported estimates, but they also suggested that the choice in the type of datasets could significantly affect the conclusions in regards of the main origin of the CIL. Studies that include both data assimilation and numerical modeling favor the role of the north-western part, whereas climatological data estimated higher or equal contribution of the open sea to the CIL formation. For instance, the study from Belokopytov (2004) is based on climatological data and found the following ratios for the CIL volume: 60% western gyre, 15% eastern gyre and 25% north-western continental slope and NWS. Miladinova et al. (2018) also tried to tackle the question and establish the relative importance of the two sources for the CIL formation by looking at shelf - deep basin exchange of cold-water masses using a passive tracer model. The main mechanisms (*i.e.* cooling of the surface waters in the central basin or transportation of cold-water masses from the NWS by the Rim Current) that controls the refilling of the CIL in the different areas of the basin was also investigated. An example of the tracer result is shown in Figure 4.2.

From March to June of Figure 4.2, it is noticeable that waters from the NWS moves with the Rim Current to the eastern convergence and anticyclonic areas, and participate in their subsequent refilling. Only a small fraction of the tracer is transported to the central part of the basin. They observe that even if the amount of cold-water mass from the NWS that makes up the CIL formation does not change significantly, the mechanism of replenishment of the CIL volume varies in the different parts of the basin. From 1960 to 1981, the western gyre is mainly refilled by the mechanism of transportation of waters from the NWS. However, from 1982 to 2009, there is less cold water from the NWS that reaches the western gyre, as it is instead mainly carried along the Rim Current. Overall, the contribution of the two mechanisms in the refilling of the CIL for the interior Black Sea vary over time and space. But, the mechanism of transportation seems to prevail in the renewal of the CIL along the Rim Current and the south eastern basin. An important take home message from their study is that both mechanisms of

cooling and transportation weakened in the last decade due to the increase in sea surface temperature.

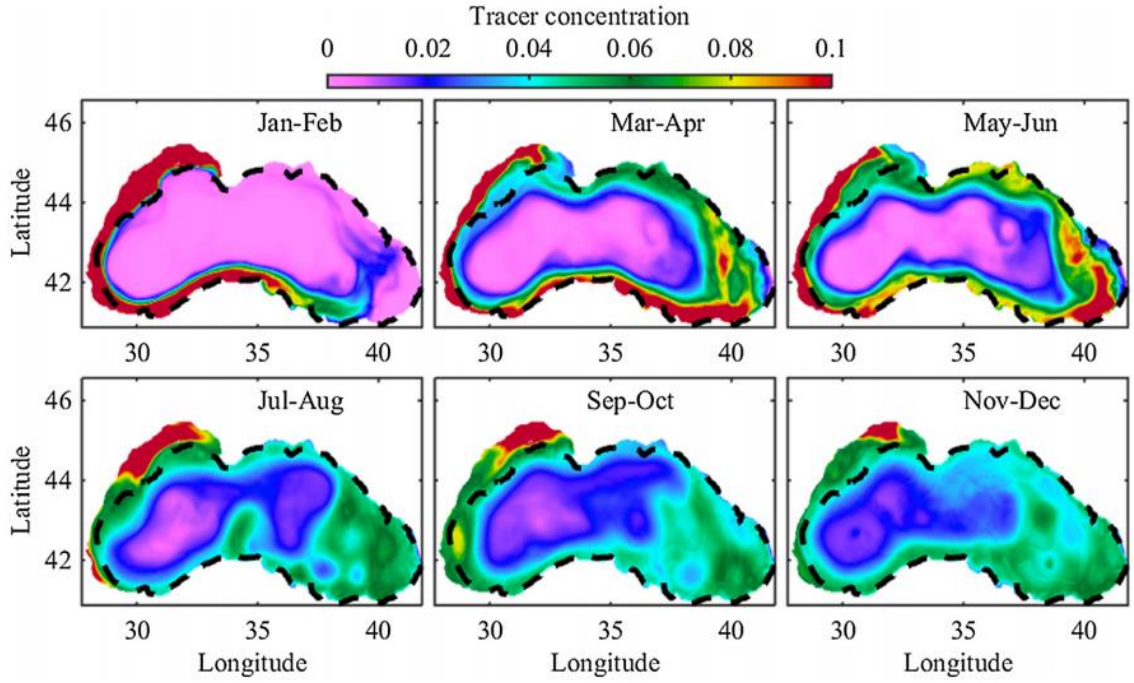

Figure 4.2: Bimonthly mean tracer concentration at 40 m depth in 1996 (extracted from Miladinova et al. (2018)). The dashed line is the 200 m isobaths. The passive tracers are initially injected in the NWS (for latitudes higher than 43°N and depth less than 200m) with concentration of 1 mol m^{-3}. At the beginning of the simulation (*i.e.* start of January), the rest of the tracer concentration is set to 0. The trajectories are then studied throughout the whole basin in a given year.

To characterize water masses and the vertical structure of the water column, density values are better suited than depth levels (Tugrul et al., 1992). Stanev et al. (2003) classify waters belonging to the CIL for densities higher than the threshold of 14.5 kg m^{-3}. A density criteria is then used to diagnose the CIL and we choose its definition by comparing values found in the literature (Table 4.1) with the densities associated with the 8°C threshold in our model (see Section 4.3.1).

In Chapter 3, the ability of the numerical model to reproduce and maintain the CIL over a long period was demonstrated. The first objective in this chapter is to set out the theory of Walin and introduce the diagnostics used to study the CIL water mass transformation over seasonal and annual time scales, with an emphasis on how surface fluxes (heat and freshwater) drive

diapycnal flow. Despite the focus on surface fluxes, the role of mixing is indirectly evaluated here. The second objective is to assess the regional contribution (Coastal versus Deep regions) of the surface fluxes to the volume of the CIL. Finally, the link between the formation rates and global climatic indexes as drivers of the interannual and decadal variability is also studied. The first section presents the diagnostic framework (Walin) used to look at water mass transformation. The second section shows the results regarding the annual and seasonal diagnostics in water mass transformation and formation rates, with an implicit estimation of the mixing. The last section compares some of the results with literature and discuss the strengths and limitations of the method.

Table 4.1: CIL boundaries in terms of density as used in the literature.

References	**CIL density range (σ_θ, kg m^{-3})**	**Regions**	**Type of data**	**Period**
Murray et al. (1991)	14.6 - 14.7	Central western basin	*In situ*	16 April to 29 July 1988
Ivanov et al. (2001)	14.61 14.8 14.3	Center of western gyre Western side of the Rim current Convergence of the Rim current	Model 1D	Winter of October 1992 - April 1993
Konovalov and Murray (2001)	15.2 - 15.8 14.5 - 14.6	Lower boundary of the CIL Core of the CIL	*In situ*	Distributed from 1960 to 1995

Table 4.1 (Continue): CIL boundaries in terms of density as used in the literature.

Staneva and Stanev (2002)	>14 - 14.5	Classification of waters at the surface as newly formed CIL	Model (3D)	July 1991 - June 1995
Stanev et al. (2003)	14.3 - 15.5 >14.5	Continental slope General definition	Model (3D) + *In situ*	1991 - 1994
Yunev et al. (2005)	14.5 to 14.6	Core of the CIL (Open Black Sea during warm months)	Typical diagram (see Fig.C.2 in Appendix C)	-
Belokopytov (2011)	14.9 - 15	Core of the CIL at the center of cyclonic gyres	*In situ*	1996 - 2008
Özkan et al. (2012)	14.5	CIL core in the southern Black Sea	*In situ* (see Fig. C.4 in Appendix C)	Distributed from 1960 to 2008
Korotaev et al. (2014)	>14.25	Middle of the main cyclonic gyres	Model (3D)	1971 - 1993
Mikaelyan et al. (2013)	14.3 - 14.9	Core of the CIL, Open water Black Sea (>200m)	*In situ* (see Fig. C.3 in Appendix C)	May to October average from 1970s to 2000s

Table 4.1 (Continue): CIL boundaries in terms of density as used in the literature.

Mihailov et al. (2016)	14.0 - 15.5	General definition	*In situ*	1981 - 1985
Akpinar et al. (2017)	Down to 15.5 14.5 - 15	Cyclonic gyres Rim current periphery	*In situ*	2002 - 2015
Miladinova et al. (2018)	>14	General definition (from Stanev et al. (2003))	Model (3D)	1960 - 2015

4.2 Diagnostic framework: Walin (1982) formalism

4.2.1 Background theory

Iselin (1939) first suggested the concept that a core water mass acquires its basics characteristics in a source region at the surface of the ocean. Since temperature and salinity are known as conservative properties, these characteristics would be changed through processes such as mixing with other water masses. The direct contact of water masses with the atmosphere (air-sea fluxes) and the subsequent effect of turbulent mixing with adjacent seawater elements, creates new density classes, setting up water mass characteristics. The understanding of water mass transformation from one density class to another and the quantification of water mass formation rates was introduced by Walin (1982) and further developed by Speer and Tziperman (1992) for the North Atlantic water masses. A recent review from Groeskamp et al. (2019) defines the water mass transformation as "the mass transport of seawater through a surface with a constant property value". The formalism and equations set out in Nurser et al. (1999) and used in Badin et al. (2010), are detailed in this chapter for the description of the Walin method.

The Walin framework assumes that a volume of fluid ΔV, delimited by two potential density surfaces, ρ and $\rho + \Delta\rho$, outcrop over the sea surface and exit the domain via an open boundary (Fig. 4.3). In this case, the domain considered is the entire Black Sea basin and the open boundary is the Bosphorus Strait, which connects the Black Sea with the Mediterranean Sea. The associated volume flux of fluid spreading out of the Black Sea and bounded by the two isopycnal surfaces is noted $\Delta\psi$. In the diagram, $G(\rho)$ and $G(\rho + \Delta\rho)$ represents the diapycnal volume flux of fluid crossing the potential density surfaces ρ and $\rho + \Delta\rho$ respectively. By convention, G is positive if directed towards increasing ρ (from light to dense).

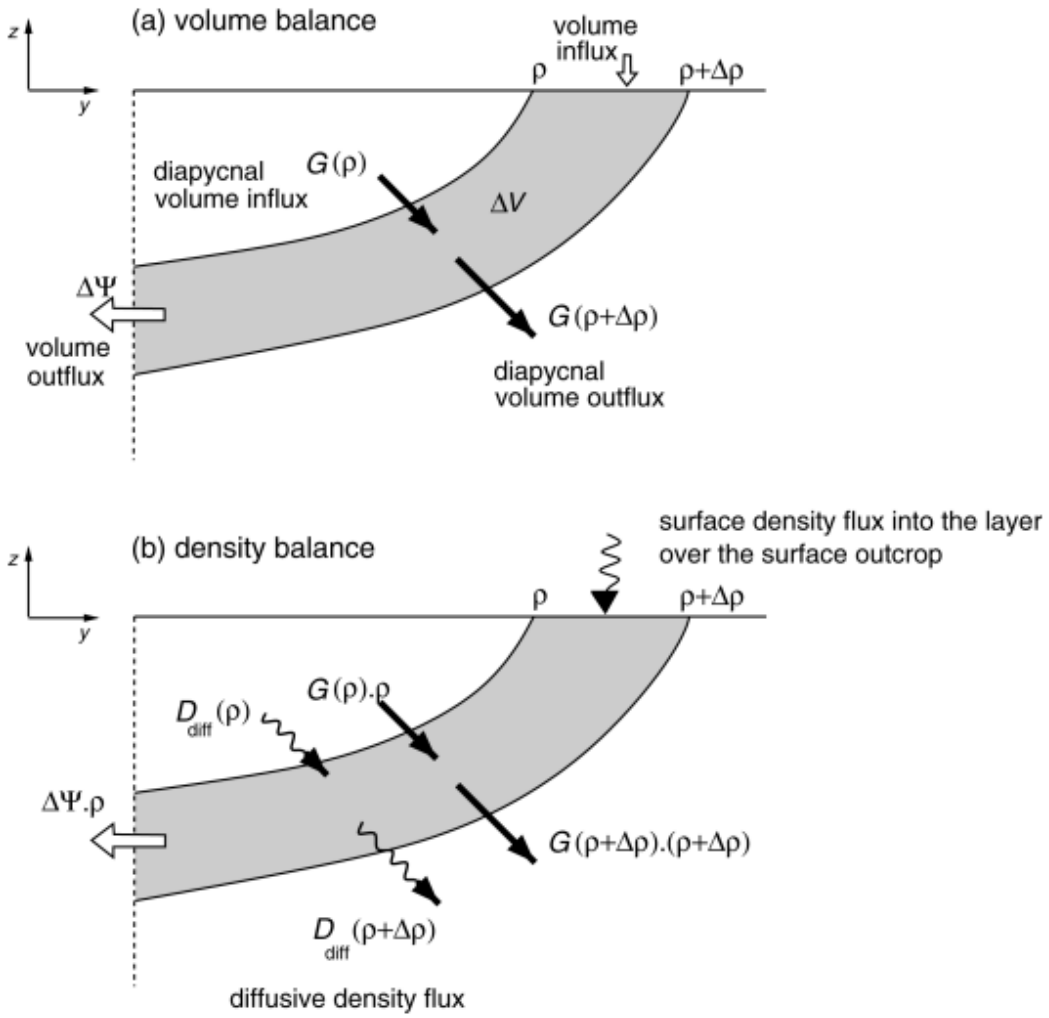

Figure 4.3: Schematic vertical section from Badin et al. (2010). The diagram indicates (a) the volume and (b) density budgets for a volume element ΔV bounded by the density surfaces ρ and $\rho + \Delta\rho$ that outcrop at the surface. In (a), The volume of the layer depends on the divergence of the diapycnal volume flux G, crossing the density surfaces, the volume flux exiting the domain $\Delta\psi$, and the surface influx of freshwater $\Delta\psi_{\varepsilon-P-R}$ (see Table C.1 in Appendix C for the meaning of the variables).

Air-sea fluxes combined with mixing can alter the volume of water between two isopycnals, but this amount of water is constrained by a volume and density budget, detailed in the following sections.

4.2.2 Volume budget

The volume budget is balanced by four main terms: the temporal increase in the volume (ΔV) between two density classes ρ and $\rho + \Delta\rho$, the volume flux out of the domain through the open boundary ($\Delta\psi$), the volume flux entering the domain from surface freshwater inputs ($\Delta\psi_{\varepsilon-P-R}$) and the difference in the diapycnal volume fluxes passing into the layer $G(\rho)$ and out of the layer $G(\rho + \Delta\rho)$:

(Eq. 4.1) $$\left(\frac{\partial \Delta V}{\partial t} + \Delta\psi - \Delta\psi_{P+R-\varepsilon}\right) = G(\rho) - G(\rho + \Delta\rho) = -\Delta\rho \frac{\partial G}{\partial \rho} \equiv M\Delta\rho$$

where the volume fluxes, G and $\Delta\psi$, have units of $m^3\ s^{-1}$.

$M\Delta\rho$ is the water-mass formation rate (see section 4.2.4) and is defined as the rate of accumulation of water between two isopycnals ρ and $\rho + \Delta\rho$ due to the flow through the isopycnal surfaces. The total accumulation is the first term $\frac{\partial \Delta V}{\partial t}$.

4.2.3 Density budget

The density budget of the volume between ρ and $\rho + \Delta\rho$ isopycnals is balanced by advective and diffusive density fluxes:

$$\underbrace{\left(\frac{\partial \Delta V}{\partial t} + \Delta\psi - \Delta\psi_{P+R-\varepsilon}\right)}_{\textit{density gain}} \underbrace{\rho + (\rho + \Delta\rho)G(\rho + \Delta\rho) - \rho G(\rho)}_{\textit{advective density fluxes}}$$

$$\underbrace{= -(D_{diff}(\rho + \Delta\rho) - D_{diff}(\rho))}_{\textit{diffusive fluxes}} \underbrace{+ \int_{outcrop} D_{in} dA}_{\textit{surface flux}}$$

or more concisely:

(Eq. 4.2) $$\left(\frac{\partial \Delta V}{\partial t} + \Delta\psi - \Delta\psi_{P+R-\varepsilon}\right)\rho + \Delta\rho\frac{\partial}{\partial\rho}(\rho G) = -\Delta\rho\frac{\partial D_{diff}}{\partial\rho} + \int_{outcrop} D_{in}dA$$

where D_{in} is the surface density flux into the ocean expressed in kg m^{-2} s^{-1}, integrated in the area across isopycnals and driven by surface heat and freshwater fluxes.

(Eq. 4.3) $$D_{in} = -\frac{\alpha_T}{C_p}\mathcal{H} + \rho_0\beta_s S(\varepsilon - P - R)$$

with α_T the temperature dependent thermal expansion coefficient of seawater, C_p the heat capacity for seawater at constant pressure, $\mathcal{H}$ is the heat flux into the ocean (>0 when directed into the ocean), ρ_0 a reference density, β_s the haline contraction coefficient of seawater, S the salinity and ε and P are respectively the evaporation and precipitation rate. For α_T, C_p and β_s, the functions used to compute them are referred in Table C.1 inside Appendix C.

4.2.4 Water mass transformation (G) and formation (M) rates diagnostics: numerical formalism

The volume and density budget combined (Eq. 4.1 and Eq. 4.2 respectively) and divided by $\Delta\rho$ provides the diapycnal volume flux $G(\rho)$, also called the transformation. This is the volume flux directed across density surfaces, and depends on the gradients in the surface and diffusive fluxes in density spaces:

(Eq. 4.4) $$G = -\frac{\partial D_{diff}}{\partial\rho} + \frac{1}{\Delta\rho}\int_{outcrop} D_{in}dA$$

G is expressed in m^3 s^{-1} and for $G(\rho) > 0$ the diapycnal volume flux transform water from light to denser classes. The water mass transformation then comes either from a convergence of diffusive density fluxes $-\frac{\partial D_{diff}}{\partial\rho} > 0$, or from the effective surface density flux, $\int_{outcrop} D_{in}dA > 0$.

D_{in} drives a water mass transformation $G_{air-sea}$, which is calculated by integrating the surface density flux along surface outcrops (right term of Eq. 4.4). When calculating this from model data, is equivalent to:

(Eq. 4.5) $$G_{air-sea}(\rho_0;\tau) = \frac{1}{\tau}\sum_t \left[\frac{1}{\Delta\rho}\left(\sum_i D_{in}(i;t) \times \prod_{air-sea}[\rho_0;\rho(i;t)]\right) \times dA\right] \Delta t$$

with ρ_0 (in kg m^{-3}) the reference density, $\tau = t_1 - t_0$ is the time interval, i refers to a point coordinate, dA is the area of the grid cell (in m^2) where $dA = dx \times L_y$, dx (m) and L_y (m) are respectively the latitudinal and longitudinal distance between two grid points.

The term $\prod_{air-sea}[\rho_0;\rho(i;t)]$ is defined as:

(Eq. 4.6) $$\prod_{air-sea}[\rho_0;\rho(i;t)] = \begin{cases} 1 \; if \; \rho_0 - \Delta\rho/2 < \rho < \rho_0 + \Delta\rho/2 \\ 0 \; otherwise \end{cases}$$

The formation rate $M_{air-sea}$ is then given by the convergence of the surface transformation rate ($-\Delta\rho\frac{\partial G}{\partial \rho}$) calculated for two different outcropping ispoycnals ρ_0 and $\rho_0 + \Delta\rho$. The quantitative estimation of the formation rate is calculated as followed:

(Eq. 4.7) $$M_{air-sea}(\rho_0 + \Delta\rho/2;\tau) = \frac{1}{\tau}\sum_t [G_{air-sea}(\rho_0 + \Delta\rho;\tau) - G_{air-sea}(\rho_0;\tau)]\,\Delta t$$

with ρ_0 (in kg m^{-3}) the reference density, $\tau = t_1 - t_0$ is the time interval.

The accumulation or destruction of a parcel of water between two isopycnals, and affected by air-sea fluxes, is (Eq. 4.8): $M\Delta\rho = G(\rho) - G(\rho + \Delta\rho)$. It demonstrates that a decrease of the transformation over a certain surface density range indicates water mass formation, whereas an increase would suggest a destruction of the water mass by surface exchanges.

The analysis of the transformation and formation rates was done for three distinct regions of the Black Sea, based on the 200 m isobaths (Fig. 4.4). The total surface area of the Whole, Coast and Deep regions are the following: 4.5x10^{11} m^2, 1.4x10^{11} m^2 and 3.1x10^{11} m^2.

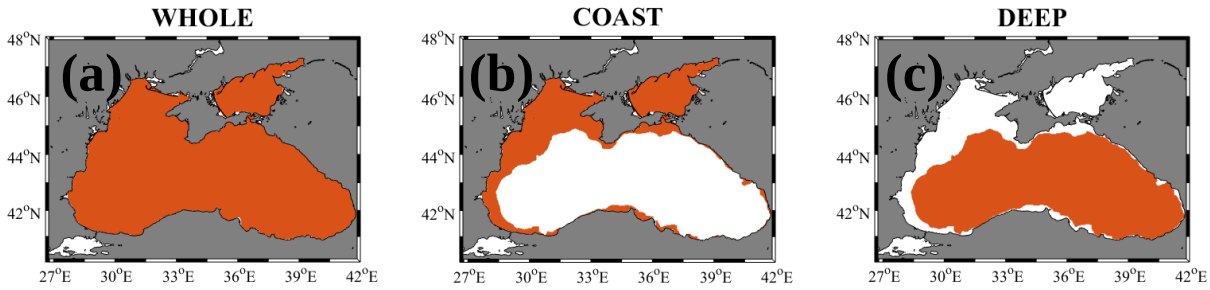

Figure 4.4: Masks coverage used for the Walin diagnostics analysis. (a) The entire Black Sea is considered. The 200 m isobath is used to separate (b) the Coastal from (c) the Deep region.

Most of the estimates are expressed in units of Sverdrup. For information, 1Sv ≡ 10^6 m^3 s^{-1}.

4.2.5 Model (NEMO - BLACK SEA) datasets used for Walin method

The diagnostic elements of the Walin framework are principally based on surface water properties (temperature, salinity) and air-sea fluxes. Monthly datasets of surface fields of temperature and salinity are extracted from the model (NEMO - BLACK SEA, see Section 3.2.3, the method section in Chapter 3) and used to compute surface potential density anomaly σ_θ (kg m^{-3}), defined as $\rho_\theta - 1000$ (also in kg m^{-3}). The surface potential density anomaly (σ_θ) is calculated using the function *gsw_sigma0* from Gibbs SeaWater (GSW) Oceanographic Toolbox of TEOS-10 (IOC, SCOR and IAPSO, 2010) and uses the 75-term expression for specific volume (Roquet et al., 2015). This function uses as inputs absolute salinity (in g kg^{-1}, calculated using the function *gsw_SA_from_SP*) and conservative temperature (in °C, calculated using the function *gsw_CT_from_t*). The conservative temperature takes the place of potential temperature and has the advantage of representing more accurately the "heat content" of seawater. The heat and freshwater fluxes, that makes up the density fluxes, are output from the model with the units of respectively W m^{-2} and kg m^{-2} s^{-1}.

The analysis emphasizes the study of the particular water mass that is the CIL. The densities associated with the 8°C threshold from the model were investigated. T-S profiles were then randomly selected inside two regions of the Black Sea (Western and Eastern Gyre). In each region, a total of 400 profiles were investigated in order to capture the main features of the CIL

from the model. For each profile, the portion (*i.e.* lower/upper boundaries and core) of the T-S curve which describes the properties of the water mass (CIL) was then extracted in terms of density values. This analysis is done to assess and choose the density-based definition of the CIL and see how it compares with the literature values.

The analysis uses the New Reference run presented in Chapter 3, *i.e.* the one including the changes decided by the sensitivity tests.

4.2.6 Climatic indexes

To look at the interannual variability, the formation rates (Eq.4.7) rather than the transformation rates (Eq.4.5) are used. The temporal variability of the formation rates extracted from the Walin method may be linked to changes in heat fluxes due to global atmospheric patterns. To understand what drives the variability in those rates, the link with climatic indexes was studied. Three different climate indexes were used, namely the North Atlantic Oscillation (NAO), the East Atlantic/ Western Russia (EA/WR) and the Multivariate ENSO index (MEI). The definition of these indexes was already introduced in Chapter 2. Monthly average values of these indexes are produced by the National Oceanic and Atmospheric Administration (NOAA) Climate Prediction Center. The exact link of the data for the NAO and EA/WR is the following: https://www.cpc.ncep.noaa.gov/data/teledoc/telecontents.shtml. The raw data of the monthly time series of NAO and EA/WR from 1980 to 2018 are shown in the Appendix A (Figs. A.2 to A.4). For both the NAO and EA/WR, the indices have been standardized by the 1981 - 2010 climatology. The MEI index is an assessment of ENSO and combines both oceanic and atmospheric variables and was downloaded in the following link: https://www.esrl.noaa.gov/psd/data/correlation/meiv2.data.

4.3 Results

In this section, the density values that defines the CIL from the model (NEMO - BLACK SEA) are first presented. Then, all the steps leading to the assessment of the transformation and formation rates from the Walin method are described and illustrated in details for the year 2018. This is then expanded to all the individual years from 1980 to 2018 for the study of the interannual variability in the diagnostics from the Walin method.

4.3.1 Example of T-S diagram from the model

An example of modeled temperature and salinity profile over the entire water column for the western Black Sea is depicted in Figure 4.5.

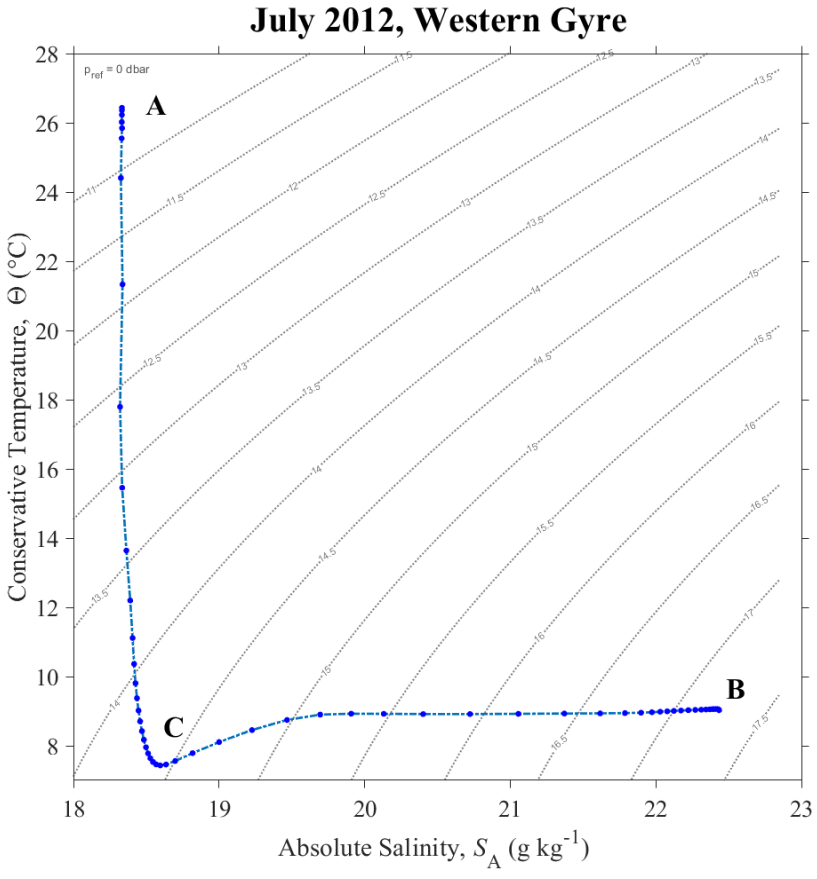

Figure 4.5: T-S diagram from a model location inside the Western Gyre (43.37°N; 30.63°E) for July 2012, with indication of the potential density contours. The diagram is obtained with gsw_SA_CT_plot function from the TEOS-10 toolbox. A indicates the surface waters, B the deep waters and C the CIL.

The month of July is selected to emphasize typical conditions of Black Sea waters during summer time. The surface value of salinity is around 18.52 g kg^{-1} (letter A in Fig.4.5) and reaches the value of 18.58 g kg^{-1} at the depth of the CIL, here located around 76.11 m (letter C in Fig.4.5). The bottom of the water column reached at 1583 m depth has a salinity of 22.42 g kg^{-1} (letter B in Fig.4.5). In the upper part of the profile, there is a strong decrease in the conservative temperature, going from the surface value of 26.63°C to the minimum value of 7.61°C in the CIL core. The right side of the diagram is marked by an increase in the conservative temperature, reaching the maximum value of 9.05 °C at the bottom of the water column. The potential density goes from around 10.5 kg m^{-3} at the surface to 17.25 kg m^{-3} at the bottom. The profile has an L - shape, suggesting weak mixing between A (the surface water) and B (the deep waters). Similar variations were described in Murray et al. (1991) for a profile in the central western gyre during June 1988 (see Fig.C.5 in Appendix C).

The CIL density criteria was not obtained by looking at only one profile of temperature and salinity, but instead, 400 profiles were used to have a better representation of the density range of the CIL. To explain how the values in Table 4.2 were obtained, we take for example the value of lower CIL in the Western Gyre of the Year 2006. Inside the Western Gyre, a total of 400 profiles of T-S were randomly selected inside the Western Gyre. For each profile, the three main boundaries of the CIL (lower, core and upper) were defined and their associated density was calculated. Then, all the densities values for the lower part of the CIL were averaged among the 400 profiles, and this was also done for the core and upper CIL. This was repeated for all the other months of 2006 (giving a total of 12 densities values for the lower CIL) and the annual average was computed, giving a single value reported in Table 4.2. The years 2006 and 2012 were used to assess the density definition of the CIL because in Chapter 3, those years were characterized with a high volume of CIL.

Table 4.2: Comparison of potential density anomalies (kg m^{-3}) of the CIL boundary for different regions in the Black Sea, obtained using 400 individual profiles of temperature and salinity from the model (NEMO - BLACK SEA) and averaged for each month over the example year.

Regions	Lower CIL	Core CIL	Upper CIL
YEAR 2006			
Western Gyre	14.53	14.38	14.28
Eastern Gyre	14.58	14.47	14.36
YEAR 2012			
Western Gyre	14.55	14.41	14.29
Eastern Gyre	14.53	14.43	14.38

Considering both the years 2006 and 2012, the results give an average of 14.55 kg m^{-3} for the lower CIL, 14.42 kg m^{-3} for the core, and 14.33 kg m^{-3} for the upper CIL. Those results fit inside the range of 14 - 15.5 kg m^{-3} from the literature (see Table 4.1).

In the following analysis, the range of 14 - 15 kg m^{-3} is then used as delimitation of the CIL boundaries. Because the density bin used for the analysis equals 0.5 kg m^{-3}, this splits the CIL range into two part: [14.0 - 14.5] kg m^{-3} and [14.5 - 15.0] kg m^{-3}.

4.3.2 Surface potential density and outcrop areas of the CIL

Two years (2018 and 2016) are used as examples to illustrate the outcrop areas of the CIL for the range of potential density anomalies 14.0 - 14.5 kg m^{-3} (Figs.4.6 and 4.7).

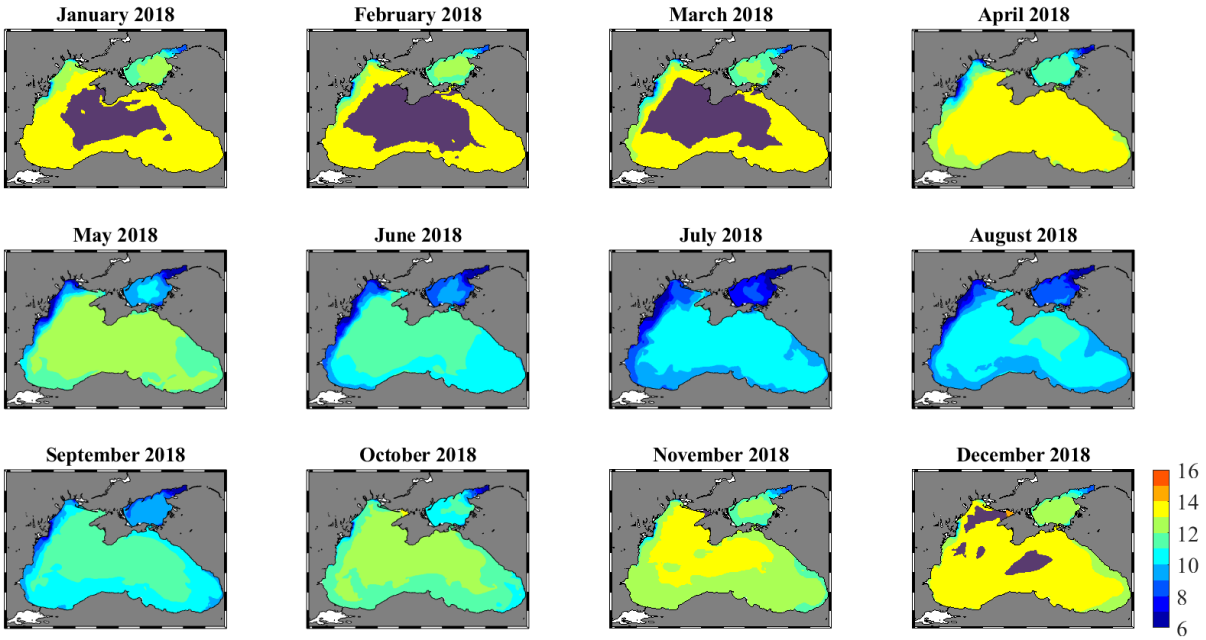

Figure 4.6: Monthly maps of surface potential density anomaly (σ_θ, kg m^{-3}) for the year 2018 obtained from the model (NEMO - BLACK SEA). The overlapping mauve color indicates the areas with values between 14.0-14.5 kg m^{-3}.

The highest surface potential density anomaly (σ_θ) are observed in the deep basin during the winter period with values in the range of 13 - 14 kg m^{-3}. The lowest σ_θ are observed along the northwestern coast (signature of the river inputs) and in the Azov Sea, especially during the summer months (July - August 2018). In summer, the deep basin has values of σ_θ around 10-12 kg m^{-3}. The CIL is represented in mauve on top of the maps in Figure 4.6, and it does not outcrop at the surface from April to November 2018. It can be detected only during the winter period. In January 2018, it is located in the central part of the basin and progressively spreads out until March 2018 towards the Southern area of the shelf break and towards the eastern side of the basin. In December 2018, the CIL outcrop is more fragmented and restricted to the northern part of the NWS and in the middle of the basin.

The outcrop of the CIL with the density class of 14.0-14.5 kg m^{-3} for 2018, is detected mainly during January - March. In comparison, the outcrop regions for the year 2016 is presented in Figure 4.7.

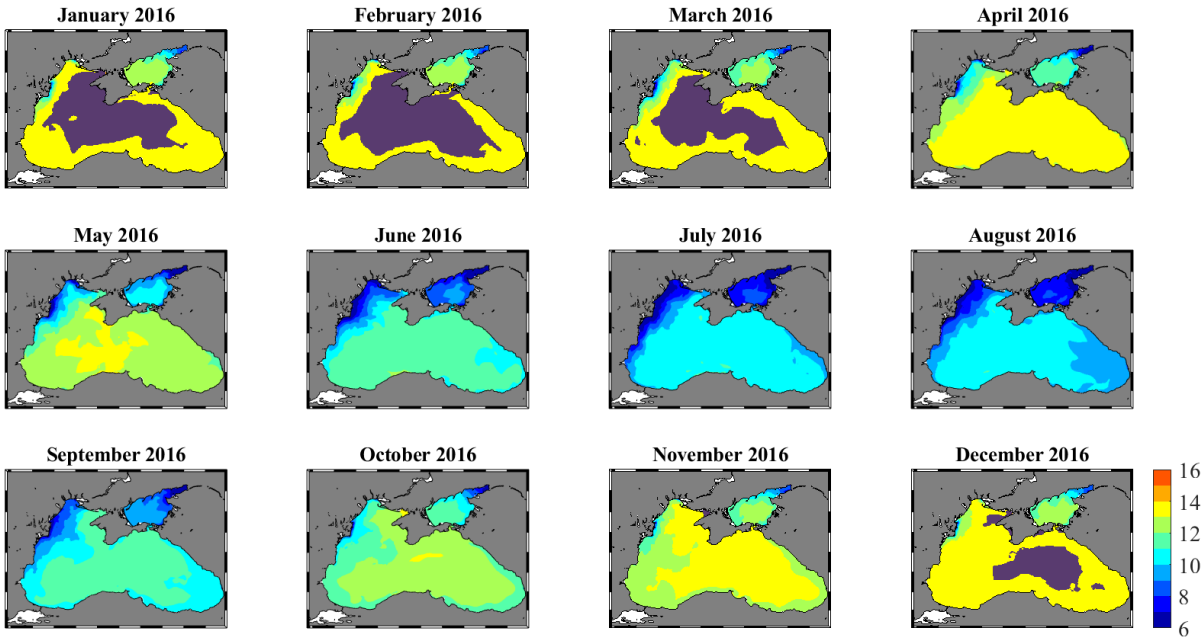

Figure 4.7: Monthly maps of surface potential density anomaly (σ_θ, kg m^{-3}) for the year 2016 obtained from the model (NEMO - BLACK SEA). The overlapping mauve color indicates the areas with values comprised between 14.0-14.5 kg m^{-3}.

The temporal appearance of the CIL outcrop is similar to what was described for the year 2018. It is still happening during the winter time from January to March and in December. For both the years 2016 and 2018, the month of February has the highest surface of CIL outcrop. In contrast, December presents the lowest winter coverage of CIL outcrops for both years.

4.3.3 Surface fluxes (heat and freshwater)

The air-sea fluxes components for the year 2018 are described in this section.

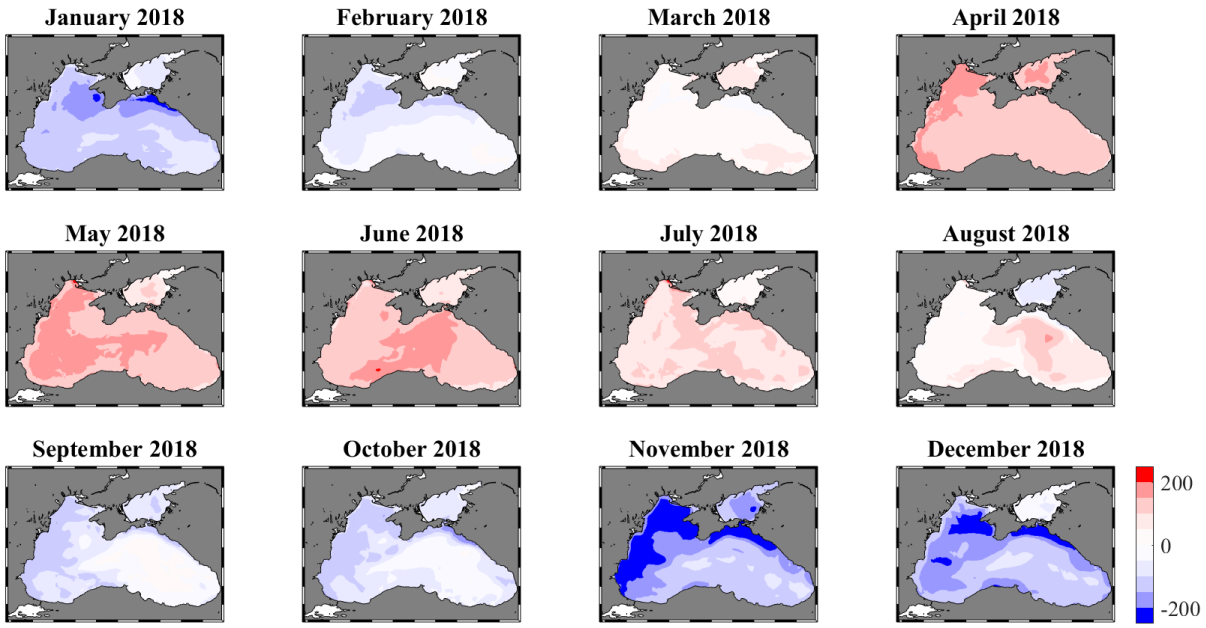

Figure 4.8: Monthly surface maps of heat fluxes (W m^{-2}) obtained from the model (NEMO - BLACK SEA) for the year 2018. Positive values correspond to heat flux into the ocean.

From April to June 2018, the heat flux inside the basin is between 100 - 200 W m^{-2}. In July and August, the flux is still going into the ocean but has lower values, in the range of 0 - 150 W m^{-2}. In September and October 2018, the flux is mainly out of the ocean, going down to -150 W m^{-2} in the western part of the basin. The values tend to decrease in magnitude towards the center and eastern part of the basin. The minimum values are observed in November and December, mainly along the NWS and around the Kerch Strait (connecting the Azov Sea with the main Black Sea basin) with values below -200 W m^{-2}. The same range of annual variation in the heat flux, going from -300 to +200 W m^{-2} was described in Stanev et al. (2003) (see Fig.C.6 in Appendix C). Based on the sign of the heat fluxes, they define the period from September until February (heat fluxes out of the ocean) as the cooling season whereas March to August is the warming season (heat fluxes into the ocean).

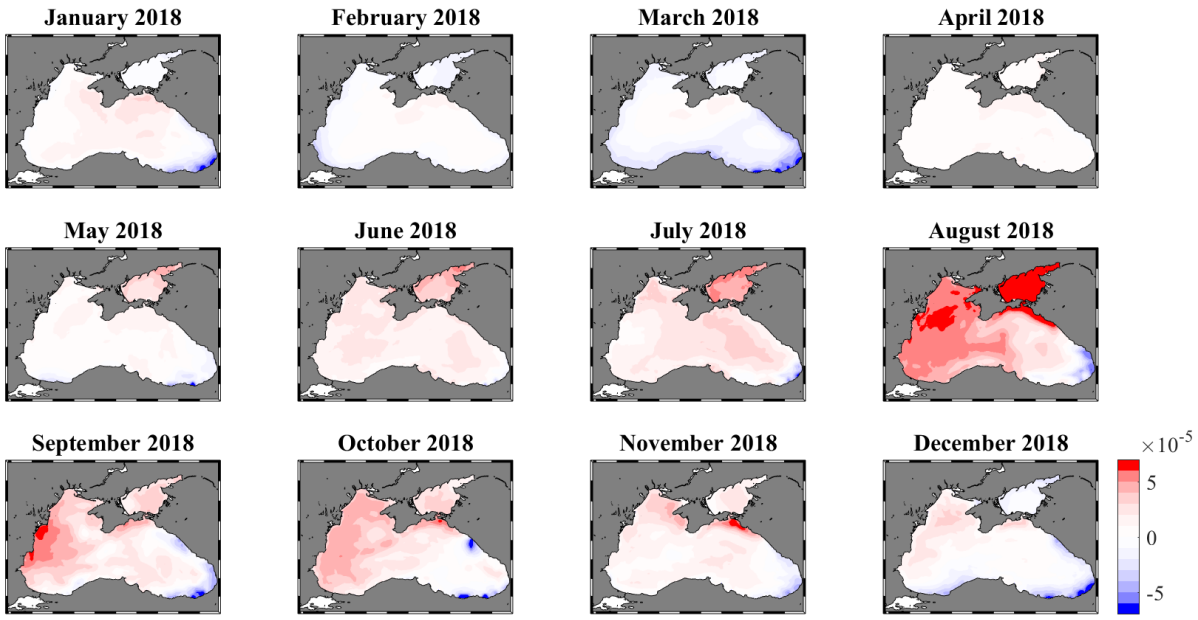

Figure 4.9: Monthly surface maps of freshwater fluxes (kg s^{-1} m^{-2}) obtained from the model (NEMO - BLACK SEA) for the year 2018. Positive values indicate a flux out of the ocean, *i.e.*, evaporation is larger than precipitation and runoff.

The freshwater fluxes reach maximum values in August 2018 in the Azov Sea (around +7.5x10^{-5} kg s^{-1} m^{-2}) and in the western area of the Black Sea basin (> 5x10^{-5} kg s^{-1} m^{-2}). The minimum values are localised and observed in the eastern most part of the basin in January, March, September and December, with values going below -6x10^{-5} kg s^{-1} m^{-2}.

4.3.4 Surface density fluxes

The density bin used here equals 0.5 kg m^{-3}. The surface density fluxes obtained from equation 4.3 for the year 2018 are described in this section. The surface fluxes of heat and freshwater determine the surface density flux. It is worth mentioning that the figures presented in this section do not always use the same scale.

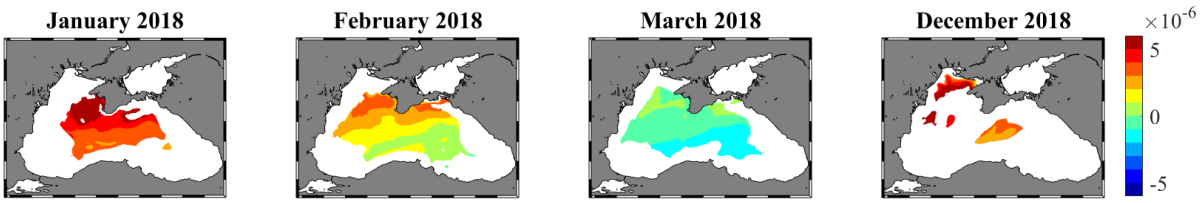

Figure 4.10: Surface density fluxes (D_{in}, kg s^{-1} m^{-2}) with heat and freshwater contributions for the outcrop density class of 14.0 to 14.5 kg m^{-3}. Only the results for the months when the CIL outcrop are represented. Positive values correspond to flux out of the ocean.

In Figure 4.10, white areas indicate that the studied density class does not outcrop at the surface. Flux out of the ocean values are observed for January, February and December 2018. The highest average of the density flux is observed for January and December, with values greater than $3x10^{-6}$ kg s^{-1} m^{-2}. In March, the surface density fluxes are mainly into the ocean, going down to $-2x10^{-6}$ kg s^{-1} m^{-2}.

The heat and freshwater components to the density fluxes were also separately estimated (Figs. 4.11 and 4.12). For example, to assess only the heat component to the density fluxes, only the left component of equation 4.3 was considered, which gives:

(Eq. 4.9) $$D_{in} = -\frac{\alpha_T}{c_p}\mathcal{H}$$

In the same way, the freshwater components to the density fluxes considers only the right component of the equation 4.3, leading to:

(Eq. 4.10) $$D_{in} = \rho_0 \beta_s S(\varepsilon - P - R)$$

HEAT ONLY

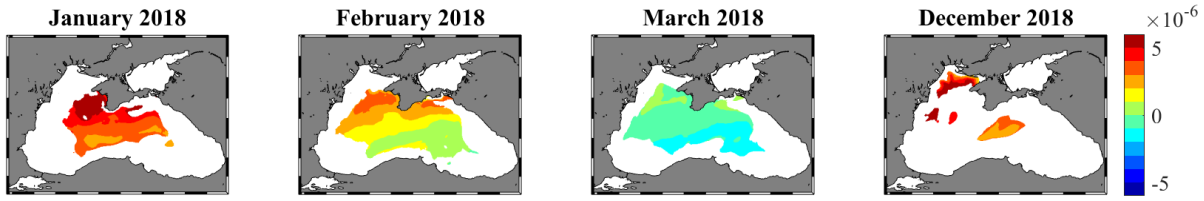

Figure 4.11: Surface density fluxes (D_{in}, kg s^{-1} m^{-2}) with only the heat contribution for the outcrop density class of 14.0 to 14.5 kg m^{-3}. Only the results for the months when the CIL outcrop are represented. The flux is positive when directed out of the ocean.

FRESHWATER ONLY

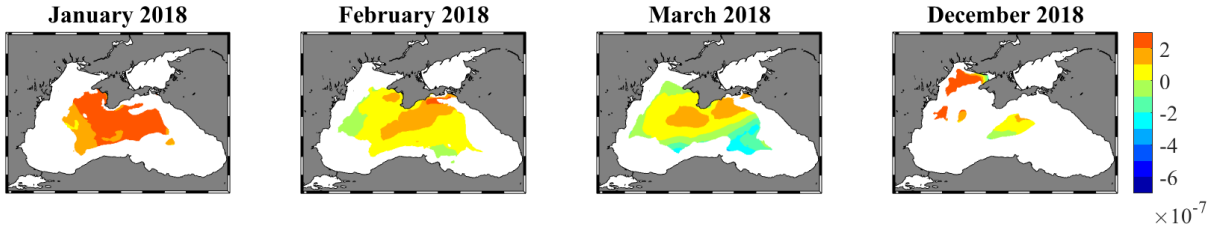

Figure 4.12: Surface density fluxes (D_{in}, kg s^{-1} m^{-2}) with only freshwater contribution for the outcrop density class of 14.0 to 14.5 kg m^{-3}. Only the results for the months when the CIL outcrop are represented. Note change in scale to 4.11. Positive values indicate a flux out of the ocean, *i.e.*, evaporation is larger than precipitation and runoff.

The freshwater components (Fig.4.12) contribute to a density flux that is 10 times lower compared to the heat contribution (Fig.4.11).

4.3.5 Surface water mass transformation (G): Seasonal

The surface densities and the air-sea density fluxes allow the surface water mass transformation to be calculated from equation 4.5, shown in figure 4.13.

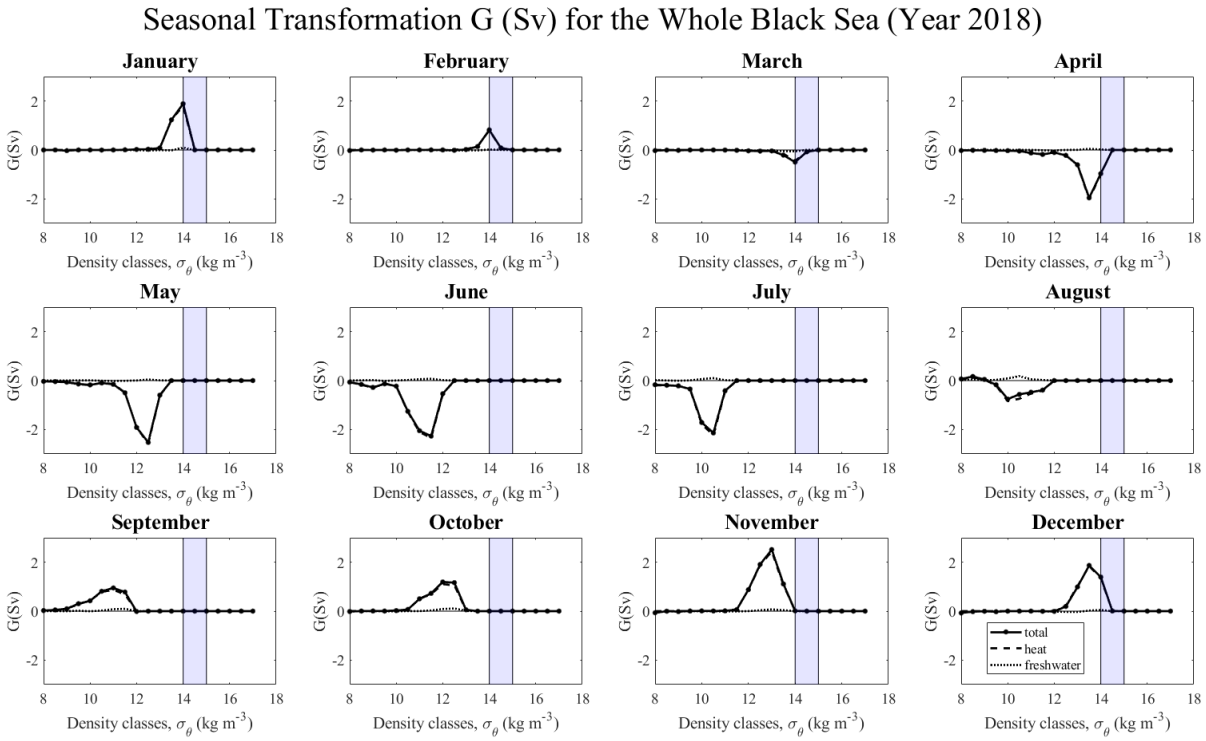

Figure 4.13: Seasonal diapycnal volume flux or transformation rate (Sv, 1Sv ≡ 10^6 m^3 s^{-1}) in density space (bin = 0.5 kg m^{-3}) for the year 2018 over the whole surface of the Black Sea. Positive values represent transformation to denser water. The blue band indicates the CIL density range. The total transformations (solid line) along with the heat (dashed line) and freshwater (dotted line) contributions is indicated.

From April to August 2018, there is an overall negative transformation (lightening) directed from dense to light waters as expected from surface warming. Lightening is minimum in May with a value of -2.53 Sv at 12.5 kg m^{-3}. The intensity of the transformation then decreases throughout summer and is shifted towards lighter density classes. In August 2018, the transformation is around -0.75 Sv at 10 kg m^{-3}. The transformation is then positive in September, with the value of +0.95 Sv at 11 kg m^{-3}. The intensity of the transformation then progressively increases and is directed from light to dense waters. The transformation is maximal in November, reaching around +2.52 Sv at 13 kg m^{-3}. From January to February 2018, the magnitude of the transformation diminishes by the factor 2.3, over the surface density of 14 kg m^{-3}, suggesting an accumulation of water as more water enters this density than flows out (see formation rates in section 4.3.7 for a quantitative estimation).

On seasonal scale, the heat density fluxes contribution (dashed line in Fig. 4.13) principally overlap with the total density fluxes (separated using Eq. 4.9 and Eq. 4.10). The freshwater fluxes contribution is then negligible in comparison to the heat fluxes for the Whole Black Sea.

4.3.6 Surface water mass transformation (G): Annual

The sum of the monthly transformation (Fig. 4.13) provides an estimation of the annual transformation over the year 2018.

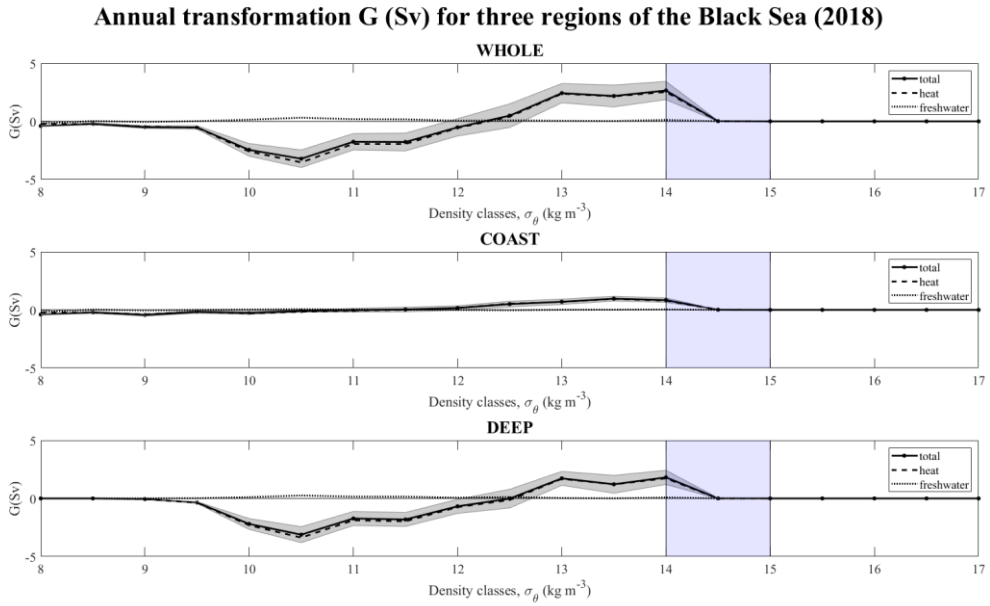

Figure 4.14: Annual diapycnal volume flux or transformation rates (Sv) in density space for three regions of the Black Sea (Whole, Coast and Deep). The grey area represents the standard deviation in the diagnostic for the year 2018. The blue band indicates the CIL density range. The total transformation (solid line) along with the heat (dashed line) and freshwater (dotted line) contributors are indicated.

For density classes strictly lower than 12.5 kg m^{-3}, the annual transformation for 2018 is negative for the three regions analysed. At 10.5 kg m^{-3}, it reaches the minimum values of -3.22 ± 0.76 Sv and -3.12 ± 0.68 Sv for respectively the Whole and Deep regions. For the Coast, the values remain close to 0 Sv. The surface fluxes in this density range tend to create light density waters from denser waters. For the other half of the density range (12.5 - 14. 5 kg m^{-3}), the

transformation is positive for the three regions. In the density range of the CIL, around 14 kg m^{-3}, the total transformation of the Whole area is around 3.2 times more important than in the Coastal area, with the values of 2.65 ± 0.78 Sv and 0.84 ± 0.19 Sv for the whole area and coast respectively. The heat contribution to the transformation mainly coincides with the total transformation.

From the results in Figure 4.14, the transformation rates around the CIL density classes for the Whole Black Sea are positive and can reach ~3Sv, suggesting a volume flux directed from light to dense, mainly driven by the surface heat fluxes.

4.3.7 Formation rate (M): Seasonal

The convergence of the transformation rates in density space gives the formation rate (Fig. 4.15), provided here on a seasonal scale. From the equation of the water mass formation (Eq. 4.8), a negative value of $G(\rho) - G(\rho + \Delta\rho)$ indicates water mass formation, whereas a positive value suggests a destruction of the water mass by surface exchanges.

A positive formation rate is observed in the range of the CIL density for the months of January, February and December (Fig.4.15). The magnitude of the formation rate for the CIL is maximum in January 2018, reaching the rate of 1.89 Sv at 14.25 kg m^{-3}. It then decreases by a factor 2.56 in February. In December, the peak of the formation rate for the CIL is around 1.39 Sv at 14.25 kg m^{-3}. In March and April 2018, the formation rate for the CIL density range is negative, with the respective values of -0.42 Sv and -0.97 Sv. From May until November, the values in the CIL density range are then equal to 0 Sv.

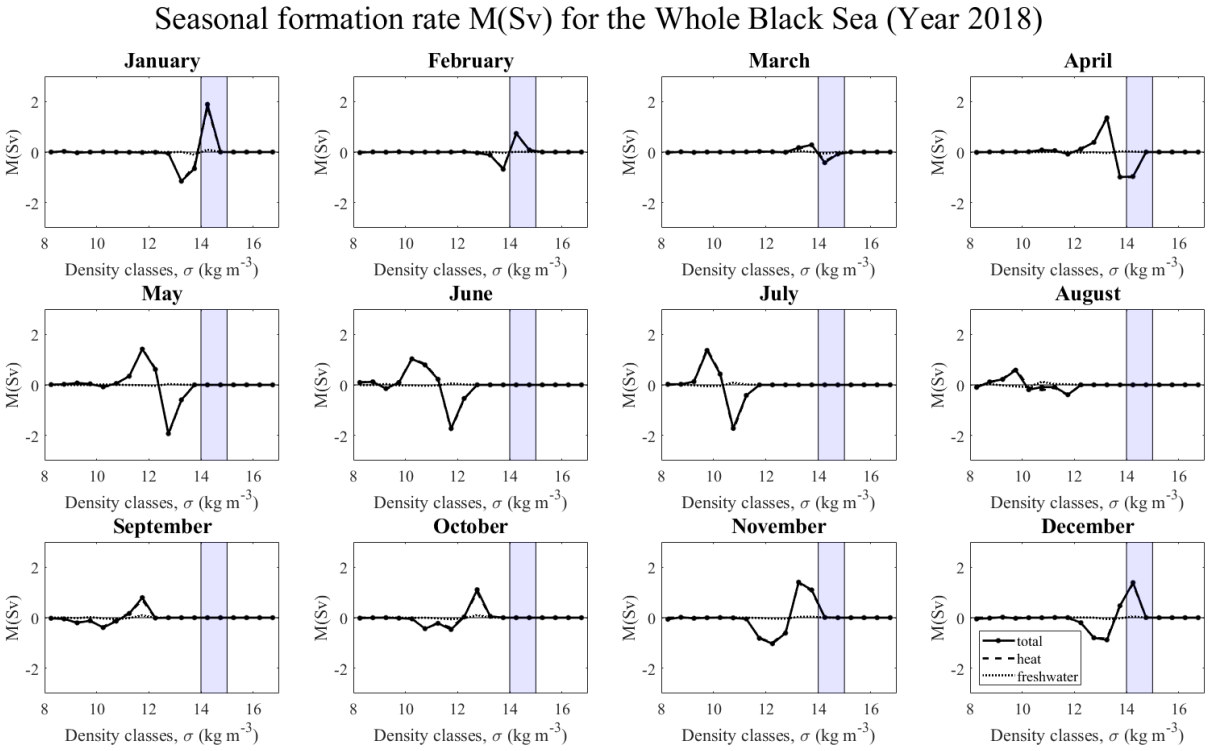

Figure 4.15: Seasonal formation rates M (Sv) in density space (bin = 0.5 kg m^{-3}) diagnosed with the Walin method for the year 2018 over the whole surface of the Black Sea. The blue band indicates the CIL density range. The contributions to the formation rates from the heat fluxes (dashed line), freshwater fluxes (dotted line) and their sum (solid line) are indicated.

4.3.8 Formation rate (M): Annual

The formation rate is also analysed on the annual scale and presented in Figure 4.16.

The formation of CIL is observed with a maximum rate of 2.64 Sv at 14.25 kg m^{-3} for the Whole Black Sea area. For the Coastal area, the intensity of the formation rate reaches only 0.84 Sv, which is around 3.2 times smaller compared to the Whole area. When considering the area of the specific region, the rate for the Whole Black Sea is around 5.81×10^{-12} Sv m^2 and 5.99×10^{-12} Sv m^2 for the Coastal area. The formation rates for the Deep basin, are broadly similar to the ones described for the Whole area, but the CIL rate is around 1.81 Sv.

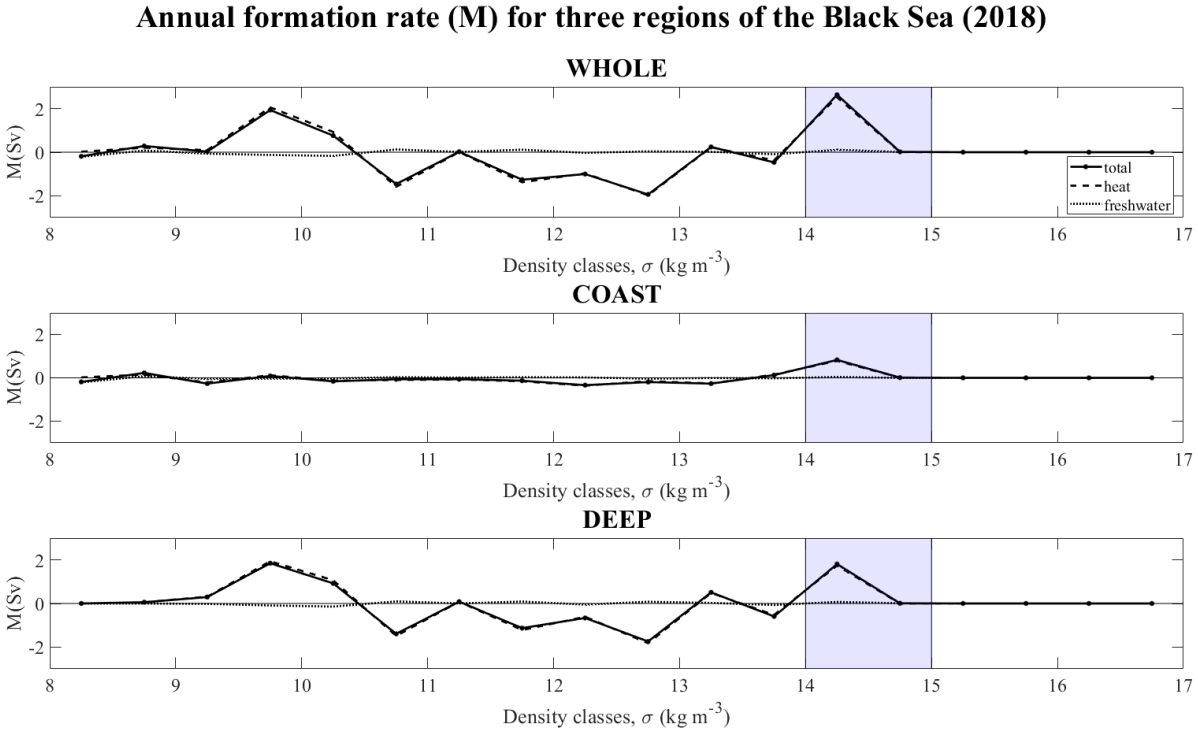

Figure 4.16: Annual formation rates (Sv) in density space for three regions of the Black Sea (Whole, Coast and Deep). The blue band indicates the CIL density range. The contributions to the formation rates from the heat fluxes (dashed line), freshwater fluxes (dotted line) and their sum (solid line) are indicated.

For all three regions, the heat contributions to the formation rates (dashed line, Fig.4.16) overlap with the total values (solid line, Fig.4.16) which suggests that the heat fluxes control principally the formation of CIL at 14.25 kg m^{-3}.

4.3.9 Importance of mixing

Besides the relative role of the surface forcings, another key process that is involved in the water transformation is the diapycnal mixing. Without mixing, the formation rate is obtained from the air-sea fluxes only (Nurser et al., 1999), but this is not a realistic view. Besides that, it is known that the mixing tends to cancel the action of air-sea fluxes over long spatio-temporal scales, *i.e.* when the steady-state is reached (see Fig.4.17 for illustration).

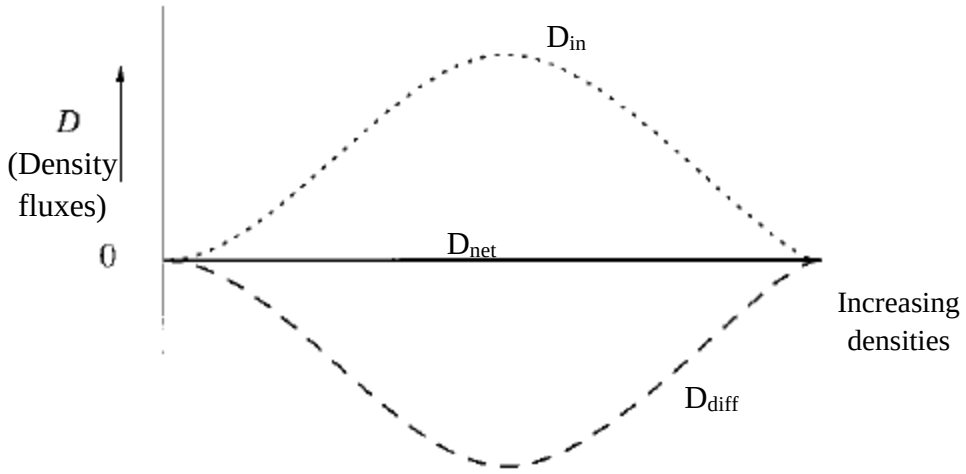

Figure 4.17: Density fluxes for an idealized basin in a steady state. The dotted line represents the surface integrated density fluxes (D_{in}), the dashed line is the mixing component (D_{diff} or mixing) and the net flux (D_{net}) is the black line. Figure extracted from Nurser et al. (1999). The effect of air-sea fluxes is balanced by the diapycnal mixing for a steady state condition.

Estimating the mixing contribution from a model is not always straightforward and is hard to calculate, although this has been done by a few articles (*e.g.* Nurser et al., 1999). Through the Walin formulation, transformation rates due to air-sea fluxes and mixing are linked, allowing one to be deduced from the other. In that sense, the mixing can be inferred based upon the total volume changes minus the water mass formation rates provided by the air-sea fluxes (Badin et al., 2013; Nurser et al., 1999). The difference in volume between the months of January and December of the year 2018, was used to obtain the volume changes for each of the density classes. The results are displayed on Figure 4.18d. It is then possible to infer the total interior mixing within the basin from the total volume change (Fig.4.18d) minus that provided by the air-sea fluxes ($M_{air\text{-}sea}$, Fig.4.18b), and the results are presented in Figure 4.18c.

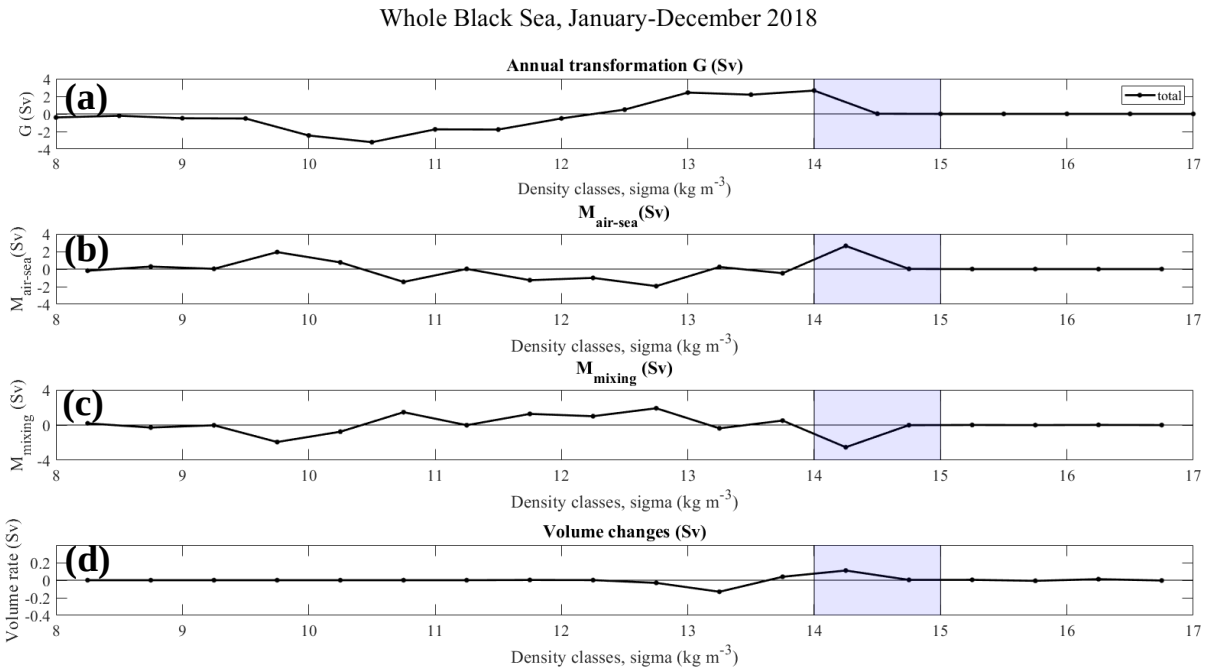

Figure 4.18: Panel plots of quantities averaged over the whole basin and assessed over the whole year 2018, for (a) the annual transformation G (Sv), (b) the formation rate from the air-sea fluxes $M_{air\text{-}sea}$ (Sv), (c) the mixing component M_{mixing} (Sv) and (d) the volume rate of change (Sv). The scale in (d) is different from (a), (b) and (c).

By comparing M_{mixing} with $M_{air\text{-}sea}$, it can be seen that the mixing tends to oppose the action of the air-sea fluxes. At light density classes, *e.g.* at 9.75 kg m^{-3}, the action of $M_{air\text{-}sea}$ (1.93 Sv) is opposed by the effect of mixing (-1.93 Sv) and the associated volume change is close to 0 Sv (Fig.18d). However, for denser density classes, *e.g.* at 14.25 kg m^{-3}, the action of $M_{air\text{-}sea}$ (2.64 Sv) is not entirely opposed by the mixing (-2.53 Sv) and there is a residual in the volume (0.11 Sv). This can be explained by the fact that the Black Sea is not entirely at steady state, but is still quite close to it as most of the volume residuals (Fig. 4.18d) are very close to 0. As a remark, the mixing is inferred from the volume budget and the recent article of Gunduz et al. (2020) show that the part of the Bosphorus flow is quite small. Indeed, the net water transport at the North section of the Bosphorus is around 0.006 Sv from their model (Gunduz et al., 2020), and 0.004 Sv from observations (Altıok and Kayişoğlu, 2015).

4.3.10 Interannual variability

In the previous sections, the diagnostics of the Walin method were illustrated for the single year 2018. All the same calculations were also done for all the other years available from the model outputs, *i.e.*, from 1980 to 2018, which provides a total of 39 years (Fig. 4.19). Only the results for the Whole Black Sea area are presented in this section and the total contribution of heat/freshwater fluxes is considered.

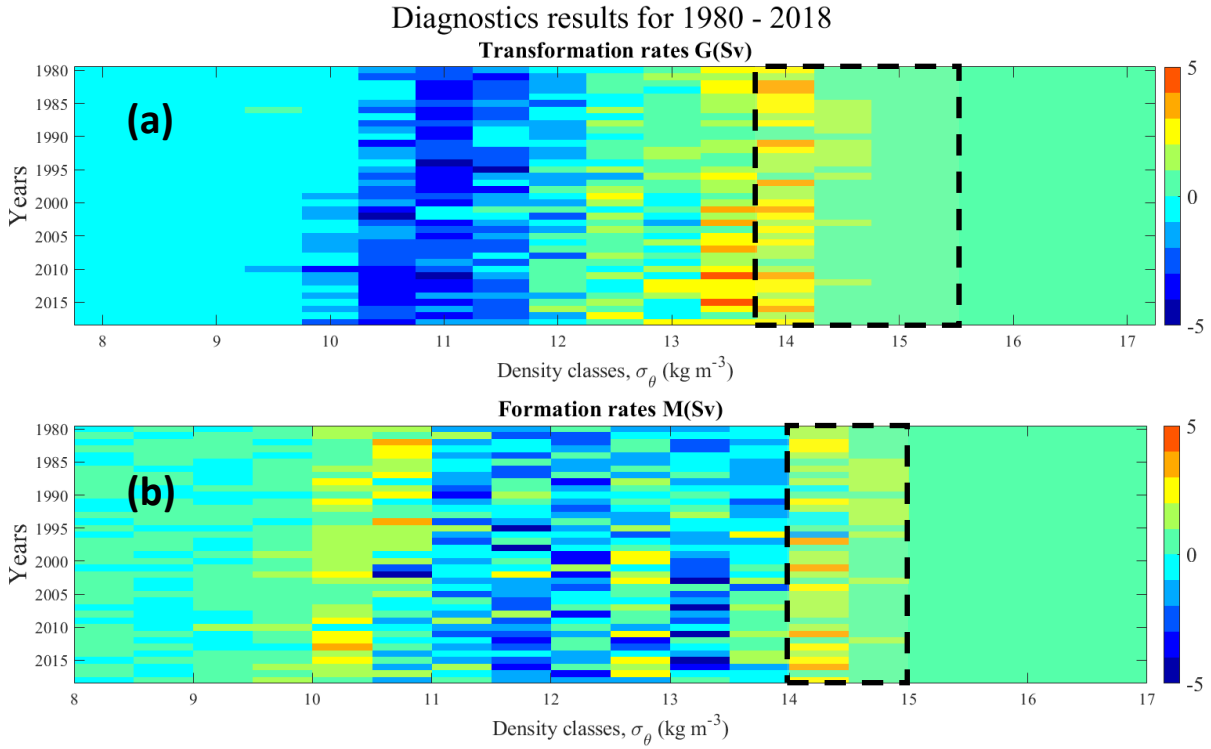

Figure 4.19: (a) Transformation and (b) formation rates (Sv) over the period 1980 to 2018 for the Whole Black Sea, considering the heat and freshwater fluxes together. The black dashed line delimits the CIL density.

The results of the transformation rates show mainly negative values below the density of 12 kg m^{-3}. The highest values are observed for the density of 13.5 kg m^{-3} in the years 2011 and 2015 with the respective values of 5.28 Sv and 4.02 Sv. For the density at 14 kg m^{-3} (indicated within the black dashed line), the transformation rates fluctuate between the minimum value of 0.21 Sv in 1996 and the maximum value of 3.88 Sv in 2016. At 14.5 kg m^{-3}, all the years have a transformation rate below 2 Sv. Then the transformation rate is either null or close to it at 15 kg m^{-3} for all the years shown.

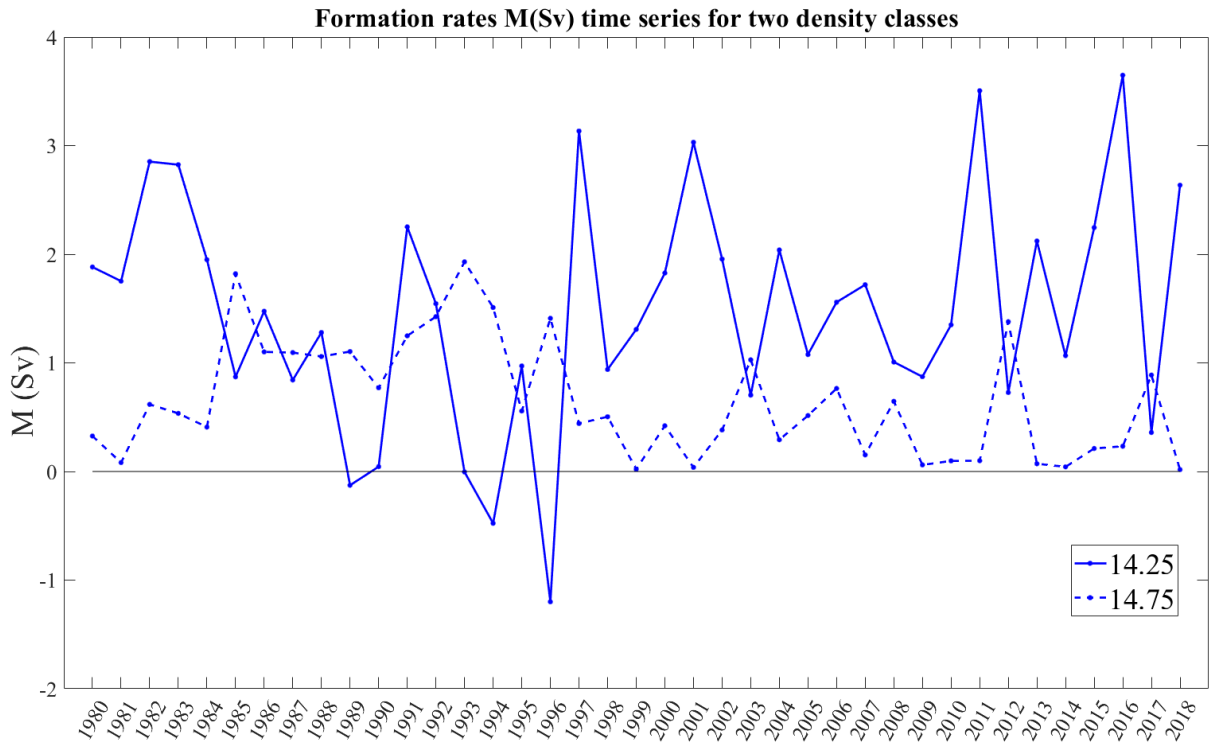

Figure 4.20: Time series of the formation rates M (Sv) for the density classes of 14.25 kg m^{-3} (solid blue line) and 14.75 kg m^{-3} (dashed blue line) from 1980 to 2018. The baseline equals a formation rate of 0 Sv.

The associated formation rates for the CIL shows a strong variability from 1980 to 2018. The formation rates at the density of 14.25 kg m^{-3} and 14.75 kg m^{-3} are extracted and plotted as a time series in Figure 4.20. The annual variations of the formation rates for the density at 14.25 kg m^{-3} (solid line) are first described. The rates are negative for the years 1989, 1993, 1994 and 1996, with the respective values of -0.13 Sv, -0.004 Sv, -0.47 Sv and -1.19 Sv. After the year 1996, the formation rate is always positive, and never goes below the value of 0.4 Sv that is observed in 2017. Several peaks in the formation rate occur and are the most noticeable occur for the years 1997 (3.13 Sv), 2001 (3.03 Sv), 2011 (3.50 Sv) and 2016 (3.65 Sv). Now, the annual variations in the formation rates for the density of 14.75 kg m^{-3} are described (dashed line). Over the whole period from 1980 to 2018, the rates never reach a negative value. Several peaks in the formation rates with values higher than 1.3 Sv occur. They are observed for the following years: 1985 (1.82 Sv), 1993 (1.93 Sv), 1996 (1.41 Sv) and 2012 (1.38 Sv). Otherwise, the years 1981, 1999, 2001, 2009, 2010, 2011, 2013, 2014 and 2018 have values close to the baseline of 0 Sv.

In Chapter 2 and 3, the volume of the CIL was estimated using temperature (<8°C) and salinity ([17.98 - 19.84] psu) criteria. The annual volume of CIL obtained through this method is then compared with the two-time series (solid and dashed blue line in Figure 4.20) of the formation rates obtained in this section.

No correlation was observed between the volume of the CIL and the formation rates at 14.25 kg m^{-3}. However, a significant and positive correlation was observed with the formation rates at 14.75 kg m^{-3}, shown in Figure 4.21, which gives confidence in the value of the Walin approach.

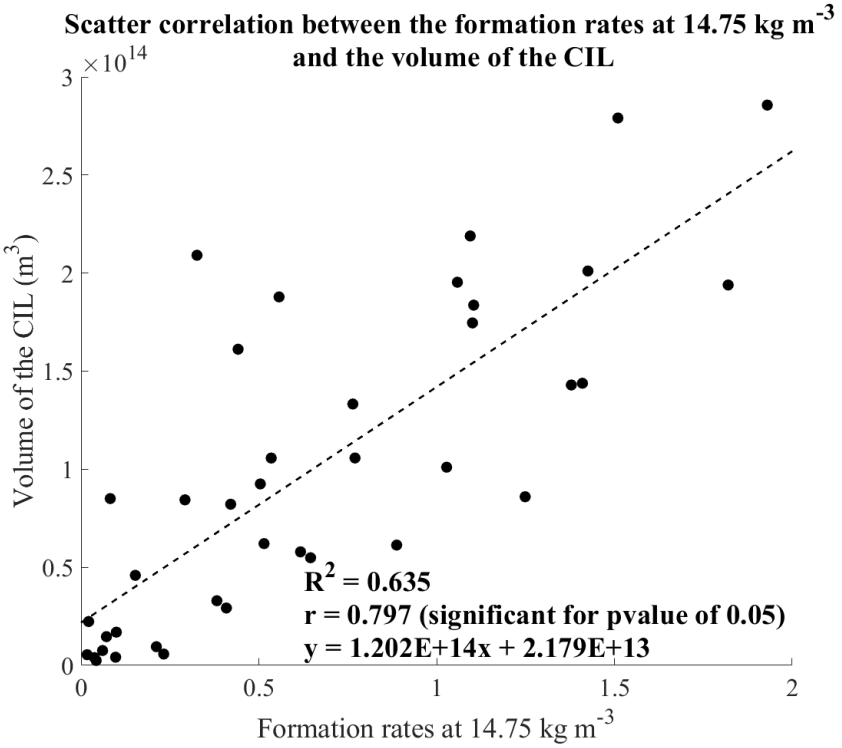

Figure 4.21: Correlation between the formation rates at 14.75 kg m^{-3} and the volume of the CIL.

The link between climatic indexes and atmospheric variables was already analysed in Chapter 3. Here, the link between the variability in the formation rates for the two density classes (14.25 kg m^{-3} and 14.75 kg m^{-3}) and the climatic indexes is investigated.

Over the Whole area, no significant correlation is observed between the annual/winter of all climatic indexes (NAO, EA/WR, MEI) and the formation rates for the density class of 14.25 kg m^{-3}. The formation rates at 14.75 kg m^{-3} are significantly correlated (positively) with the annual/winter EA/WR. They also show a negative correlation with the air temperature

anomalies for both annual (R^2 = 0.40) and winter (R^2 = 0.74) means over the period 1980 - 2018 (Fig. 4.22).

Table 4.3: Values of R^2 between climatic index (NAO, EA/WR, MEI) and Air Temperature (°C) with the formation rates at 14.25 kg m^{-3} and 14.75 kg m^{-3}. Winter period for a specific year goes from January to March and it also includes December from the previous year (DJFM). An asterisk (*) indicates a significant correlation. The data indicated on the left column are results for the Whole Black Sea area, whereas the ones on the right column concern the Coastal area. The sign of the correlation is in parenthesis. For indication, the results for the Deep Black Sea are put in the Appendix C (Table C.2).

Values of R^2 over 1980 - 2018 Whole Black Sea || Coastal area		Annual formation rates at the density classes (kg m^{-3}):	
		14.25	14.75
NAO	Annual	0.003 (+) || 0.010 (+)	0.008 (+) || 0.003 (-)
	Winter	0.0008 (-) || 0.001 (+)	0.009 (+) || 0.00017 (-)
EA/WR	Annual	0.0002 (+) || 0.004 (+)	0.15* (+) || 0.063 (+)
	Winter	0.004 (-) || 0.013 (-)	0.11* (+) || 0.05 (+)
MEI	Annual	0.024 (+) || 0.033 (+)	0.056 (+) || 0.017 (+)
	Winter	0.002 (+) || 0.004 (+)	0.02 (+) || $8x10^{-6}$ (+)
Air temperature (°C) anomalies	Annual	0.01 (+) || 0.002 (+)	0.40* (-) || 0.23* (-)
	Winter	0.23* (+) || 0.17* (+)	0.74* (-) || 0.59* (-)

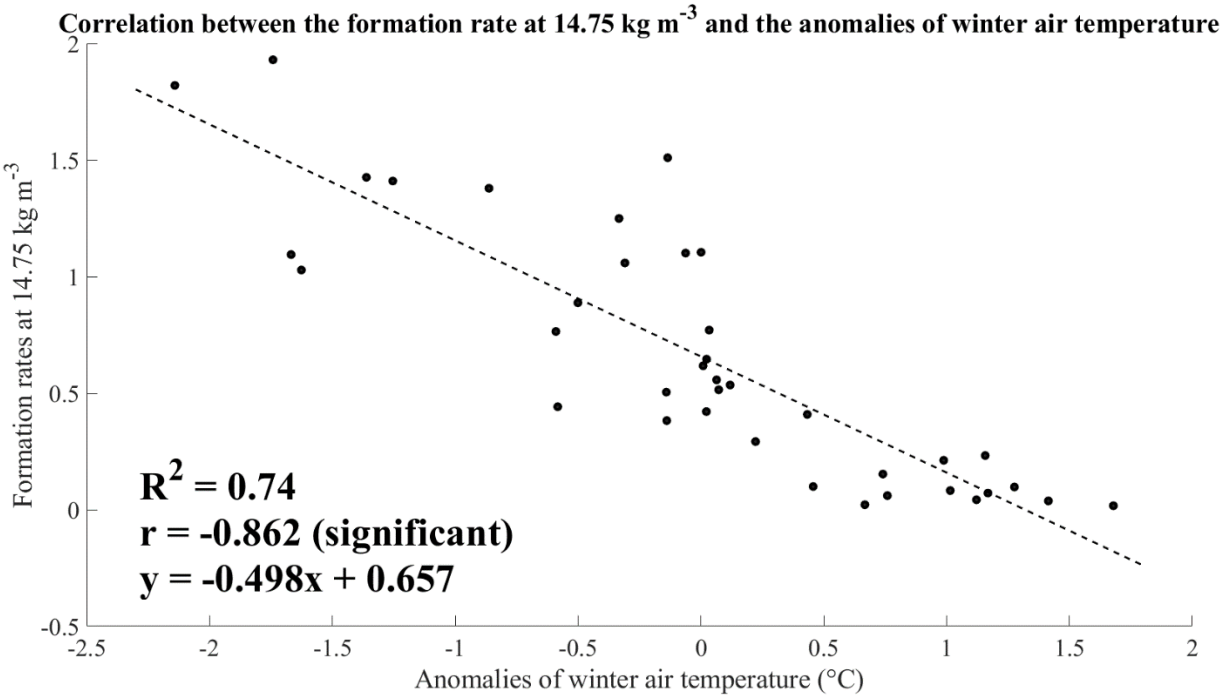

Figure 4.22: Scatter plot of comparison between the formation rate at 14.75 kg m^{-3} and the anomalies of winter air temperature (°C) for the Whole area.

4.4 Discussion

The surface density fluxes (D_{in}) for the year 2018 have been analysed over the outcrop density class of 14-14.5 kg m^{-3}. The freshwater contribution to the surface density fluxes are lower by a factor 10 compared to the heat contribution (Figs. 4.11 and 4.12).

The results of the Walin method at the seasonal scale highlight two main regimes (warming and cooling period). Between April to August 2018, the CIL is not outcropping at the surface and the heat fluxes are positive over the whole basin, being generally above 50 W m^{-2}. In this warming phase, there is an overall negative transformation directed from dense to light densities, with values going from -1.96 Sv at 13.5 kg m^{-3} in April to -0.75 Sv at 10 kg m^{-3} in August. Then, from September until the end of the year 2018, the heat flux is negative, reaching minimum values (below -200 W m^{-2}) in November. During this cooling phase, the transformation is positive, directed from light to dense densities, going from 0.95 Sv at 11 kg m^{-3} to 1.87 Sv at 13.5 kg m^{-3}. The increase in the volume of the CIL is mainly driven by the heat contribution from the air-sea fluxes. The resulting seasonal water mass formation from the

convergence of the transformation rates is positive between 14.0 kg m^{-3} to 15.0 kg m^{-3} for January, February and December. The maximum rate reaches 1.89 Sv at 14.25 kg m^{-3} in January.

The annual transformation diagnosed using air-sea fluxes from the model was compared for the three following regions: Whole Black Sea area, Coast and the Deep basin. For all the three regions, the freshwater contribution to the total transformation is negligible. This suggests that the heat fluxes are the main drivers in the transformation towards dense waters, reaching 2.65 Sv at 14.0 kg m^{-3} for the Whole Black Sea. The formation rates indicate that the Coastal area participate in around a third to the whole CIL formation.

In the following sections, some of the previous results obtained for the year 2018 are discussed and compared with other years.

4.4.1 Differences in the outcrop regions based on the density range

The density bin used in the analysis equals 0.5 kg m^{-3}, which splits the defined CIL ranges into the lighter density part (14.0 - 14.5 kg m^{-3}) and the denser part (14.5 - 15.0 kg m^{-3}). Only the outcropping regions of the lighter range of the CIL were presented in section 4.3.2 for the year 2016 and 2018. It is interesting to look also at the distribution of the outcrop areas of the CIL for the denser part of the CIL. In order to choose adequate years to investigate changes in the outcrop regions in regards to the density class, the interannual variability in the formation rates for the density of 14.25 kg m^{-3} were compared with the denser class of 14.75 kg m^{-3}. For the year 2018, the values at 14.75 kg m^{-3} are near 0 Sv. Some of the highest values of formation rates at this density were observed in 1985 (1.82 Sv), 1993 (1.93 Sv), 2003 (1.03 Sv) and 2012 (1.38 Sv). The period 1984 - 1985 was described with an extremely severe winter (Konovalov and Murray, 2001; Ginzburg et al., 2004). This had a significant impact on the mean temperature of the core of the CIL (Fig. 4.23a). Other unusually cold winters occurred in 1985 and 1993 (Fig. 4.23b; and Kontoyiannis et al., 2012).

(a)

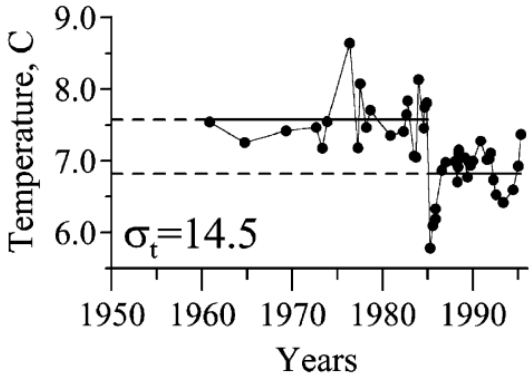

(b)

Character of summer and winter extreme SSTs during the El Niño/La Niña events

El Niño		La Niña	
Date	SST character	Date	SST character
November 1964–December 1966	WS in 1966 WW in 1966	January 1967–July 1968	–
August 1968–April 1970	WW in 1970	May 1970–March 1972	–
April 1972–April 1973	WS in 1972	May 1973–May 1976	CW in 1976
June 1976–April 1978	–	May 1978–July 1979	–
August 1979–April 1981	WW in 1981	May 1981–March 1982	–
April 1982–September 1983	CS in 1982 WW in 1984 CS in 1984 CW and CS in 1985		
August 1986–February 1988	CW in 1987 WW in 1988	March 1988–July 1989	–
October 1989–March 1990, June 1990–November 1995	WS in 1991 and 1992 CW in 1992 and 1993 WW in 1995	December 1995–December 1996	–
February 1997–April 1998	WS in 1998	May 1998–December 2000	WW in 1999 WS in 1999

WS—warm summer, WW—warm winter, CS—cold summer, CW—cold winter.

Figure 4.23: (a) Average temperature (°C) at the density of 14.5 kg m^{-3}, obtained from cruises. Figure from Konovalov et al. (2001). (b) Table from Ginzburg et al. (2004), which indicates the characteristic of the winter for the years 1985 and 1993 (red squares).

Those observations go along with the computed anomalies of the winter air temperature from 1980 to 2018 (see Appendix C, Fig.C.16). The lowest anomaly is observed for the winter 84-85, reaching -2.14°C. The anomalies for the winter 92-93, 02-03 and 11-12 are respectively -1.74°C, -1.63°C and -0.86°C.

Two of the recent years with a positive peak in the formation rates at 14.75 kg m^{-3} (*i.e.* 1993 and 2012) were analysed in terms of the outcrops distributions for the lighter and denser density parts of the CIL (Figs.4.24 and 4.25).

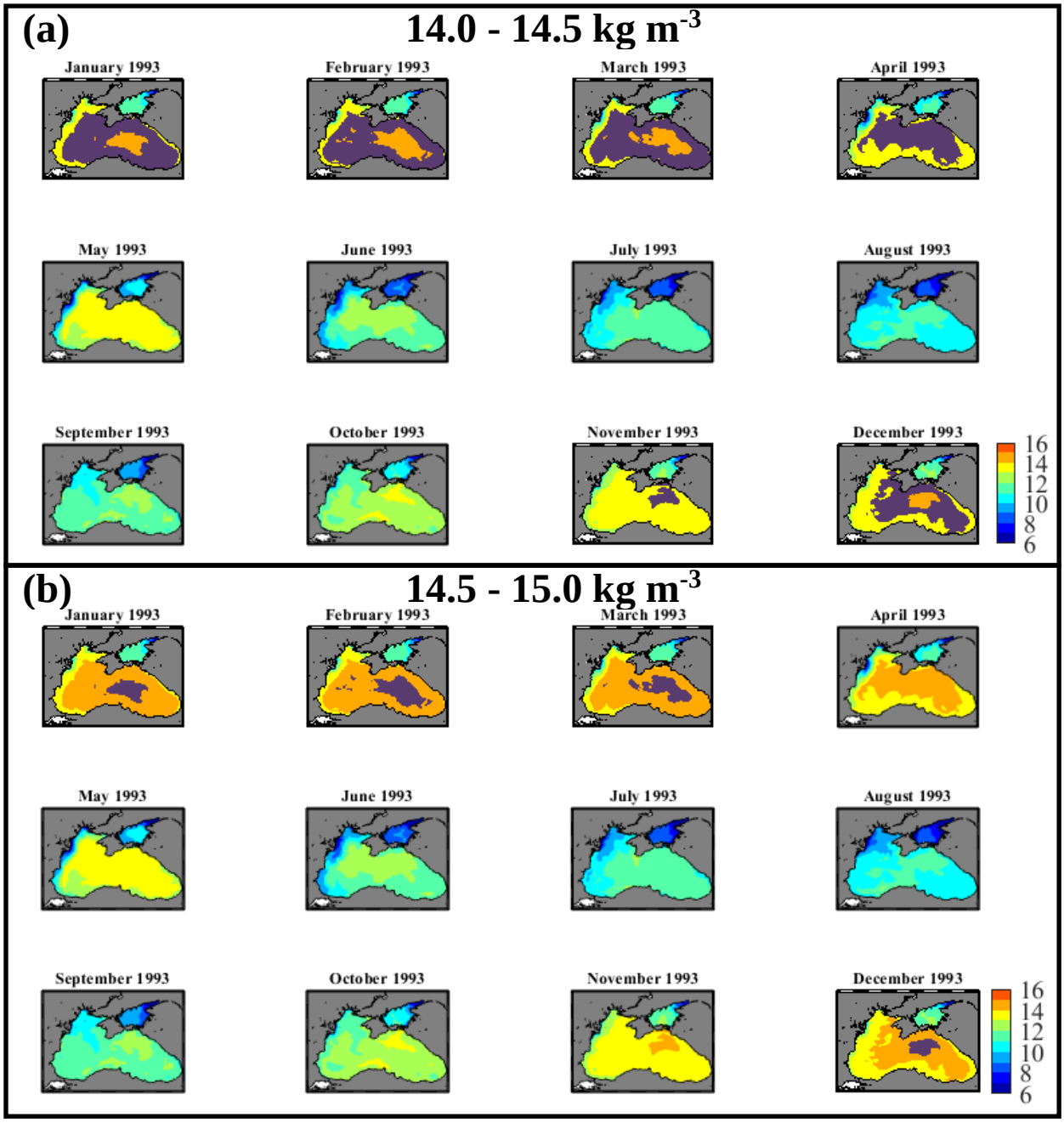

Figure 4.24: Monthly maps of surface potential density anomaly (σ_θ, kg m^{-3}) for the year 1993 obtained from the model (NEMO - BLACK SEA). The overlapping mauve color indicates the areas with values comprised between (a) 14.0-14.5 kg m^{-3} and (b) 14.5-15.0 kg m^{-3}.

The density range of 14 - 14.5 kg m^{-3} for the year 1993 is first described (Fig. 4.24a). From January to March, the outcrop overlaps with the location of the Rim Current and is dominant

inside the western gyre and the southern east part of the basin. Then, in April 1993, the outcrop is more centered in the interior basin in both gyres and follows the continental shelf break of the north western shelf. November 1993 presents outcropping regions in the southern part of the Kerch Strait, which has also been characterised as a region of CIL formation (Ivanov et al., 1997). In contrast, the outcrops of the denser part of the CIL (14.5 - 15.0 kg m^{-3}) in Figure 4.24b, owns a reduced coverage and are mainly observed in the center/eastern areas of the basin.

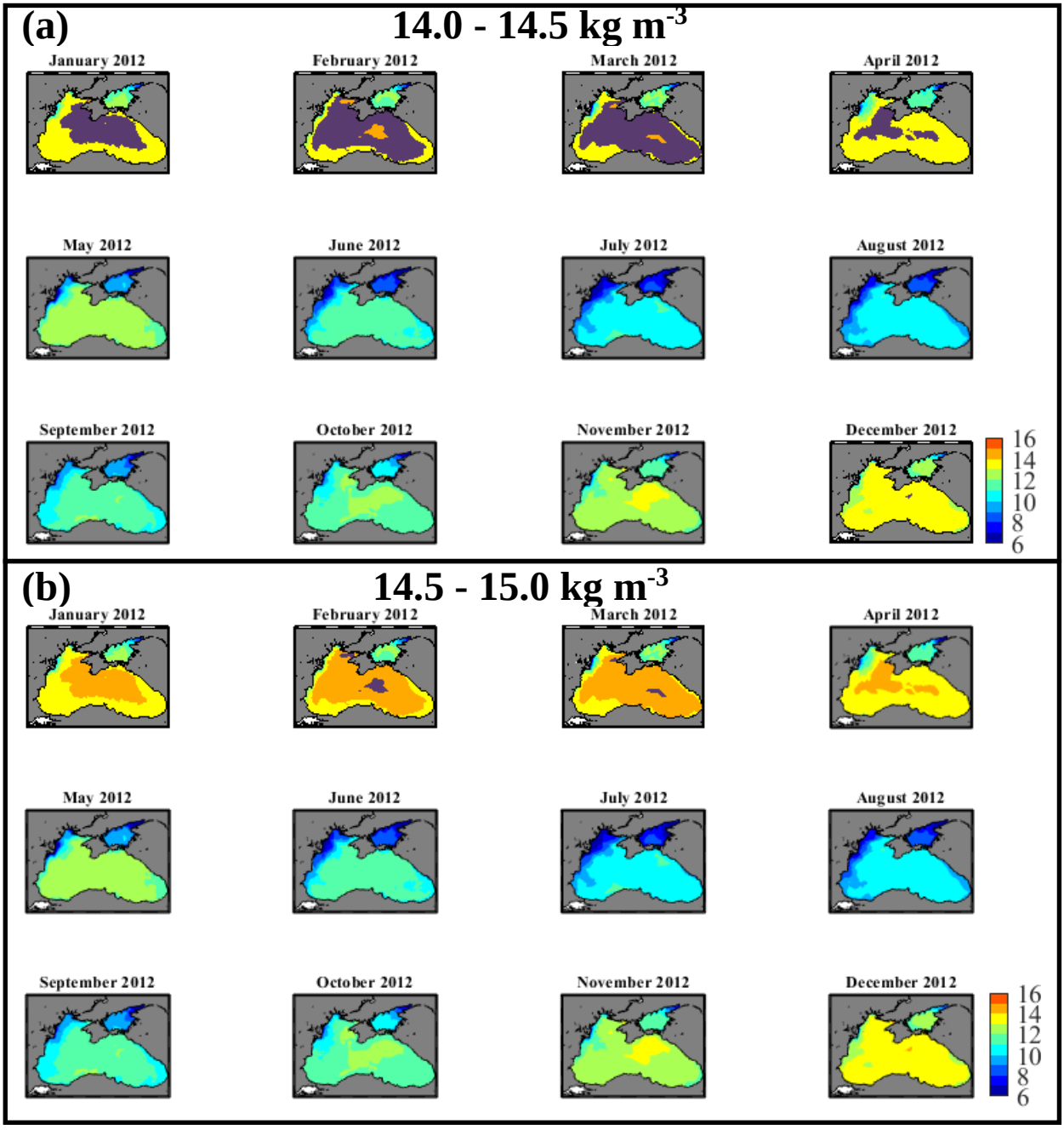

Figure 4.25: Monthly maps of surface potential density anomaly (σ_θ, kg m^{-3}) for the year 2012 obtained from the model (NEMO - BLACK SEA). The overlapping mauve color indicates the areas with values comprised between (a) 14.0-14.5 kg m^{-3} and (b) 14.5-15.0 kg m^{-3}.

Concerning the year 2012 (Fig. 4.25), most of the outcrops of the light part of the CIL (14.0 - 14.5 kg m^{-3}) are also observed from January to March. The outcrops for the denser part of the CIL are very reduced and localised inside the central basin in February 2012, but they can hardly be detected the rest of the winter period.

4.4.2 How reliable are these estimates?

The Walin framework is an exact and robust method which is based on an integrated view of a specific area, and is time dependent. This is also a very powerful method as it allows us to infer values of the total interior mixing. But like any other methods, there are some limitations, and these are discussed below.

One of the issues that can be brought to attention is the fact that because it is an area-integrated method, any information from a local gain in volume can be lost and cancelled by another loss in volume from another place. Besides that, the method has been shown to be very dependent on the inputs used. Studies that focused on formation rates are often based on surface fluxes (*e.g.* Speer and Tzipermann (1992), Lascaratos (1993) and Badin et al. (2013) for respectively the North Atlantic, the Mediterranean basin and the Southern Ocean). Therefore, there is a need to have access to accurate air-sea fluxes in order to apply the method rigorously. In Lascaratos et al. (1993) and Badin et al. (2013), climatologic data are used, whereas the present one uses yearly fluxes from ERA5 with CORE bulk formulae in the model (NEMO - BLACK SEA). In Staneva and Stanev 2002, they looked at the evolution of vertical profiles of temperature, and estimated the volume of newly formed CIL by measuring the cooling assessed from the decrease in the heat content between 14.5 and the lower boundary of the CIL. They draw attention to the inadequacy of climatic data for the estimation of formation rates of the CIL in the Black Sea (Fig. 4.26b). Indeed, the CIL formation that is normally observed south of the Kerch Strait, was not detected through the use of climatic data. However, the rates of the CIL formation to the west of Crimea Peninsula were observed as comparable between their model estimates and the climatic data. The formation rates for the shelf edge region (Region A in Fig.4.26a) are higher than 12 m yr^{-1} and for the eastern region (Region D in Fig. 4.25a) the rates are lower than 6 m yr^{-1}.

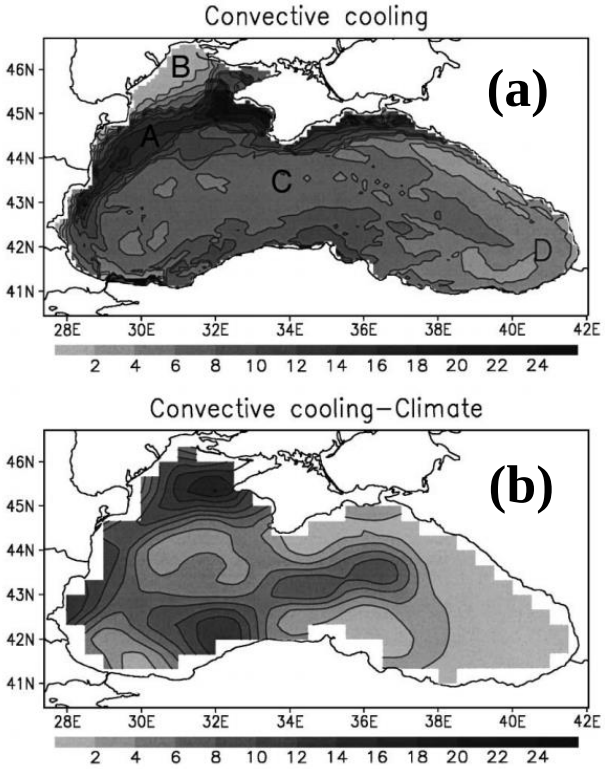

Formation rates:
Region (A): > 12 m y^{-1}
Region (D): < 6 m y^{-1}

Figure 4.26: Rate of water mass formation, presented as thickness of water column (m) formed every year. Top figure (a) is obtained by convective cooling. Bottom figure (b) are results based on climatic data. Figures extracted from Staneva and Stanev (2002).

The results presented in this Chapter consider each individual year separately, and a strong annual variability is observed in the estimation of the formation rates for the CIL. From 1980 to 2018, the difference in the magnitude of the formation rate can be as big as 4.85 Sv for 14.25 kg m^{-3} and 2 Sv for 14.75 kg m^{-3}. Therefore, the use of climatic data might not be reliable in this case.

A last point worth noticing is that the transformation estimation requires a good knowledge not only in the surface fluxes, but also in the mixing. The diapycnal mixing component can be diagnosed from the volume changes as it was done in this Chapter, or it can come from direct *in situ* measurements, as done in Badin et al. (2013) which used Argo floats data.

4.4.3 Regionalisation of the formation rates

The contribution of the formation rates from the coast to the total basin was investigated over the whole period from 1980 to 2018. Only the positive values of the formation rates over the whole basin were used to compute the percentage of contribution.

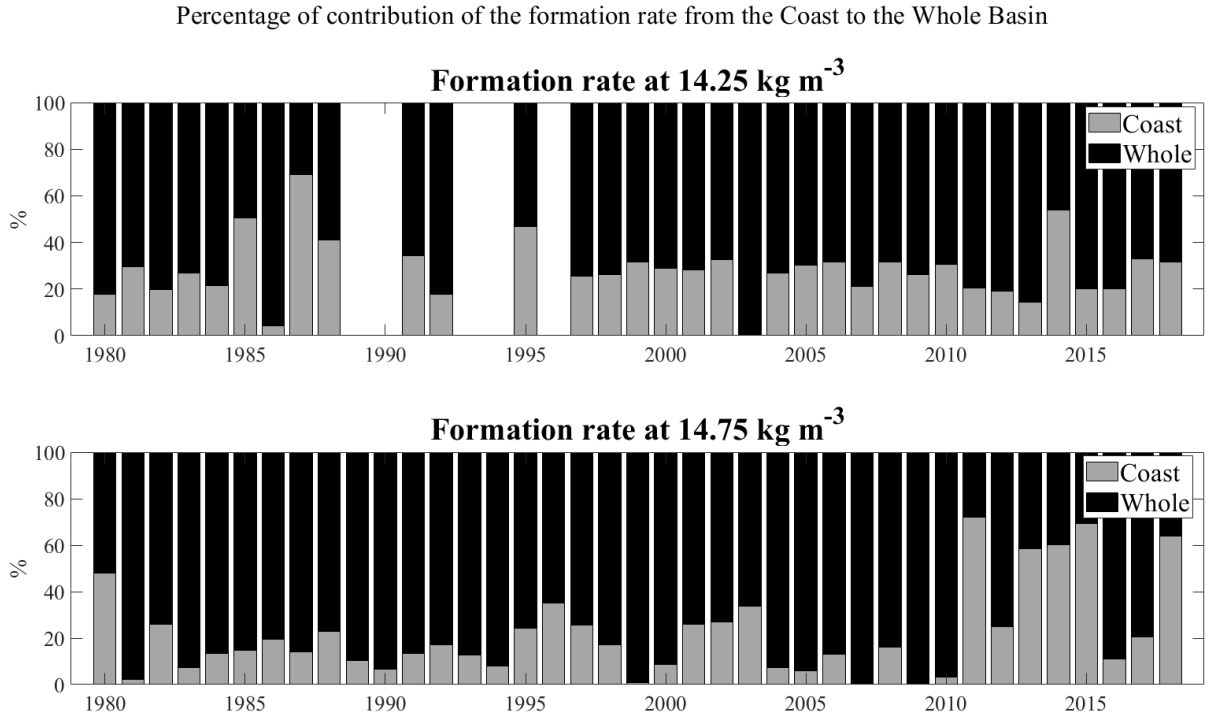

Figure 4.27: Percentage of contribution of the coast (light grey) to the whole basin (dark color) of the Black Sea in terms of the formation rates at (a) 14.25 kg m^{-3} and (b) 14.75 kg m^{-3}. The absence of data indicates that the formation rates over the whole basin were negative for the particular year.

From Figure 4.27, it can be observed that for the density 14.25 kg m^{-3}, the formation rates of the CIL from the coast mainly fluctuate around the value of 30%, but with some exceptions. For example, the coast contributes to more than 50% for the years 1985, 1987 and 2014, reaching the respective values of 51%, 69% and 54%. It is less than 1% for the year 2003.
For the formation rates at 14.75 kg m^{-3}, the contribution from the coast tends to dominate for the recent years. In 2011, the contribution from coast is around 72% and greater than 58% between 2013 to 2015. Before, 2011, the contribution from the coast is relatively small, and remains below the threshold of 35%, except in 1980 where it reached 48%. Overall, the coastal contribution is usually less important compared to the rest of the basin.

The formation rates over the coastal area at 14.75 kg m^{-3} anti-correlates with the annual river discharge with $R^2 = 0.15$ (r = 0.39, significant for the p_{value} of 0.05, see Fig.C.18 in the Appendix C).

4.5 To conclude

In this Chapter, an example of analysis of model results using the theory of Walin was presented for the Black Sea case. This method relies principally on air - sea fluxes (the main physical processes considered are represented in Fig.4.28 under the red square) and provides quantitative estimates of the transformation and formation rates for a specific density range which is taken here as the Cold Intermediate Layer. This is a reliable method to understand the processes that regulate the water mass transformation. The regional variation of the CIL formation for the Whole and Coastal Black Sea areas was also investigated.

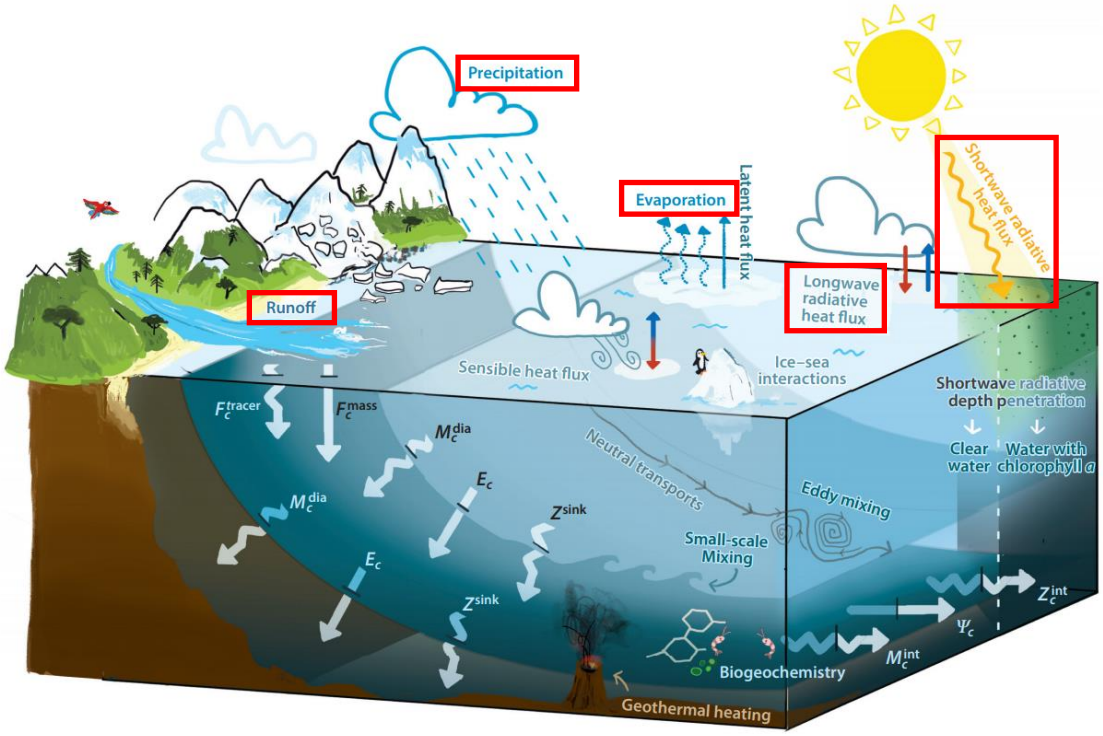

Figure 4.28: Synthetic view of processes that can have an impact on the volume of a water mass bounded by two isopycnals. The processes investigated in this chapter are indicated under a red square. Red arrow indicates heating whereas blue ones represents cooling. Drawing from Groeskamp et al. (2019).

The CIL outcrop mainly during winter time and its lighter part (14.0 to 14.5 kg m^{-3}) covers a larger surface area in comparison to its denser part (14.5 to 15.0 kg m^{-3}). The calculated maps of surface density fluxes were used to compute the formation rates of the CIL on seasonal and interannual time scales. The key results from this Chapter are the following:

i) The heat fluxes were the main contributors in driving the CIL formation.

The surface density fluxes (Din) take into account both the heat and freshwater fluxes. The results showed that the heat contribution to the surface density fluxes were around 10 times higher than the freshwater ones (Figs 4.11 and 4.12).

ii) Year to year fluctuations in the formation rates of the denser part of the CIL (14.75 kg m^{-3}) was strongly determined by winter atmospheric temperature.

A strong interannual variability in the formation rates of the CIL was observed at 14.25 kg m^{-3} (lighter component) which could reach up to 3.65 Sv in 2016. Such a variability could not be explained by the variability in the climatic indexes (NAO, EA/WR and MEI). Only the interannual variability of the denser part of the CIL at 14.75 kg m^{-3} showed a small positive correlation with the EA/WR index. Most importantly, a strong negative correlation between the interannual variability of the denser part of the CIL with the winter atmospheric temperature anomalies was observed (R^2 = 0.74, Fig. 4.22).

iii) The coastal contribution to the formation of the CIL was less important than the rest of the basin but was nonetheless not negligible.

A broad regionalization of the formation rates was used which allows to estimate the contribution of the coast (defined below the 200m isobath) to the whole Black Sea. In 2018, the coastal area contributed to 1/3 of the total formation of the CIL when driven by air-sea fluxes, which is not negligible (Fig. 4.27).

Although this chapter had a strong focus on the Black Sea physics, it is also of interest from the biogeochemical perspective. Indeed, different zones inside the Black Sea (Coastal areas versus Deep areas for example) are tied with their own signature in terms of tracers such as inorganic nutrients or oxygen concentrations, *i.e.* different biogeochemical properties. The CIL of Coastal origin is likely to subduct more nutrients and while this is usually a comparatively small component, in some years it can contribute to >50%. During the renewal of the CIL, such

properties from the surface can then be transferred deeper into the water column, representing then a potential subsurface reservoir of nutrients. By providing appropriate quantification of water mass formation and their drivers, this can be a step forward in understanding ecosystem change. The Walin method was applied in the context of density surfaces, based on temperature and salinity properties. However, the method can also be expanded by looking instead at the transformation of a tracer (such as nutrients), which would then be regarded in terms of nutrient space, as it was done in Badin et al. (2010). This could provide other insights and a deeper understanding on the role of the CIL as a potential conveyor of nutrients and test the hypothesis of nutrients being unable to fuel immediate production in the surface waters. Overall, processes regulating ocean biogeochemistry could be explored.

Chapter 5: Conclusion

In this thesis, two complementary tools have been used (satellite in Chapter 2 and 3D numerical modelling in Chapters 3 and 4) to study multi-annual changes in the biophysical environment of the Black Sea. The Black Sea is of special interest due to its very specific environment and its unique thermohaline structure. This is also a basin that suffered major changes over the last three decades and there is a need in understanding the driving factors to assist further management policy. Concerning the modelling aspect, the choice of an almost enclosed basin is a major advantage compared to open seas because the boundary conditions are then easier to consider. Chapter 2 focused on the biological component of the Black Sea, whereas Chapter 3 and 4 were more focused on the physical aspects, especially the Cold Intermediate Layer. The most important findings from the successive Chapters of this thesis are enumerated below:

(i) **A reconciliation of the bimodal/U-shaped curve dilemma by separating the sea into different regions with different behaviours.**

(ii) **The analysis of the effect of water flow (precipitation, river discharge and CIL) and sea surface temperature on the interannual variability of chlorophyll *a* produce only weak evidence for their influence.**

(iii) **The activation of the light penetration and its good configuration is a crucial condition in representing correctly the CIL. The light attenuation model needs to be spectrally resolved and account for the presence of phytoplankton.**

(iv) **An increase of the mixing in the 3D numerical model helped stabilize the salinity budget.**

(v) **The riverine discharge had a strong influence on the volume of the CIL, where a decrease in the river discharge is associated with an increase in the volume of the basin average CIL. This is the major and novel result from Chapter 3.**

(vi) **The heat fluxes were the main contributors in driving the CIL formation.**

(vii) Year to year fluctuations in the formation rates of the denser part of the CIL (14.75 kg m^{-3}) was most strongly determined by winter atmospheric temperature.

In Chapter 2, the variability of chlorophyll *a* was studied in the Black Sea through the analysis of satellite products (NASA and CMEMS), over seasonal and interannual time scales. Although the time series analysis of chlorophyll *a* is already a well-studied subject in the literature, the novelty aspect presented here concerned the harmonic analysis. Indeed, it was an instructive method as it allowed to split the Black Sea into 8 different biogeographical zones with their unique seasonal cycle **(i)**. The regionalisation includes: 5 regions for the NWS, 2 regions for the main basin (Deep and Coastal areas) and the Azov Sea. The amplitude and the phase of the signal in chlorophyll *a* displayed similar patterns for both satellites products from 2003 to 2017 (NASA and CMEMS, Fig. 2.3). The amplitude was minimum inside the main basin (Regions 6 and 7) whereas the highest values were located near the Danube mouth (Region 4) and in the Azov Sea (Region 8). The seasonal cycle of chlorophyll *a* for the inner basin (Region 6) of the Black Sea was described as U-shaped with minimum values in summer and maximal ones in winter. The phase is an indication of the timing of the peak of the signal and was homogeneous over the central basin and occurs mainly between December to January. In contrast, the NWS had a heterogeneity in the phase values.

No significant correlation was observed between the seasonal Danube river flow and the seasonal chlorophyll *a*, except when considering one-month lag where a positive correlation was observed with $R^2 = 0.53$ for Region 3 and $R^2 = 0.57$ for Region 4 (Fig. 2.8). A localized analysis (pixel by pixel) between monthly chlorophyll *a* and SST indicated a significant negative correlation in the main basin of the Black Sea, suggesting this area to be nutrient limited (Fig. 2.6). Considering the interannual variability of chlorophyll *a* over Region 3 and 4, no correlation was observed with the Danube discharge. However, a small positive correlation was obtained between the interannual variability of chlorophyll *a* and the precipitation over the catchment area with an R^2 around 0.3 for both Regions 3 and 4. Overall, the results cannot establish a causality of the river outflow on chlorophyll concentration. An investigation into changes in the turbulence structure and/or directly assessing an increase in nutrients could be useful as a future work. Moreover, we could not conclude of a link between the CIL volume

and the chlorophyll *a* on interannual time scales (Fig. 2.21b). The localized analysis between annual temperature and chlorophyll *a* suggested only a weak positive correlation for some areas inside the main Black Sea basin (Fig. 2.17). Temperature was used as a proxy and the direct impact of nutrients on chlorophyll concentration was not clearly demonstrated.

For Chapter 3 and 4, the core results obtained on some aspects of the Black Sea dynamics depended on the development of a 3D numerical model that represented well enough the reality. The final setup of the model was assessed using sensitivity analyses for the light field and various mixing schemes which were compared with *in situ* data and another model Reanalysis. To maintain a realistic thermal structure, especially the formation of the CIL, a proper light penetration parametrization was proven to be an important feature (Fig. 3.12). The configuration needed to activate the light penetration using the red-green-blue light penetration together with a shading due to phytoplankton (**iii**). The chlorophyll concentration corresponded to a climatology of the seasonal cycle from 2003 to 2018. A better temporal resolution on the chlorophyll concentration *e.g.* using yearly values instead of one simple climatology of the seasonal cycle, could be investigated for any future model improvement. In addition to the results **iii**), it was shown that the details of the mixing scheme also played an important role, especially in the regulation of salinity (Figs. 3.14 and 3.15). Indeed, an increase of the mixing by either changing the stability function or increasing the Galperin value, was shown to reduce the positive salinity drift **(iv)**. We speculated that this might be due to a decrease in sea surface temperature, which in turn decreased evaporation, hence better stability in salinity. Another explanation could be that the increase in mixing would decrease the Bosphorus inflow and then reduce the positive salinity drift. Besides that, the initial drift of salinity could be explained by an inadequate precipitation dataset. Indeed, the article of Gunduz et al. (2020) showed that ERA5 precipitation is significantly lower than ERA-Interim precipitation with a ratio of about 2 in the Black Sea. This is something that could be investigated in a future work.

Using the optimized parametrization from the sensitivity analysis, long term simulations were then performed for almost four decades (1980 to 2018). Several diagnostics (depth of the minimum temperature, thickness, temperature associated to the minimum depth, average temperature, cold content and volume) were used to carry out analysis on the long-term changes of the Cold Intermediate Layer structure. The main results indicated that winter SST had a strong influence on the CIL structure (Figs. 3.29 to 3.34). Indeed, colder winters were associated not only with a thicker CIL (R^2 = 0.77) but also with a greater cold content (R^2=

0.71). Also, colder winter are associated with lower values in both the minimum of the CIL temperature (R^2 = 0.70) and the average temperature (R^2 = 0.70). The effect of an increasing annual trend of sea surface temperature of 0.04°C from 1980 to 2018 seemed to be transferred into deeper depth, as the CIL tended to disappear in the most recent years. A last result which is novel and very significant, was the impact of the river flow on the CIL formation on decadal time scales **(v)**. Rivers were demonstrated to have a significant influence on the interior properties of the water column (Fig. 3.36). Indeed, freshwater input resulted in an increase in the CIL formation, and such influence has been observed basin-wide. If we suppose that a decrease of the volume of the CIL results in a reduction of the nutrients subducted, then the pool of nutrients available for the biology would increase. Using the model for particle tracing (here the particle being the nutrient), could be implemented to study the fate of nutrients.

The last Chapter 4 looked at the processes impacting the formation of the CIL using diagnostics from the Walin method. The heat fluxes components were the main contributors in driving the CIL formation **(vi)** (Fig. 4.11). In addition to the salinity control on longer time scales identified in Chapter 3, Chapter 4 highlighted that winter mean temperature were the strongest controlling factor of the CIL formation over interannual time scales (**vii)** (Fig. 4.22). A strong interannual variability in the formation rates of the CIL was observed and the denser part of the CIL at 14.75 kg m^{-3} showed a strong negative correlation with winter atmospheric temperature anomalies (R^2 = 0.74). A broad regionalization of the formation rates was used which allows to estimate the contribution of the coastal region (defined below the 200m isobath) to the whole Black Sea. In 2018, the coastal area contributed to 1/3 of the total formation of the CIL (but in some other years, it can be higher or smaller) when driven by air-sea fluxes, which is not negligible (Fig. 4.27).

Each of the three-science chapters in this thesis indicated a strong interannual variability in either chlorophyll *a* (Chapter 2, Section 2.3.6), or in both the structure (Chapter 3, Section 3.3.3.2) and formation rates (Chapter 4, Section 4.3.10) of the CIL. Climatic variations are important drivers of the Black Sea ecosystem (Oguz et al., 2006). Future scenarios become then vital in understanding how the Black Sea properties may develop as a result of climate change and/or policy decisions (through construction of dams for example). Studying the sensitivity of the Black Sea system is rather important especially when the ecosystem suffered a series of perturbations imposed by changes in the river discharge, eutrophication, species introduction and excessive fishing (Zaitsev and Mamaev, 1997). Chapter 3 presented results from a

sensitivity experiments in regards of the river discharge and showed a direct impact of the riverine discharge on the CIL volume. The fresh-water balance is then very important, and it determines the physical (and chemical) structure. Tackling the eutrophication issue is in theory easier to manage, but practically, it suggests major changes in industrial production of detergent, effective waste treatment changes in agricultural techniques, which is notably limited by the financial aspects and the trans-national boundary nature of the nutrient pollution problem. From the results, it is then possible to speculate that future construction of dams (or increased water extraction for agriculture) would increase the volume in the CIL. In the same time, by reducing riverine discharge, it would also reduce locally the large nutrients inputs which could be a solution to eutrophication issues. Also, according to the hypothesis that link nutrients to the CIL, it would lead to more nutrients trapped inside the CIL.

Being a regional sea, the coastal area of the Black Sea is an important component and assessing the optical properties from operational oceanography near the coast is not always straightforward and requires strong efforts for the development of accurate algorithms. Concerning the modelling aspect, all the results presented in Chapter 3 and 4 uses a model that does not include data assimilation. This is a key challenge and a possible future step that will need to be addressed.

It is by bringing together the little pieces of the puzzle that a synthetic view can be obtained. However, in science every step leads to a range of other questions, and as Richard Feynman said so well: “I would rather have questions that can't be answered than answers that can't be questioned.”

APPENDIX A

NASA - CHLA ALGORITHMS (OC3 AND CI)

NASA - Chla product combines two algorithms (OC3 and CI) which are detailed below.
OC3 algorithm is a fourth-order polynomial relationship between a ratio of Rrs (Remote sensing reflectance) and chlorophyll *a*:

$$(Eq.A.1)\ Chla = 10^{(a+bR+cR^2+dR^3+eR^4)}$$

where $R = \log_{10}(\max[(\frac{Rrs(443)}{Rrs(547)}), (\frac{Rrs(488)}{Rrs(547)}])$ and the coefficients specific to MODIS satellite are: a=0.2424, b= -2.7423, c=1.8017,d= 0.0015 and e= -1.2280

Concerning the color index (*CI*) algorithm, it is a three band (green, blue and red) reflectance difference algorithm and the equation is:

$$(Eq.A.2)\ CI = Rrs(\lambda_{green}) - [Rrs(\lambda_{blue}) + \frac{(\lambda_{green} - \lambda_{blue})}{(\lambda_{red} - \lambda_{blue})} * (Rrs(\lambda_{red}) - Rrs(\lambda_{blue}))]$$

where λ_{green}, λ_{blue} and λ_{red} are specific to the instrument and closest to 555, 443 and 670nm respectively.

For MODIS sensor, the exact values are then:

$$(Eq.A.3)\ CI = Rrs(547) - [Rrs(443) + \frac{(547-443)}{(667-443)} * (Rrs(667) - Rrs(443))]$$

CI algorithm is used for chlorophyll *a* retrieval below 0.15 mg m^{-3}, whereas OC3 algorithm applies for chlorophyll retrievals above 0.2 mg m^{-3}. The CI and OC3 algorithms are blended using a weighted approach for intermediate chlorophyll retrievals.

BSAlg: CMEMS - CHLA ALGORITHM

This section details the equations used by the CMEMS - Chla algorithm.

RRS is first converted into the normalised water leaving radiances (nLw) with the following formula: (Eq.A.4) $nLw = Rrs * F0$, where $F0$ is the top of the atmosphere solar irradiance (details for the estimation of $F0$ can be found on Thuillier et al. (2003)). Then, using the sub-regions of the Black Sea defined by Kopelevich et al. (2013) (Fig.A.1 below), a specific empirical ocean color algorithm for chlorophyll *a* retrieval is applied.

For the coastal regions (sub-regions 1-5 on Fig.A.1), the chlorophyll *a* is calculated with the following equation:

$$(Eq.A.5)\ \ Chl = 1.13\left(\frac{nLw(510)}{nLw(555)}\right)^{-3.33}$$

For open regions (sub-regions 6-8 on Fig. A.1):

$$(Eq.A.6)\ \ Chl = 0.88\left(\frac{nLw(510)}{nLw(555)}\right)^{-2.24}$$

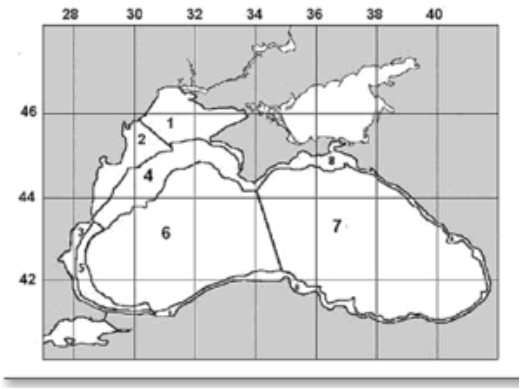

Figure A.1: Optical sub-regions delimited in Kopelevich et al. (2013)

TRIGONOMETRIC THEOREM

In this section, it is explained how the sum of two trigonometric functions with the form of $a\cos x + b\sin x$ can be expressed as a single trigonometric function in the form of $A\cos(x-\alpha)$.

$$A\cos(x-\alpha) = A(\cos x\cos\alpha + \sin x\sin\alpha)$$
$$= A\cos x\cos\alpha + A\sin x\sin\alpha$$

By re-ordering,

$$A\cos(x-\alpha) = (A\cos\alpha)\cos x + (A\sin\alpha)\sin x$$

Then, $a\cos x + b\sin x$ is comparable with $(A\cos\alpha)\cos x + (A\sin\alpha)\sin x$ where

$$a = A\cos\alpha$$
$$b = A\sin\alpha$$

It was just demonstrated that $a\cos x + b\sin x = A\cos(x-\alpha)$, therefore using the equations in Chapter 2 (Eq. 2.1 in section 2.2.2):

$$b_1\sin(2\pi tf) + a_1\cos(2\pi tf) = A_1\cos(2\pi tf - \varphi_1)$$
$$b_2\sin(4\pi tf) + a_2\cos(4\pi tf) = A_2\cos(4\pi tf - \varphi_2)$$

By squaring the coefficients a and b, and adding them, it gave:

$$a^2 + b^2 = A^2\cos^2\alpha + A^2\sin^2\alpha$$
$$= A^2(\cos^2\alpha + \sin^2\alpha)$$
$$= A^2$$

Indeed, $\cos^2\alpha + \sin^2\alpha = 1$.

Therefore,

$A = \sqrt{a^2+b^2}$ This is the amplitude of the signal

Also, $\frac{A\sin\alpha}{A\cos\alpha} = \frac{b}{a}$, so that $\tan\alpha = \frac{b}{a}$.

IN SITU PROFILES FROM MET OFFICE HADLEY CENTER

Table A.1: Coordinates (in degree decimal) and maximal depth sampled of the selected stations from the Met Office Hadley Centre. The stations are located inside three main regions of the Black Sea (Western Gyre, Eastern Gyre and South Coast) and for each station, vertical profiles of temperature and salinity were extracted.

Regions	Date	Latitude (degree decimal)	Longitude (degree decimal)	Maximal depth sampled (m)
Western Gyre	23/04/2006	42.01	29.43	1481.62
	15/05/2006	41.79	29.63	1531.19
	05/06/2006	41.95	30.07	1482.02
	04/07/2006	41.64	30.71	1482.16
	08/08/2006	42.11	31.14	1481.41
	11/04/2007	42.91	32.08	1531.13
	10/05/2007	42.77	31.76	1530.76
	15/06/2007	42.65	31.05	1530.97
	07/07/2007	42.85	31.05	1531.34
	20/08/2007	42.87	31.17	1531.34
East Coast	30/04/2006	42.44	38.81	1481.85
	29/05/2006	42.26	39.08	1481.98
	05/06/2006	42.31	39.11	1531.41
	19/07/2006	42.41	39.15	1481.66
	03/08/2006	42.52	39.13	1481.65
	13/04/2007	42.26	40.68	1531.42
	12/05/2007	42.34	40.85	1531.31

	10/06/2007	42.21	39.63	1531.53
	02/07/2007	42.57	39.76	1482.03
	15/08/2007	42.61	40.41	1284.63
South Coast	19/07/2006	41.63	31.50	1481.96
	31/08/2006	42.08	32.79	1531.45
	06/04/2007	41.52	37.76	1531.43
	13/04/2007	41.36	37.86	1482.39
	18/04/2007	41.90	36.49	988.70
	03/05/2007	41.72	36.68	740.52
	25/05/2007	41.63	36.64	691.19
	15/06/2007	41.55	36.71	493.72
	14/07/2007	41.53	36.69	394.61
	21/07/2007	41.46	36.83	138.37

MODEL (BLKSEA_REANALYSIS_PHYS_007_004) PERFORMANCE

Table A.2: Summary of BLKSEA_REANALYSIS_PHYS_007_004 performance for different parameters and depth ranges over the entire time period 1995-2015 (first entry in red) and over 2005-2015 for temperature and salinity (second entry in blue). Extracted from the QUID document of the data (http://resources.marine.copernicus.eu/documents/QUID/CMEMS-BS-QUID-007-004.pdf)

Parameter	BIAS V4	RMS V4
SST [°C]	-0.07 / -0.07	0.58 / 0.59
T [°C] 0-100	-0.02 / 0.025	0.87 / 0.74
T [°C] 100-300	-0.03 / -0.003	0.15 / 0.09
T [°C] 300-800	-0.02 / -0.02	0.11 / 0.05
S [psu] 0-100	-0.014 / 0.002	0.33 / 0.26
S [psu] 100-300	-0.006 / 0.009	0.19/ 0.15
S [psu] 300-800	-0.005 / -0.002	0.05 / 0.03
SLA [cm]	0.055/ 0.045	4.377/ 4.356

RAW DATA OF CLIMATIC INDEXES (NAO, EA/WR AND MEI)

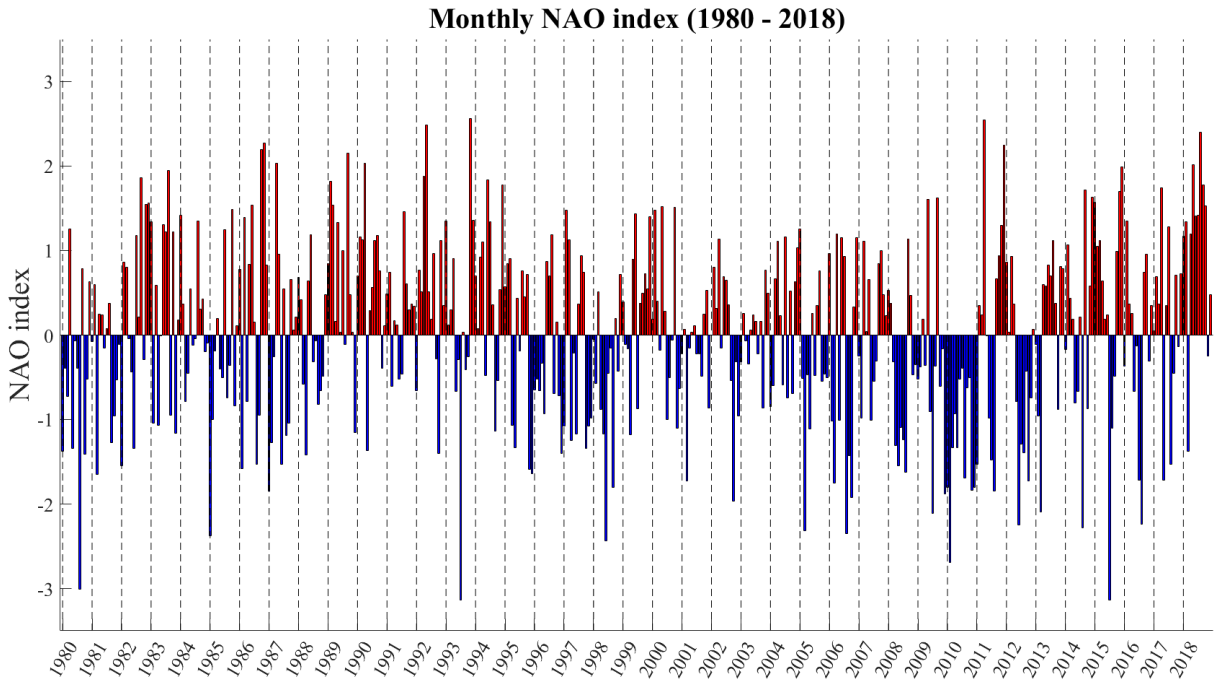

Figure A.2: Monthly NAO index (1980 - 2018). The index was normalized using the 1981-2010 based period monthly means and standard deviations.

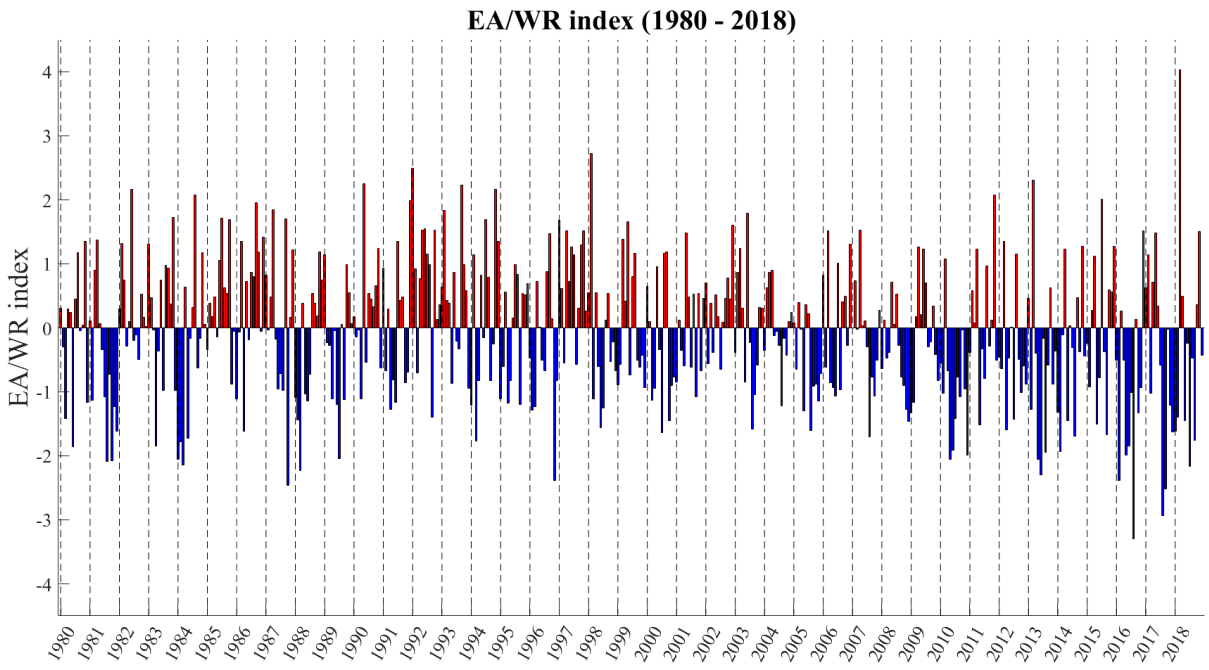

Figure A.3: Monthly EA/WR index (1980 - 2018). The index was normalized using the 1981-2010 based period monthly means and standard deviations.

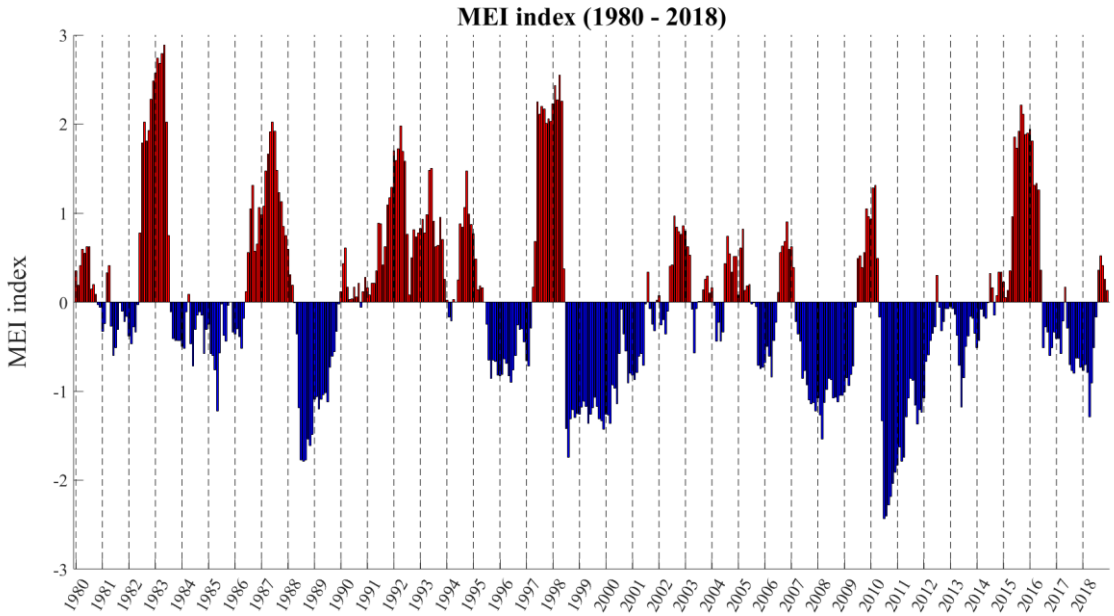

Figure A.4: Monthly MEI index (1980 - 2018).

PRECIPITATION OVER THE CATCHMENT AREA OF THE BLACK SEA

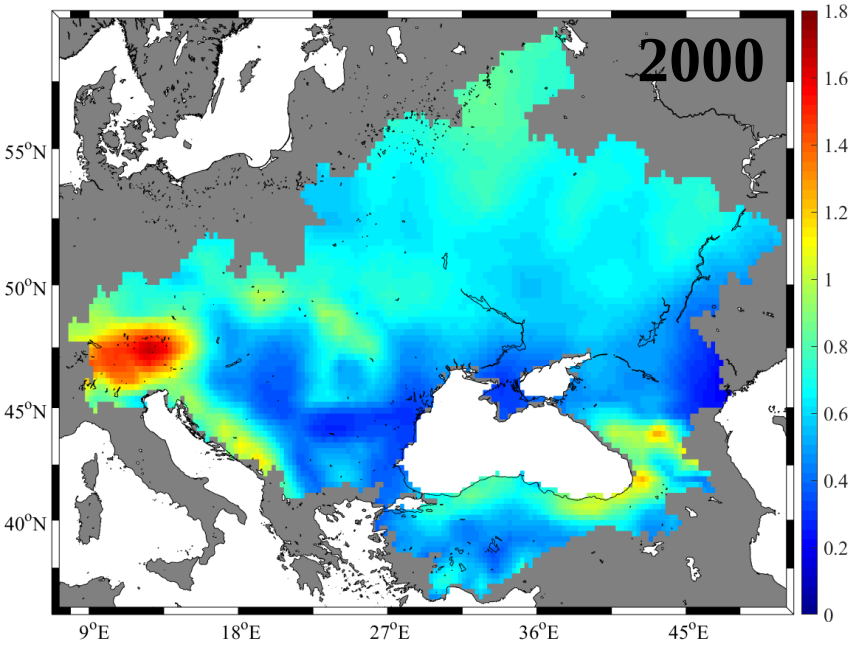

Figure A.5: Spatial maps of the total precipitation (m) over the entire catchment area of the Black Sea for the year 2000.

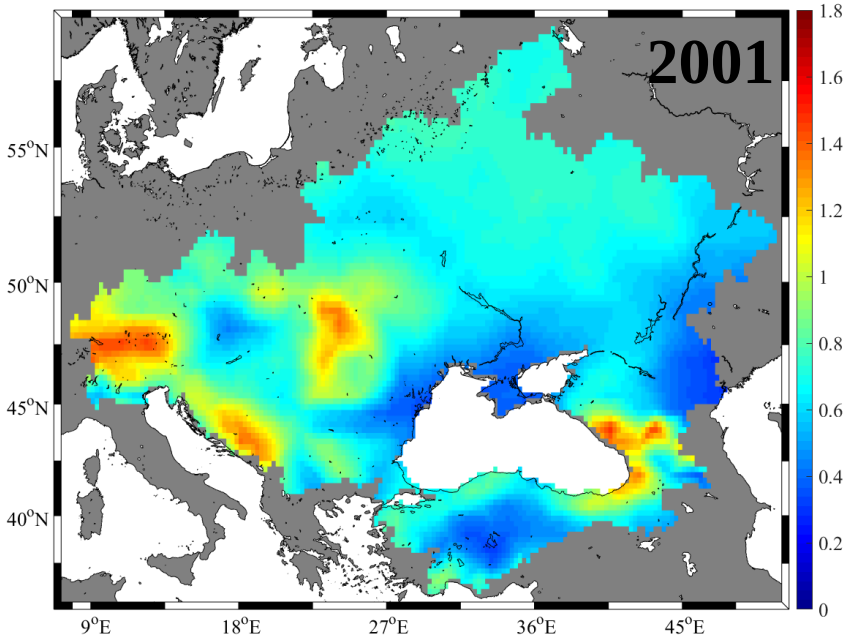

Figure A.6: Spatial maps of the total precipitation (m) over the entire catchment area of the Black Sea for the year 2001.

ANNUAL TIME SERIES AZOV SEA

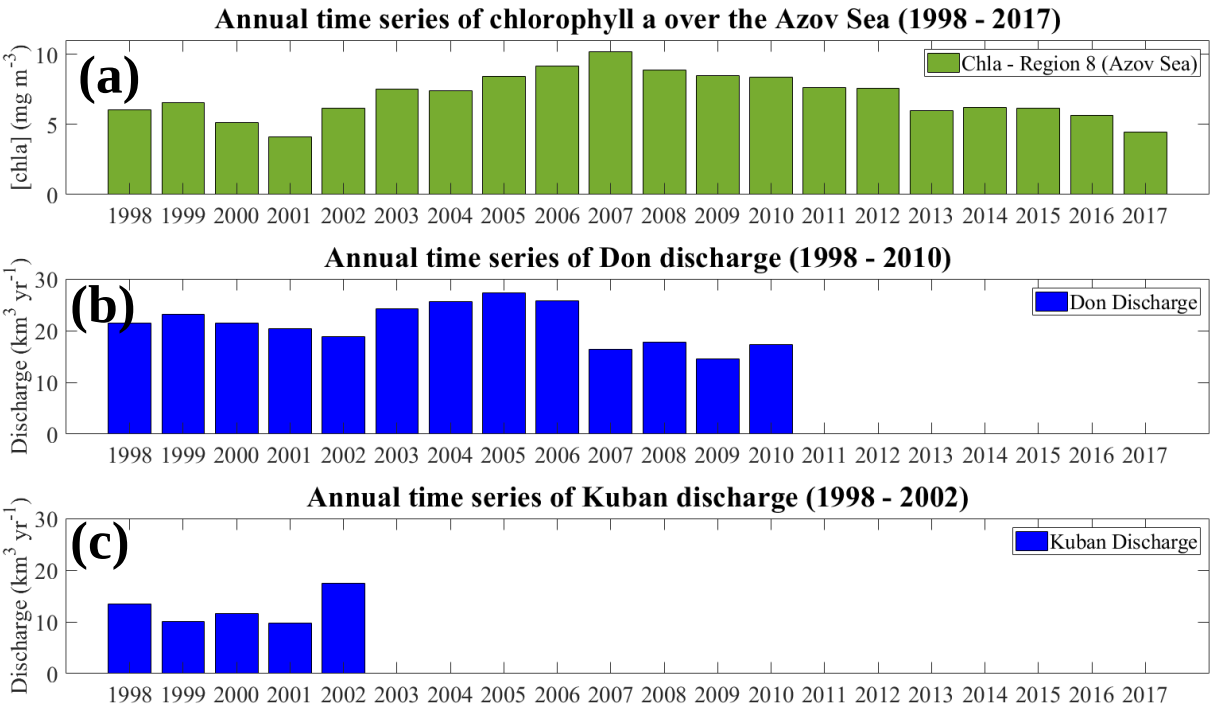

Figure A.7: Annual time series of (a) chlorophyll *a* in the Azov Sea from 1998 to 2017. (b) Don discharge (1998 - 2010) and (c) Kuban discharge (1998 - 2002)

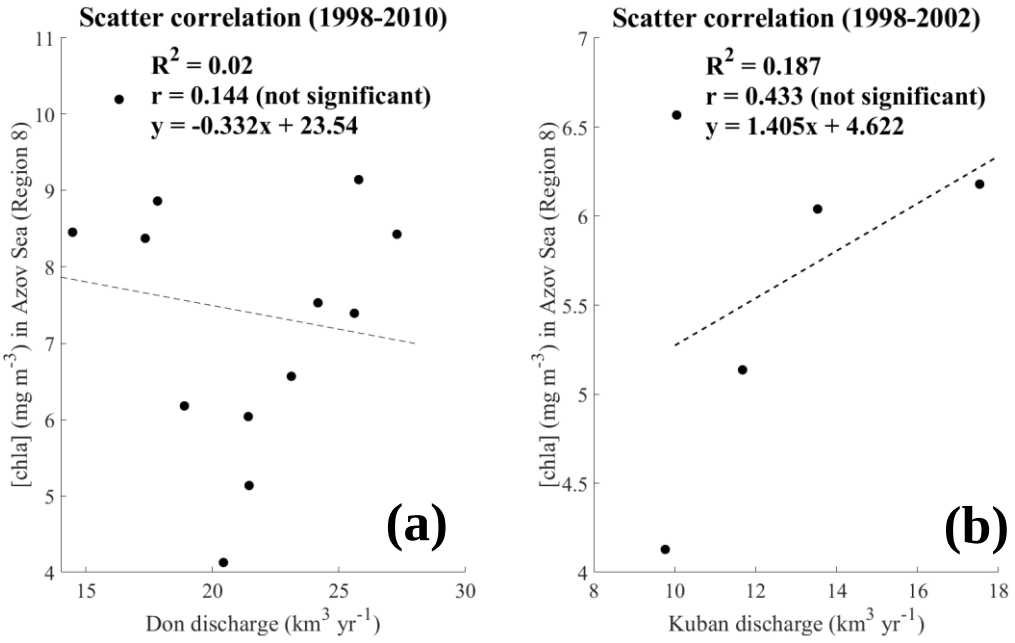

Figure A.8: Scatter correlation between river discharges (Don and Kuban) in the Azov Sea and CMEMS-Chla (Region 8).

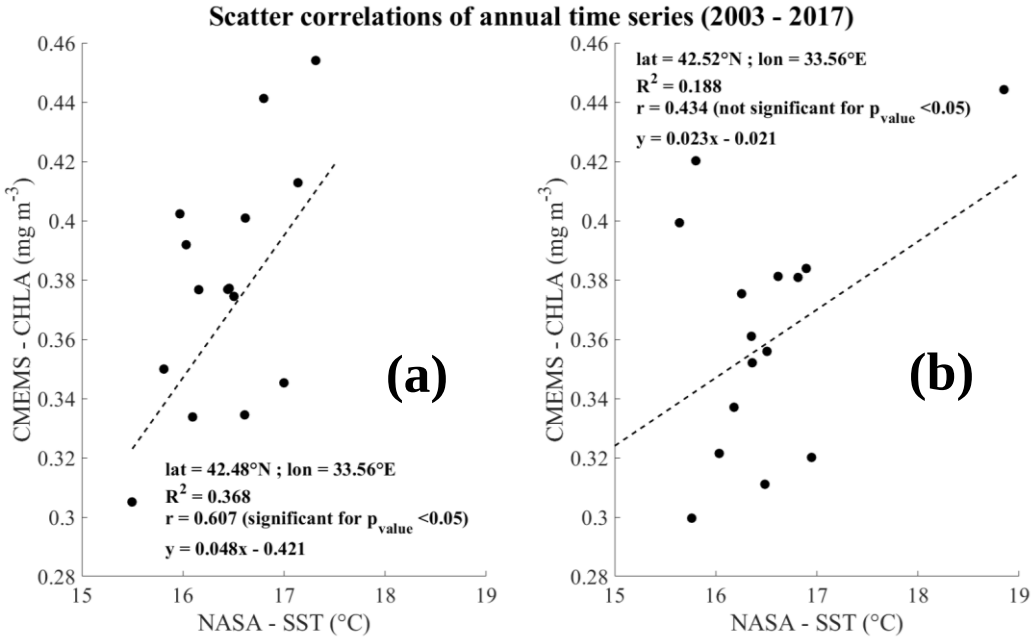

Figure A.9: Scatter correlation between the annual time series of NASA-SST and CMEMS-Chla for two close points coordinates. (a) First coordinate showing a significant correlation (b) Second point coordinate where the time series are not correlated.

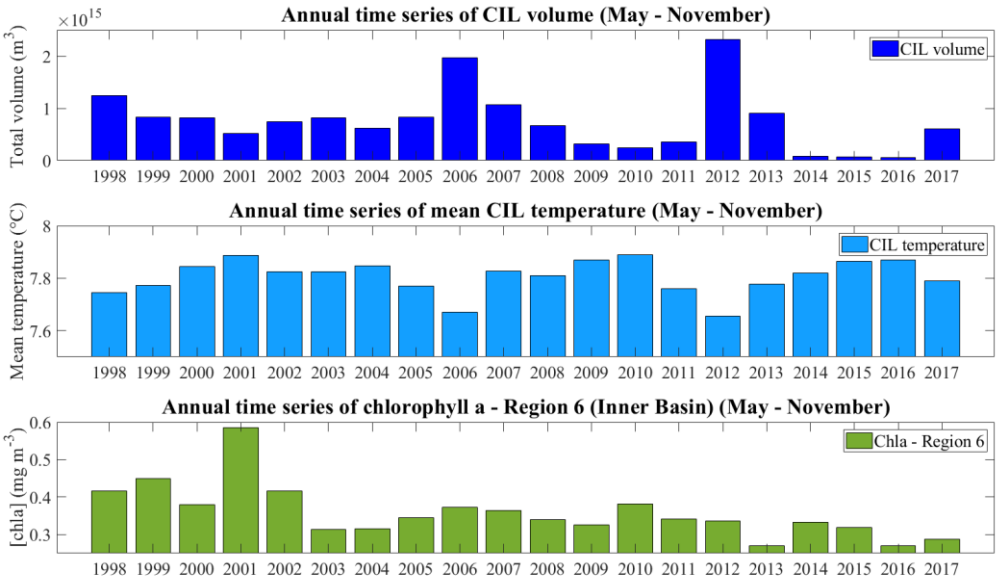

Figure A.10: (a) Total volume of CIL (m^3). (b) Mean temperature of the CIL. (c) Annual mean chlorophyll *a* concentration from CMEMS-Chla over Region 6 (Inner Basin). All time series are from 1998 to 2017 and consider only the period between May to November.

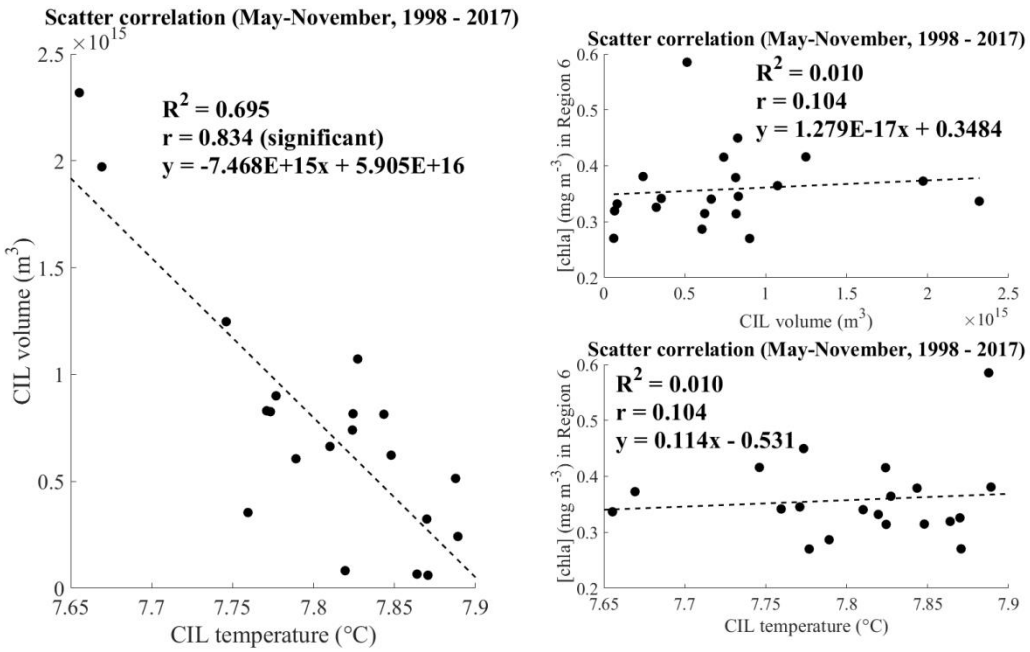

Figure A.11: Scatter correlation between (a) the CIL temperature and the CIL volume, (b) the CIL volume and the chlorophyll *a* concentration in Region 6 and (c) the CIL temperature and the chlorophyll *a* concentration in Region 6.

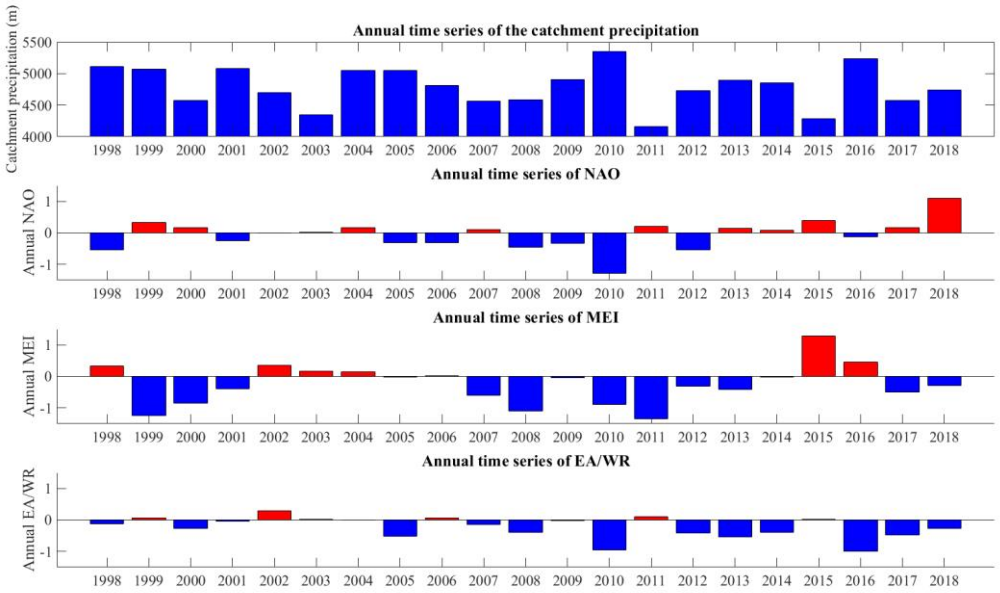

Figure A.12: Time series of the catchment precipitation and the climatic indexes from 1998 to 2018.

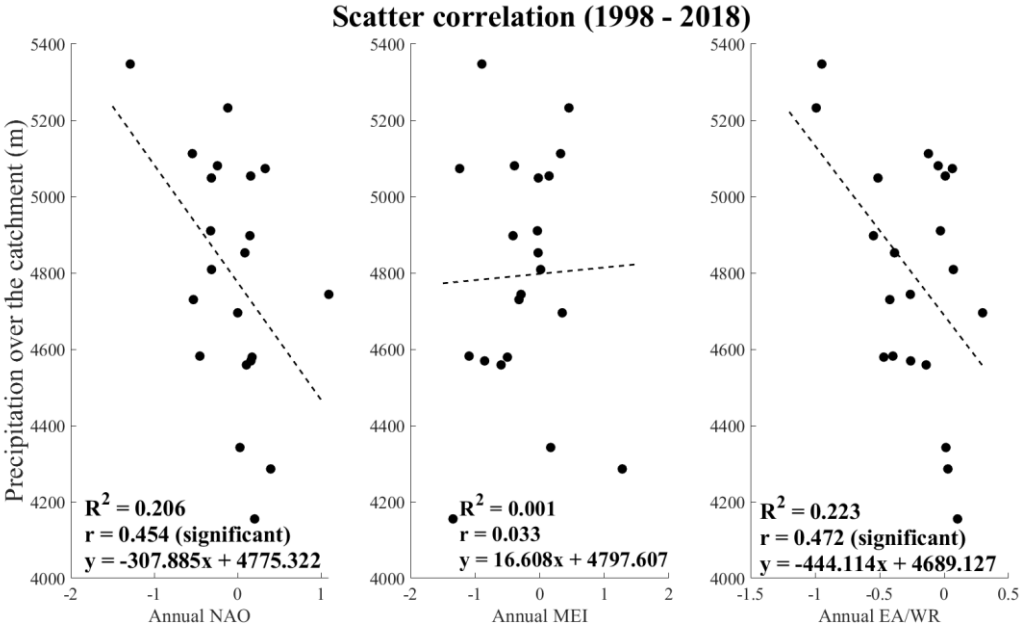

Figure A.13: Scatter correlation between climatic indexes and precipitation over the catchment

APPENDIX B

DAMMING OF THE DANUBE RIVER

Figure B.1: Indication of the Iron Gates Reservoir with highlight of the Danube river (black line). Figure from Teodoru 2005. Iron Gate I is located approximately 900 km upstream from the Black Sea. Iron Gate I Dam was constructed in 1972, and the smaller Iron Gate II Dam was completed downstream in 1984 (Teodoru and Wehrli, 2005).

ARAKAWA GRID C-TYPE

Figure B.2: Diagram of the Arakawa C-type grid classification employed for the spatial discretisation in numerical models (figure from https://www.nemo-ocean.eu). The diagram indicates how physical quantities are arranged on three space directions. Velocities (u, v, w) are calculated at the centre of each face of the cell, whereas quantities such as temperature, salinity and pressure are defined at the center of the grid cell.

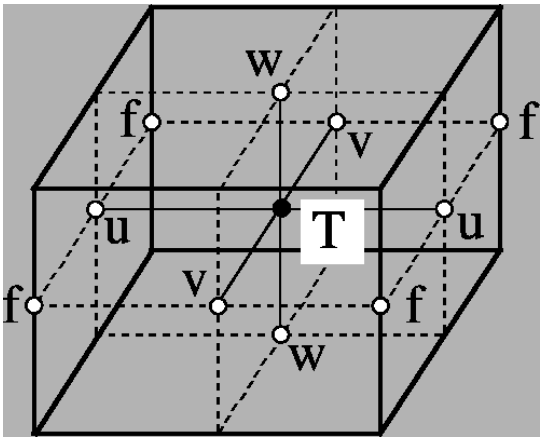

MODEL VERTICAL SPACING (NEMO - BLACK SEA)

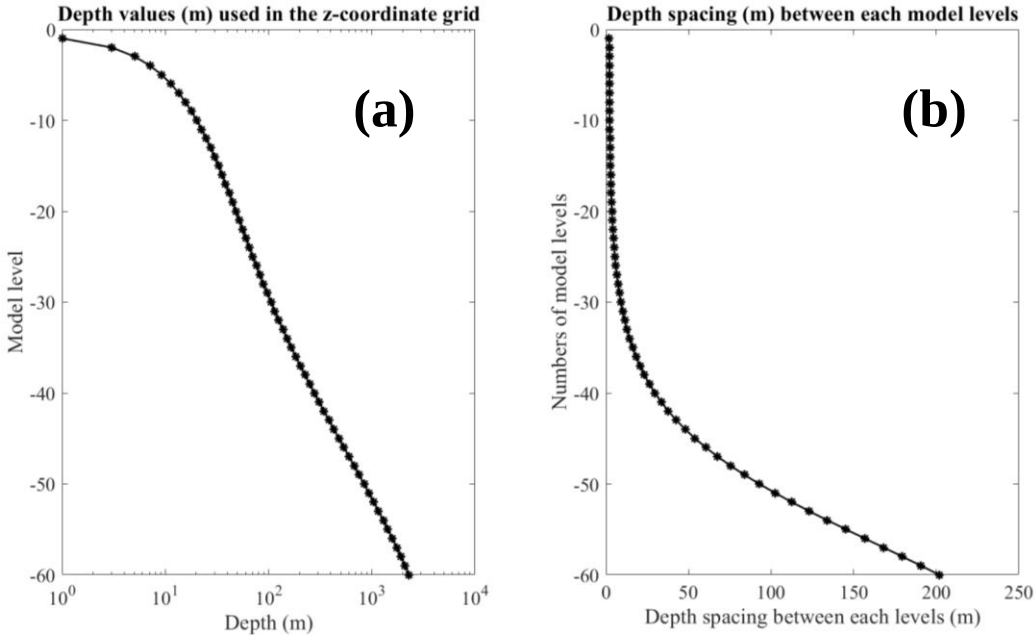

Figure B.3: (a) Depths values used for the z-coordinates grid. (b) Depth spacing between each model levels. The resolution is increased at the surface. The depth values over the 60 model levels are : 1.0, 3.0, 5.1, 7.1, 9.2, 11.3,13.5, 15.6, 17.9, 20.2, 22.5, 24.9, 27.4, 30.0, 32.7, 35.5, 38.4, 41.5, 44.8, 48.3, 52.1, 56.1, 60.5, 65.3, 70.4, 76.1, 82.4, 89.3, 96.9, 105.5, 115.0, 125.7, 137.7, 151.2, 166.3, 183.5, 202.8, 224.7, 249.4, 277.3, 308.8, 344.4, 384.6, 429.9, 480.8, 537.9, 601.9, 673.3, 752.8, 841.1, 938.6, 1046.0, 1163.8, 1292.3, 1431.9, 1582.9, 1745.3, 1919.1, 2104.2, 2300.5.

Z-COORDINATES (PARTIAL STEP VS FULL STEP)

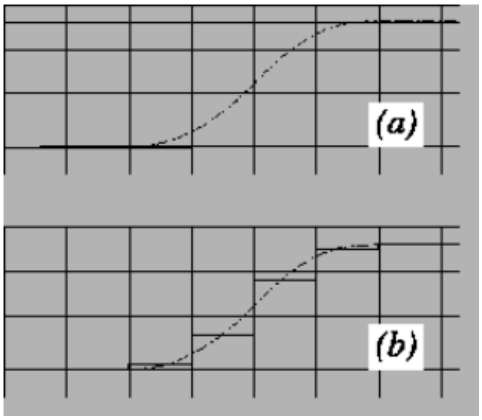

Figure B.4: Indication on how the model "sees" the ocean bottom in a z-level grid (figure from https://www.nemo-ocean.eu/doc/). (a) Z-coordinate with full step, the vertical size of the cells do not change. (b) Z-coordinate with partial step (Pacanowski and Gnanadesikan 1998), which is the configuration used in the numerical model presented in this manuscript. The vertical resolution of the bottom cells can vary according to topographic features.

MAIN TYPES OF VERTICAL GRID COORDINATES

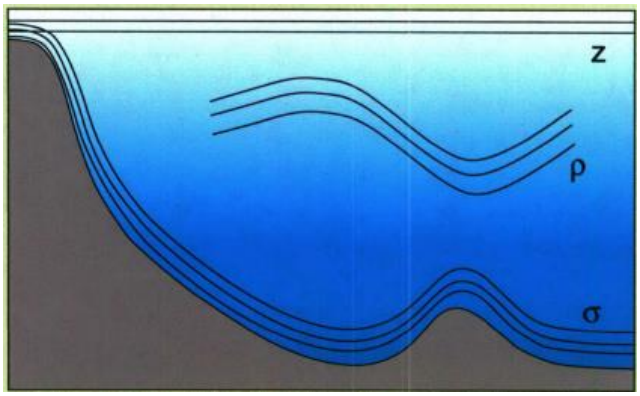

Figure B.5: Illustration and comparison of three main vertical coordinates that relates to fundamental regimes of ocean dynamics (schematic from Chassignet et al. (2006)). Z - coordinates types uses a fixed depth (z) as coordinates and it performs well in well - mixed areas, but not usually used ideal for the ocean interior. A suitable representation for the ocean interior uses surfaces of constant potential density (ρ) as vertical coordinates. Sigma (σ) type coordinates are preferred to represents the bottom part of the sea, as it allows to follow the terrain irregularities, but have a disadvantage due to the errors in calculation of the pressure gradient force (*e.g.* Mellor et al., 1994).

INITIAL CONDITIONS OF TEMPERATURE AND SALINITY (NEMO - BLACK SEA)

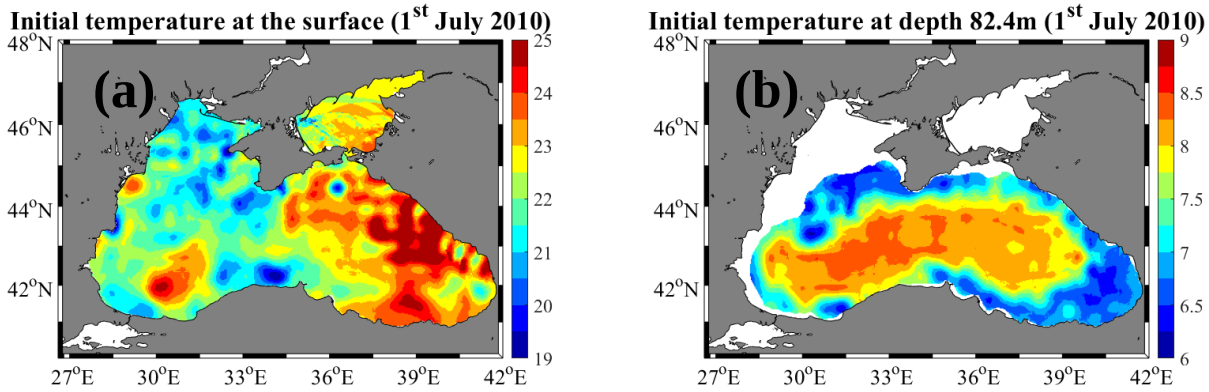

Figure B.6: Initial condition of temperature in the numerical model (NEMO - BLACK SEA) for (a) the surface and (b) depth = 82.4m.

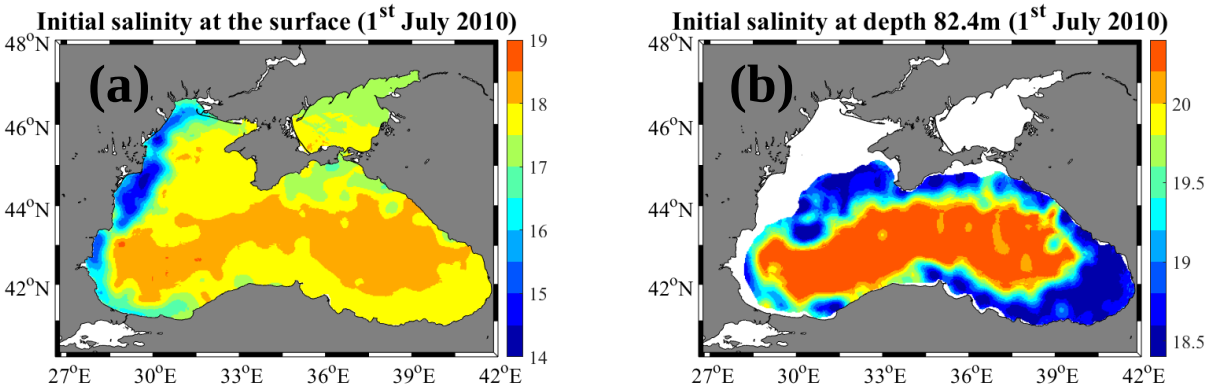

Figure B.7: Initial condition of salinity in the numerical model (NEMO - BLACK SEA) for (a) the surface and (b) depth = 82.4m.

MODEL BOUNDARY DATA (NEMO - BLACK SEA)

The boundary data come from a location inside the Sea of Marmara, which has a shallow and maximal depth of 65.25m.

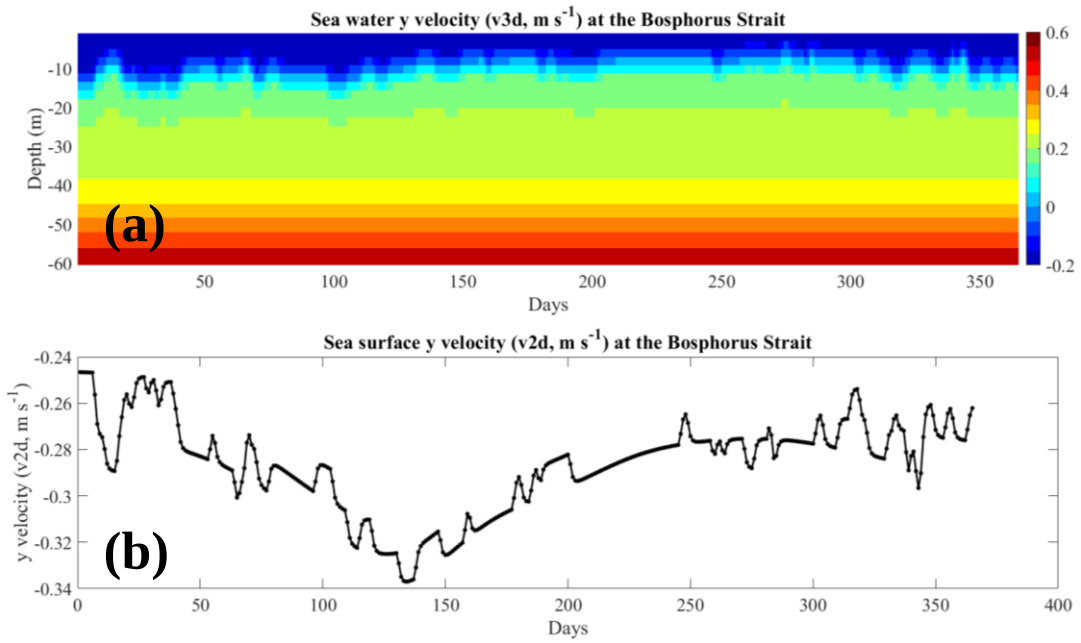

Figure B.8: (a) Three-dimensional y velocities (v3d, m s^{-1}) datasets used at the model boundary. (b) Sea surface velocities (v2d, m s^{-1}).

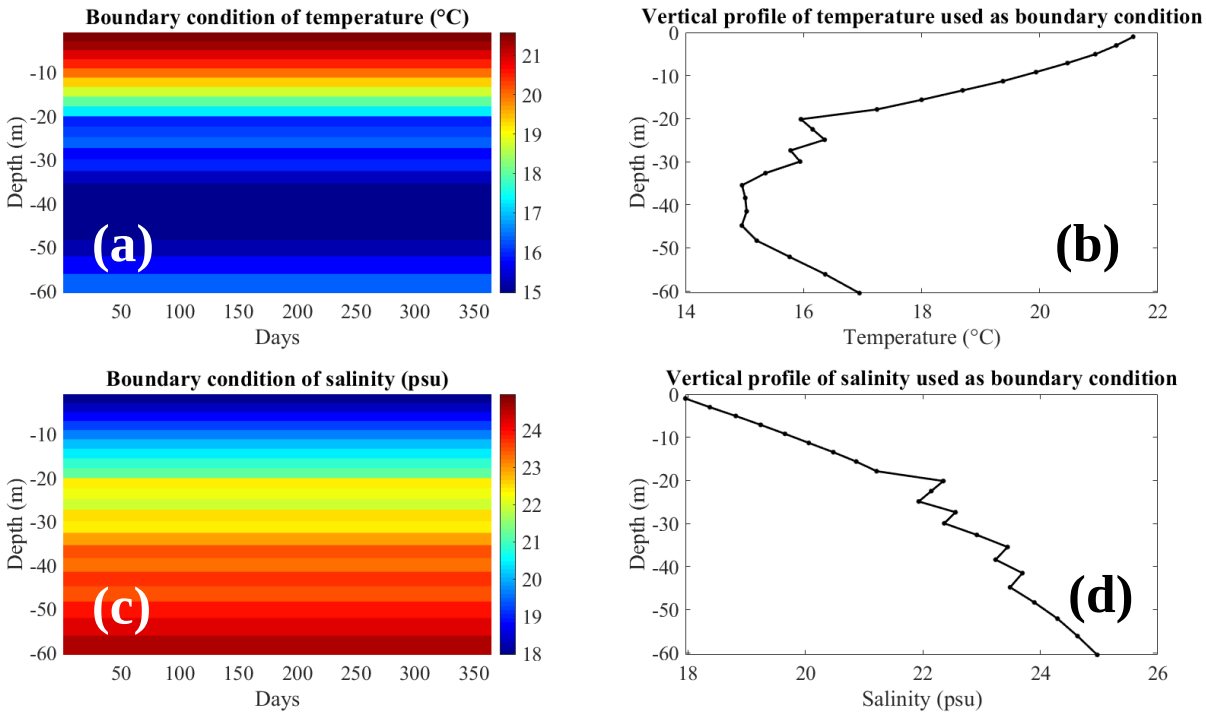

Figure B.9: Three-dimensional data of (a) temperature (°C) and (c) salinity (psu) used as boundary condition with the corresponding vertical profile of (b) temperature and (d) salinity.

The current implementation of the model uses constant profiles of temperature and salinity. A more realistic representation of the boundary condition can be considered in the future. In figure B.10 is represented an example of a more realistic profile of temperature and salinity, extracted from the Copernicus website (GLOBAL_REANALYSIS_PHY_001_025, http://marine.copernicus.eu). The coordinates are latitude = 40.75°N and longitude = 28.75°E.

A trial run was tested with those new values but the model was unstable and failed to run over long period of time, even after reducing the time step.

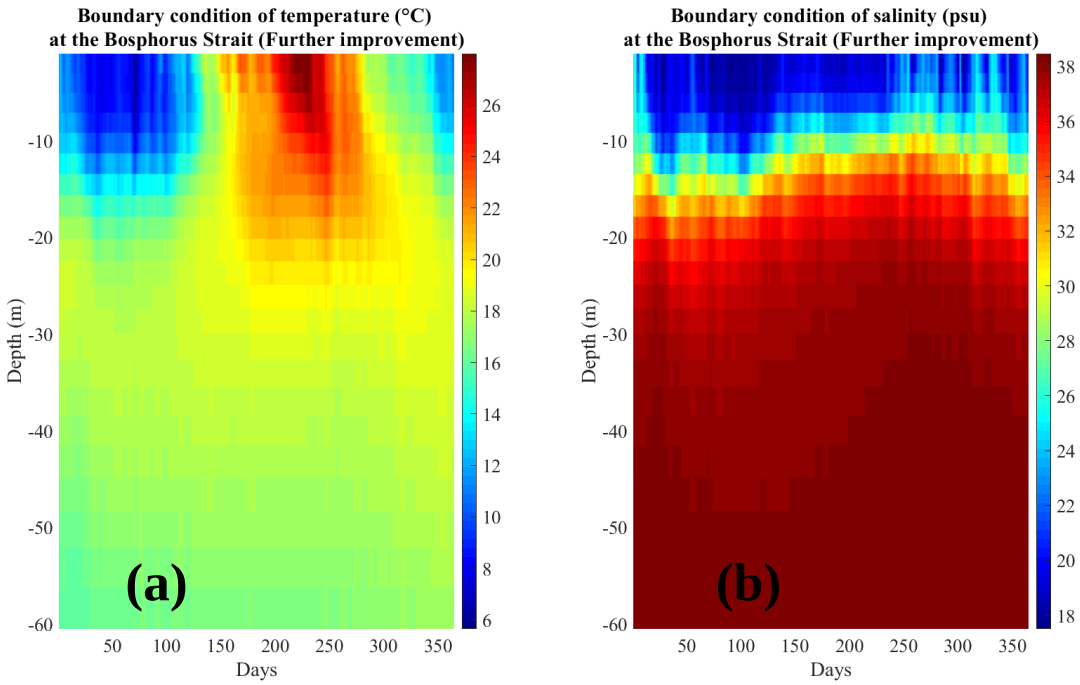

Figure B.10: Time varying profiles of (a) temperature (°C) and (b) salinity (psu) for the year 2010.

LATERAL BOUNDARY CONDITION

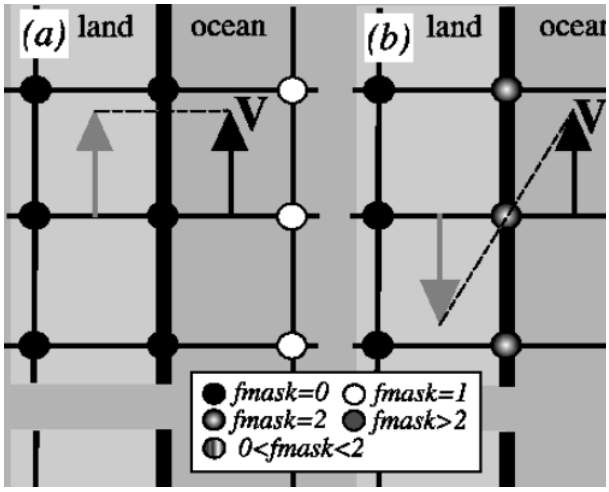

Figure B.11: Illustration of two possible lateral boundary conditions (www.nemo-ocean.eu). (a) Free slip (rn_shlat = 0) condition. The tangential velocity at the coastline is equal to the offshore velocity, meaning that the normal derivative of the tangential velocity is zero at the coast, so the mask f (vorticity) is set to 0 inside the land and just at the coast. (b) No-slip (rn_shlat = 2) condition. The tangential velocity vanishes at the coastline, assuming a linear decrease from the closest velocity grid point to the coastline. This condition is used in the model setup used in this manuscript.

ATMOSPHERIC FORCINGS (ERA5)

For the mean snowfall rate and the mean total precipitation rate, we assume that 1kg of rain water spread over 1 square meter of surface is 1 mm in thickness *i.e.* 1 kg m^{-2} ~ 1mm (water density is 1000 kg m^{-3}).

Table B.1: Description of the ERA5 atmospheric variables used in NEMO - BLACK SEA.

ERA5 VARIABLES, CDS (Climate Data Store), Long name	**ERA5 VARIABLES, Short name**	**Type**	**ERA5 UNITS**	**NEMO UNITS**
WIND				
10m_u_component_of_wind	u10	Instantaneous	m s^{-1}	m s^{-1}
10m_v_component_of_wind	v10	Instantaneous	m s^{-1}	m s^{-1}
TEMPERATURE AND PRESSURE				
2m_temperature	t2m	Instantaneous	K	K
surface_pressure	sp	Instantaneous	Pa	Pa
2m_dewpoint_temperature	d2m	Instantaneous	K	K
MEAN RATES				
mean_sea_level_pressure	msl	Averaged	Pa	Pa
mean_snowfall_rate	msr	Averaged	Kg m^{-2} s^{-1}	mm s^{-1} = Kg m^{-2} s^{-1}
mean_surface_downward_long_wave_radiation_flux	msdwlwrf	Averaged	W m^{-2}	J m^{-2} s^{-1} = W m^{-2}
mean_surface_downward_short_wave_radiation_flux	msdwswrf	Averaged	W m^{-2}	J m^{-2} s^{-1} = W m^{-2}

mean_total_precipitation_rate	mtpr	Averaged	Kg m^{-2} s^{-1}	mm s^{-1} = Kg m^{-2} s^{-1}
COMPUTED				
Specific humidity (computed from surface_pressure and 2m_dewpoint_temperature)		Instantaneous		%

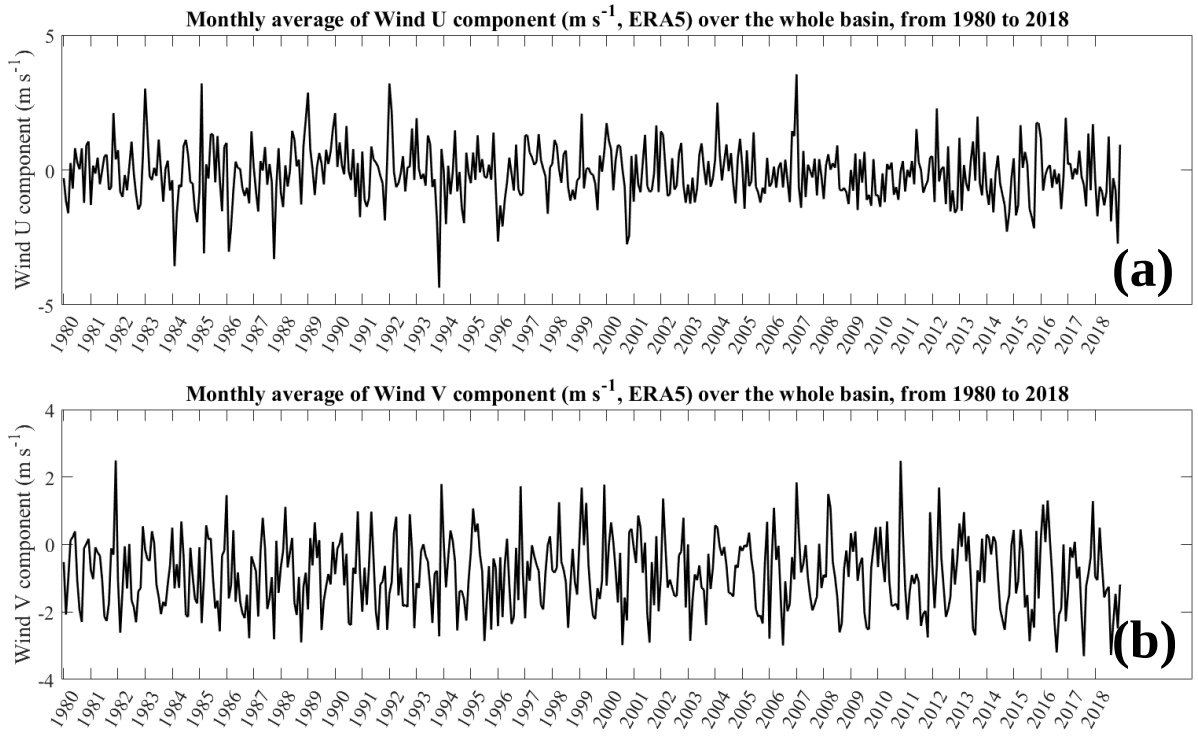

Figure B.12: Monthly time series (1980 to 2018) averaged of the whole Black Sea, of (a) the wind U component (m s^{-1}) and (b) the wind V component (m s^{-1}), both extracted from ERA5 and used as forcing for the model.

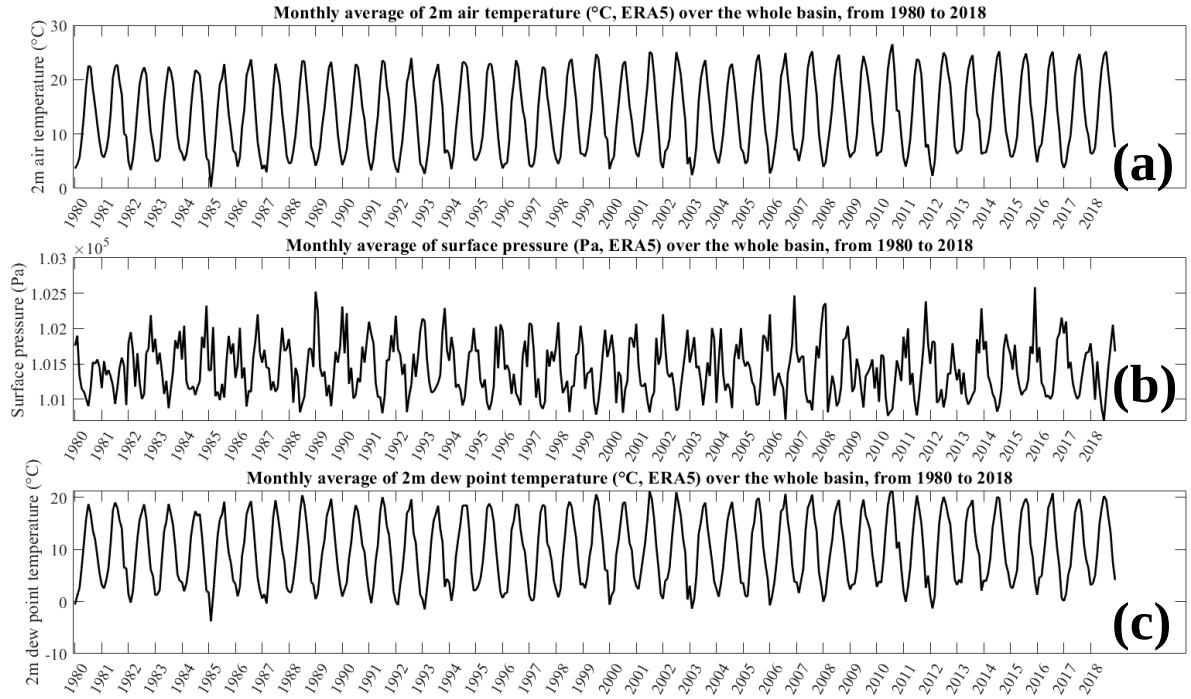

Figure B.13: Monthly time series (1980 to 2018) averaged of the whole Black Sea, of (a) the air temperature at 2m (°C), (b) the surface pressure (Pa) and (c) the dew point temperature at 2m (°C), all extracted from ERA5 and used as forcing for the model.

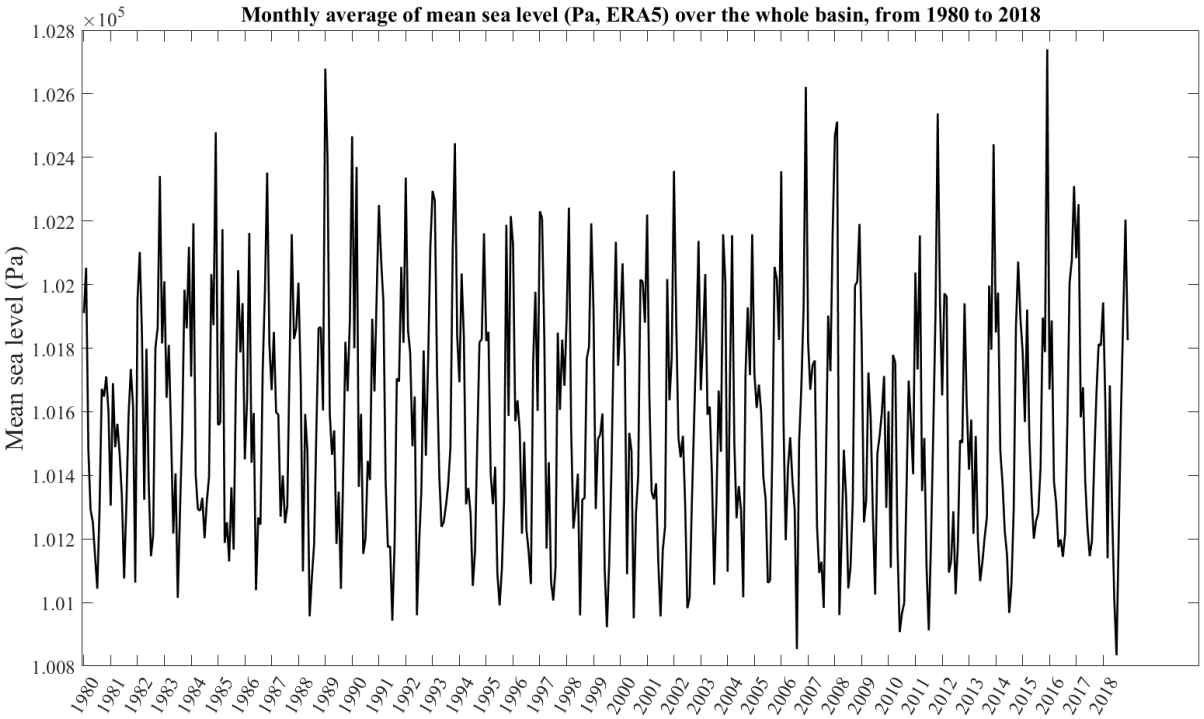

Figure B.14: Monthly time series (1980 to 2018) averaged of the whole Black Sea, of the mean sea level (Pa), extracted from ERA5 and used as forcing for the model.

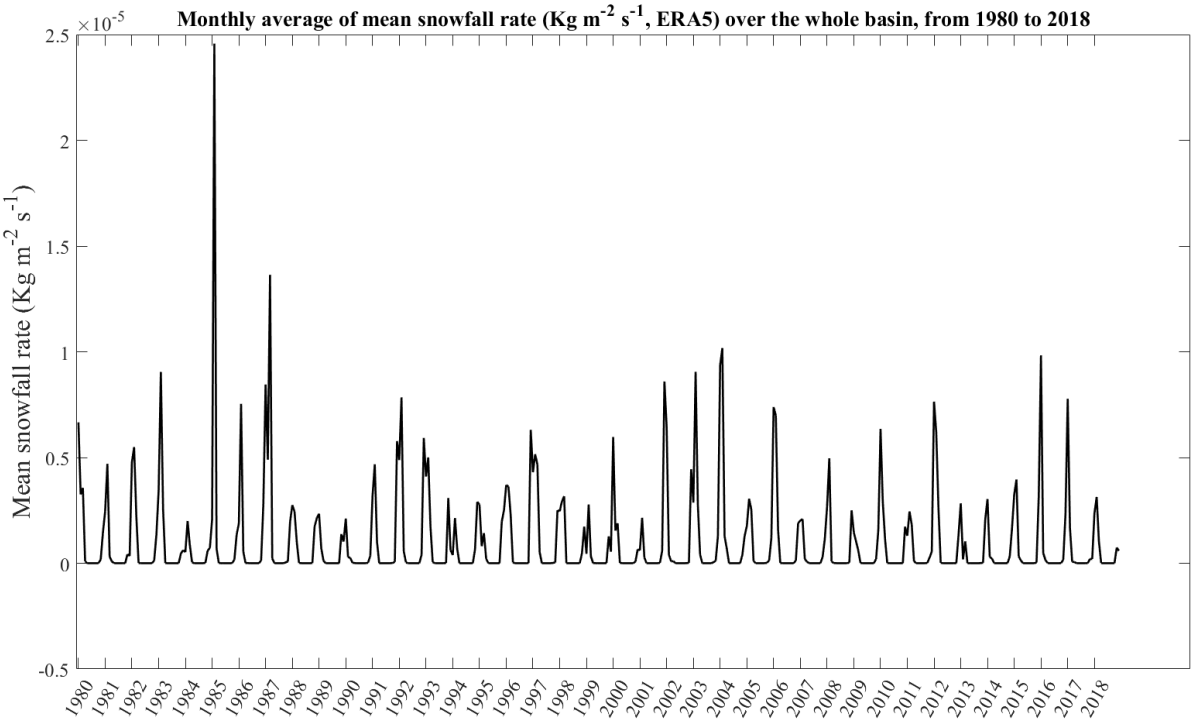

Figure B.15: Monthly time series (1980 to 2018) averaged of the whole Black Sea, of the mean snowfall rate (kg m^{-2} s^{-1}) extracted from ERA5 and used as forcing for the model.

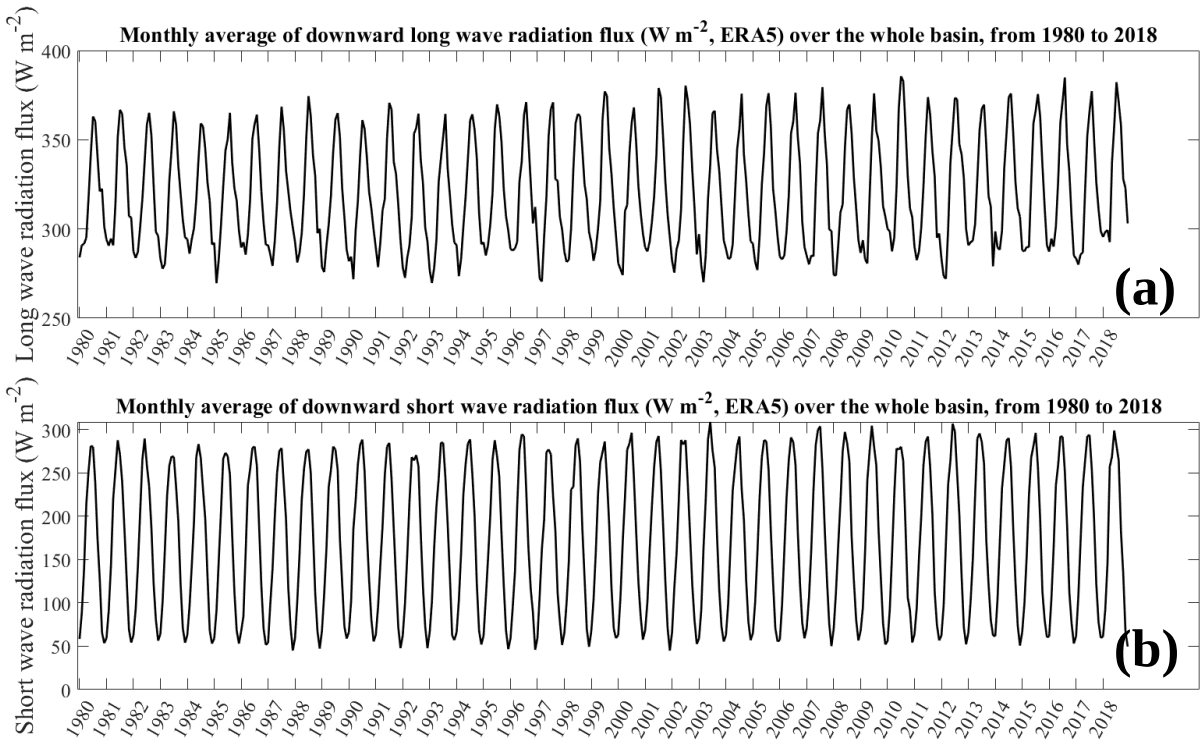

Figure B.16: Monthly time series (1980 to 2018) averaged of the whole Black Sea, of (a) the long wave radiation flux (W m^{-2}) and (b) the short-wave radiation flux (W m^{-2}), both extracted from ERA5 and used as forcing for the model.

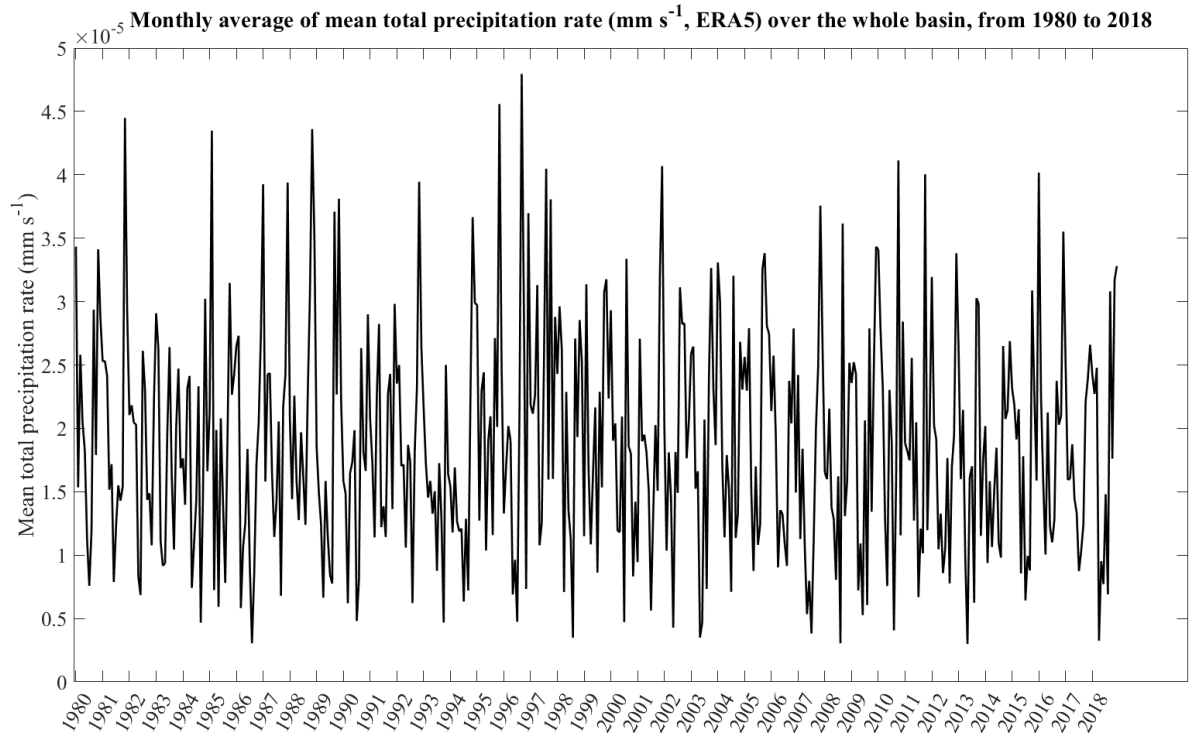

Figure B.17: Monthly time series (1980 to 2018) averaged of the whole Black Sea, of the mean total precipitation rate (mm s^{-1}), extracted from ERA5 and used as forcing for the model.

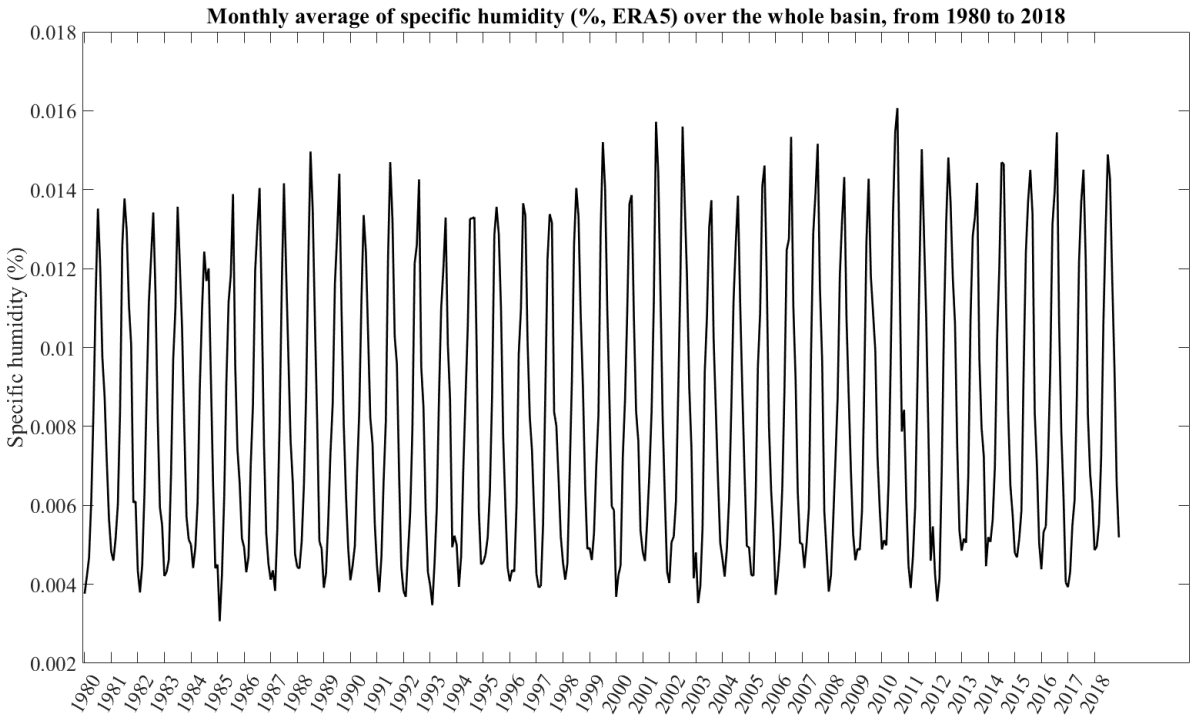

Figure B.18: Monthly time series (1980 to 2018) averaged of the whole Black Sea, of the specific humidity (%), extracted from ERA5 and used as forcing for the model.

LAND/SEA MASK (ERA5)

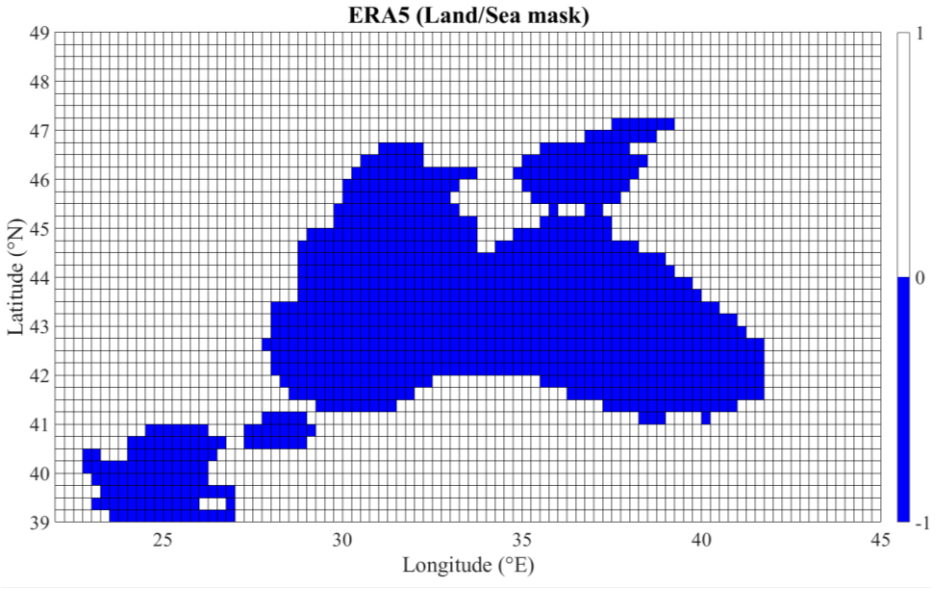

Figure B.19: Land/Sea mask from the atmospheric forcing (ERA5), used for the model interpolation (in the fly).

RIVER REFERENCES FROM THE GLOBAL RUNOFF DATA CENTER (GRDC)

Table B.2: Detailed information on the rivers extracted from The Global Runoff Data Center (GRDC). From left to right column: River number, GRDC code, River name, Station name, Period available in the archive and actual period (in red) used for the climatology computation (due to missing values), the frequency of the discharge data and the hydrological station coordinates (longitude; latitude). Only periods without NaNs were extracted and this is why the period computed differs sometimes from the period available.

N°	GRDC - Code	River name	Station name	Available period (Period used)	Frequen -cy of data	Station position (lon; lat)
1	6866500	KAMCHIA	GROZDOVO	1965 - 1979 **(1965 - 1979)**	Monthly	27.53; 43.02

2(*)	6742900	DANUBE RIVER	CEATAL IZMAIL	1921 - 2010 **(1921 - 1984)**	Monthly	28.72; 45.22;
3	6781800	DNIESTER	TIGHINA (BENDERY)	1881 - 1985 **(1965 - 1984)**	Monthly	29.47; 46.83
4	6688150	SAKARYA NEHRI	BOTBASI	1975 - 1986 **(1977-1983)**	Monthly	30.52; 40.97
5	6680802	DNIEPR	KAKHOVSKOYE VODOKHRANILISH-CHE GES	1959 - 1988 **(1959 - 1988)**	Monthly	33.18; 46.77
6	6680300	PIVDENNYY BUH	ALEKSANDROVKA	1965 - 1984 **(1965 - 1984)**	Monthly	31.27; 47.70
7	6688600	KIZILIRMAK	INOEZUEKOSACA	1975 - 1986 **(1977 - 1983)**	Monthly	35.83; 41.37
8	6688650	YESILIRMAK	CARSAMBA	1975 - 1986 **(1979 - 1981)**	Monthly	36.72; 41.19
9	6983350	KUBAN'	TIKHOVSKY	1911 - 2002 **(1965 - 1984)**	Monthly	38.23 45.19;
10	6978250	DON	RAZDORSKAYA	1881 - 2010 **(1891 - 1984)**	Monthly	40.65; 47.5
11	6885320	RIONI	SAKOCHAKIDZE	1965 - 1984 **(1965 - 1984)**	Monthly	41.8; 42.22

Note: (*) Due to the high values in the Danube discharge, the flow was spread into three different grid cells, around the Danube Delta.

Table B.3: Indices of the rivers coordinates. From left to right column: River number, GRDC code, River name, Station name, Matrix index (longitude; latitude) and river coordinates associated (longitude; latitude)

N°	**GRDC - Code**	**River name**	**Station Name**	**Matrix index (longitude; latitude)**	**River mouth coordinate in the matrix grid (longitude; latitude)**
1	6866500	KAMCHIA	GROZDOVO	16; 92	27.90; 43.00
2.a)	6742900	DANUBE RIVER	CEATAL IZMAIL	71; 172	29.62; 44.83
2.b)	6742900	DANUBE RIVER	CEATAL IZMAIL	75; 190	29.75; 45.24
2.c)	6742900	DANUBE RIVER	CEATAL IZMAIL	77; 199	29.81; 45.45
3	6781800	DNIESTER	TIGHINA (BENDERY)	97; 227	30.44; 46.08
4	6688150	SAKARYA NEHRI	BOTBASI	104; 10	30.66; 41.13
5	6680802	DNIEPR	KAKHOVSKOYE VODOKHRANILISH-CHE GES	138; 242	31.72; 46.43
6	6680300	PIVDENNYY BUH	ALEKSANDROVKA	128; 248	31.41; 46.57
7	6688600	KIZILIRMAK	INOEZUEKOSACA	274; 37	35.98; 41.74

8	6688650	YESILIRMAK	CARSAMBA	296; 21	36.67; 41.38
9	6983350	KUBAN'	TIKHOVSKY	318; 194	37.36; 45.33
10	6978250	DON	RAZDORSKAYA	379; 271	39.27; 47.09
11	6885320	RIONI	SAKOCHAKIDZE	454; 56	41.62; 42.18

How to compute the rate of flow based on the river discharge?

The rate of river flow used by the model (NEMO, v3.6) is expressed in kg m^{-2} s^{-1} and is calculated from the discharge data and consider the surface area of the grid box at the river mouth:

$$sorunoff = \frac{(River\ Dicharge * Density\ of\ water)}{Area\ of\ the\ river\ mouth\ grid\ cell}$$

with river discharge in m^3 s^{-1}, density equals 1000 kg m^{-3} and area is in m^2.

The Danube is split into three boxes.

Table B.4: For each river, the mean monthly discharge values ($m^3\ s^{-1}$) is indicated (left value in each grid cells) and the associated river flow (kg $m^{-2}\ s^{-1}$) (right value in each grid cells). The number of grid cells corresponds to the number of cells used to spread the discharge.

Months\ Rivers	**1. Kamchia**	**2.a) Danube**	**2.b) Danube**	**2.c) Danube**
Number of grid cells	1	1	1	2
Jan.	30.07 | 0.005	1360.47 | 0.216	1133.72 | 0.182	3446.52 | 0.277
Feb.	42.80 | 0.006	1424.26 | 0.227	1186.88 | 0.190	3608.13 | 0.290
Mar.	45.47 | 0.007	1687.12 | 0.268	1405.93 | 0.225	4274.03 | 0.344
Apr.	32.07 | 0.005	1963.50 | 0.313	1636.25 | 0.262	4974.22 | 0.400
May	25.47 | 0.004	2046.85 | 0.326	1705.71 | 0.273	5185.37 | 0.417
June	20.13 | 0.003	1904.36 | 0.303	1586.96 | 0.254	4824.37 | 0.388
July	10.87 | 0.002	1631.10 | 0.259	1359.25 | 0.218	4132.13 | 0.332
Aug.	8.00 | 0.001	1263.92 | 0.201	1053.26 | 0.169	3201.93 | 0.257
Sept.	7.93 | 0.001	1077.19 | 0.171	897.66 | 0.144	2728.89 | 0.219
Oct.	6.13 | $9.47.10^{-4}$	1018.29 | 0.162	848.58 | 0.136	2579.68 | 0.207
Nov.	13.93 | 0.002	1144.13 | 0.182	953.44 | 0.153	2898.45 | 0.233
Dec.	22.13 | 0.003	1337.39 | 0.213	1114.49 | 0.179	3388.06 | 0.273

Table B.4: Continue.

Months\ Rivers	**3. Dniester**	**4. Sakarya Nehri**	**5. Dniepr**	**6. Pivdennyy Buh**
Number of grid cells	**1**	**1**	**1**	**1**
Jan.	205.85 | 0.335	273.86 | 0.041	1639.48 | 0.014	86.75 | 0.269
Feb.	290.60 | 0.047	278.86 | 0.042	1754.55 | 0.020	124.35 | 0.287
Mar.	541.10 | 0.088	309.28 | 0.046	1819.75 | 0.042	258.50 | 0.298
Apr.	649.45 | 0.106	273.71 | 0.041	1814.36 | 0.035	215.20 | 0.297
May	431.00 | 0.070	187.86 | 0.028	1962.76 | 0.014	86.10 | 0.322
June	522.45 | 0.085	152.57 | 0.023	1253.54 | 0.012	70.90 | 0.205
July	495.65 | 0.081	126.28 | 0.019	892.73 | 0.015	89.50 | 0.146
Aug.	347.65 | 0.056	116.71 | 0.017	783.98 | 0.012	66.35 | 0.128
Sept.	286.75 | 0.047	118.00 | 0.018	715.21 | 0.011	67.15 | 0.117
Oct.	245.25 | 0.039	123.57 | 0.018	913.76 | 0.014	88.35 | 0.149
Nov.	256.20 | 0.042	233.86 | 0.035	1195.22 | 0.014	84.95 | 0.196
Dec.	247.70 | 0.040	195.57 | 0.029	1475.58 | 0.014	85.70 |0.242

Table B.4: Continue

Months\ Rivers	**7. Kizilirmak**	**8. Yesilirmak**	**9. Kuban**	**10. Don**
Number of grid cells	**1**	**1**	**1**	**1**
Jan.	222.71 | 0.034	189.67 | 0.028	242.50 | 0.039	301.58 | 0.050
Feb.	264.71 | 0.040	192.00 | 0.029	217.75 | 0.035	425.65 | 0.071
Mar.	320.57 | 0.048	237.00 | 0.036	288.15 | 0.046	819.07 | 0.136
Apr.	298.43 | 0.045	376.00 | 0.056	343.80 | 0.055	2048.69 | 0.339
May	235.71 | 0.036	382.00 | 0.057	496.10 | 0.079	2588.15 | 0.429
June	160.14 | 0.024	166.00 | 0.025	474.10 | 0.076	822.71 | 0.136
July	120.14 | 0.018	91.33 | 0.014	427.95 | 0.069	458.14 | 0.076
Aug.	125.43 | 0.019	86.67 | 0.013	335.70 | 0.054	390.85 | 0.065
Sept.	150.28 | 0.027	101.00 | 0.015	260.40 | 0.042	359.55 | 0.059
Oct.	167.86 | 0.025	85.33 | 0.013	232.10 | 0.037	362.07 | 0.060
Nov.	172.86 | 0.026	128.00 | 0.019	210.80 | 0.034	359.54 | 0.059
Dec.	197.86 | 0.029	174.67 |0.026	276.75 | 0.044	286.28 | 0.047

Table B.4: Continue

Months\ Rivers	**11. Rioni**
Number of grid cells	**1**
Jan.	302.40 | 0.046
Feb.	345.45 | 0.053
Mar.	429.75 | 0.065
Apr.	652.85 | 0.099
May	610.10 | 0.093
June	533.60 | 0.081
July	426.95 | 0.065
Aug.	325.45 | 0.049
Sept.	240.15 | 0.036
Oct.	293.65 | 0.045
Nov.	356.60 | 0.054
Dec.	385.10 | 0.058

LIGHT PENETRATION NOT ACTIVATED: INITIAL CONFIGURATION RESULTS

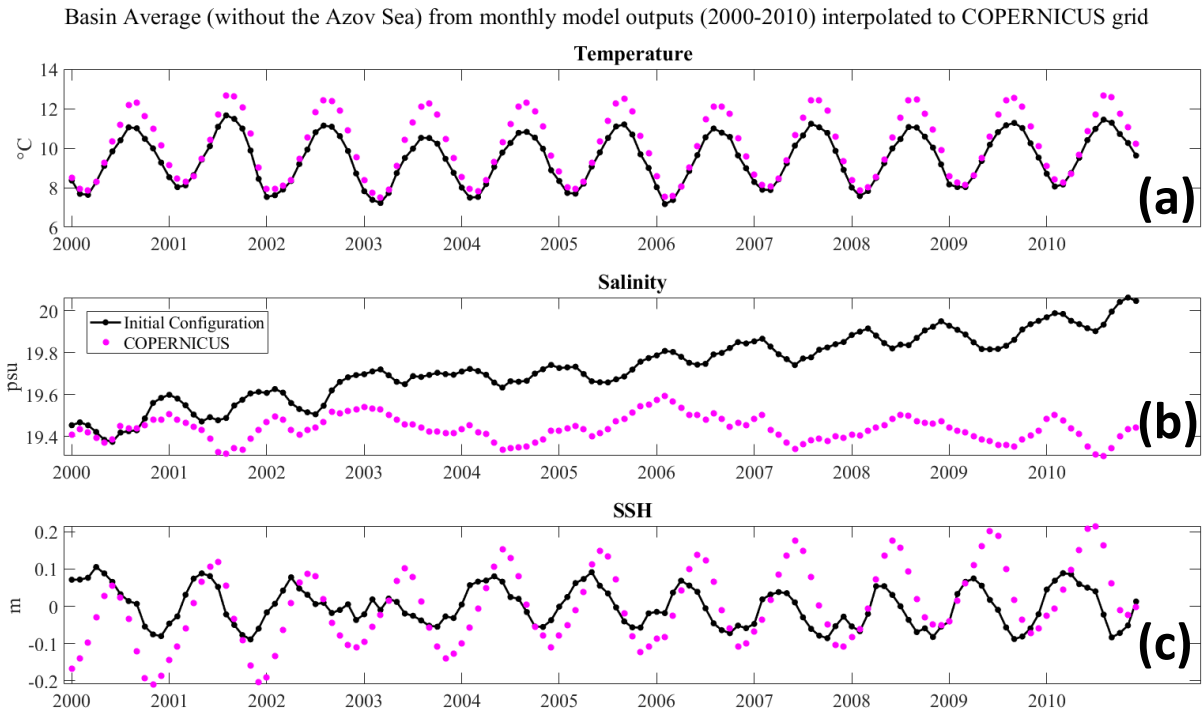

Figure B.20: Initial configuration of the model in regards of (a) temperature (°C), (b) salinity (psu) and (c) SSH (m). The light penetration scheme is **not activated**. The monthly data were averaged over the whole basin (excluding the Azov Sea) from 2000 to 2010 and interpolated into Copernicus grid. For the SSH, the mean of each time series has been substracted over the time period.

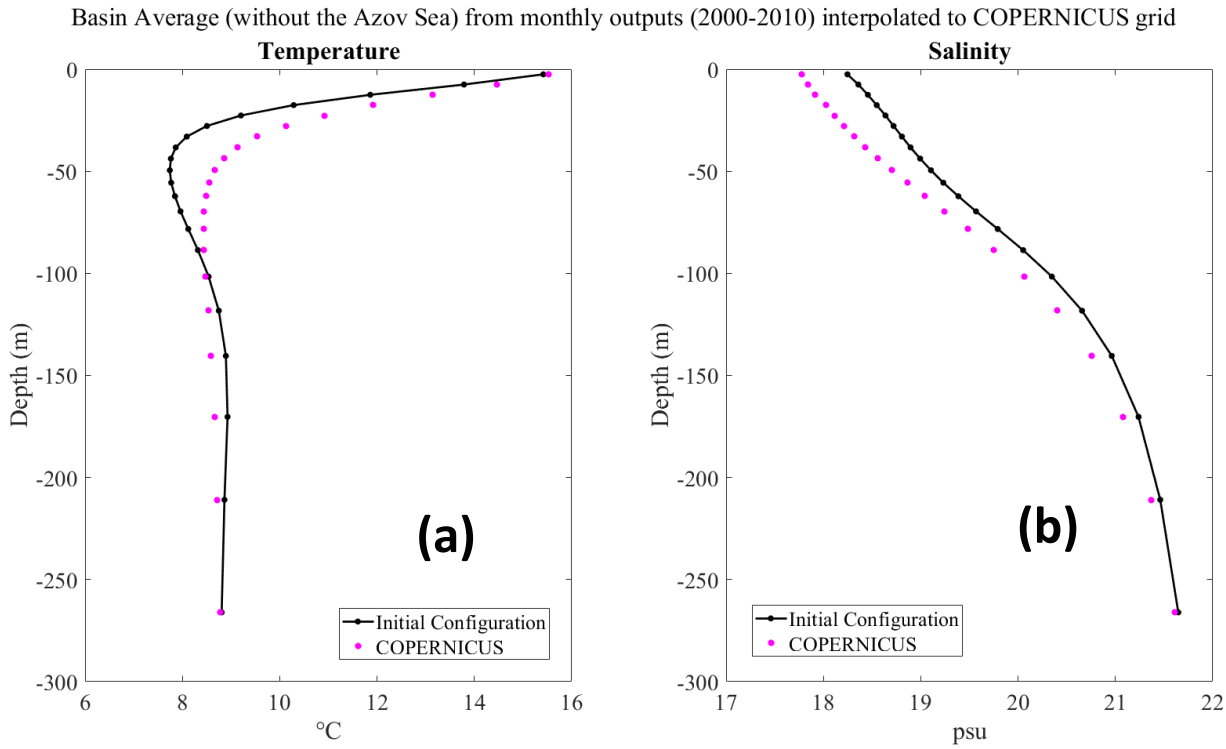

Figure B.21: Vertical profiles of (a) temperature (°C) and (b) salinity (psu) averaged over the basin without the Azov Sea for the initial configuration (no light penetration). The data were interpolated and compared to Copernicus values.

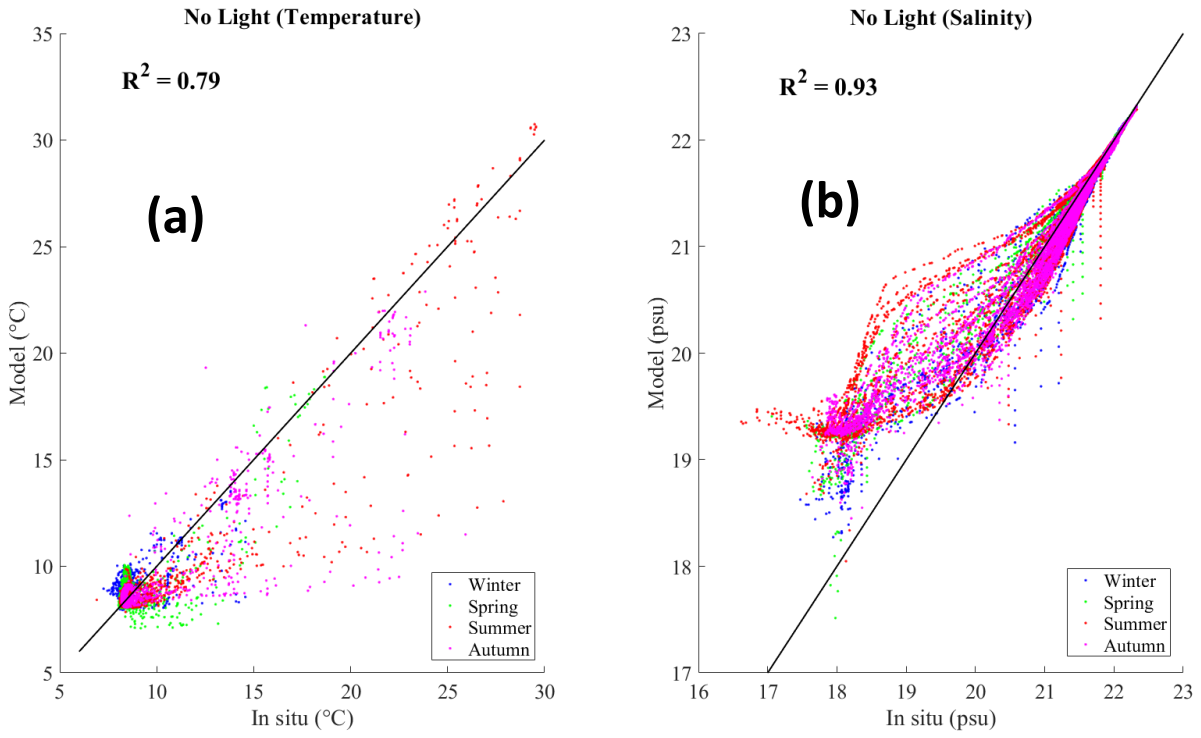

Figure B.22: Scatter plot comparison for (a) temperature (°C) (b) salinity between in situ (EN4) versus interpolated modeled values for the initial run configuration (no light penetration). The

color indicates different seasons: winter (December - March), Spring (April - May), summer (June - August) and autumn (September - November). The black line is a 1:1 line, not the linear regression. The R^2 from the linear regression is indicated for each graph.

CHLOROPHYLL *A* CLIMATOLOGY MAPS

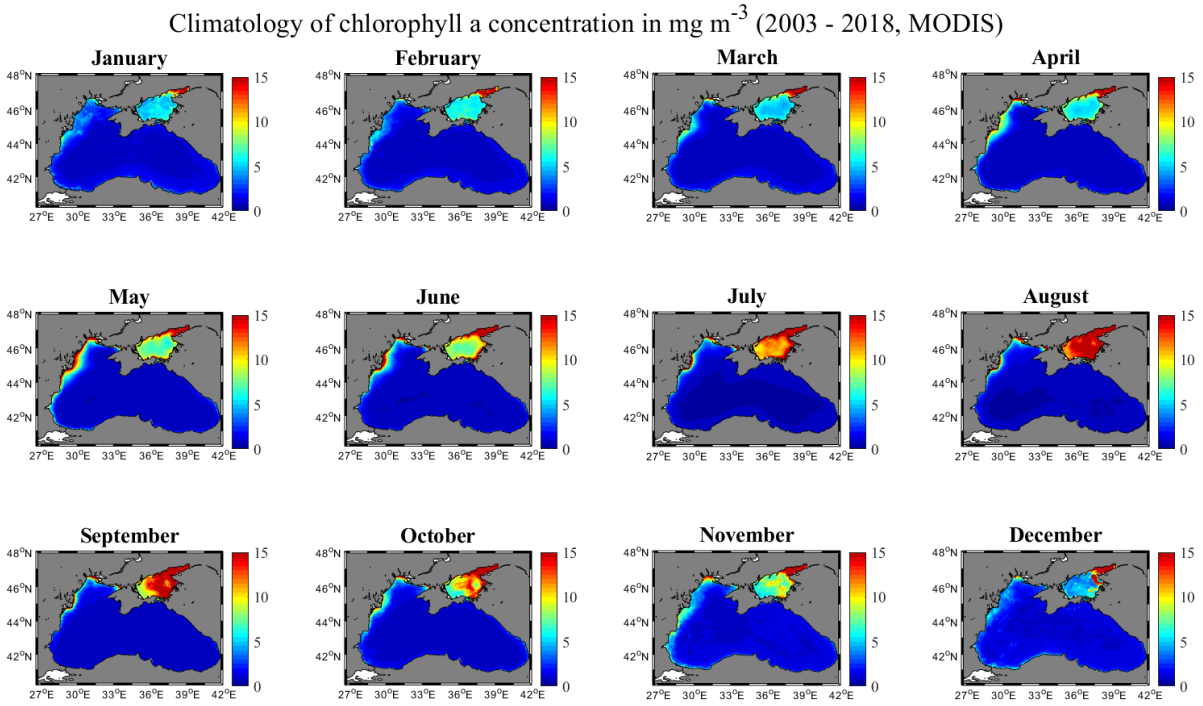

Figure B.23: Monthly climatology of chlorophyll *a* concentration (mg m^{-3}), computed from MODIS over 2003 to 2018.

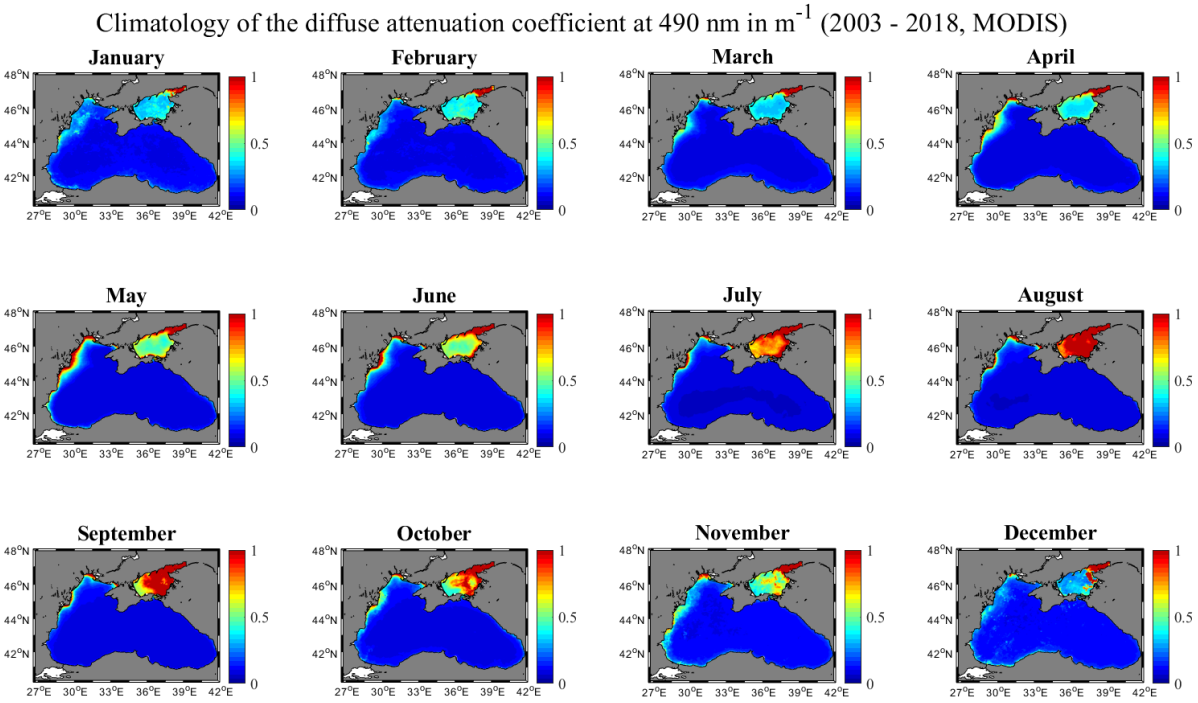

Figure B.24: Monthly climatology of diffuse attenuation coefficient at 490 nm (m^{-1}), computed from MODIS over 2003 to 2018.

COMPARISONS OF OCEAN MODELS PARAMETRISATIONS BETWEEN AMM7 - NEMO BLACK SEA AND GOTM

The comparison in the model parametrization between AMM7 (Atlantic Margin Model, 7km; O'Dea et al. 2017), NEMO (Madec et al., 2015**)** and GOTM (Umlauf et al., 2006) configurations is referred in this section.

Table B.5: Comparison between different ocean models parametrisations (AMM7, BLACK SEA - NEMO and BLACK SEA GOTM) in regards of some mixing parameters values. The comparison in the light scheme is also presented.

PARAMETERS	**OCEAN MODEL CONFIGURATIONS**		
	AMM7	**BLACK SEA-NEMO**	**BLACK SEA - GOTM**
PENETRATIVE SOLAR RADIATION			
ln_traqsr(Light penetration (T) or not (F))	**T**	**F**	
ln_qsr_rgb(RGB (Red-Green-Blue) light penetration)	**F**	**T**	
nn_chldta (RGB: Chl data (=1) or cst value (=0)),	**0**	**1**	
RUNOFFS NAMELIST SURFACE BOUNDARY CONDITION			
rn_hrnf (depth over which enhanced vertical mixing is used), in m	**1000**	**15.e0**	
rn_avt_rnf (value of the additional vertical mixing coef.), in m^2 s^{-1}	**10**	**1.e0**	
ln_rnf_depth (read in depth information for runoff)	**T**	**F**	
LATERAL MOMTENTUM BOUNDARY CONDITION			

Rn_shlat (lateral momentum boundary condition)	**0**	**2.**	
BOTTOM BOUNDARY CONDITION			
Rn_bfrien (local multiplying factor of bfr)	**50**	**1.**	
ln_bfrimp (implicit bottom friction)	**T**	**F**	
ln_loglayer (logarithmic formulation)	**T**	**F**	
nn_bbl_ldf (diffusive bbl)	**0**	**1**	
rn_ahtbbl (lateral mixing coefficient in the bbl), in $m^2\ s^{-1}$	**1000**	**2000.**	
LATERAL DIFFUSION SCHEME FOR TRACERS			
ln_traldf_hor (horizontal geopotential)	**T**	**F**	
ln_traldf_iso (iso-neutral)	**F**	**T**	
rn_aht_0 (horizontal eddy diffusivity for tracers), in $m^2\ s^{-1}$	**50**	**10.**	
TRACERS: T & S NEWTONIAN DAMPING			
nn_zdmp (vertical shape)	**0**	**1**	
HYDROSTATIC PRESSURE GRADIENT OPTION			

ln_hpg_zps (z-coordinate -partial steps)	**F**	**T**	
ln_hpg_prj (s-coordinate)	**T**	**F**	
LATERAL DIFFUSION ON MOMENTUM			
ln_dynldf_lap (laplacian operator)	**FALSE**	**.true.**	
ln_dynldf_bilap (biplacian operator)	**TRUE**	**.false.**	
ln_dynldf_level (iso-level)	**TRUE**	**.false.**	
ln_dynldf_iso (iso-neutral)	**FALSE**	**.true.**	
VERTICAL PHYSICS			
rn_avm0 (vertical eddy viscosity in m^2 s^{-1})	**0.1e-6**	**1.e-6**	**Avmolu (molecular viscosity for momentum in m^2 s^{-1}) = 1.3e-06 (default)**
ln_zdfevd (enhanced vertical diffusion)	**F**	**.true.**	
nn_evdm (evd apply on tracer or on tracer and momentum)	**1**	**0**	
rn_avevd (evd mixing coefficients in m^2 s^{-1})	**100**	**1.**	
TURBULENT EDDY KINETIC DEPENDENT VERTICAL DIFFUSION			

rn_emin (minimum value of the tke in m^2 s^{-2})	**1.e-6**	**1.e-6**	**K_min (minimum TKE in m^2 s^{-2}) = 1.e-07 (changed)**
GLS VERTICAL DIFFUSION			
rn_emin (minimum value of e in m^2 s^{-2})	**1.0e-6**	**0.5e-6**	
rn_epsmin (minimum value of eps in m^2 s^{-3})	**1.0e-12**	**1.e-9**	**Eps_min (minimum dissipation rate in m^2 s^{-3}) = 1.0e-12 (changed)**
rn_clim_galp (galperin limit, limit on the dissipation rate under stable stratification)	**0.267**	**0.1**	**Galp (coef for length scale limitation) = 0.53 (default)**
rn_charn (charnock constant for wb induced roughness length)	**100000.0**	**70000.**	**Charnock_val (emp. constant in Charnock formula) = 1400.0 (default)**
nn_z0_met (Method for surface roughness computation)	**1**	**2**	
rn_hsro (minimum surface roughness)	**0.003**	**0.02**	

DEFAULT PARAMETERS VALUES FOR THE MIXING SCHEME

Details of the default namelist set up in NEMO v3.6. In red are indicated the parameters that were investigated.

CONTROL RUN

```
...
!-----------------------------------------------------------------------
&namlbc        !   lateral momentum boundary condition
!-----------------------------------------------------------------------
   rn_shlat    =    2.     !  shlat = 0  !  0 < shlat < 2  !  shlat = 2  !  2 < shlat
                       !  free slip  !   partial slip  !   no slip   ! strong slip
   ln_vorlat   = .false.   !  consistency of vorticity boundary condition with analytical eqs.
/


...


!-----------------------------------------------------------------------
&namzdf_gls                !   GLS vertical diffusion                   ("key_zdfgls")
!-----------------------------------------------------------------------
   rn_emin       = 0.5e-6  !  minimum value of e   [m2/s2]
   rn_epsmin     = 1.e-9   !  minimum value of eps [m2/s3]
   ln_length_lim = .true.  !  limit on the dissipation rate under stable stratification (Galperin et al., 1988)
   rn_clim_galp  = 0.1     !  galperin limit
   ln_sigpsi     = .true.  !  Activate or not Burchard 2001 mods on psi schmidt number in the wb case
   rn_crban      = 100.    !  Craig and Banner 1994 constant for wb tke flux
   rn_charn      = 70000.  !  Charnock constant for wb induced roughness length
   rn_hsro       =  0.02   !  Minimum surface roughness
   rn_frac_hs    =   1.3   !  Fraction of wave height as roughness (if nn_z0_met=2)
   nn_z0_met     =    2    !  Method for surface roughness computation (0/1/2)
```

```
   nn_bc_surf    =    1   !  surface condition (0/1=Dir/Neum)
   nn_bc_bot     =    1   !  bottom condition (0/1=Dir/Neum)
   nn_stab_func  =  2     !  stability function (0=Galp, 1= KC94, 2=CanutoA, 3=CanutoB)
   nn_clos       =  1     !  predefined closure type (0=MY82, 1=k-eps, 2=k-w, 3=Gen)
/
...
```

APPENDIX C

- **SPATIAL MAP OF THE CIL**

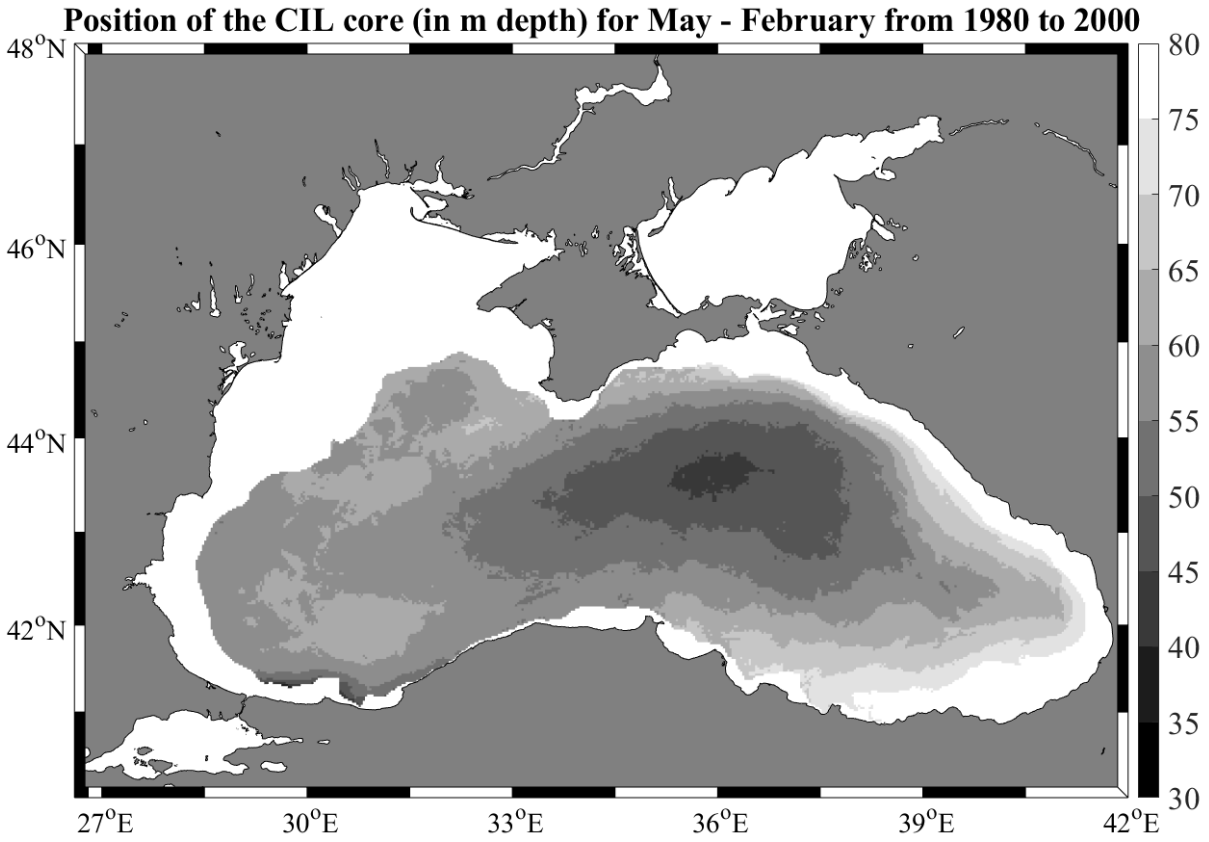

Figure C.1: Results from the model NEMO-BLACK SEA which indicates the position of the CIL core depth (m) from May – February 1980 to 2000.

CIL DENSITY BOUNDARIES (EXAMPLES FROM THE LITERATURE)

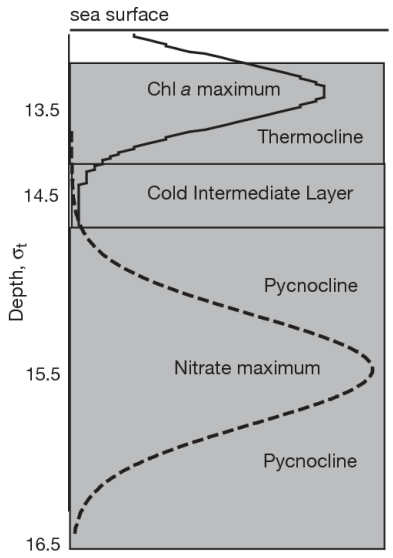

Figure C.2: Indication of the CIL location in the water column inside the open Black Sea during warm months (from Yunev et al. (2005)).

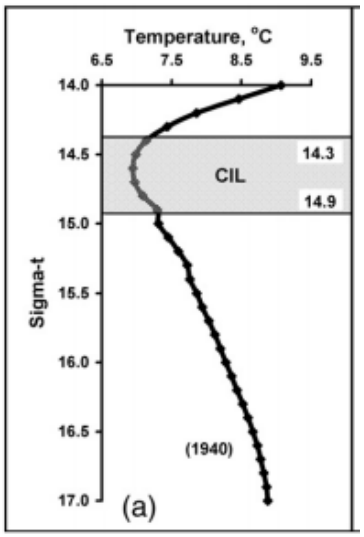

Figure C.3: Vertical average of temperature versus density for May-October (from Mikaelyan et al. (2013)).

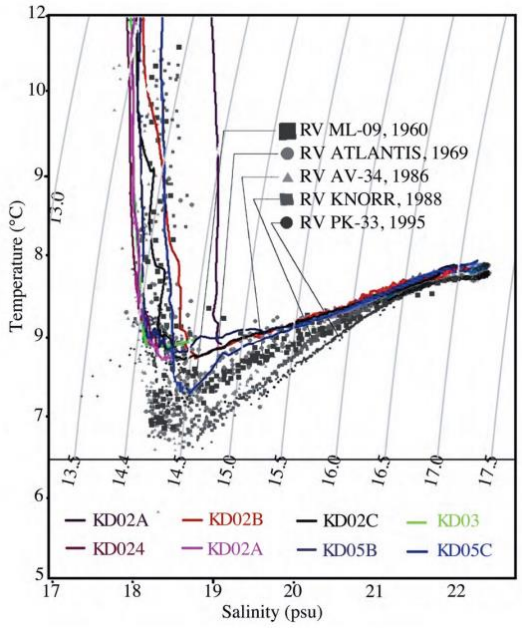

Figure C.4: TS diagram from CTD data obtained from different expeditions made from 1960 to 2008 for southern stations in the Black Sea (details of the datasets are in Ozkan et al. (2012)).

Table C.1: Table of physical symbols used for the Walin framework.

Variable name	**Description**	**Units**	**Directly calculated (C) / Diagnosed from other quantities (D) / NEMO output (M)?**
C_p	Heat capacity for seawater at constant pressure	J kg^{-1} K^{-1}	(C): gsw toolbox in Matlab (gsw_cp_t_exact function)
D_{diff}	Diffusive density flux	kg s^{-1}	
D_{in}	Surface density flux into the ocean	kg m^{-2} s^{-1}	(D): see equation (4.3)
dx	Latitudinal distance between two grid points	m	~ 2.63*10^3 m

ε	Evaporation rate	kg m^{-2} s^{-1}	Not used
$\varepsilon - P - R$	Evaporation - precipitation - runoff (positive when the flux is out of the ocean)	kg m^{-2} s^{-1}	(M) : ($empmr$ variable)
G	Diapycnal volume flux or transformation $G(\rho) > 0$ -> directed from light to dense	m^3 s^{-1}	(D): see equations (4.4 and 4.5)
$\mathcal{H}$	Heat flux into the ocean $\mathcal{H} > 0$: directed into the ocean	J m^{-2} s^{-1} = W m^{-2}	(M): (qt variable)
L_y	Longitudinal distance between two grid points	m	~ 2.54*10^3 m
$M\Delta\rho$	Water-mass transformation in a density interval, $\Delta\rho$	m^3 s^{-1}	(D): see equation (4.8)
P	Precipitation rate	kg m^{-2} s^{-1}	Not used
S	Salinity, concentration of dissolved mass	g kg^{-1}	(M): ($soce$ variable)
T	Temperature	°C	(M): ($toce$ variable)
α_T	Temperature dependent thermal expansion coefficient of seawater	K^{-1}	(C): gsw toolbox in Matlab (gsw_alpha function)

β_s	Haline contraction coefficient of seawater	$(g\ kg^{-1})^{-1}$	(C): gsw toolbox in Matlab (gsw_beta function)
θ	Potential temperature	°C	
ρ	Density	$kg\ m^{-3}$	
ρ_0	Constant reference density	$kg\ m^{-3}$	-
ρ_θ	Potential density	$kg\ m^{-3}$	-
σ_θ	Sigma theta, $\rho_\theta - 1000$ $Kg\ m^{-3}$	$kg\ m^{-3}$	-
τ	$t_1 - t_0$	Units of time	
$\Delta\psi$		$m^3\ s^{-1}$	

- **TYPICAL T-S DIAGRAM INSIDE THE WESTERN GYRE IN SUMMER**

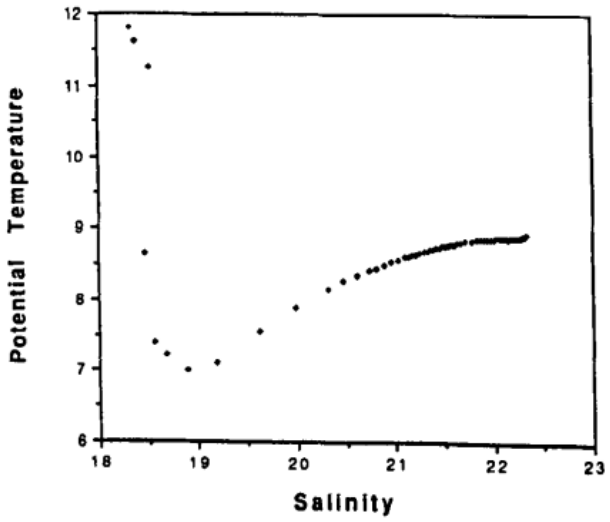

Figure C.5: Potential temperature - salinity diagram extracted from Murray et al. (1991). Profile representative of the center of the western gyre. Date of extraction is 7th June 1988 at the location of 42°50.53'N and 31°58.85'E.

HEAT FLUXES FROM STANEV ET AL. (2003)

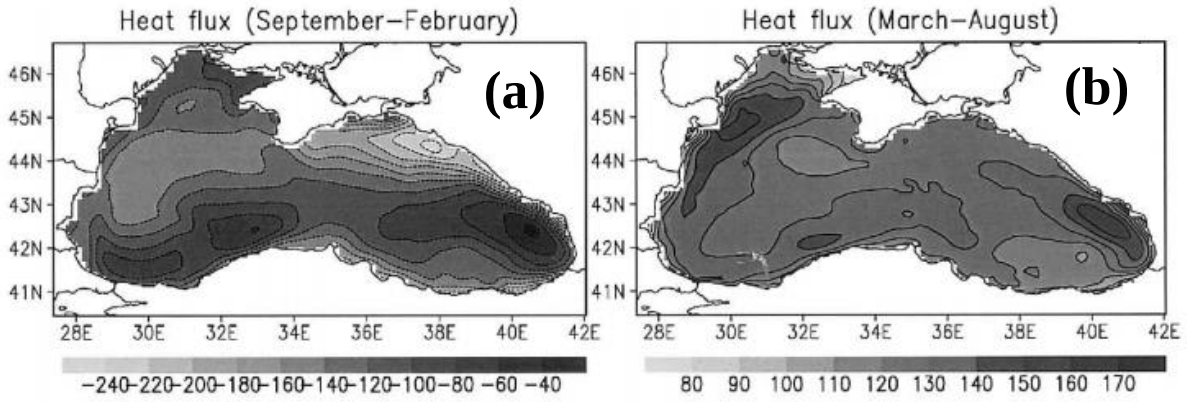

Figure C.6: Heat fluxes (W m^{-2}) during (a) the cold season (September to February) and (b) the warm season (March to August).

NAO CLIMATIC INDEX: TIME SERIES

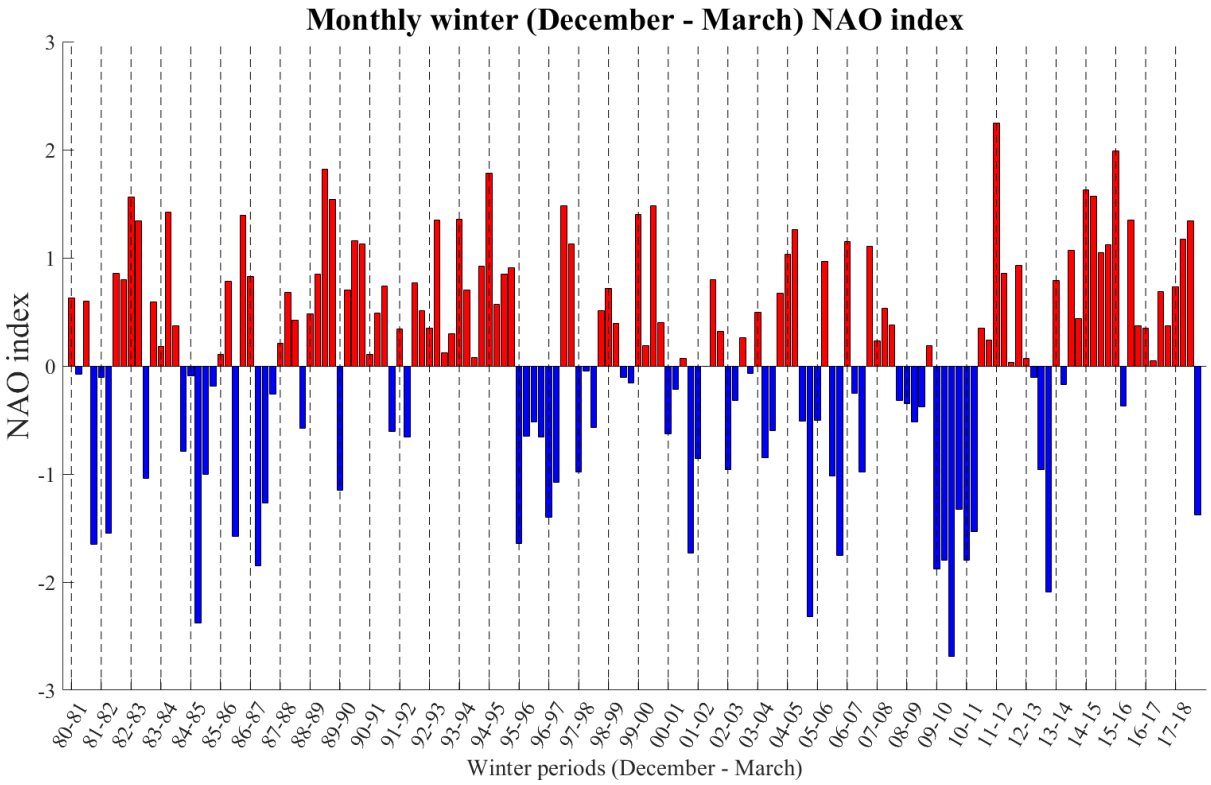

Figure C.7: Monthly winter (December - March) NAO index from 1980 to 2018.

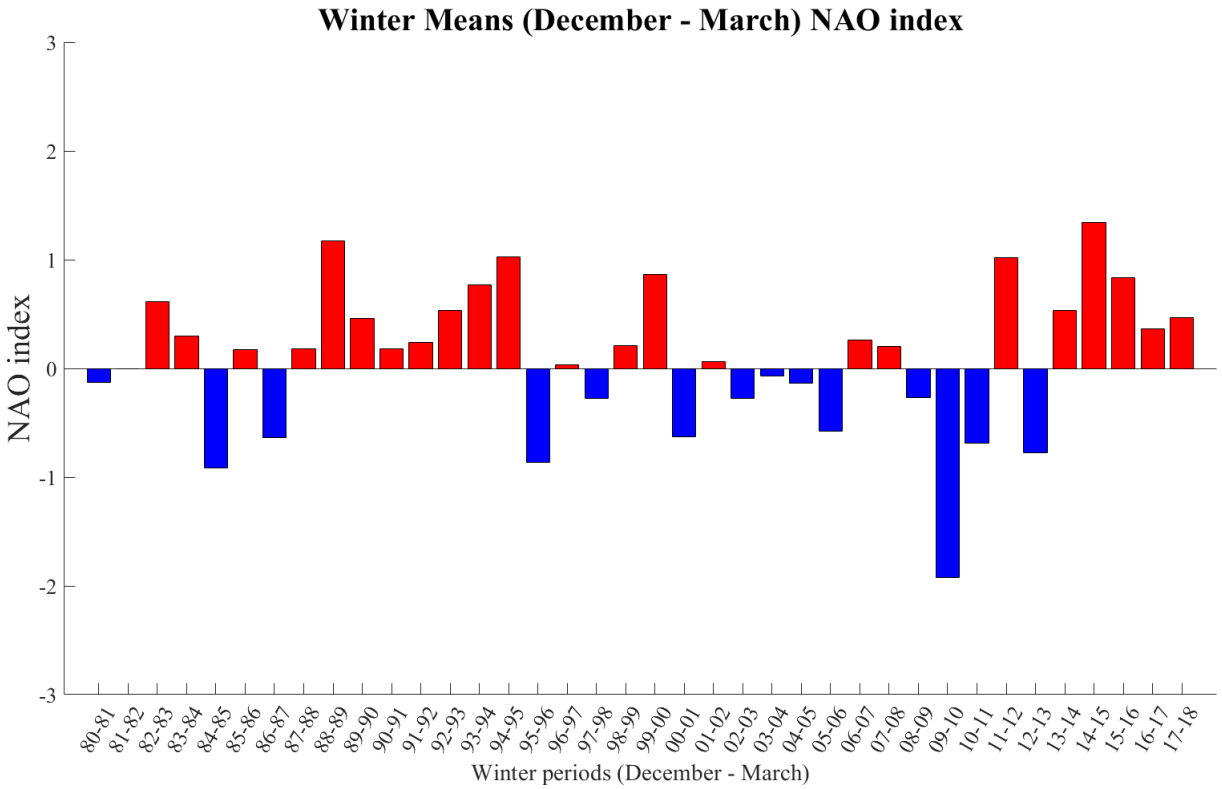

Figure C.8: Winter means (December - March) from 1980 to 2018 of the NAO index.

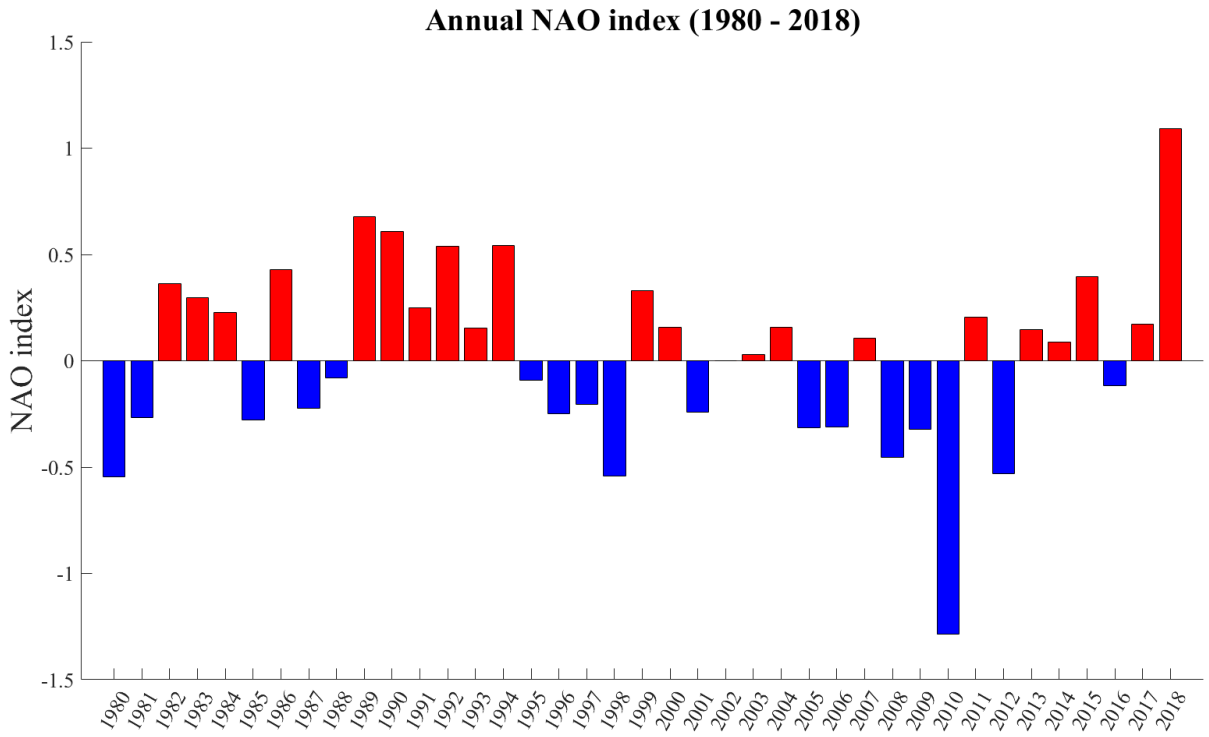

Figure C.9: Time series of annual NAO from 1980 to 2018.

EA/WR CLIMATIC INDEX: TIME SERIES

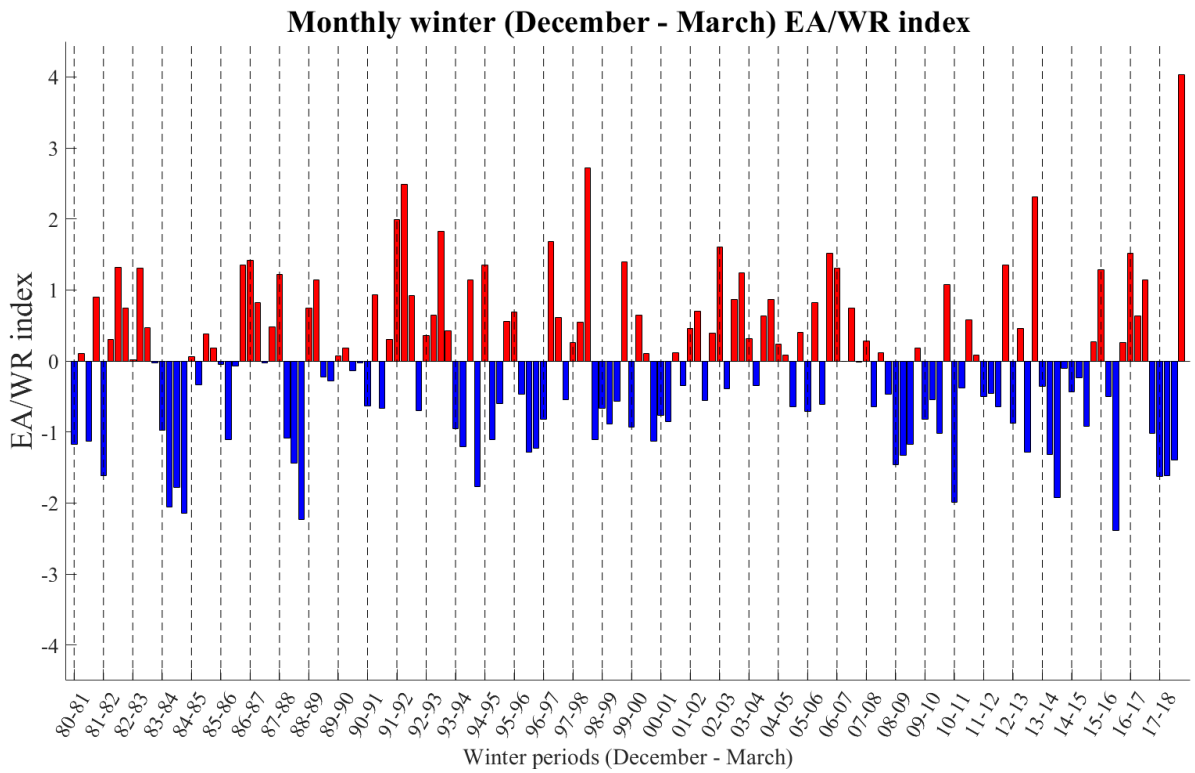

Figure C.10: Monthly winter (December - March) EA/WR index from 1980 to 2018.

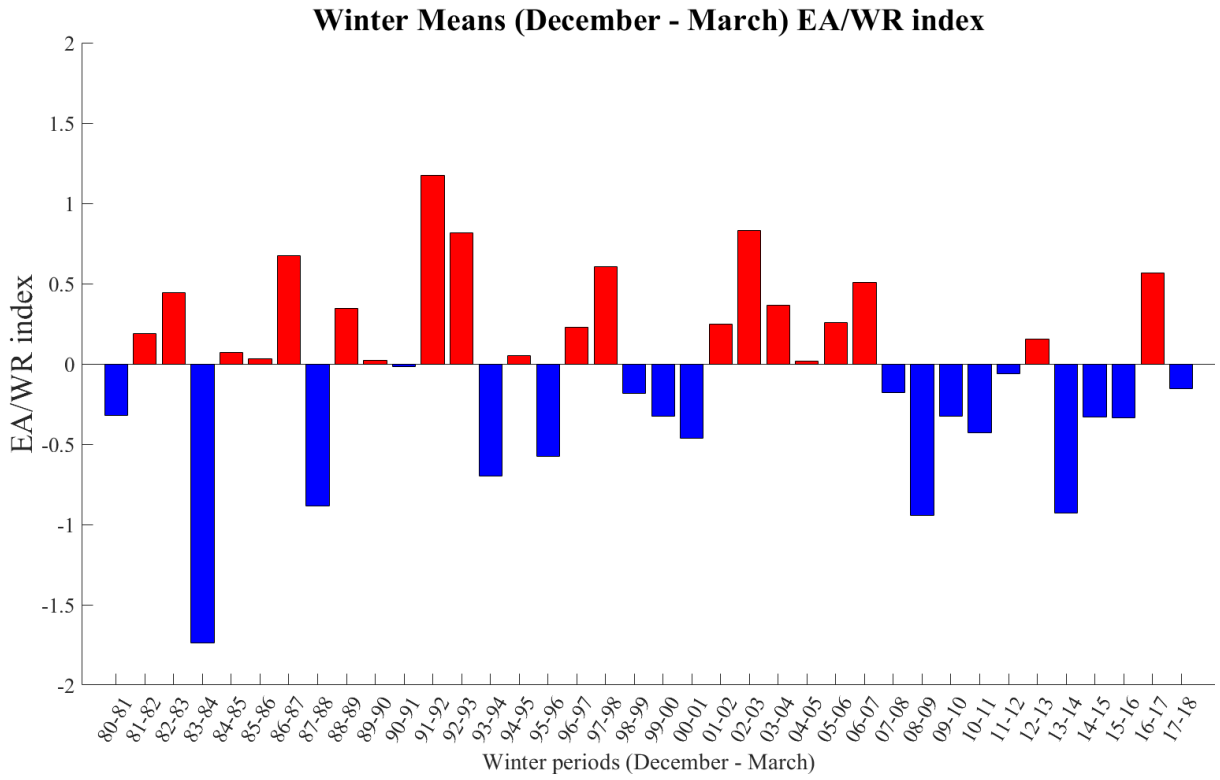

Figure C.11: Winter means (December - March) from 1980 to 2018 of the EA/WR index.

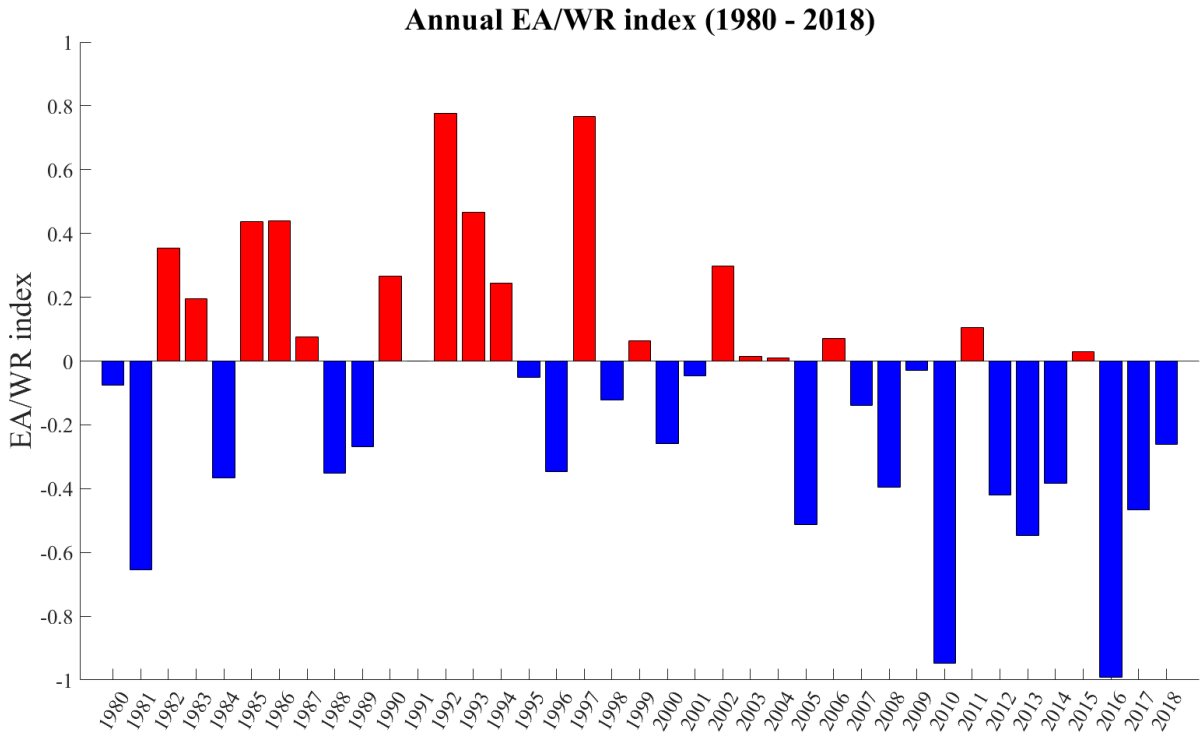

Figure C.12: Time series of annual EA/WR from 1980 to 2018.

MEI CLIMATIC INDEX: TIME SERIES

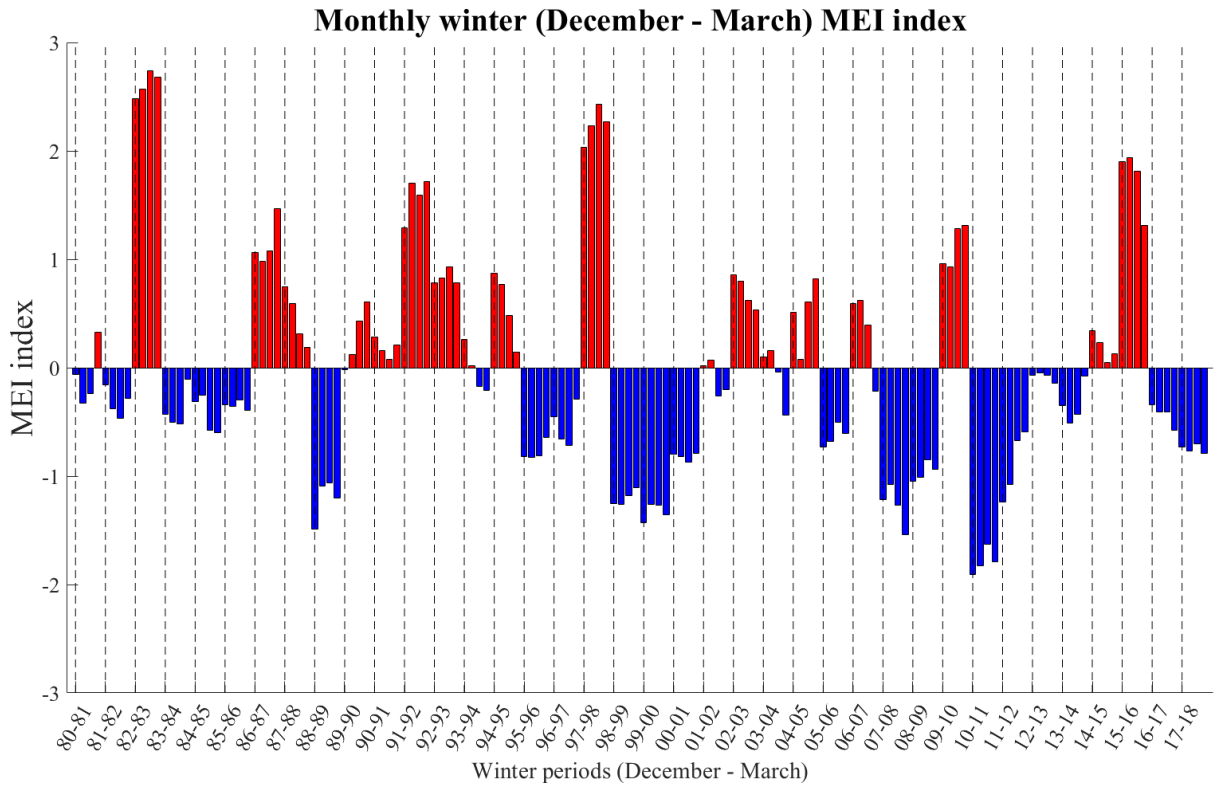

Figure C.13: Monthly winter (December - March) MEI index from 1980 to 2018.

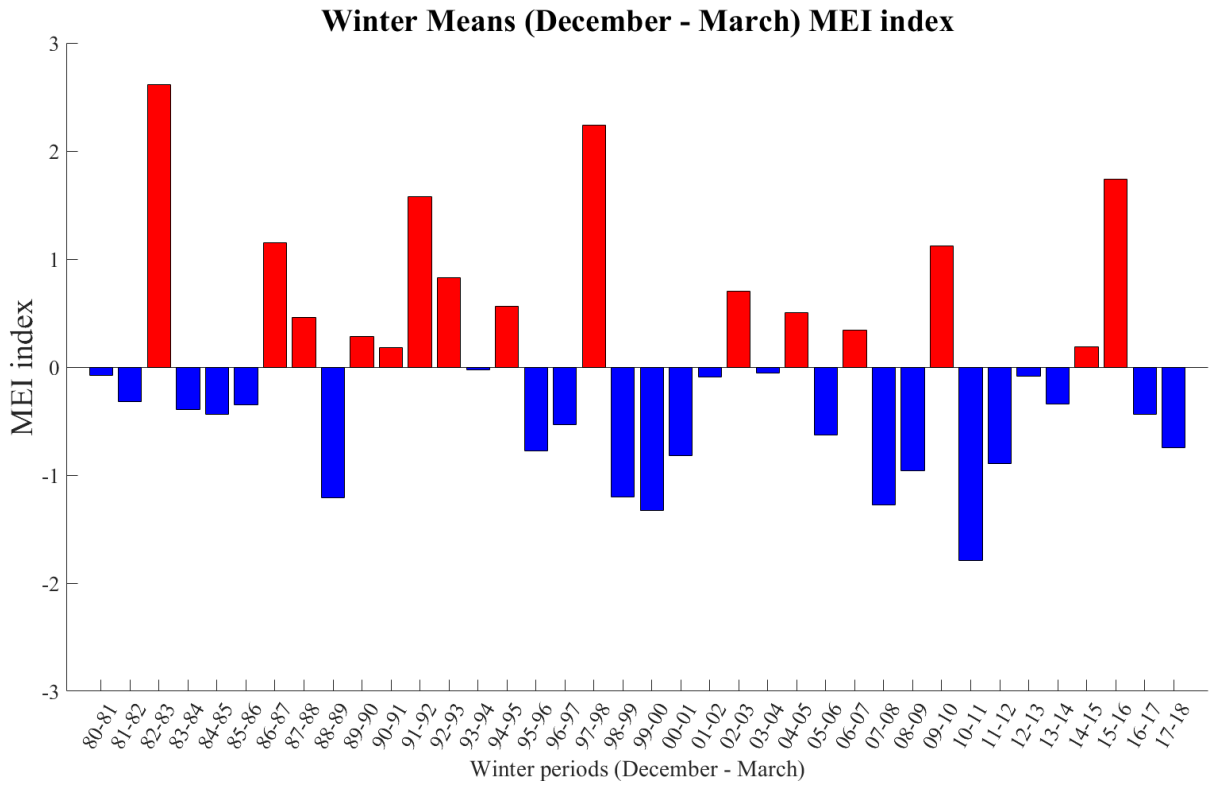

Figure C.14: Winter means (December - March) from 1980 to 2018 of the MEI index.

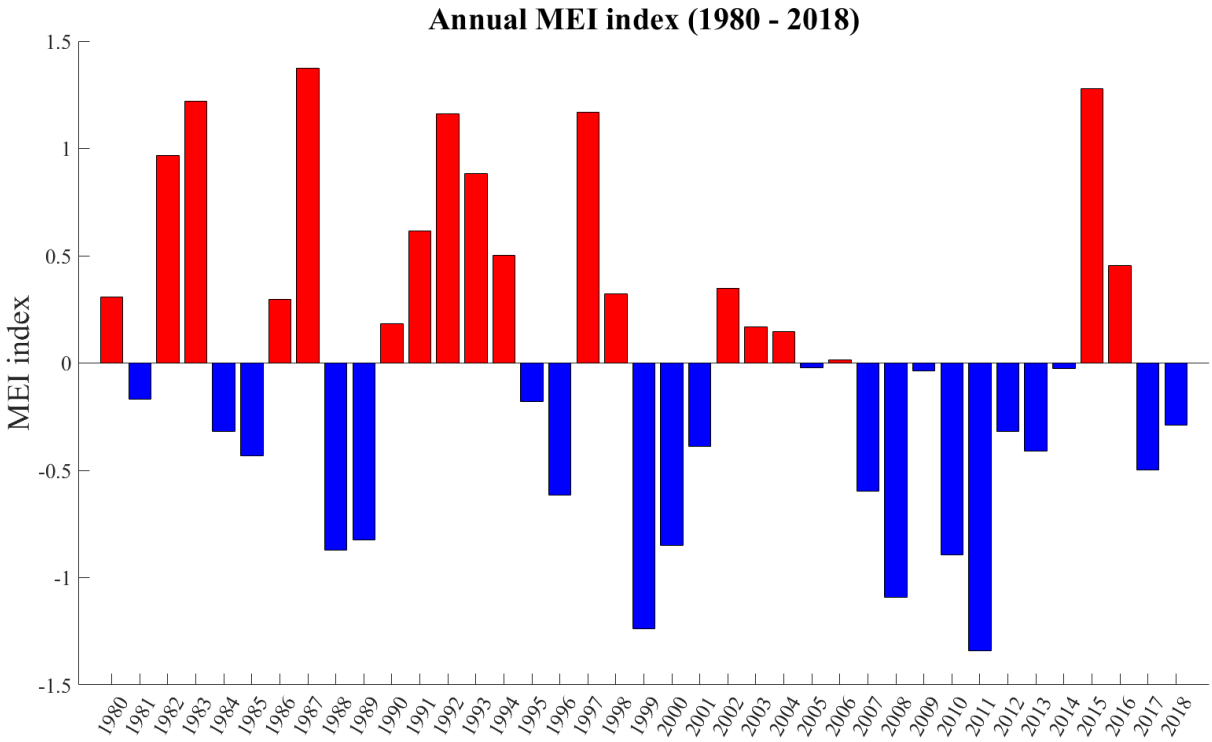

Figure C.15: Time series of annual MEI from 1980 to 2018.

AIR TEMPERATURE ANOMALIES (WINTER AND ANNUAL)

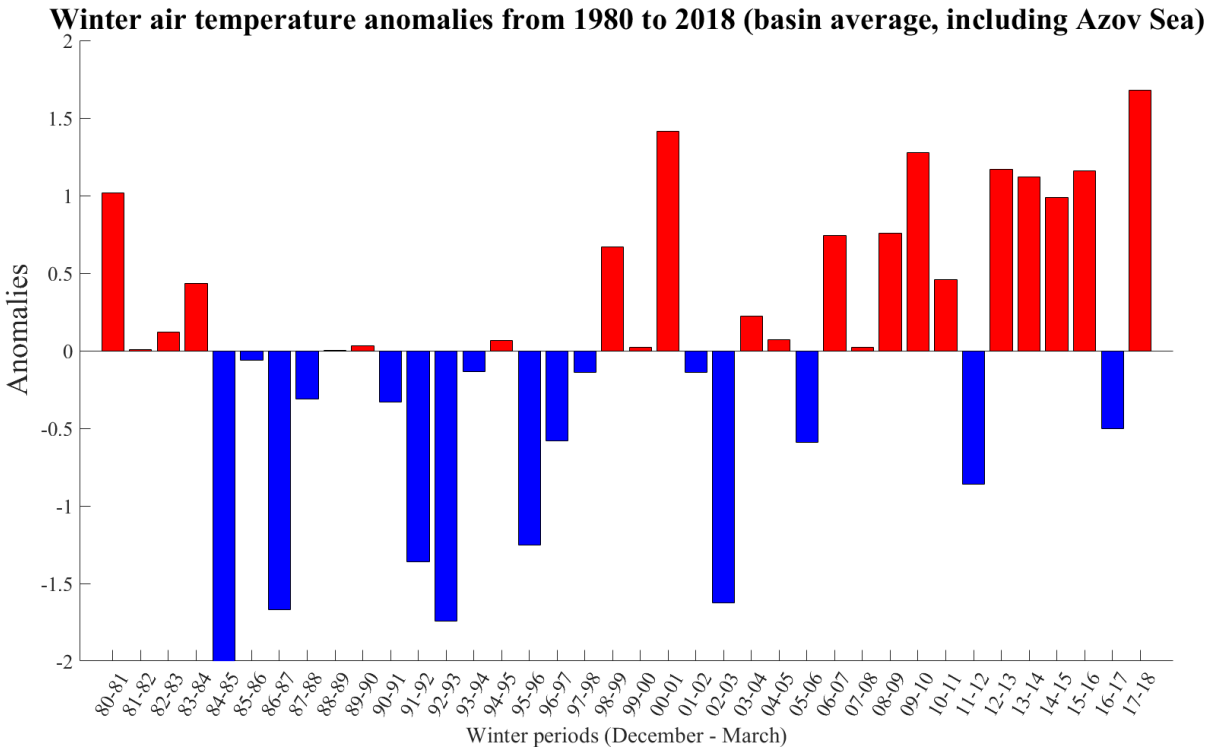

Figure C.16: Winter anomalies of air temperature (°C), averaged from December to March.

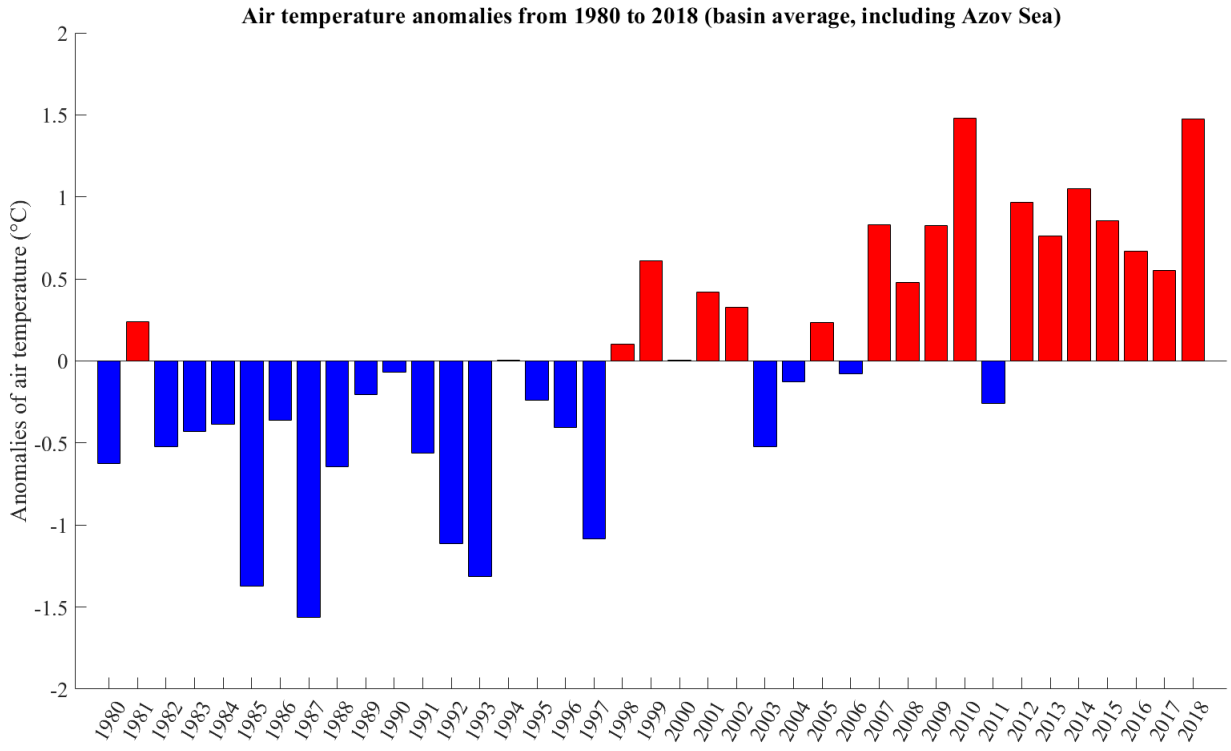

Figure C.17: Annual anomalies of air temperature (°C), averaged from December to March.

Table C.2: Values of R^2 between climatic index (NAO, EA/WR, MEI), Air Temperature (°C) with the formation rates at 14.25 kg m^{-3} and 14.75 kg m^{-3}. Winter period is between December to March. An asterisk (*) indicates a significant correlation. The results are for the Deep Black Sea area. The sign of the correlation is in parenthesis.

Values of R^2 over 1980 - 2018 Deep Black Sea		Annual formation rates at the density classes (kg m^{-3}):	
		14.25	14.75
NAO	Annual	0.002 (+)	0.015 (+)
	Winter	0.002 (-)	0.013 (+)
EA/WR	Annual	$7x10^{-6}$ (-)	0.162* (+)
	Winter	0.002 (-)	0.111* (+)
MEI	Annual	0.019 (-)	0.061 (+)
	Winter	0.001 (+)	0.022 (+)
Air temperature (°C) anomalies	Annual	0.017 (+)	0.397* (-)
	Winter	0.22* (+)	0.687* (-)

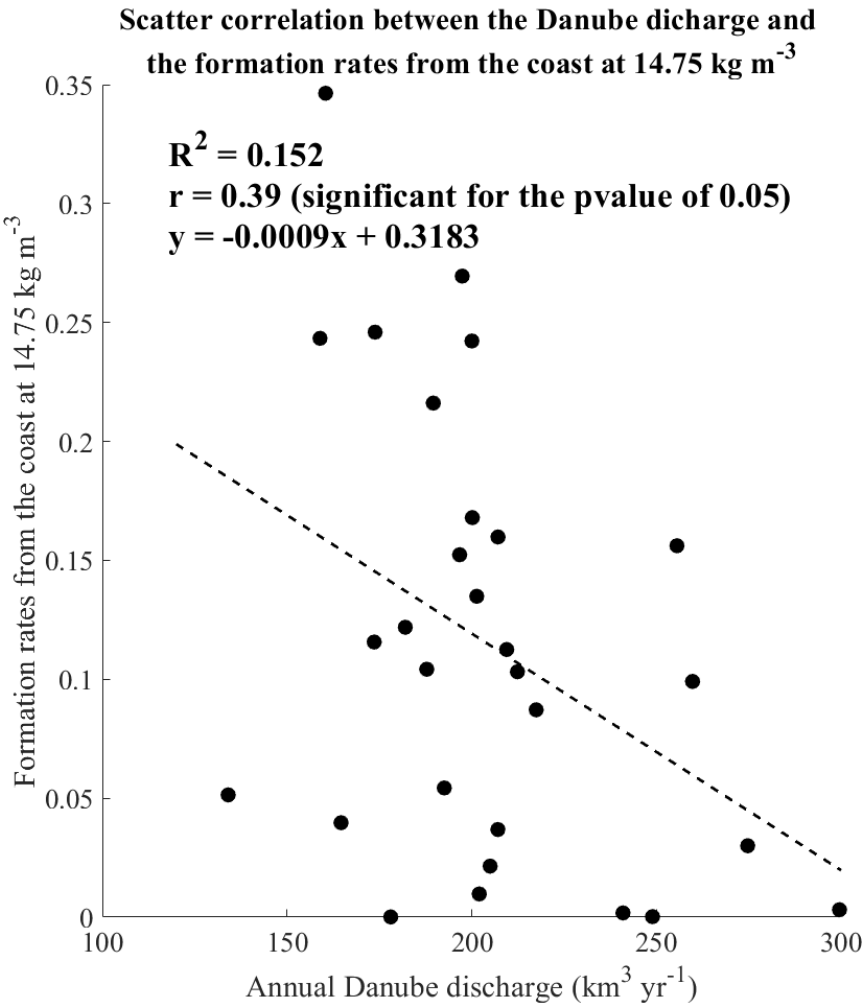

Figure C.18: Scatter correlation between the annual Danube discharge and the formation rates over the coast at 14.75 kg m^{-3} from 1980 to 2017.

Bibliography

Agirbas, E., Feyzioglu, A. M., Aytan, U., Valente, A., & Yildiz, I. (2015). Are trends in SST, surface Chlorophyll-*a*, primary production and wind stress similar or different over the decadal scale in the south-eastern Black Sea. *Cah. Biol. Mar , 56* (4), 329-336.

Akpinar, A., Fach, B. A., & Oguz, T. (2017). Observing the subsurface thermal signature of the Black Sea cold intermediate layer with Argo profiling floats. *Deep Sea Research Part I: Oceanographic Research Papers , 124*, 140-152.

Alkan, A., Serdar, S., Fidan, D., Akbaş, U., Zengin, B., & Kılıç, M. B. (2013). Physico-chemical characteristics and nutrient levels of the eastern Black Sea rivers. *Turkish Journal of Fisheries and Aquatic Sciences , 13* (5), 847-859.

Altıok, H., Sur, H., & Yüce, H. (2012). Variation of the cold intermediate water in the Black Sea exit of the Strait of Istanbul (Bosphorus) and its transfer through the strait. *Oceanologia , 54* (2), 233-254.

Altıok, H., & Kayışoğlu, M. (2015). Seasonal and interannual variability of water exchange in the Strait of Istanbul. Mediterranean Marine Science, 16 (3), 644-655.

Arpe, K., Bengtsson, L., Golitsyn, G., Mokhov, I., Semenov, V., & Sporyshev, P. (2000). Connection between Caspian Sea level variability and ENSO. *Geophysical research letters , 27* (17), 2693-2696.

Badin, G., Williams, R. G., & Sharples, J. (2010). Water-mass transformation in the shelf seas. *Journal of Marine Research , 68* (2), 189-214.

Badin, G., Williams, R. G., Jing, Z., & Wu, L. (2013). Water mass transformations in the Southern Ocean diagnosed from observations: Contrasting effects of air--sea fluxes and diapycnal mixing. *Journal of Physical Oceanography , 43* (7), 1472-1484.

Barnston, A. G., & Livezey, R. E. (1987). Classification, seasonality and persistence of low-frequency atmospheric circulation patterns. Monthly weather review, 115(6), 1083-1126.

Behrenfeld, M. J., Boss, E., Siegel, D. A., & Shea, D. M. (2005). Carbon-based ocean productivity and phytoplankton physiology from space. *Global biogeochemical cycles , 19* (1).

Belokopytov, V. (2004). Thermohaline and Hydrological-Acoustic Structure of Waters in the Black Sea. *Candidate-Degree Thesis (Geography), Marine Hydrophysical Institute, Ukrainian National Academy of Sciences, Sevastopol* .

Belokopytov, V. (2011). Interannual variations of the renewal of waters of the cold intermediate layer in the Black Sea for the last decades. *Physical Oceanography , 20* (5), 347-355.

Berrisford, P., Dee, D., Poli, P., Brugge, R., Fielding, K., Fuentes, M., et al. (2011). The ERA-Interim archive, version 2.0.

Blondeau-Patissier, D., Gower, J. F., Dekker, A. G., Phinn, S. R., & Brando, V. E. (2014). A review of ocean color remote sensing methods and statistical techniques for the detection, mapping and analysis of phytoplankton blooms in coastal and open oceans. *Progress in oceanography , 123*, 123-144.

Blough, N., & Del Vecchio, R. (2002). Biogeochemistry of marine dissolved organic matter. *Chromophoric DOM in the coastal environment in* , 509-546.

Bodeanu, N. (2002). Algal blooms in Romanian Black Sea waters in the last two decades of the XXth century. *Cercetari Marine , 34*, 7-22.

Bondar, C. (2007). The Black Sea level variations and the river-sea interactions. *GeoEcoMarina , 13* (1).

Borysova, O., Kondakov, A., Paleari, S., Rautalahti-Miettinen, E., Stolberg, F., & Daler, D. (2005). Eutrophication in the Black Sea region; Impact assessment and Causal chain analysis. *University of Kalmar, Sweden. 62* , 2005.

Boyer, T. P., Antonov, J. I., Baranova, O. K., Garcia, H. E., Johnson, D. R., Mishonov, A. V., et al. (2013). World ocean database 2013.

Buesseler, K., Livingston, H., Ivanov, L., & Romanov, A. (1994). Stability of the oxic-anoxic interface in the Black Sea. *Deep Sea Research Part I: Oceanographic Research Papers , 41* (2), 283-296.

Cannaby, H., Fach, B. A., Arkin, S. S., & Salihoglu, B. (2015). Climatic controls on biophysical interactions in the Black Sea under present day conditions and a potential future (A1B) climate scenario. *Journal of Marine Systems , 141*, 149-166.

Canuto, V. M., Howard, A., Cheng, Y., & Dubovikov, M. (2001). Ocean turbulence. Part I: One-point closure model—Momentum and heat vertical diffusivities. *Journal of Physical Oceanography , 31* (6), 1413-1426.

Capet, A., Barth, A., Beckers, J.-M., & Marilaure, G. (2012). Interannual variability of Black Sea's hydrodynamics and connection to atmospheric patterns. *Deep Sea Research Part II: Topical Studies in Oceanography , 77*, 128-142.

Capet, A., Troupin, C., Carstensen, J., Grégoire, M., & Beckers, J.-M. (2014). Untangling spatial and temporal trends in the variability of the Black Sea Cold Intermediate Layer and mixed Layer Depth using the DIVA detrending procedure. *Ocean Dynamics , 64* (3), 315-324.

Capet, A., Stanev, E., Beckers, J.-M., Murray, J., & Grégoire, M. (2016). Decline of the Black Sea oxygen inventory. *Biogeosciences , 13*, 1287-1297.

Chassignet, E. P., Hurlburt, H. E., Smedstad, O. M., Halliwell, G. R., Wallcraft, A. J., Metzger, E. J., et al. (2006). *Generalized vertical coordinates for eddy-resolving global and coastal ocean forecasts.* Tech. rep., Naval Research Lab Stennis Space center MS Oceanopgraphy DIV.

Chu, P. C., Ivanov, L. M., & Margolina, T. M. (2005). Seasonal variability of the Black Sea chlorophyll-*a* concentration. *Journal of Marine Systems , 56* (3-4), 243-261.

Cleland, E. E., Chuine, I., Menzel, A., Mooney, H. A., & Schwartz, M. D. (2007). Shifting plant phenology in response to global change. *Trends in ecology \& evolution , 22* (7), 357-365.

Cociasu, A., Dorogan, L., Humborg, C., & Popa, L. (1996). Long-term ecological changes in Romanian coastal waters of the Black Sea. *Marine Pollution Bulletin , 32* (1), 32-38.

Codispoti, L., Friederich, G., Murray, J., & Sakamoto, C. (1991). Chemical variability in the Black Sea: implications of continuous vertical profiles that penetrated the oxic/anoxic interface. *Deep Sea Research Part A. Oceanographic Research Papers , 38,* S691--S710.

Cullen, J. J. (1982). The deep chlorophyll maximum: comparing vertical profiles of chlorophyll *a*. *Canadian Journal of Fisheries and Aquatic Sciences , 39* (5), 791-803.

Daskalov, G. M. (2003). Long-term changes in fish abundance and environmental indices in the Black Sea. *Marine Ecology Progress Series , 255,* 259-270.

Demidov, A. (2008). Seasonal dynamics and estimation of the annual primary production of phytoplankton in the Black Sea. *Oceanology , 48* (5), 664-678.

Demyshev, S., Knysh, V., & Korotaev, G. (2002). Numerical simulation of the seasonal variability of hydrophysical fields in the Black Sea. *Physical Oceanography , 12* (3), 126-141.

Dierssen, H. M., & Randolph, K. (2012). Remote sensing of ocean color. *Encyclopedia of sustainability science and technology* , 8952-8975.

Dorofeev, V., & Sukhikh, L. (2017). Study of long-term variability of Black Sea dynamics on the basis of circulation model assimilation of remote measurements. *Izvestiya, Atmospheric and Oceanic Physics , 53* (2), 224-232.

Dutkiewicz, S., Hickman, A. E., Jahn, O., Henson, S., Beaulieu, C., & Monier, E. (2019). Ocean colour signature of climate change. *Nature communications , 10* (1), 578.

Falkowski, P. G., & Oliver, M. J. (2007). Mix and match: how climate selects phytoplankton. *Nature Reviews Microbiology , 5* (10), 813.

Falkowski, P. G., & Raven, J. A. (2013). *Aquatic photosynthesis.* Princeton University Press.

Filippov, D. (1965). The cold intermediate layer in the Black Sea. *Oceanology , 5*, 47-52.

Fekete, B. M., Vörösmarty, C. J., & Grabs, W. (1999). Global, composite runoff fields based on observed river discharge and simulated water balances. Global, composite runoff fields based on observed river discharge and simulated water balances. Global Runoff Data Centre Koblenz.

Finenko, Z., Suslin, V., & Kovaleva, I. (2014). Seasonal and long-term dynamics of the chlorophyll concentration in the Black Sea according to satellite observations. *Oceanology , 54* (5), 596-605.

Follows, M., & Dutkiewicz, S. (2001). Meteorological modulation of the North Atlantic spring bloom. *Deep Sea Research Part II: Topical Studies in Oceanography , 49* (1-3), 321-344.

Friedl, G., Teodoru, C., & Wehrli, B. (2004). Is the Iron Gate I reservoir on the Danube River a sink for dissolved silica?. Biogeochemistry, 68(1), 21-32.

Galperin, B., Kantha, L., Hassid, S., & Rosati, A. (1988). A quasi-equilibrium turbulent energy model for geophysical flows. *Journal of the Atmospheric Sciences , 45* (1), 55-62.

Garnier, J., Beusen, A., Thieu, V., Billen, G., & Bouwman, L. (2010). N: P: Si nutrient export ratios and ecological consequences in coastal seas evaluated by the ICEP approach. *Global Biogeochemical Cycles , 24* (4).

Geider, R. J. (1987). Light and temperature dependence of the carbon to chlorophyll *a* ratio in microalgae and cyanobacteria: implications for physiology and growth of phytoplankton. *New Phytologist* , 1-34.

Ginzburg, A. I., Kostianoy, A. G., & Sheremet, N. A. (2004). Seasonal and interannual variability of the Black Sea surface temperature as revealed from satellite data (1982--2000). *Journal of Marine Systems , 52* (1-4), 33-50.

Ginzburg, A. I., Kostianoy, A. G., & Sheremet, N. A. (2007). Sea surface temperature variability. Dans *The Black Sea Environment* (pp. 255-275). Springer.

Good, S. A., Martin, M. J., & Rayner, N. A. (2013). EN4: Quality controlled ocean temperature and salinity profiles and monthly objective analyses with uncertainty estimates. Journal of Geophysical Research: Oceans, 118 (12), 6704-6716.

Gordon, H. (1983). A. Morel, Remote assessment of ocean color for interpretation of satellite visible imagery. *Lecture Notes on Coastal and Estuarine Studies. Springer-Verlag. New York* .

Gouretski, V., & Reseghetti, F. (2010). On depth and temperature biases in bathythermograph data: Development of a new correction scheme based on analysis of a global ocean database. *Deep Sea Research Part I: Oceanographic Research Papers , 57* (6), 812-833.

Grayek, S., Stanev, E. V., & Kandilarov, R. (2010). On the response of Black Sea level to external forcing: altimeter data and numerical modelling. *Ocean Dynamics , 60* (1), 123-140.

Greatbatch, R. J. (2000). The north Atlantic oscillation. Stochastic Environmental Research and Risk Assessment , 14 (4-5), 213-242.

Gregg, M. C., & Özsoy, E. (2002). Flow, water mass changes, and hydraulics in the Bosphorus. Journal of Geophysical Research: Oceans, 107 (C3), 2-1.

Gregg, M., & Yakushev, E. (2005). Surface ventilation of the Black Sea's cold intermediate layer in the middle of the western gyre. *Geophysical Research Letters , 32* (3).

Griffies, S. (2018). *Fundamentals of ocean climate models.* Princeton university press.

Groeskamp, S., Griffies, S. M., Iudicone, D., Marsh, R., Nurser, A. G., & Zika, J. D. (2019). The water mass transformation framework for ocean physics and biogeochemistry. *Annual review of marine science , 11,* 271-305.

Gunduz, M., Özsoy, E., & Hordoir, R. (2020). A model of Black Sea circulation with strait exchange (2008--2018). Geoscientific Model Development, 13 (1).

He, Y., Stanev, E. V., Yakushev, E., & Staneva, J. (2012). Black Sea biogeochemistry: response to decadal atmospheric variability during 1960--2000 inferred from numerical modeling. *Marine environmental research , 77*, 90-102.

Holland, P. W., & Welsch, R. E. (1977). Robust regression using iteratively reweighted least-squares. Communications in Statistics-theory and Methods, 6(9), 813-827.

Holt, J., & Umlauf, L. (2008). Modelling the tidal mixing fronts and seasonal stratification of the Northwest European Continental shelf. *Continental Shelf Research , 28* (7), 887-903.

Hu, C., Lee, Z., & Franz, B. (2012). Chlorophyll *a* algorithms for oligotrophic oceans: A novel approach based on three-band reflectance difference. *Journal of Geophysical Research: Oceans , 117* (C1).

Humborg, C., Ittekkot, V., Cociasu, A., & Bodungen, B. v. (1997). Effect of Danube River dam on Black Sea biogeochemistry and ecosystem structure. *Nature , 386* (6623), 385.

Hurrell, J. W. (1995). Decadal trends in the North Atlantic Oscillation: regional temperatures and precipitation. *Science , 269* (5224), 676-679.

Ieva, R., & Otto, S. (2011). Vital Caspian Graphics 2 Opportunities, Aspirations and Challenges. *Zoi Environment Network and GRID-Arendal* .

Ionita, M. (2014). The impact of the East Atlantic/Western Russia pattern on the hydroclimatology of Europe from mid-winter to late spring. Climate , 2 (4), 296-309.

Iselin, C. O. (1939). The influence of vertical and lateral turbulence on the characteristics of the waters at mid-depths. *Eos, Transactions American Geophysical Union , 20* (3), 414-417.

Ivanov, L., Beşiktepe, & Özsoy, E. (1997). The Black Sea cold intermediate layer. Dans *Sensitivity to change: Black Sea, Baltic Sea and North Sea* (pp. 253-264). Springer.

Jaoshvili, S. (2002). The rivers of the Black Sea.

Ivanov, L., Backhaus, J., Özsoy, E., & Wehde, H. (2001). Convection in the Black Sea during cold winters. *Journal of marine systems , 31* (1-3), 65-76.

Jarosz, E., Teague, W. J., Book, J. W., & Beşiktepe,. (2011). On flow variability in the Bosphorus Strait. Journal of Geophysical Research: Oceans, 116 (C8).

Jerlov, N. (1974). Significant relationships between optical properties of the sea. *Optical aspects of oceanography* , 77-94.

JGOFS (Joint Global Ocean Flux Study) 1994. Protocols for E. AGIRBAS, A.M. FEYZIOGLU, U. KOPUZ, A. VALENTE, I. YILDIZ 335 the Joint Global Ocean Flux Study (JGOFS). Core Measurements, Manual and Guides, 29: 97-100.

Jickells, T. (1995). Atmospheric inputs of metals and nutrients to the oceans: their magnitude and effects. *Marine Chemistry , 48* (3-4), 199-214.

Käse, L., & Geuer, J. K. (2018). Phytoplankton responses to marine climate change--an introduction. Dans *YOUMARES 8--Oceans Across Boundaries: Learning from each other* (pp. 55-71). Springer.

Kantha, L. H., & Clayson, C. A. (2000). *Numerical models of oceans and oceanic processes* (Vol. 66). Elsevier.

Kara, A. B., Wallcraft, A. J., & Hurlburt, H. E. (2005). How does solar attenuation depth affect the ocean mixed layer? Water turbidity and atmospheric forcing impacts on the simulation of seasonal mixed layer variability in the turbid Black Sea. *Journal of climate , 18* (3), 389-409.

Karakaş, D., Ölmez, I., Tosun, S., & Tuncel, G. (2004). Trace and major element compositions of Black Sea aerosol. *Journal of radioanalytical and nuclear chemistry , 259* (1), 187-192.

Kazmin, A. S., Zatsepin, A. G., & Kontoyiannis, H. (2010). Comparative analysis of the long-term variability of winter surface temperature in the Black and Aegean Seas during 1982--2004

associated with the large-scale atmospheric forcing. *International Journal of Climatology , 30* (9), 1349-1359.

Kideys, A. E. (1994). Recent dramatic changes in the Black Sea ecosystem: the reason for the sharp decline in Turkish anchovy fisheries. *Journal of Marine Systems , 5* (2), 171-181.

Kideys, A. E. (2002). Fall and rise of the Black Sea ecosystem. *Science , 297* (5586), 1482-1484.

Koçak, M., Mihalopoulos, N., Tutsak, E., Violaki, K., Theodosi, C., Zarmpas, P., et al. (2016). Atmospheric Deposition of Macro Nutrients (DIN and DIP) onto the Black Sea and implications on marine productivity. *J. Atmos. Sci. , 13*, 1727-1739.

Konovalov, S., & Murray, J. (2001). Variations in the chemistry of the Black Sea on a time scale of decades (1960--1995). *Journal of Marine Systems , 31* (1-3), 217-243.

Konovalov, S. K., Murray, J. W., & Luther III, G. W. (2005). Black Sea Biogeochemistry. *Oceanography , 18* (2), 24.

Kontoyiannis, H., Papadopoulos, V., Kazmin, A., Zatsepin, A., & Georgopoulos, D. (2012). Climatic variability of the sub-surface sea temperatures in the Aegean-Black Sea system and relation to meteorological forcing. *Climate dynamics , 39* (6), 1507-1525.

Kopelevich, O., Sheberstov, S., Yunev, O., Basturk, O., Finenko, Z., Nikonov, S., et al. (2002). Surface chlorophyll in the Black Sea over 1978--1986 derived from satellite and in situ data. *Journal of marine systems , 36* (3-4), 145-160.

Kopelevich, O., Sheberstov, S., Sahling, I., Vazyulya, S., & Burenkov, V. (2013). Bio-optical characteristics of the Russian Seas from satellite ocean color data of 1998-2012. *Proceedings of the VII International Conference "Current problems in Optics of Natural Waters (ONW 2013)", St.-Petersburg (Russia).*

Korotaev, G., Oguz, T., Nikiforov, A., & Koblinsky, C. (2003). Seasonal, interannual, and mesoscale variability of the Black Sea upper layer circulation derived from altimeter data. *Journal of Geophysical Research: Oceans , 108* (C4).

Korotaev, G., Knysh, V., & Kubryakov, A. (2014). Study of formation process of cold intermediate layer based on reanalysis of Black Sea hydrophysical fields for 1971--1993. *Izvestiya, Atmospheric and Oceanic Physics , 50* (1), 35-48.

Krichak, S., Tsidulko, M., & Alpert, P. (2000). Monthly synoptic patterns associated with wet/dry conditions in the eastern Mediterranean. *Theoretical and Applied Climatology , 65* (3-4), 215-229.

Krichak, S., Kishcha, P., & Alpert, P. (2002). Decadal trends of main Eurasian oscillations and the Eastern Mediterranean precipitation. Theoretical and Applied Climatology , 72 (3-4), 209-220.

Krichak, S. O., & Alpert, P. (2005). Decadal trends in the east Atlantic--west Russia pattern and Mediterranean precipitation. International journal of climatology: a journal of the Royal Meteorological Society , 25 (2), 183-192.

Kubilay, N., Yemenicioglu, S., & Saydam, A. (1995). Airborne material collections and their chemical composition over the Black Sea. *Marine Pollution Bulletin , 30* (7), 475-483.

Kubryakov, A., & Stanichny, S. (2015). Seasonal and interannual variability of the Black Sea eddies and its dependence on characteristics of the large-scale circulation. *Deep Sea Research Part I: Oceanographic Research Papers , 97*, 80-91.

Kubryakov, A. A., Stanichny, S. V., Zatsepin, A. G., & Kremenetskiy, V. V. (2016). Long-term variations of the Black Sea dynamics and their impact on the marine ecosystem. *Journal of Marine Systems , 163*, 80-94.

Lancelot, C., Staneva, J., Van Eeckhout, D., Beckers, J.-M., & Stanev, E. (2002). Modelling the Danube-influenced north-western continental shelf of the Black Sea. II: Ecosystem response

to changes in nutrient delivery by the Danube River after its damming in 1972. *Estuarine, Coastal and Shelf Science , 54* (3), 473-499.

Lascaratos, A. (1993). Estimation of deep and intermediate water mass formation rates in the Mediterranean Sea. *Deep Sea Research Part II: Topical Studies in Oceanography , 40* (6), 1327-1332.

Leppäkoski, E., & Mihnea, P. E. (1996). Enclosed seas under man-induced change: a comparison between the Baltic and Black Seas. *Ambio* , 380-389.

Levang, S. J., & Schmitt, R. W. (2015). Centennial changes of the global water cycle in CMIP5 models. Journal of Climate, 28(16), 6489-6502.

Llope, M., Daskalov, G. M., Rouyer, T. A., Mihneva, V., CHAN, K.-S., Grishin, A. N., et al. (2011). Overfishing of top predators eroded the resilience of the Black Sea system regardless of the climate and anthropogenic conditions. *Global Change Biology , 17* (3), 1251-1265.

Longhurst, A. (1995). Seasonal cycles of pelagic production and consumption. *Progress in oceanography , 36* (2), 77-167.

Longhurst, A. R. (2010). *Ecological geography of the sea.* Elsevier.

Ludwig, W., Dumont, E., Meybeck, M., & Heussner, S. (2009). River discharges of water and nutrients to the Mediterranean and Black Sea: major drivers for ecosystem changes during past and future decades? *Progress in oceanography , 80* (3-4), 199-217.

Ludwig, W., Bouwman, A., Dumont, E., & Lespinas, F. (2010). Water and nutrient fluxes from major Mediterranean and Black Sea rivers: Past and future trends and their implications for the basin-scale budgets. *Global biogeochemical cycles , 24* (4).

Luneva, M. V., Wakelin, S., Holt, J. T., Inall, M. E., Kozlov, I. E., Palmer, M. R., et al. (2019). Challenging vertical turbulence mixing schemes in a tidally energetic environment: 1. 3-D shelf-sea model assessment. *Journal of Geophysical Research: Oceans , 124* (8), 6360-6387.

Madec, G., Delecluse, P., Imbard, M., & Levy, C. (1997). Ocean general circulation model reference manual. *Note du Pôle de modélisation* .

Madec, G., & others. (2015). NEMO ocean engine.

Maritorena, S., Siegel, D. A., & Peterson, A. R. (2002). Optimization of a semianalytical ocean color model for global-scale applications. *Applied optics , 41* (15), 2705-2714.

Mascarenhas, V., & Keck, T. (2018). Marine Optics and Ocean Color Remote Sensing. Dans *YOUMARES 8--Oceans Across Boundaries: Learning from each other* (pp. 41-54). Springer.

Mazzarella, A., Giuliacci, A., & Liritzis, I. (2010). On the 60-month cycle of multivariate ENSO index. Theoretical and applied climatology, 100 (1-2), 23-27.

McClain, C. R. (2009). A decade of satellite ocean color observations. *Annual Review of Marine Science , 1*, 19-42.

McDougall, T. J., & Barker, P. M. (2011). Getting started with TEOS-10 and the Gibbs Seawater (GSW) oceanographic toolbox. *SCOR/IAPSO WG , 127*, 1-28.

McQuatters-Gollop, A., Mee, L. D., Raitsos, D. E., & Shapiro, G. I. (2008). Non-linearities, regime shifts and recovery: The recent influence of climate on Black Sea chlorophyll. *Journal of Marine Systems , 74* (1-2), 649-658.

Medinets, S., & Medinets, V. (2012). Investigations of atmospheric wet and dry nutrient deposition to marine surface in western part of the Black Sea. *Turkish Journal of Fisheries and Aquatic Sciences , 12* (5), 497-505.

Mee, L. D. (1992). The Black Sea in crisis: a need for concerted international action. *Ambio , 21* (4), 278-86.

Mellor, G. L., Ezer, T., & Oey, L. Y. (1994). The pressure gradient conundrum of sigma coordinate ocean models. *Journal of atmospheric and oceanic technology*, *11*(4), 1126-1134.

Mesinger, F., & Arakawa, A. (1976). Numerical methods used in atmospheric models.

Mihailov, M.-E., Stefan, S., Diaconu, V., & Lazar, L. (2016). Longterm variability of the water mass structure on the Romanian Black Sea shelf. *Romanian Reports in Physics , 68* (1), 377-392.

Mikaelyan, A. (1995). Winter bloom of the diatom Nitzschia delicatula in the open waters of the Black Sea. *Marine Ecology Progress Series , 129*, 241-251.

Mikaelyan, A. S., Zatsepin, A. G., & Chasovnikov, V. K. (2013). Long-term changes in nutrient supply of phytoplankton growth in the Black Sea. *Journal of Marine Systems , 117*, 53-64.

Miladinova, S., Stips, A., Garcia-Gorriz, E., & Moy, D. M. (2018). Formation and changes of the Black Sea cold intermediate layer. *Progress in oceanography , 167*, 11-23.

Mobley, C. D. (2004). Optical modeling of ocean waters: Is the case 1-case 2 classification still useful? *Oceanogr , 17* (2), 60-67.

Morel, A., & Prieur, L. (1977). Analysis of variations in ocean color 1. *Limnology and oceanography , 22* (4), 709-722.

Moses, W. J., Gitelson, A. A., Berdnikov, S., & Povazhnyy, V. (2009). Satellite estimation of chlorophyll_*a* concentration using the red and NIR bands of MERIS—The Azov sea case study. *IEEE Geoscience and Remote Sensing Letters , 6* (4), 845-849.

Murray, J., Jannasch, H., Honjo, S., Anderson, R., Reeburgh, W., Top, Z., et al. (1989). Unexpected changes in the oxic/anoxic interface in the Black Sea. *Nature , 338* (6214), 411.

Murray, J. W., Top, Z., & Özsoy, E. (1991). Hydrographic properties and ventilation of the Black Sea. *Deep Sea Research Part A. Oceanographic Research Papers , 38*, S663--S689.

Murray, J. W. (1995). Oxidation-reduction environments: the suboxic zone in the Black Sea. *Aquatic chemistry: interfacial and interspecies processes* .

Nezlin, N. P., Kostianoy, A. G., & Grégoire, M. (1999). Patterns of seasonal and interannual changes of surface chlorophyll concentration in the Black Sea revealed from the remote sensed data. *Remote Sensing of Environment , 69* (1), 43-55.

Nezlin, N., Afanasyev, Y. D., Ginzburg, A., & Kostianoy, A. (2002). Remotely sensed studies of phytoplankton dynamics under physical forcing in different ocean regions. *Advances in Space Research , 29* (1), 99-106.

Nezlin, N. P. (2006). Seasonal and interannual variability of remotely sensed chlorophyll. Dans *The Black Sea Environment* (pp. 333-349). Springer.

Nurser, A., Marsh, R., & Williams, R. G. (1999). Diagnosing water mass formation from air--sea fluxes and surface mixing. *Journal of physical oceanography , 29* (7), 1468-1487.

O'Dea E, Furner R, Wakelin S, Siddorn J, While J, Sykes P, King R, Holt J, Hewitt H (2017) The CO5 configuration of the 7km Atlantic margin model: large-scale biases and sensitivity to forcing, physics options and vertical resolution. Geosci Model Dev 10(8):2947–2969.

Oguz, T., Latun, V., Latif, M., Vladimirov, V., Sur, H., Markov, A., et al. (1993). Circulation in the surface and intermediate layers of the Black Sea. *Deep Sea Research Part I: Oceanographic Research Papers , 40* (8), 1597-1612.

Oguz, T., Malanotte-Rizzoli, P., & Aubrey, D. (1995). Wind and thermohaline circulation of the Black Sea driven by yearly mean climatological forcing. *Journal of Geophysical Research: Oceans , 100* (C4), 6845-6863.

Oguz, T., & Besiktepe, S. (1999). Observations on the Rim Current structure, CIW formation and transport in the western Black Sea. *Deep Sea Research Part I: Oceanographic Research Papers , 46* (10), 1733-1753.

Oguz, T., Deshpande, A., & Malanotte-Rizzoli, P. (2002). The role of mesoscale processes controlling biological variability in the Black Sea coastal waters: inferences from SeaWIFS-derived surface chlorophyll field. *Continental Shelf Research , 22* (10), 1477-1492.

Oguz, T., Cokacar, T., Malanotte-Rizzoli, P., & Ducklow, H. W. (2003). Climatic warming and accompanying changes in the ecological regime of the Black Sea during 1990s. *Global Biogeochemical Cycles , 17* (3).

Oguz, T., & Ediger, D. (2006). Comparision of in situ and satellite-derived chlorophyll pigment concentrations, and impact of phytoplankton bloom on the suboxic layer structure in the western Black Sea during May--June 2001. *Deep Sea Research Part II: Topical Studies in Oceanography , 53* (17-19), 1923-1933.

Oguz, T., Dippner, J. W., & Kaymaz, Z. (2006). Climatic regulation of the Black Sea hydro-meteorological and ecological properties at interannual-to-decadal time scales. *Journal of Marine Systems , 60* (3-4), 235-254.

Oguz, T., Salihoglu, B., & Fach, B. (2008). A coupled plankton--anchovy population dynamics model assessing nonlinear controls of anchovy and gelatinous biomass in the Black Sea. *Marine Ecology Progress Series , 369*, 229-256.

Oguz, T., & Velikova, V. (2010). Abrupt transition of the northwestern Black Sea shelf ecosystem from a eutrophic to an alternative pristine state. *Marine Ecology Progress Series , 405*, 231-242.

Özkan, E. Y., & BÜYÜKIŞIK, H. B. (2012). Recent changes in the physicochemical parameters of the Black Sea. *Turkish Journal of Engineering and Environmental Sciences , 36* (2), 153-160.

Özsoy, E., Top, Z., White, G., & Murray, J. W. (1991). Double diffusive intrusions, mixing and deep sea convection processes in the Black Sea. Dans *Black Sea Oceanography* (pp. 17-42). Springer.

Özsoy, E., Latif, M., Tugrul, S., & Ünlüata, (1995). Exchanges with the Mediterranean, fluxes and boundary mixing processes in the Black Sea. *Bulletin de l'Institut Océanographique. Mediterranean Tributary Seas, Monaco* , 1-25.

Özsoy, E., & Ünlüata, (1997). Oceanography of the Black Sea: a review of some recent results. *Earth-Science Reviews , 42* (4), 231-272.

O'Reilly, J. E., Maritorena, S., Mitchell, B. G., Siegel, D. A., Carder, K. L., Garver, S. A., et al. (1998). Ocean color chlorophyll algorithms for SeaWiFS. *Journal of Geophysical Research: Oceans , 103* (C11), 24937-24953.

Organization, W. H., & others. (2018). *The state of food security and nutrition in the world 2018: building climate resilience for food security and nutrition.* Food \& Agriculture Org.

Ovchinnikov, I., & POPOV, I. (1984). The formation of a cold intermediate layer in the Black Sea. *DOKLADY AKADEMII NAUK SSSR , 279* (4), 986-989.

Palazov, A., Ciliberti, S., Peneva, E., Gregoire, M., Staneva, J., Lemieux-Dudon, B., et al. (2019). Black sea observing system. Frontiers in Marine Science , 6, 315.

Panin N. 1996. Impact of global changes on geo-environmental and coastal zone state of the BlackSea. Danube Delta-Black Sea System under Global Change Impact. In: Malit A., Gomoiu M.-T.and Panin N. (eds.), Geo-Eco-Marina 1, pp. 1–6.

Platt, T., Bouman, H., Devred, E., Fuentes-Yaco, C., & Sathyendranath, S. (2005). Physical forcing and phytoplankton distributions. *Scientia Marina , 69* (S1), 55-73.

Polonsky, A., & Popov, Y. I. (2011). Conditions for Formation of the Cold Intermediate Layer in the Black Sea. *MGI, Sevastopol (In Russian)* .

Pommier, J., Gosselin, M., & Michel, C. (2008). Size-fractionated phytoplankton production and biomass during the decline of the northwest Atlantic spring bloom. *Journal of plankton research , 31* (4), 429-446.

Popa, A. (1993). Liquid and sediment inputs of the Danube River into the north-western Black Sea. *Transport of carbon and nutrients in lakes and estuaries* (Part 6), 137-149.

Rîmbu, N., Boroneanţ, C., Buţă, C., & Dima, M. (2002). Decadal variability of the Danube river flow in the lower basin and its relation with the North Atlantic Oscillation. *International Journal of Climatology: A Journal of the Royal Meteorological Society , 22* (10), 1169-1179.

Ragueneau, O., Lancelot, C., Egorov, V., Vervlimmeren, J., Cociasu, A., Deliat, G., et al. (2002). Biogeochemical transformations of inorganic nutrients in the mixing zone between the Danube River and the north-western Black Sea. *Estuarine, Coastal and Shelf Science , 54* (3), 321-336.

Rîmbu, N., Treut, H. L., Janicot, S., Boroneant, C., & Laurent, C. (2001). Decadal precipitation variability over Europe and its relation with surface atmospheric circulation and sea surface temperature. *Quarterly Journal of the Royal Meteorological Society , 127* (572), 315-329.

Rimbu, N., Onac, B. P., & Racovita, G. (2012). Large-scale anomaly patterns associated to temperature variability inside Scarisoara Ice Cave. *International journal of climatology , 32* (10), 1495-1502.

Roquet, F., Madec, G., McDougall, T. J., & Barker, P. M. (2015). Accurate polynomial expressions for the density and specific volume of seawater using the TEOS-10 standard. *Ocean Modelling , 90*, 29-43.

Roy, S., Llewellyn, C. A., Egeland, E. S., & Johnsen, G. (2011). *Phytoplankton pigments: characterization, chemotaxonomy and applications in oceanography*. Cambridge University Press.

Sathyendranath, S., Longhurst, A., Caverhill, C. M., & Platt, T. (1995). Regionally and seasonally differentiated primary production in the North Atlantic. *Deep Sea Research Part I: Oceanographic Research Papers , 42* (10), 1773-1802.

Seber, G. A. (2015). Nonlinear regression models. In The linear model and hypothesis (pp. 117-128). Springer, Cham.

Shapiro, G., Wobus, F., & Aleynik, D. (2011). Seasonal and inter-annual temperature variability in the bottom waters over the western Black Sea shelf. *Ocean Science , 7* (5), 585-596.

Shapiro, G., Luneva, M., Pickering, J., & Storkey, D. (2013). The effect of various vertical discretization schemes and horizontal diffusion parameterization on the performance of a 3-D ocean model: the Black Sea case study. *Ocean Science , 9* (2), 377.

Shchepetkin, A. F., & McWilliams, J. C. (2005). The regional oceanic modeling system (ROMS): a split-explicit, free-surface, topography-following-coordinate oceanic model. *Ocean modelling , 9* (4), 347-404.

Shiganova, T., Musaeva, E., Arashkevich, E., Kamburska, L., Stefanova, K., Mihneva, V., et al. (s.d.). State of Environment Report 2001-2006/7.

Sommerwerk, N., Hein, T., Schneider-Jacoby, M., Baumgartner, C., Ostojic, A., Siber, R., et al. (2009). The Danube river basin. *Rivers of Europe* , 59-112.

Sorokin, Y. I. (2002). The Black Sea: ecology and oceanography.

Speer, K., & Tziperman, E. (1992). Rates of water mass formation in the North Atlantic Ocean. *Journal of Physical Oceanography , 22* (1), 93-104.

Spencer, D. W., & Brewer, P. G. (1971). Vertical advection diffusion and redox potentials as controls on the distribution of manganese and other trace metals dissolved in waters of the Black Sea. *Journal of Geophysical Research , 76* (24), 5877-5892.

Stanev, E. V. (1990). On the mechanisms of the Black Sea circulation. *Earth-Science Reviews , 28* (4), 285-319.

Stanev, E. V., & Beckers, J.-M. (1999). Numerical simulations of seasonal and interannual variability of the Black Sea thermohaline circulation. *Journal of Marine Systems , 22* (4), 241-267.

Stanev, E. V., Bowman, M. J., Peneva, E. L., & Staneva, J. V. (2003). Control of Black Sea intermediate water mass formation by dynamics and topography: Comparison of numerical simulations, surveys and satellite data. *Journal of Marine Research , 61* (1), 59-99.

Stanev, E. V. (2005). Black Sea dynamics. *Oceanography , 18* (2), 56.

Stanev, E., He, Y., Grayek, S., & Boetius, A. (2013). Oxygen dynamics in the Black Sea as seen by Argo profiling floats. *Geophysical Research Letters , 40* (12), 3085-3090.

Stanev, E. V., He, Y., Staneva, J., & Yakushev, E. (2014). Mixing in the Black Sea detected from the temporal and spatial variability of oxygen and sulfide–Argo float observations and numerical modelling. Biogeosciences, 11(20), 5707-5732.

Stanev, E. V., Peneva, E., & Chtirkova, B. (2019). Climate change and regional ocean water mass disappearance: case of the Black Sea. *Journal of Geophysical Research: Oceans , 124* (7), 4803-4819.

Staneva, J. V., Dietrich, D. E., Stanev, E. V., & Bowman, M. J. (2001). Rim current and coastal eddy mechanisms in an eddy-resolving Black Sea general circulation model. *Journal of Marine Systems , 31* (1-3), 137-157.

Staneva, J., & Stanev, E. (2002). Water mass formation in the Black Sea during 1991--1995. *Journal of Marine Systems , 32* (1-3), 199-218.

Starosolszky, O. (1998). Effect of precipitation and temperature changes on the flow regime of the Danube river. *Proc. Second Int. Conf. Climate and Water (Helsinki Univ. Technol., Helsinki, Finland), 1998.*

Stewart, K., Kassakian, S., Krynytzky, M., DiJulio, D., & Murray, J. W. (2007). Oxic, suboxic, and anoxic conditions in the Black Sea. Dans *The Black Sea flood question: Changes in coastline, climate, and human settlement* (pp. 1-21). Springer.

Strokal, M., & Kroeze, C. (2013). Nitrogen and phosphorus inputs to the Black Sea in 1970--2050. *Regional Environmental Change , 13* (1), 179-192.

Sur, H., Ö zsoy, E., & Ünlüata, (1994). Boundary current instabilities, upwelling, shelf mixing and eutrophication processes in the Black Sea. *Progress in Oceanography , 33* (4), 249-302.

Sverdrup, H. (1953). On conditions for the vernal blooming of phytoplankton. *J. Cons. Int. Explor. Mer , 18* (3), 287-295.

Takahashi, K., Kuwata, A., Saito, H., & Ide, K. (2008). Grazing impact of the copepod community in the Oyashio region of the western subarctic Pacific Ocean. *Progress in Oceanography , 78* (3), 222-240.

Teodoru, C., & Wehrli, B. (2005). Retention of sediments and nutrients in the Iron Gate I Reservoir on the Danube River. *Biogeochemistry , 76* (3), 539-565.

Theodosi, C., Stavrakakis, S., Koulaki, F., Stavrakaki, I., Moncheva, S., Papathanasiou, E., et al. (2013). The significance of atmospheric inputs of major and trace metals to the Black Sea. *Journal of Marine Systems , 109*, 94-102.

Tolmazin, D. (1985). Changing coastal oceanography of the Black Sea. I: Northwestern shelf. *Progress in Oceanography , 15* (4), 217-276.

Tugrul, S., Basturk, O., Saydam, C., & Yilmaz, A. (1992). Changes in the hydrochemistry of the Black Sea inferred from water density profiles. *Nature , 359* (6391), 137.

Tugrul, S., & Salihoglu, I. (2003). Spatial and temporal variations in the hydro-chemical properties of the Black Sea upper layer. *Oceanography of the Eastern Mediterranean and Black Sea: Similarities and Differences of Two Interconnected Basins. Tubitak Publishers, Ankara, Turkey* , 578-582.

Umlauf, L., & Burchard, H. (2003). A generic length-scale equation for geophysical turbulence models. *Journal of Marine Research , 61* (2), 235-265.

Umlauf, L., Burchard, H., & Bolding, K. (2006). GOTM: source code and test case documentation. *Devel version-pre , 4*.

U.S. National Oceanographic Data Center (2006), Global Temperature-Salinity Profile Programme, U.S. Dep. of Commer., Natl. Oceanic and Atmos. Admin., Natl. Oceanogr. Data Cent., Silver Spring, Md. [Available at http://www.nodc.noaa.gov/GTSPP/]

Valty, P., de Viron, O., Panet, I., & Collilieux, X. (2015). Impact of the North Atlantic Oscillation on Southern Europe water distribution: Insights from geodetic data. *Earth Interactions , 19* (10), 1-16.

Varenik, A., Konovalov, S., & Stanichny, S. (2015). Quantifying importance and scaling effects of atmospheric deposition of inorganic fixed nitrogen for the eutrophic Black Sea. *Biogeosciences , 12* (21), 6479-6491.

Vedernikov, V., & Demidov, A. (2002). Long-term and seasonal variability of chlorophyll and primary production in the eastern regions of the Black Sea. *Multidisciplinary investigations of the northeast part of the Black Sea* , 212-234.

Velikova, V., Moncheva, S., & Petrova, D. (1999). Phytoplankton dynamics and red tides (1987--1997) in the Bulgarian Black Sea. *Water Science and Technology , 39* (8), 27-36.

Vershinin, A., Moruchkov, A., Leighfield, T., Sukhanova, I., Pan'kov, S., Morton, S., et al. (2005). Potentially toxic algae in the coastal phytoplankton of the northeast Black Sea in 2001--2002. *Oceanology , 45* (2), 224-232.

Vinberg, G.G., Muravleva E. P., and Finenko Z. Z., Some data on chlorophyll concentration and primary production in the Black Sea plankton, Tr. Sevast. Biol. Stn. 17, 212–220 (1964).

Vinogradov, M., Shushkina, E., Mikaelyan, A., & Nezlin, N. (1999). Temporal (seasonal and interannual) changes of ecosystem of the open waters of the Black Sea. Dans *Environmental Degradation of the Black Sea: Challenges and Remedies* (pp. 109-129). Springer.

Walin, G. (1982). On the relation between sea-surface heat flow and thermal circulation in the ocean. *Tellus , 34* (2), 187-195.

Werdell, P. J., McKinna, L. I., Boss, E., Ackleson, S. G., Craig, S. E., Gregg, W. W., et al. (2018). An overview of approaches and challenges for retrieving marine inherent optical properties from ocean color remote sensing. *Progress in oceanography , 160*, 186-212.

West, S. (2003). 'The Most Marvellous of All Seas'; the Greek Encounter with the Euxine. *Greece & Rome , 50* (2), 151-167.

Yakushev, E., Chasovnikov, V., Murray, J., Pakhomova, S., Podymov, O., & Stunzhas, P. (2007). Vertical hydrochemical structure of the Black Sea. Dans *The Black Sea Environment* (pp. 277-307). Springer.

Yoder, J. A., McClain, C. R., Feldman, G. C., & Esaias, W. E. (1993). Annual cycles of phytoplankton chlorophyll concentrations in the global ocean: A satellite view. Global Biogeochemical Cycles, 7(1), 181-193.

Yunev, O. A., Vedernikov, V. I., Basturk, O., Yilmaz, A., Kideys, A. E., Moncheva, S., et al. (2002). Long-term variations of surface chlorophyll *a* and primary production in the open Black Sea. *Marine ecology progress series , 230*, 11-28.

Yunev, O. A., Moncheva, S., & Carstensen, J. (2005). Long-term variability of vertical chlorophyll *a* and nitrate profiles in the open Black Sea: eutrophication and climate change. *Marine Ecology Progress Series , 294*, 95-107.

Yunev, O. A., Carstensen, J., Moncheva, S., Khaliulin, A., Ærtebjerg, G., & Nixon, S. (2007). Nutrient and phytoplankton trends on the western Black Sea shelf in response to cultural eutrophication and climate changes. *Estuarine, Coastal and Shelf Science , 74* (1-2), 63-76.

Zaitsev, Y. P. (1992). Recent changes in the trophic structure of the Black Sea. *Fisheries Oceanography , 1* (2), 180-189.

Zaitsev, Y., & Mamaev, V. (1997). Biological diversity in the Black Sea. *Black Sea Environmental Series , 3*, 14-17.

Zaitsev, Y., Aleksandrov, B., Berlinsky, N., & Zenetos, A. (2002). The Black Sea. Europe's biodiversity--biogeographical regions and seas. *European Environment Agency, Copenhagen* .

Zatsepin, A. G., Ginzburg, A. I., Kostianoy, A. G., Kremenetskiy, V. V., Krivosheya, V. G., Stanichny, S. V., et al. (2003). Observations of Black Sea mesoscale eddies and associated horizontal mixing. *Journal of Geophysical Research: Oceans , 108* (C8).

Zibordi, G., Mélin, F., Berthon, J.-F., & Talone, M. (2015). In situ autonomous optical radiometry measurements for satellite ocean color validation in the Western Black Sea. *Ocean Science , 11* (2), 275-286.

Zinke, A. (1999). Dams and the Danube: lessons from the environmental impact. *Presentation at the first World Commission of Dams Forum Meeting, March,* (pp. 25-26).